# Novel Methods and Circuits for Field Shaping In Deep Brain Stimulation

**Virgilio Valente**

A thesis submitted to

University College London for the degree of

**DOCTOR OF PHILOSOPHY**

Supervised by

*Professor Andreas Demosthenous*

*Professor Richard Bayford*

**Department of Electronic Engineering**

*University College London*

# Declaration

I, Virgilio Valente, confirm that the work presented in this thesis is my own. Where information has been derived from other sources, I confirm that this has been indicated in the thesis.

**‘Anyone who has never made a mistake, has never tried anything new’**

*Albert Einstein*

# Acknowledgement

It is a pleasure to thank all the people that have made this thesis possible.
I would like to start by showing my gratitude to my PhD supervisors, Prof. Andreas Demosthenous and Prof. Richard Bayford, who have accompanied me through this journey, providing me with invaluable insight, suggestions and support that helped me strengthen the different aspects of my work and overcome arduous challenges. My gratitude also extends to Mr. Peter Langlois for his suggestions on the technical aspects of the work.

It has been a pleasure to share my daily work with the friendly and pleasant group of colleagues in office 708. The numerous technical discussions, suggestions and support have helped me to overcome difficult obstacles and improve several aspect of my work. Beyond Electronics, their friendliness has provided me with a gratifying environment throughout my PhD experience.

I am truly indebted to my family, who unconditionally supported me throughout my studies, and all my friends in Milan for all their enjoyable visits and for always taking care of me during my (short) breaks.

Finally, I want to thank my partner, Ra, who constantly believed in me, listened to me and supported me during hard times, making my PhD a pleasant cruise.

# Abstract

Deep Brain Stimulation (DBS) is a clinical tool used to treat various neurological disorders, including tremor, Parkinson's disease (PD) and dystonia. Today's routine use of this therapy is a result of the pioneering work of Benabid and colleagues, who assessed the benefits of applying high-frequency stimulation to the ventral intermediate nucleus and reported substantial long-term improvements in PD patients. Clinical applications of DBS, however, have preceded research and left a number of challenges to optimise this therapeutic technique in terms of quality, therapy costs and understanding of its underlying mechanisms. DBS is based on monopolar or bipolar stimulation techniques, which are characterised by a limited control over the effects of stimulation and, in particular, over the shape and direction of the electric field propagating around the electrode. This thesis proposes two approaches to achieve dynamic electric field control during deep brain stimulation. The first method is based on the use of current-steering multipolar electrode drive, adopted to split the stimulation current between 2 or more contacts, in order to shift the stimulation field to a desired location. The work included the design, development and testing of an integrated circuit current-steering tripolar current source, developed in AMS 0.35$\mu$m technology. The second method is based on the use of phased arrays (PAs) in order to create an electromagnetic beam, which can be steered to a desired location. Computational models have shown the ability to steer and focus the electromagnetic fields in brain tissue by varying the phase and frequency of stimulation. Modelling simulations have shown that the use of multipolar electrode configurations is essential to achieve dynamic control over the shape and area of tissue stimulated. Configurations with larger number of cathodes allow for several stimulation patterns, making this stimulation approach beneficial in a clinical environment. Tests on the performance of the integrated tripolar current source have

shown its capability to generate stimulation currents up to 1.86mA, to linearly steer the stimulation current to one of the anodes and to generate biphasic square and exponential current pulses, with time constant up to 28ms. In vitro experiments, carried out to map the electric potential generated by a dynamic tripolar current source, validated the model results, by showing the ability to shape the potential distribution around the electrode during stimulation. Finally, models of the behaviour of PA fields in brain tissue have shown that PAs could be introduced to DBS to allow for more accurate field steering and shaping in DBS. This thesis presents methods and implementations to achieve dynamic field shaping in DBS, which can greatly ameliorate the efficacy of clinical DBS.

# Contents

# Abbreviations

| | |
|---|---|
| AF | Array Factor |
| AMS | Austriamicrosystems |
| ASIC | Application Specific Integrated Circuit |
| CMOS | Complementary Metal-Oxide Semiconductor |
| CPA | Constant Phase Angle |
| CPE | Constant Phase Element |
| DAC | Digital to Analog Converter |
| DBS | Deep Brain Stimulation |
| DC | Direct Current |
| DNL | Differential Nonlinearity |
| DTI | Diffusion Tension Imaging |
| EBI | Electrode Brain Interface |
| EEI | Electrode Electrolyte Interface |
| EM | Electromagnetic |

| | |
|---|---|
| ET | Essential Tremor |
| ETI | Electrode Tissue Interface |
| FDA | Food and Drug Administration |
| FEM | Finite Element Method |
| FS | Full Scale |
| GP | Globus Pallidus |
| IC | Integrated Circuit |
| INL | Integral Nonlinearity |
| IPG | Implanted Pulse Generator |
| LSB | Least Significant Bit |
| MOSFET | Metal-Oxide Semiconductor Field Effect Transistor |
| NMOS | n-channel MOSFET |
| OTA | Operational Transconductance Amplifier |
| PA | Phased Array |
| PD | Parkinson's Disease |
| PMOS | p-channel MOSFET |
| SN | Substantia Nigra |
| SR | Slew Rate |
| STN | Subthalamic Nucleus |
| TS | Tourette Syndrome |

| | |
|---|---|
| VIC | Voltage-to-current Converter |
| VIM | Ventral Intermediate |
| VTA | Volume of Tissue Activated |

# List of Figures

# List of Tables

# 1

# Introduction

Deep brain stimulation (DBS) is a clinical tool used to treat various neurological disorders, including chronic pain, incontinence and movement disorders. Today's routine use of such therapy derives from promising results obtained by the pioneering work of Benabid and colleagues, who assessed the benefits of applying high-frequency stimulation to the ventral intermediate nucleus [1]. Substantial long-term improvements were reported on several cases of patients affected by Parkinson's disease (PD), along with mild adverse events. Thanks to these findings DBS has been widely accepted as a therapy for the treatment of tremor and all major symptoms of PD. The Food and Drug Administration (FDA) approved DBS of the thalamus for PD and essential tremor (ET) in 1997, of subthalamic nucleus (STN) and globus

pallidus (GP) for PD in 2002 and for dystonia in 2003[1].

More recently DBS has been assessed as a possible therapy for additional neurological conditions including dystonia, Tourette Syndrome (TS) and epilepsy [3]. The clinical efficacy of DBS has been reported in a large number of studies, in terms of overall short, intermediate-term positive outcome in patients' ability to perform daily activities, and few cases of long-term sustained benefits [3].

Although the introduction of DBS as a clinically approved therapy occurred in recent years, the history of DBS goes back to the $19^{th}$ century, when direct stimulation of brain cortex was first introduced [2]. A brief history of the key achievements since then is reported in Figure 1.1.

## 1.1 DBS Modelling

Clinical applications have preceded research and raised a number of challenges to optimise this therapeutic technique in terms of efficacy, therapy costs and understanding of its underlying mechanisms [4]. The limited accessibility of brain's anatomical structures for measuring and recording during stimulation has led to the development of computational models that represent the stimulation target area and the effects of varying stimulation factors, including electrode configuration and location, electrode geometry, number and orientation of active contacts [5, 6, 7, 8]. A key parameter, thought to be strictly related to the behaviour and efficacy of DBS, is represented by the volume of tissue activated (VTA) during stimulation [9]. Due to the inability to measure the VTA during therapeutic stimulation, researchers have attempted to quantitatively characterise the VTA by the adoption of three-dimensional representations of the DBS electrodes and the anatomical structure of the stimulation target [10, 11, 12]. The VTA is usually quantitatively estimated as a function of stimulation parameters, electrode configuration and geometry. One

[1]Source: www.fda.gov

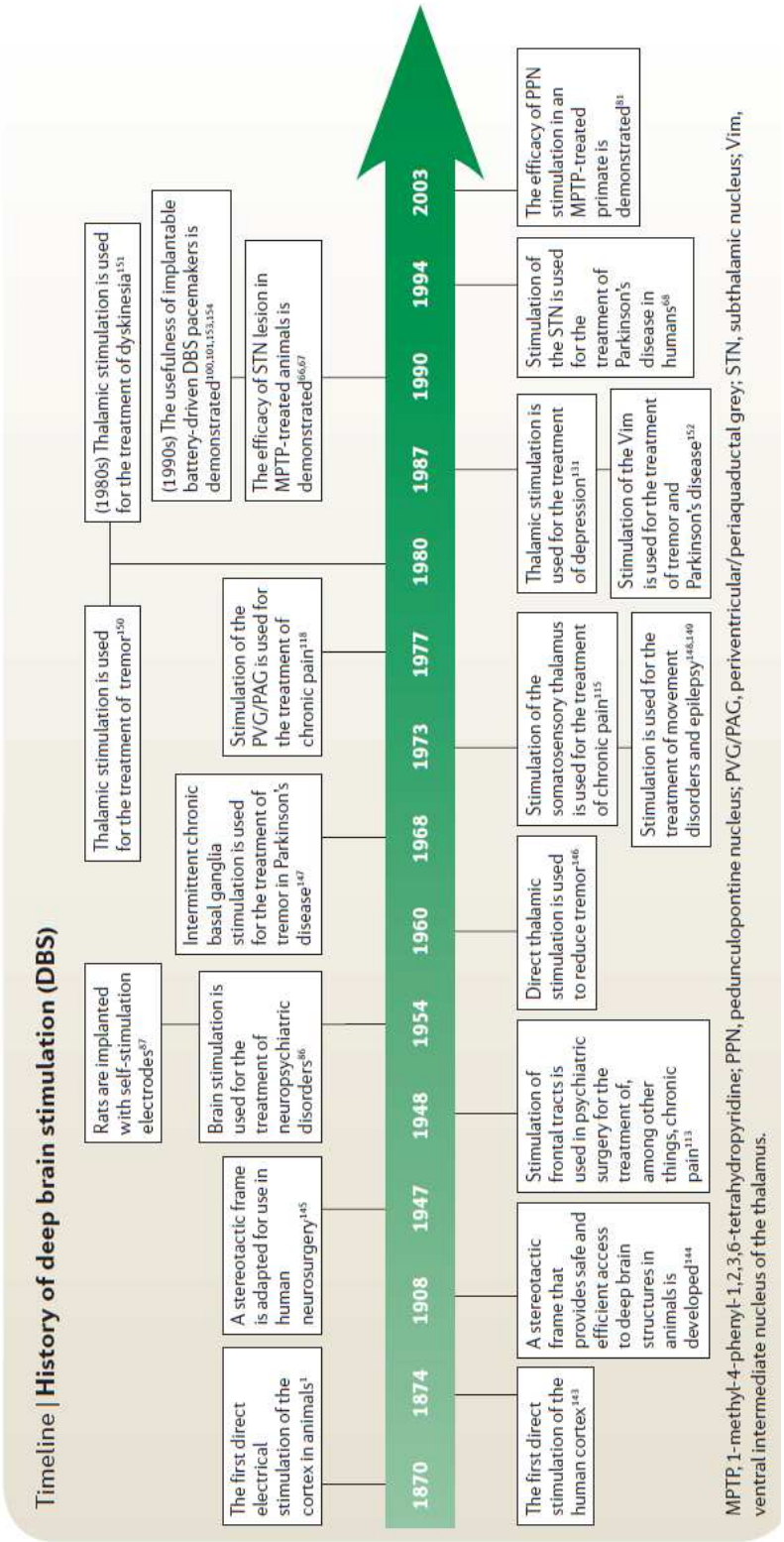


**Figure 1.1:** History of deep brain stimulation (DBS) [2].

example of such models is given in Figure 1.2, which illustrates a DBS electrode implanted in the thalamus and the VTA during stimulation relative to MRI slices of the brain [12].

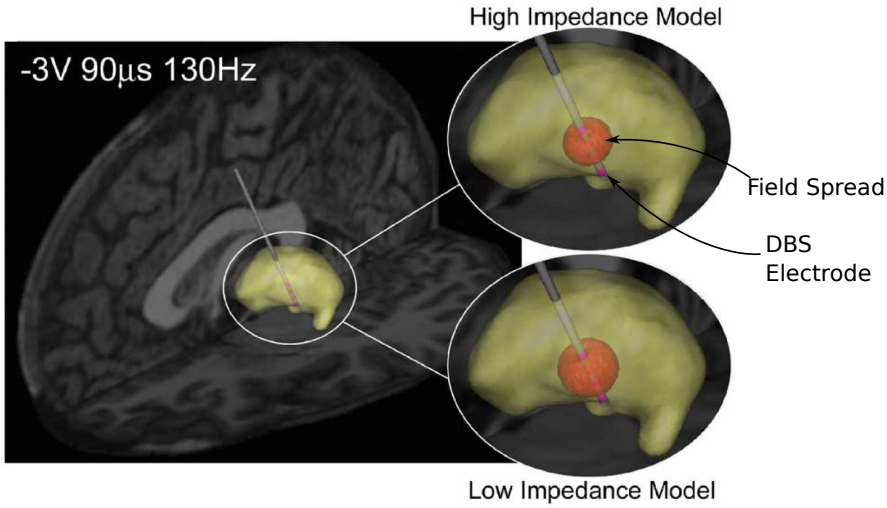


**Figure 1.2:** 3D Model of field spread caused by DBS [12].

Several studies have accounted for additional factors contributing to a more accurate estimation of the VTA, including electrode impedance [12, 13], electrode contact location [5, 14], tissue inhomogeneities and anisotropies [12, 15] and local conductivity changes (encapsulation layer) [11, 12, 16]. Figure 1.3 shows a comparison between the VTA calculated using isotropic medium properties and the VTA calculated adopting diffusion tension MRI (DTI) data representing the anisotropies and inhomogeneities of the tissue surrounding the electrode [17]. Intraoperative anatomical and DT MRIs have become common techniques to extract realistic information on the anatomical position of the implanted electrode with respect to the anatomical regions of the brain and fibre orientation, and dielectric properties of live brain tissue [17].

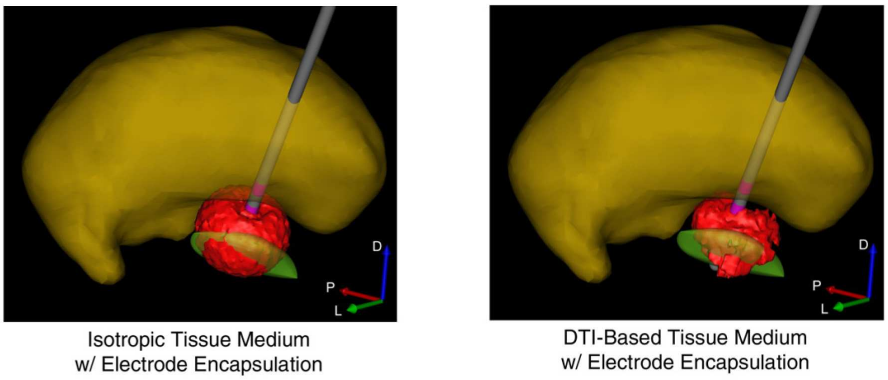


**Figure 1.3:** Simulated stimulation spread in DBS using isotropic of DTI-based tissue properties [17].

## 1.2 Limitations of clinical DBS

Two main questions arise from the analysis of the behaviour of clinical DBS, highlighted by a large number of model studies. Firstly, *How can we assess what region of the brain is activated*? and secondly, *How can we target specific regions of the brain*? These questions stem from the fundamental limitations of today's DBS systems: DBS systems provide only a limited degree of spatial control over the location of the stimulation field. Selection of different active contacts on the DBS electrode results in a coarse shift of the stimulation field along the electrode axis. Intra-operative electrophysiological recordings are usually adopted to guide the localisation of the optimal stimulation target [3]. Optimal positioning of DBS electrode reduces the risk of side effects caused by stimulation of fibres adjacent to the target area. The diffusion of current outside the boundaries of the target area, due to excessive stimulation or incorrect placement of the DBS electrode may result in a number of stimulation-induced side effects, including dysarthria, ocular deviation and flushing [18]. Additionally, the geometry of clinical DBS electrodes imposes a symmetrical field distribution around the electrode axis. Excessive current spread can be prevented only by varying the stimulus settings, including frequency, pulse width and amplitude. This can be further described with the aid of the illustration in Figure 1.4.

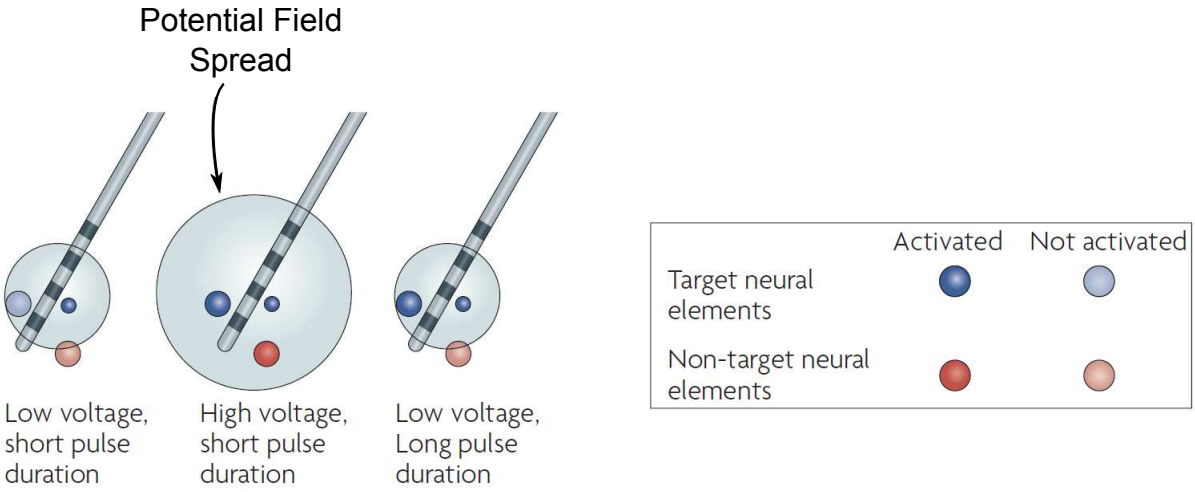


**Figure 1.4:** Conceptual illustration of the effects of varying the pulse setting combinations on the electric potential spread around the electrode [2].

When a voltage stimulus is applied to the electrode, an electric field distributes symmetrically around the electrode in all directions. A combination of pulse settings may trigger the activation of a limited number of targeted neural clusters. By changing this combination, the stimulation may achieve the activation of all targeted neural elements, although this may result in the activation of non-targeted areas, resulting in the occurrence of side effects. Given the 12,964 possible combinations of pulse width, amplitude and frequency within the charge density limit and 64 combinations of electrode geometry [5], the definition of optimal stimulation settings that maximise the efficacy and minimise the side effects is an extremely challenging task. There is an evident need, therefore, for a system that can allow a more accurate control over the shape, size, location and intensity of the electric field spreading around the electrode, resulting in stimulation focus and selectivity, with the aim of providing a stimulation tool which could better answer the above questions.

## 1.3 Proposed stimulation techniques for DBS

This thesis addresses the above issues from a technology perspective, by looking into alternative stimulation strategies that can result in the development of more efficient DBS systems. This thesis proposes two approaches to achieve dynamic electric field control during deep brain stimulation. The first method is based on the use of current-steering multipolar stimulation. Three or more electrode contacts are driven simultaneously in current mode, which has the benefit, as compared to voltage mode, to allow for accurate control over the total charge injected in the tissue during stimulation. The lateral (or outer) contacts of the multipolar electrode are driven as anodes and the inner contact(s) as cathode(s). Stimulation is provided in the proximity of the cathodes, whereas the anodes allow to block the spread of neural activation, thus providing stimulation focus. Additionally, steering the current towards a specific contact allows to shift the electric field along the axial distance of the electrode, permitting for dynamic field control. The basic multipolar configuration is a tripole, characterised by two lateral anodes and one central cathode. The number of cathodes can be increased to two or more, in order to allow for more accurate focus and dynamic shifting.

In this thesis we will look at the results of modelling the behaviour of electric fields in brain tissue, generated by current-steering multipolar sources. The work includes the design, development and testing of an integrated circuit (IC) for current-steering tripolar stimulation, developed in austriamicrosystems (AMS) 0.35$\mu$m technology, along with experimental validation of the behaviour of dynamic tripolar fields in a saline-filled tank. Results have shown how a dynamic electrode configuration can help achieve better focus and control of the electric field, which translates to a better focus of the VTA and a reduction of the stimulation of unwanted areas of the brain, which is responsible for the occurrence of side effects. This work forms the basis to address the issues related to the development of multipolar DBS systems.

The second method proposed in this thesis is based on the use of phase arrays (PAs). PAs are specific forms of antennas, which allow to control the radiation beam by controlling the relative phase (or delay) between the excitation of adjacent antenna elements (beam steering). To date, in medicine, PAs have found promising applications in such areas as medical imaging and hyperthermia cancer treatment [19, 20, 21, 22]. The use of PAs for stimulation of human tissue has not been investigated. This thesis includes an analysis of the applicability of PA systems to DBS. Computational models are adopted to simulate the behaviour of electromagnetic fields in brain tissue, resulting from the adoption of PAs.

These models take into account the frequency-dependent dielectric properties of brain tissue, and show the capability of steering and focusing the beam to a desired location only by varying the phase shift and frequency of operation of the PA signals. In addition, issues related to beam forming and beam steering in brain tissue, neural activation resulting from the use of electromagnetic waves and the conceptual design and development of the PA systems for DBS are explored. The application of PA to DBS can represent a major shift of technology towards the development of more accurate and efficient DBS systems.

## 1.4 Original Contributions

The work reported in this thesis aims at providing the following contributions to research in the field of DBS:

(a) Understanding of the behaviour of clinical DBS systems, in terms of loading effects of the electrode impedance on the injected current, which represents an essential aspect in terms of safety and efficacy.

(b) The introduction of novel stimulation techniques based on the adoption of current-steering multipolar electrode configurations, which allow to shape the stimulation field around the electrode and focus it to a desired location.

(c) Novel circuit ideas for the IC implementation of current-steering tripolar stimulators with on-chip generation of tunable time constants, necessary to provide anodal blocking.

(d) Introduction of a novel idea for a stimulation system based on PAs to achieve accurate field steering during stimulation. Notions about the stimulation through electromagnetic waves and concepts related to the IC implementation of PA stimulation systems are discussed.

## 1.5 Author's Publications

The work reported in this thesis has given rise to the following publications:

Valente, V.; Demosthenous, A. and Bayford, R. (2011) **Tripolar Current-Steering Stimulator Output Stage For Field Shaping in Deep Brain Stimulation**. *Submitted to the IEEE Transactions of Biomedical Circuits and Systems.*

Valente, V.; Demosthenous, A. and Bayford, R. (2011) **Characterisation of the Loading Effects of a Deep Brain Stimulation System: Electrical Model and Experimental Validation**. *Manuscript in preparation for submission to the Journal of Physiological Measurements.*

Valente, V.; Demosthenous, A. and Bayford, R. **Design of a Current-Steering Implantable Stimulator with Electric Field Shifting for Deep Brain Stimulation.** *Proc. IEEE Biomedical Circuits and Systems Conference BioCAS 2010*, **2010**.

Valente, V.; Demosthenous, A. and Bayford, R. **Electric Field Focusing and Shifting Technique in Deep Brain Stimulation Using a Dynamic Tripo-**

**lar Current Source**. *Proceedings of the International Symposium on Circuits and Systems*, **2010**, 2091-2094

Valente, V.; Demosthenous, A. and Bayford, R. **Application of phased array systems to deep brain stimulation.** *Proc. 16th IEEE Int. Conf. Electronics, Circuits, and Systems ICECS 2009*, **2009**, 643-646.

Valente, V.; Demosthenous, A. and Bayford, R. **Towards the development of phased array systems for deep brain stimulation**. *Proc. IEEE Biomedical Circuits and Systems Conference BioCAS 2008*, **2008**, 261-264.

## 1.6 Patents arising from the work reported in this thesis

**(WO/2010/058178)** METHOD AND APPARATUS FOR PERFORMING DEEP BRAIN STIMULATION WITH AN ELECTROMAGNETIC FIELD. Inventors: Demosthenous A., Valente V. and Bayford R.
International application number: PCT/GB2009/002721

## 1.7 Thesis Overview

This thesis is divided into seven chapters. **Chapter 1** has given a brief introduction stating the issues related to DBS that the work in this thesis has tried to challenge, and the contributions that this work has provided to research in DBS.

**Chapter 2** provides an overview of the fundamentals of DBS, including a description of the anatomical region of the brain targeted by DBS and effects of damages within this region. The chapter expands on the concepts of electrophysiological ef-

fects of stimulating excitable tissue and, in specific, brain tissue and concludes with an overview of clinical DBS systems and a description of the different aspects, on which DBS research has focused over the last decades.

**Chapter 3** describes the modelling and experimental work carried out in order to fully characterise a DBS system, in terms of its electrical properties and the loading effects of DBS electrode on the stimulus. The model focused on describing the behaviour of the electrode-tissue interface and analysing the impact of variations of its key parameters on the applied stimulus. Experimental work looked into reproducing the behaviour of a clinical DBS system, by adopting a set of clinical DBS electrodes placed in a saline-filled tank and driven by standard monophasic and biphasic voltage pulses, and measuring the current waveforms injected into the saline.

**Chapter 4** reports the description of the model adopted to represent the proposed stimulation method, based on the use of current-steering multichannel stimulation. We consider the adoption of tripolar, quadripolar and pentapolar electrode configurations, driven by imbalanced current sources, which allow to dynamically steer the stimulation current towards a desired location and effectively shape the resulting stimulation field.

**Chapter 5** presents the design, implementation and evaluation of a current-steering tripolar stimulator output stage in a 0.35-$\mu$m high-voltage CMOS technology. The stimulator is formed by four identical current sources, configured in a push-pull arrangement. Each block forming the current source is described in detail. The experimental testing of the fabricated chip is then presented along with experimental validation of field shaping resulting from the adoption of a tripolar current-steering stimulation system.

**Chapter 6** presents the alternative method proposed in this thesis, based on the use of PA systems to provide field steering in DBS. The chapter presents results from modelling the behaviour of electromagnetic waves in brain tissue and some fundamental concepts for the design of PA stimulation systems for future research.

**Chapter 7** provides an overall discussion of the work presented in this thesis and draws some conclusions about the contributions of the work presented and outlines possible future developments towards the implementation of advanced DBS systems.

# 2

# Fundamentals of DBS

The basal ganglia is the anatomical structure targeted by clinical DBS. The involvement of basal ganglia in the control of movement and the relation between pathological changes in the basal ganglia and resulting muscular rigidity, tremor and weakness were studied by Kinnier Wilson in the early 20th century [23]. Since then, several studies have corroborated the predominant role of the basal ganglia in the control of movement. The first part of this chapter is an overview of the anatomy of the basal ganglia and the effects of basal ganglia damage. The chapter will then look into the properties of electrical stimulation as a therapeutic means to tackle the disorders caused by damages in the basal ganglia with an overview on existing clinical DBS systems.

## 2.1 Anatomy of the Basal Ganglia

The basal ganglia is found in the deep regions of the brain and comprises of a number of interconnected nuclei, directly responsible for movement. Figure 2.1 shows the anatomical structures of the basal ganglia. The striatum is the largest nucleus, comprising of the caudate nucleus and the putamen, and it is involved in a variety of processes including motor, associative and cognitive functions.

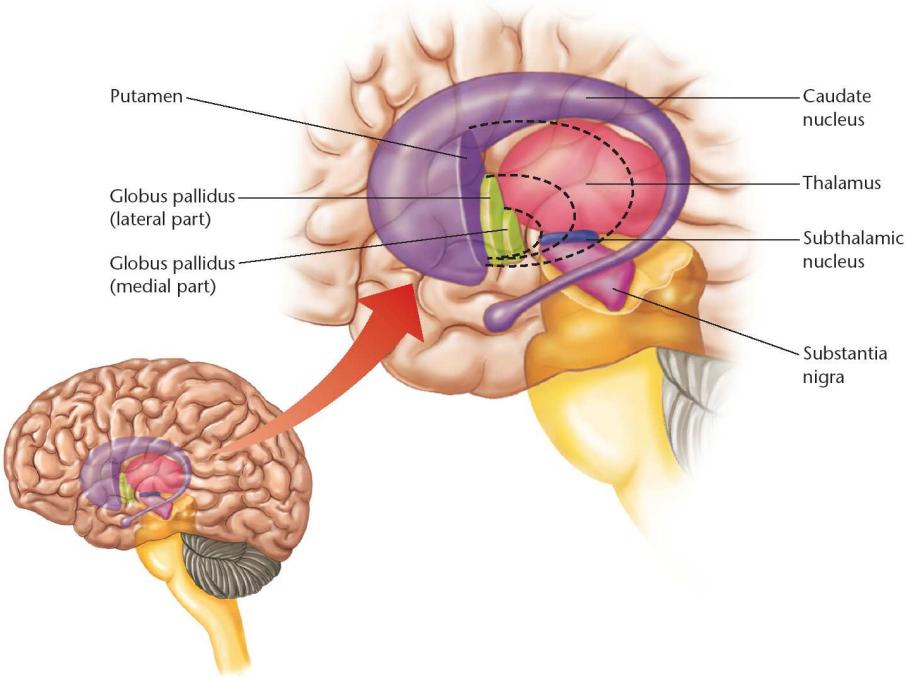


**Figure 2.1:** Anatomical structure of the basal ganglia.

The dorsal section of the basal ganglia consists of the striatum, the globus pallidus (internal, GPi and external, GPe), the subthalamic nucleus (STN) and the subtantia nigra (SN). The latter is subdivided into two groups of nuclei, the pars compacta (SNc) and the pars reticulata (SNr). The diagram of the interconnection between the different nuclei of the basal ganglia is illustrated in Figure 2.2.

The input structures of the basal ganglia are the striatum (caudate and putamen) and the STN. The striatum receives excitatory inputs from all areas of the cortex, whereas the STN receives excitatory inputs from the motor areas of the frontal lobe. The output structures are the GPi and the SNr. These output structure

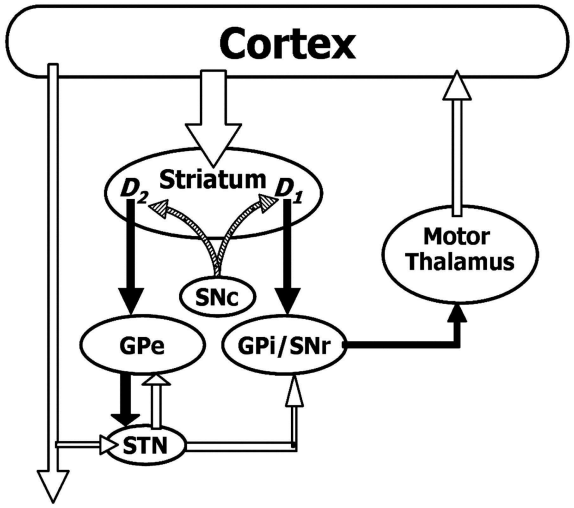


**Figure 2.2:** Basic schematic of the interconnections of the basal ganglia nuclei. The basal ganglia is a network of nuclei with defined input/output characteristics. The inputs are the striatum and STN, whereas the outputs are the GPi and the SNr. Internal connections are represented by the GPe and SNc. Adapted from [24]

receive excitatory inputs from the STN and inhibitory inputs from the striatum. The outputs from the GPi and SNr are inhibitory and travel to motor areas in the brainstem and thalamus. The GPe receives excitatory input from the STN and inhibitory input from the striatum and sends inhibitory output to the STN, GPi and SNr. The SNc is the principal area of concentration of the dopamine-containing neurons.

## 2.2 Damages in the Basal Ganglia

Lesions within the interconnections of the nuclei in the basal ganglia can cause a number of movement disorders which can result in extreme movement impairment and uncontrollable involuntary movements. These diseases include Parkinson's disease (PD), essential tremor (ET), Huntington's disease, Tourette Syndrome (TS), dystonia and several additional conditions. PD is a degenerative disease characterised by symptoms including tremor at rest, slowness of movement, muscular rigidity and postural instability, caused by a decreased dopamine release in the motor portions of the putamen. The dopamine deficiency results in a change in discharge

patterns generated by the GPe, the STN and the GPi and SNr [25]. One of the most prominent results of changes in nucleus discharge is the development of oscillatory phenomena, characterised by local field potential oscillations in the range of 10 to 25 Hz. ET is one of the most common neurological disorders. It is characterised by a bilateral postural and kinetic tremor of the upper limbs, with tremor frequencies between 4 Hz and 12 Hz. Additional symptoms of ET include postural instability and tremor at rest. Huntington's disease is a degenerative disease resulting in involuntary movements and dementia. The involuntary movements manifest as frequent, brief twitches involving any part of the body, resulting from a loss of neurons in the striatum. TS is a neurological disorder characterised by involuntary movements and vocalisations. TS patients frequently suffer from attention-deficit disorder and obsessive compulsive disorder. Dystonia is another movement disorder consisting of repetitive muscle contractions and involuntary movements caused by a mutation of a gene. The literature is very rich with clinical studies investigating the physiological causes of the above mentioned movement disorders, aimed at identifying the optimal targets of deep brain stimulation. Before we look into DBS as a routine clinical approach for movement disorders, it is important to introduce the physiological properties of therapeutic stimulation of brain tissue.

## 2.3 Therapeutic Stimulation of Brain Tissue

Brain stimulation involves complex electro-physiological processes. This section will give an overview of such processes including the electric properties of tissue, the behaviour of electric fields in brain tissue and the interactions between applied electric field and the response of the neural clusters targeted by stimulation.

### 2.3.1 Electric Properties of Brain Tissue

The dielectric properties of brain tissue are frequency-dependent and highly non-linear. The dielectric spectrum can be divided in three main regions, which describe low, medium and high frequency dielectric behaviour. Each of these regions is characterised by a polarisation mechanism governed by the Debye relation [26]:

$$\varepsilon_c(\omega) = \varepsilon_\infty + \frac{\varepsilon_s - \varepsilon_\infty}{1 + j\omega\tau}, \tag{2.1}$$

where $\varepsilon_c$ is the complex dielectric constant, $\omega$ is the angular frequency, $\varepsilon_\infty$ is the permittivity at very high frequencies (as $\omega \to \infty$), $\varepsilon_s$ is the permittivity at DC and $\tau$ is the relaxation time constant. In order to simultaneously account for the dispersions related to each frequency region, Cole and Cole added a distribution parameter, $\alpha$, to the Debye equation [26]:

$$\varepsilon_c(\omega) = \varepsilon_\infty + \frac{\varepsilon_s - \varepsilon_\infty}{1 + (j\omega\tau)^{1-\alpha}}. \tag{2.2}$$

To model the dielectric spectrum of different types of tissue, Gabriel and colleagues [27], adopted multiple Cole-Cole dispersion relations resulting in:

$$\varepsilon_c(\omega) = \varepsilon_\infty + \sum_{n=1}^{4} \frac{\Delta\varepsilon_n}{1 + (j\omega\tau_n)^{1-\alpha_n}} + \frac{\sigma_i}{j\omega\varepsilon_0} \tag{2.3}$$

where $\sigma_i$ is the ionic static conductivity and $\varepsilon_0$ is the permittivity of free space.
The above equation was adopted in this study to model the dielectric spectrum of Grey matter with parameter values reported by Gabriel and colleagues [27].

### 2.3.2 Electric Fields in Excitable Tissue

In order to fully characterised the behaviour of electric fields in brain tissue, we need to introduce the concept of volume conductor, monopole and dipole fields, which constitute the basic elements of electrophysiology. Excitable tissue is characterised

by an active region and a passive region. The active region consists of the axon membranes and will be discussed later in this chapter. The passive region is defined as a volume conductor with specific dielectric properties.

The behaviour of the current delivered by stimulation and consequently the electric field generated in the volume conductor is governed by fundamental relations known as Maxwell's equations:

$$\nabla \cdot \mathbf{D} = \rho_v \tag{2.4}$$

$$\nabla \times \mathbf{E} = -\frac{\partial \mathbf{B}}{\partial t} \tag{2.5}$$

$$\nabla \cdot \mathbf{B} = 0 \tag{2.6}$$

$$\nabla \times \mathbf{H} = \mathbf{J} + \frac{\partial \mathbf{D}}{\partial t} \tag{2.7}$$

$\mathbf{E}$ and $\mathbf{D}$ are electric field quantities related by $D = \varepsilon \mathbf{E}$, where $\varepsilon$ is the electric permittivity of the material; $\mathbf{B}$ and $\mathbf{H}$ are magnetic field quantities related by $\mathbf{B} = \mu \mathbf{H}$, where $\mu$ is the magnetic permeability for the material; $\rho_v$ is the electric charge density per unit volume in $\mathrm{C/m^3}$ defined as $\rho_v = dq/dv$ where $dq$ is the unit charge contained in the unit volume $dv$. In the case electric charge is distributed on a surface or along a line, we define the distribution as surface or line charge density. $\mathbf{J}$ is defined as the current density per unit area as $J = \rho_v \mathbf{u}$ in $\mathrm{A/m^2}$, where $\mathbf{u}$ is the mean velocity of charges.

In the static case the quantities in Maxwell's equation are independent of time. This is valid as well for charges which move at a steady rate at which $\rho_v$ and $\mathbf{J}$ are constant in time. We refer to this latter case as *quasi-static condition* [28]. At this condition Maxwell's equations reduce to:

$$\nabla \cdot \mathbf{D} = \rho_v \tag{2.8}$$

$$\nabla \times \mathbf{E} = 0 \tag{2.9}$$

for the electrostatic formulation and:

$$\nabla \cdot \mathbf{B} = 0 \tag{2.10}$$

$$\nabla \times \mathbf{H} = \mathbf{J} + \frac{\partial \mathbf{D}}{\partial t} \tag{2.11}$$

for the magnetostatic formulation. The electric field, $\mathbf{E}$, can be also expressed as a function of the scalar potential, $V$, as:

$$\mathbf{E} = -\nabla V \tag{2.12}$$

where $\nabla V$ is the gradient of $V$. Using the expression $D = \varepsilon \mathbf{E}$, we can express Eq. 2.12 as:

$$\nabla \mathbf{E} = \frac{\rho_v}{\varepsilon} \tag{2.13}$$

which, in terms of the voltage $V$ becomes:

$$\nabla \cdot (\nabla V) = -\frac{\rho_v}{\varepsilon} \tag{2.14}$$

and, for a scalar voltage $V$, can be abbreviated to:

$$\nabla^2 V = -\frac{\rho_v}{\varepsilon} \tag{2.15}$$

Eq. 2.15 is known as Poisson's equation and it provides a direct relation between the voltage and the charge density in a medium. If the medium is free of charge

Poisson's equation reduces to Laplace's equation, expressed as:

$$\nabla^2 V = 0 \tag{2.16}$$

Poisson and Laplace equations are useful for determining the electrostatic potential $V$ in regions at whose boundaries $V$ is known.

#### 2.3.2.1 Monopolar and multipolar fields

In the simplest case of stimulation, the tissue is excited by a monopolar (single unit) source (electrode). Current flows from the electrode through the extracellular fluid surrounding the tissue, to a distant electrode. If we model the volume conductor as a sphere and locate a current source $I_0$ at the origin of a spherical coordinate system, the the current density at a radius $r$ is given by the total current divided by the area of the spherical surface [29]:

$$\mathbf{J} = \frac{I_0}{4\pi r^2}\mathbf{a}_r \tag{2.17}$$

where $\mathbf{a}_r$ is the unit vector in the radial direction. By applying Ohm's law to Eq. 2.17 and assuming uniform tissue conductivity, $\sigma$, the electric field, $\mathbf{E}$ is given as:

$$\mathbf{E} = -\nabla V = \frac{I_0}{4\pi\sigma r^2}\mathbf{a}_r. \tag{2.18}$$

By integrating Eq. 2.18 with respect to $r$, we can obtain an expression of the electric potential, V, resulting from an applied current $I_0$ as:

$$V = \frac{I_0}{4\pi\sigma r}. \tag{2.19}$$

Eq. 2.19 can be generalised to $n$ sources, delivering a current $I_i$ and located at a distance $r_i$ from the recording point. The electric potential is then given by:

$$V = \frac{1}{4\pi\sigma} \sum_i \frac{I_i}{r_i}. \tag{2.20}$$

In cartesian coordinate system, with $r = \sqrt{x^2 + y^2 + z^2}$, for a monopolar source centred at $x_0 = 0$, the electric potential, $V_{MONO}$ in then given by:

$$V_{MONO} = \frac{1}{4\pi\sigma\sqrt{x^2 + y^2 + z^2}}. \tag{2.21}$$

For a dipole, with sources of magnitude $I_0 = 1$ and $I_1 = -1$ located at $x_0 = 0$ and $x_1 = 1$, the magnitude of the potential, $V_{DI}$, is given by:

$$V_{DI} = \frac{1}{4\pi\sigma} \left( \frac{1}{\sqrt{x^2 + y^2 + z^2}} - \frac{1}{\sqrt{(x-1)^2 + y^2 + z^2}} \right). \tag{2.22}$$

For a tripolar with sources of magnitude $I_{-1} = -0.5$, $I_0 = 1$ and $I_1 = -0.5$, located at $x_{-1} = -1$, $x_0 = 0$ and $x_1 = 1$, the magnitude of the electric potential, $V_{TRI}$, is given by:

$$V_{TRI} = \frac{1}{4\pi\sigma} \left( \frac{1}{\sqrt{x^2 + y^2 + z^2}} - \frac{0.5}{\sqrt{(x-1)^2 + y^2 + z^2}} - \frac{0.5.}{\sqrt{(x+1)^2 + y^2 + z^2}} \right) \tag{2.23}$$

#### 2.3.2.2 Interactions between the electric field and the tissue

The tissue is populated by clusters of neurons, which are electrically excitable. The anatomy of a neuron is depicted in Figure 2.3(a). A neuron consists of a soma (or cell body), an axon and dendrites. The soma is the part of the neuron that contains the cell nucleus. The dendrites consists of extensions that branch into trees and are responsible for connections with neighbouring cells. The axon is a cable-like extension, responsible to carry nerve signals and transmitting them to target cells via synapses. The axon is characterised by segments surrounded by myelin sheath, which consists of a dielectric material allowing fast propagation of impulses. These

segments are divided by regions, known as nodes of Ranvier, where the signals are amplified and transmitted down the axon.

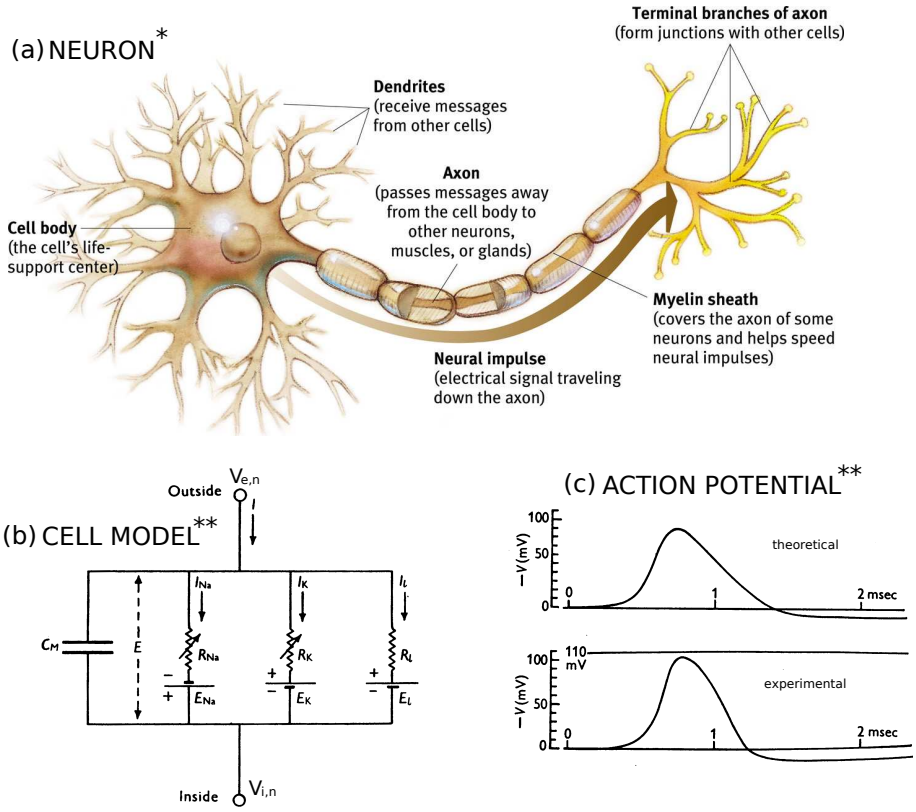


**Figure 2.3:** Neuron model. (a) Structure of a neuron. (b) Electrical model of a neural cell. (c) Theoretical and experimental action potentials. *Image source: http://www.hillcresthigh.net. **Image source [30].

The physiology of the axon membrane can be described by an electrical circuit model developed by Hodgkin and Huxley in the 1940's [30]. The components of a Hodgkin-Huxley model are shown in Figure 2.3(b). The ionic current, $I_{ION}$, through the membrane are divided into three components: potassium current, $I_K$, sodium current, $I_{Na}$ and leakage current, $I_L$. Each cell is represented by a membrane capacitance, $C_M$, a resting potential, $E$, the equilibrium potentials for each ionic channel, $E_K$, $E_{Na}$ and $E_L$, and constants representing the resistance of each channel, $R_K$, $R_{Na}$ and $R_L$. This model was adopted to describe the shape and amplitude of propagated action potentials, as well as the behaviour of the ionic channels, the excitation threshold and the refractory period following the generation of an action potential. One example of comparison between theoretical and experimental action

potential is given in Figure 2.3(c). Electrical stimulation aims at depolarising the cell membrane, ie. to induce the membrane voltage to increase in amplitude and exceed the cell threshold voltage, resulting in the generation of an action potential. Action potentials can be generated by placing an electrode directly inside the cell and delivering a positive current that will flow from the inside to the outside of the cell, resulting in the depolarisation of the membrane. Prediction of the change of the membrane voltage over time can be derived by solving the differential equation related to the membrane electric model [31]:

$$\frac{dV_m}{dt} = \frac{-I_{ION} + I_{STIM}}{C_m}, \tag{2.24}$$

where $V_m$ is the membrane voltage and $I_{STIM}$ is the stimulation current applied to the cell.

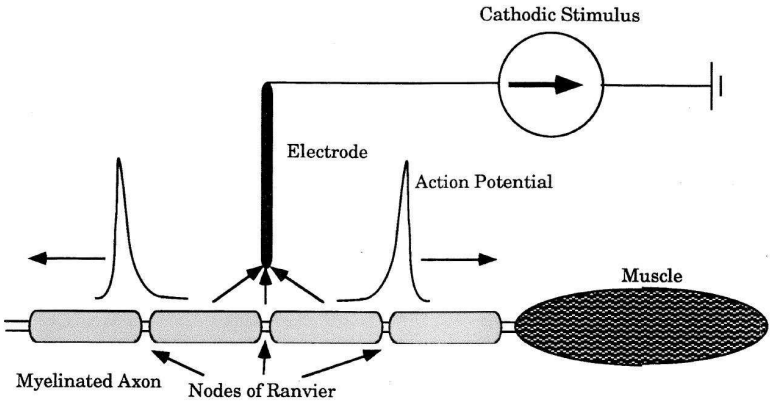


**Figure 2.4:** Principles of electrical stimulation. Adapted from [32].

#### 2.3.2.3 Activation Function

Another stimulation technique that does not require direct access to the cell, consists of locating the electrode in the extracellular space near the tissue target to be excited as illustrated in Figure 2.4. A cathodic (negative) current produces an extracellular potential, $V_e$, the effect of which is to raise the membrane potential towards the threshold voltage. If we subdivide a neuron into $n$ subunits or compartments, we

can represent the voltage inside and outside the $n$th compartment as $V_{i,n}$ and $V_{e,n}$ as shown in Figure 2.3(b). Eq. 2.24 can be then described in terms of $V_{i,n}$ and $V_{e,n}$ as [31]:

$$\frac{d(V_{i,n} - V_{e,n})}{dt} \cdot C_m + I_{ION} + \frac{V_{i,n} - V_{i,n-1}}{R_n/2 + R_{n-1}/2} + \frac{V_{i,n} - V_{i,n+1}}{R_n/2 + R_{n+1}/2} \tag{2.25}$$

where $R_n$ is the resistance of the membrane of the $n$th compartment. The direct effect of the extracellular potential on the $n$th compartment is then given by [31]:

$$f_n = \left[ \frac{V_{e,n-1} - V_{e,n}}{R_{n-1}/2 + R_n/2} + \frac{V_{e,n+1} - V_{e,n}}{R_{n+1}/2 + R_n/2} \right] / C_{m,n}, \tag{2.26}$$

which is known as the *activation function*, $f_n$. For a long homogeneous fibre the activation function is proportional to the second spatial derivative of the extracellular potential along the axon [33], as:

$$f(x) = \frac{d}{4\rho_i c_m} \cdot \frac{\delta^2 V_e}{\delta x^2}, \tag{2.27}$$

where $\rho_i$ is the intracellular resistivity and $d$ is the fibre diameter. The activation function can be adopted to obtain an estimate of the influence of an applied field on a target cluster of neurons. The activation function will describe regions of depolarisation, for $f > 0$ and regions of hyperpolarisation, for $f < 0$.

#### 2.3.2.4 Strength-duration relationship

The threshold current amplitude, $I_{TH}$, required to excite neural elements decreases with increasing pulse width according to the empirical equation derived by Lapique [32]:

$$I_{TH} = \frac{I_{RH}}{1 - exp\left(-\frac{W}{T_{CH}}\right)}, \tag{2.28}$$

where $I_{RH}$, known as *rheobase current*, is the smallest current amplitude required to

cause excitation; $T_{CH}$ is the *chronaxie*, defined as the pulse width when the stimulus amplitude is equal to twice the rheobase current and $W$ is the stimulus pulse width. The strength-duration curve is show in Figure 2.5. Another formula often used to derive the threshold stimulus current is the Weiss equation [5, 34]:

$$I_{TH} = I_{RH}\left(1 + \frac{T_{CH}}{W}\right) \tag{2.29}$$

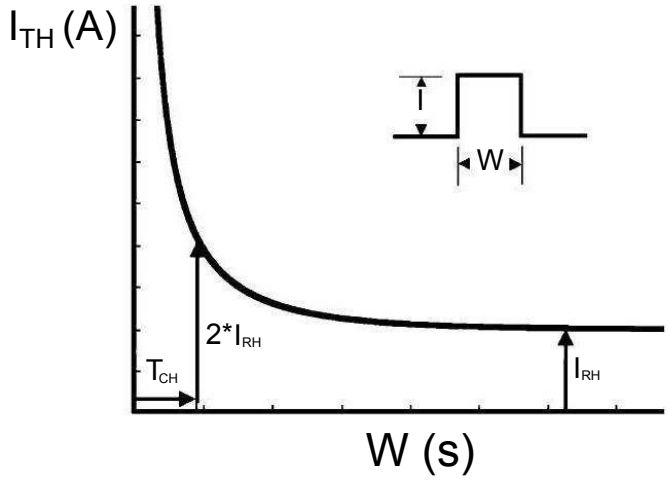


**Figure 2.5:** The strength-duration curve describes the stimulation threshold amplitude as a function of the stimulus duration. Adapted from [5].

The difference between these expressions lies on the fact that the Lapique equation models the extracellular membrane properties as a battery and a resistor, whereas the Weiss equation considers a current source model [35]. Chronaxie values can be used to predict which neural elements are excited during stimulation. Cells and fibres, in fact, have different chronaxies; cell bodies have chronaxies in the range of 1-10 ms; large myelinated fibres have chronaxies in the range of 30-200 $\mu$s and small myelinated fibres have chronaxies in the range of 200-700 $\mu$s [36]. In DBS, chronaxies were estimated to be approximately 65 $\mu$s for thalamic and 75 $\mu$s for pallidal stimulation [37].

#### 2.3.2.5 Charge injection during stimulation

Charge injected during electric stimulation is a key factor in the design of safe stimulation systems. The total charge injected needs to be low enough to avoid irreversible phenomena like tissue damage and electrode corrosion, strictly related to irreversible biological processes occurring at the electrode-tissue interface. The total charge of an electric stimulus is given by:

$$Q_{tot} = \int idt. \tag{2.30}$$

For a square pulse of amplitude $I$ and width $W$, $Q_{tot} = I \times W$. Monopolar stimulation (either a positive or negative pulse used for stimulation) does not represent a safe protocol for stimulation since it cause charge build up across the interface resulting in the occurrence of irreversible effects [38]. Biphasic pulses (one pulse cycle followed by another cycle of opposite polarity) have become the standard choice for delivery safer stimulation pulses to the tissue. This type of pulses provides charge balancing since the charge injected during the first cycle is removed during the second cycle. This, however, is not sufficient to provide safe stimulation and electrode charge density has to be taken into account, where the charge density per phase is related to the charge per phase by an empirical equation deriving safe levels of stimulation [39]. For example, for a platinum-iridium electrode of surface area of 6mm$^2$ like the ones conventionally used for DBS, the recommended maximum charge density level is in the order of 30 $\mu$C/cm$^2$/phase [34].

## 2.4 DBS Systems

A clinical DBS implant is shown in Figure 2.6. The surgical procedure consists of implanting electrodes through a burr hole into the basal ganglia. After the insertion of the electrodes and the DBS leads, clinical effects of DBS are evaluated as the

patient assesses relief and adverse effects, in order to identify optimal stimulation target. Once the electrode has been fixed in the correct position the surgeon implants a pulse generator (IPG) subcutaneously near the clavicle. The IPG is connected to the DBS lead and fixed to the burr hole on the skull [3].

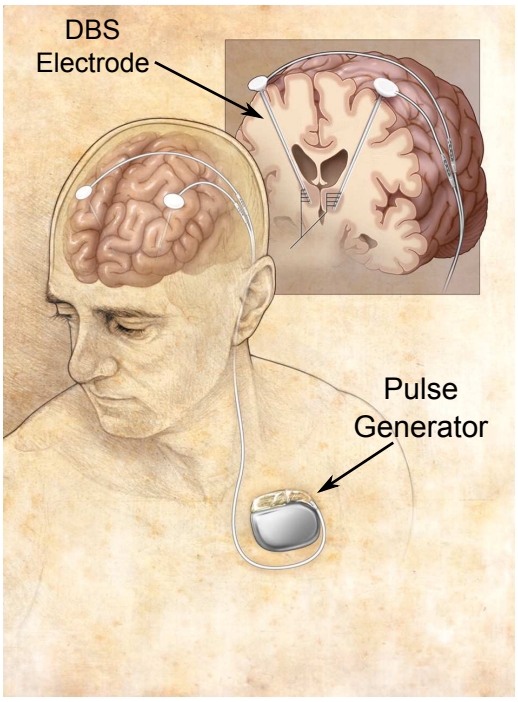


**Figure 2.6:** Components of a DBS Implant. Typical implants consist of an implanted pulse generator (IPG), which generates the set of DBS pulses required for stimulation, a set of connection cables and an electrode rod, which delivers the stimulation pulses to the brain target area. Image source: Mayo Clinic

Potential side complications related to DBS usually include side effects associated with the surgical procedures, which could be affected by complications of the anaesthesia, scalp infection, patient's bleeding; Hardware-related problems including fracture or malfunction of the stimulator of other components; battery failure or exhaustion; erosion of the IPG or the cables; migration of the stimulating electrode in deeper areas of the brain, causing substantial reduction of the DBS beneficial effects[1]. Currently available clinical DBS systems, approved by the Food and Drug Administration (FDA), include the Kinetra, Soletra and Intrel II neurostimulators

[1]Source: Department of Neurological Surgery. University of Pittsburgh, USA

for DBS, manufactured by Medtronic, USA.

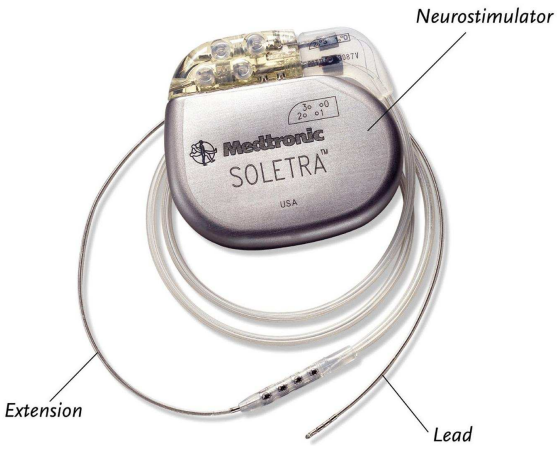


**Figure 2.7:** Soletra neurostimulator by Medtronic. A clinical Medtronic DBS system consists of an implanted pulse generator (IPG), an extension lead and an electrode lead. The electrode lead is terminated by 4 metal cylindrical contacts. Image source: http://www.medtronic.com

Figure 2.7 illustrates the Soletra neurostimulator implant clinically used for DBS, consisting of the IPG, extension lead and a 4-contact DBS electrode. The basic operation of a typical clinical DBS system involves the use of a programmer, which sets the stimulation settings. The stimulation delivered by the IPG to the electrode contacts consists of a train of cathodic (or cathodic and anodic) square voltage pulses, whose amplitude, width and pulse rate are preset by the programmer. Typical settings for a DBS neurostimulator are listed in Table 2.1. Medtronic clinical DBS systems are based on voltage-mode stimulation.

**Table 2.1:** Programming settings for clinical DBS stimulators. Data source: www.medtronic.com

| Parameter | Initial Setting | Range | Typical Setting |
|---|---|---|---|
| *Amplitude(V)* | 0 | 0-10.5 | 2.5-3.5 |
| *Pulse Width($\mu s$)* | 60-120 | 60-450 | 60-120 |
| *Rate(pps)* | 130-160 | 3-250 | 130-185 |
| *Electrode* | Unipolar | Unipolar | Unipolar |
| *Polarity* | | Bipolar | Bipolar |
| *Mode* | Continuous | Cycling | Continuous |
| | | Continuous | |

The neurostimulator offers two types of electrode configurations: unipolar, where

the IPG is set as the anode and the electrode contacts to the cathodes; bipolar, in which case one or more electrode contacts are set to a positive voltage and one or more contacts to a negative voltage. A comprehensive review of DBS devices is given in [40].

## 2.5 Advances in DBS

This section aims at summarising the main issues that DBS research has identified over the past decades, in terms of understanding of DBS underlying mechanism, identification of optimal target sites to increase DBS efficacy and reduce of side effects, assessment of DBS for a number of additional disorders, development of models to validate and understand the operation of DBS and optimisation of the design of electrodes and DBS systems.

### 2.5.1 Clinical Studies

Literature is extremely rich of studies assessing the clinical benefit of DBS along with its side effects. Volkmann [18] has reviewed several studies reporting the clinical efficacy of Vim, GPi and STN DBS. Preliminary comparison of the effects of stimulation of different targets has identified STN as the most effective target in inhibiting symptoms of PD and dyskinesia and reducing the post-operative medication doses required. Halpern and colleagues [3] have reviewed clinical outcomes of DBS for PD and a number of additional neurological disorders, including essential tremor, dystonia, Tourette Syndrome, epilepsy, obsessive compulsive disorder and treatment-resistant depression, reporting results indicating DBS as the future therapy of choice for a large number of neurological disorders and diseases. The main issue highlighted by the clinical outcomes of DBS, however, is the poor understanding of the exact mechanisms that result in the clinical benefit produced by DBS. Experimental observations about the mechanisms involved in DBS still remain

controversial, due to the anatomical and behavioural complexity of neural clusters targeted by DBS. A method clinically adopted to investigate the physiological effects of DBS consists of intraoperative recordings of the discharge patterns of neural clusters surrounding the target cells [41, 42, 43, 44]. These recordings are usually carried out using platinum-iridium or tungsten microelectrodes (with electrode tip diameter in the region of tens of micrometres and electrode impedance in the MΩ region) located at different sites within the target region (usually GPi or STN). The activity of single units is then recorded by each microelectrode during monopolar or bipolar stimulation. Evidence accumulated over the past decades suggests that DBS is involved with the direct or indirect functional inhibition of the neural targets, since lesions of such neural structures lead to similar effects [42].

### 2.5.2 Computational Models

The development of advanced computational models have supported clinical studies in the characterisation of DBS, the investigation of its underlying mechanisms and the identification of strategies to optimise the efficacy of DBS and reduce its adverse events. These strategies include optimisation of electrode geometry, identification of optimal stimulation site and derivation of optimal stimulation settings. These models aim at characterising the electric field generated during stimulation and the volume of tissue activated by the applied electric field [10]. The electric field distribution around the electrode, in fact, is strictly related to the shape and impedance of the electrode [45, 46, 47], the conductivity of the tissue [48, 15] and the stimulus settings [49]. By coupling simulated electric field distribution during stimulation with models of axon membranes, representing the properties of neural targets, it is possible to predict the volume of tissue that will be activated during stimulation [50].

#### 2.5.2.1 Finite Element Model

Models of the DBS electrode in tissue are conventionally constructed using the finite element method[2] (FEM) [9, 14, 47, 49]. FEM has several advantages over alternative approaches used to solve partial differential equations, such as the boundary element method (BEM), the mesh-free method, and the finite difference method (FDM). These advantages include the possibility to define material heterogeneities and nonlinear equations, ease of boundary condition implementation and the capability to handle complex mesh geometries [51].

In FEM, the tissue can be modelled as a homogeneous (conductivity independent of location), isotropic (conductivity independent of direction) volume conductor governed by the Laplace equation. In monopolar mode, one electrode contact is set to the stimulus voltage, whereas the boundary of the model is set to 0 V, to represent a large distant return electrode. In bipolar model, two electrode contacts are driven at opposite polarity. Solving the Laplace equation allows to derive the magnitude of the extracellular potential around the electrode. Recently FEM models have been improved by introducing anisotropic and inhomogeneous properties. The conductivity values are derived from diffusion tensor imaging [10, 17] or by empirical relations accounting for the extracellular volume fraction and the tortuosity of the extracellular space [15].

#### 2.5.2.2 Electrode Impedance Models

A number of studies have incorporated the electrode-brain interface (EBI) (also referred to as electrode-tissue interface (ETI) or electrode-electrolyte interface (EEI)) into the FEM models, to account for its impact on the system, in terms of charge delivery, power loss and filtering effects associated with the EBI impedance. The EBI impedance can be approximated by the parallel combination of a constant-phase element (pseudocapacitance) and a faradaic charge transfer resistance [52]. This

[2] A brief description of the finite element method is given in Appendix A

equivalent circuit has been integrated with a FEM model to study the properties of the current density at the interface and therefore the impact of the interface impedance on the driving stimulus [47]. The electrode impedance has also been modelled as pure capacitor and included in FEM models to assess its impact on the volume of tissue activated [48]. Another approach has been based on the generation of extra layers within the FEM models, characterised by specific dielectric properties [16, 53]. Incorporation of the ETI impedance into FEM models plays a major role in the analysis of the behaviour of the electric field in tissue and the accurate estimation of the VTA.

#### 2.5.2.3 Activation Models

A large amount of research has been dedicated to the analysis of the interactions between an applied electric field and the excitable tissue. Neuron models exposed to applied electric fields play an integral role in the understanding of the DBS mechanisms and the development of safer and more efficient DBS systems. Approaches to determine the response of neural fibres to an applied electric field can be based on linear or non-linear membrane models [54]. The latter approach consists of directly solving the set of differential equations related to the change of the membrane voltage in response to an applied stimulus [55]. The former approach assumes that the axon membrane capacitance is constant and the membrane voltage is studied in the subthreshold region. An additional approach that does not take into account axon parameters is the activation function concept [33], which predicts regions of depolarisation and hyperpolarisation. These approaches have been extensively adopted in DBS, to study the effects of DBS on single-unit cells [9, 15, 50] or to assess the volume of tissue activation during stimulation [10, 13, 17, 49, 56, 57]. The most prominent modelling approaches involve cable models of mammalian nerve fibres with explicit representations of the nodes of Ranvier. The geometry and dynamics of the fibres are based on experimental measurements from humans and lab animals.

The fibre dynamics are assessed by solving the set of partial differential equations using backward Euler integration (implemented in a commercially available software, NEURON) [58]. By coupling the extracellular potential distribution, derived by FEM models, to models of the nerve fibres, the effects of stimulation on all the neural elements surrounding the electrode can be investigated and the VTA can be derived for different stimulation parameters.

### 2.5.3 System Design

Far more research has focused on clinical trials and development of DBS models than on the design and optimisation of DBS stimulators. Some important design aspects can be taken into account for the development of future DBS systems. One main limitation of current DBS systems is the use of a large non-rechargeable battery, implanted in the chest area and connected to the electrode lead via a long extension lead running sub-cutaneously. The development of cranial-mounted pulse generator with rechargeable batteries can provide a major improvement over current DBS systems, in terms of reducing risks associated to the intensive and multiple surgical procedures and increasing the reliability of the device by shortening or reducing the number of leads [40]. The development of cranial-mounted stimulator requires the miniaturisation of the pulse generator, especially the battery. Recently research has started tackling the issue of miniaturisation applied to DBS systems [59, 60]. An additional feature that has recently been introduced in the design of novel DBS system is an integrated sensing capability, which could provide important benefits, including a better understanding of the mechanisms of DBS as well as providing closed-loop therapy [61, 62]. Finally, a major improvement over conventional DBS systems could be introduced by the design of systems that allow to steer and shape the stimulation field around the stimulating electrode, thus allowing a dynamic control over the stimulation field, after system implantation [40]. This latter issue constitutes the main aspect investigated in this thesis.

## 2.6 Conclusion

This chapter has provided with the fundamentals of DBS. We can summarise the following aspects:

(a) The basal ganglia is directly involved in the control of movement and is the anatomical structure of the brain targeted by DBS.

(b) To understand how stimulation of brain tissue works, we need to combine fundamental concepts of electric properties of the brain, the behaviour of electric fields in brain tissue and the interactions between electrode field and tissue.

(c) DBS systems are based on standard pacemaking technology and they provide low frequency monopolar and bipolar stimulation within the basal ganglia.

(d) DBS research has extensively focused on modelling and characterising the mechanisms involved in DBS.

(e) Very little effort has been dedicated to the development of novel DBS systems.

# 3

# Characterisation of the Loading Effects of a DBS System

Research on the therapeutic effects of deep brain stimulation (DBS) has focused, in the past decades, on the development of detailed computational models of the electric field generated by the DBS stimulus around the brain target area.

In most cases, these models, however, rely on the assumptions that the stimulating electrodes are perfect voltage sources and the brain tissue is a purely conductive medium.

This approach may induce substantial error in the estimation of the electric field generated by a stimulus, since it neglects the reactive characteristics of a neurostim-

ulation system that can affect the shape and amplitude of the stimulus waveform and modulate the neural response [48].

It is important, therefore, to characterise the neurostimulator system and its response to applied stimuli, by modelling its electrical behaviour during stimulation. A model that faithfully represents the response of a DBS system, provides a powerful tool for many different purposes. It provides a description of the shape and amplitude of the stimulation waveform delivered to the target area and enable a more realistic approach to the prediction of the electric field spreading around the stimulation area. It plays an essential role in the design and development of stimulation devices, by giving information about the type of physiological load that must be driven by the stimulator. Finally, it serves as a framework to study the behaviour of alternative DBS stimuli in a controlled environment [63].

Recent models have started incorporating the electrode and the electrode-tissue interface impedance into FEM models, to better estimate the area of tissue activated during stimulation [12, 15, 48]. Results of these models have shown how the electrode impedance affects the stimulus waveform delivered to the tissue, with the results of overestimating the area of tissue activated by up to 30% [48].

The study presented in the chapter aims at characterising the electrical components forming a DBS system by modelling the current injected into the tissue as a result of an applied voltage stimulus. The first aspect of the study consists of breaking the whole DBS systems into electrical components and study the effects of variations of each component on the overall injected current during stimulation. The behaviour of each component will be described mathematically using established equations derived from electrochemistry research in the past decades. By breaking the model into several components we are able to isolate the contribution of each component to the behaviour of the overall system and to adapt the model to specific systems.

The second aspect of this study involves experimental measurements of the current

injected during voltage-controlled stimulation when a set of clinical DBS electrodes are adopted. These experiments are based on the standard three-electrode configuration used in electrochemistry. Measurements involving the use of clinical electrodes can provide a contribution to future studies involving the optimisation of the efficacy of DBS systems, by providing valuable information about the real-life behaviour of DBS systems in a controlled environment.

## 3.1 Model Description

The aim of the work presented in this chapter was to characterise the electric properties of a DBS system. Each component of a DBS system is represented by an electric model in order to define an equivalent circuit model that can be adopted to study the loading effects of a DBS system on the applied stimuli. The electric model, illustrated in Figure 3.1, consists of a voltage source, $V_{in}$, a series resistance, $R_{in}$, representing the resistance of the source and the extension and electrode leads, a capacitance, $C_p$, representing the lead parasitics, the electrode-brain interface (EBI), consisting of a capacitor, $C_{DL}$ in parallel with a resistor, $R_{CT}$, a series resistance (or bulk resistance), $R_a$, representing the access resistance, which provides a resistive path for the current to flow from the working to the counter to the counter electrode, assumed to be large enough to have a negligible impedance.

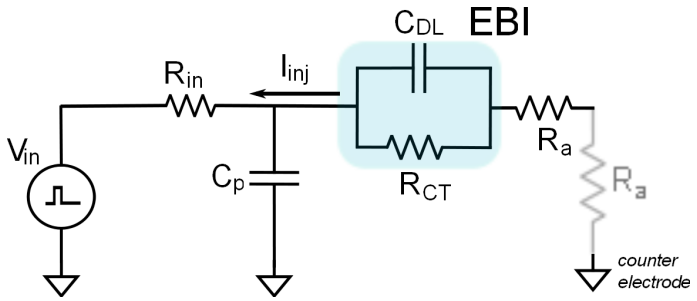


**Figure 3.1:** Electric model of a DBS system. The model consists of an ideal voltage source, $V_{in}$, and a series input resistance, $R_{in}$, representing the output resistance of the voltage source and the resistance of the leads. The EBI is represented by a parallel combination between the $C_{DL}$ and $R_{CT}$, in series with the access resistance, $R_a$.

Each component of the model will be described in detail in the following sections of this chapter.

### 3.1.1 Extension Lead

A typical extension lead, shown in Figure 3.2, contains four MP35N[1] conductor wires with a diameter of 0.1 mm, insulated by silicon rubber of resistivity[2] $\rho$=103$\mu\Omega$m.

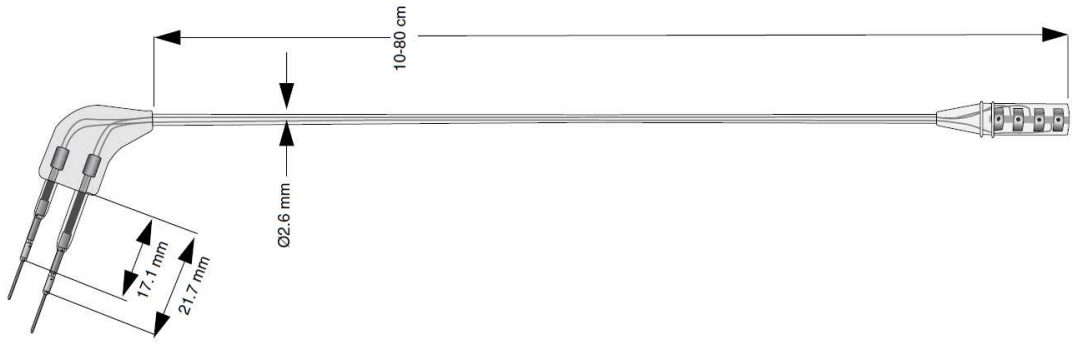


**Figure 3.2:** Extension Lead

The lead length varies between 10 and 80 cm, with a standard length of 51 cm. The extension lead can be described electrically by estimating its internal resistance and capacitance.

The resistance can be estimated by:

$$R = \frac{\rho L}{A} \tag{3.1}$$

where L and A are the cable length and cross-section area respectively. For a standard 51-cm long cable, the internal wire resistance is approximately 66Ω, but can vary between approximately 13Ω and 106Ω. An internal capacitance can appear in the form of a parallel-wire capacitance between conducting wires within the lead. This capacitance can be estimated by:

[1]Nickel (35%) alloy
[2]Source:www.asiinstruments.com

$$C_p = \frac{\pi \epsilon_0 \epsilon_r}{ln(D/a)} \tag{3.2}$$

where $\epsilon_0$ is the permittivity of free space ($8.85 \cdot 10e^{-12}$), $e_r$ is the insulating material dielectric constant (for silicon rubber $\epsilon_r$ ranges 3.2-9.8[3]), D is the distance between the wires and and a is the radius of the wire. For a standard 51-cm extension lead the parallel capacitance is in a range 127 to 398pF.

### 3.1.2 Electrode Lead

A typical electrode lead, shown in Figure 3.3, carries 4 wires terminating in 4 cylindrical platinum/iridium contacts. The conductor wires are insulated by fluoropolymer and the outer lead tubing is made of urethane. The length of the electrode lead varies between 10 and 50 cm.

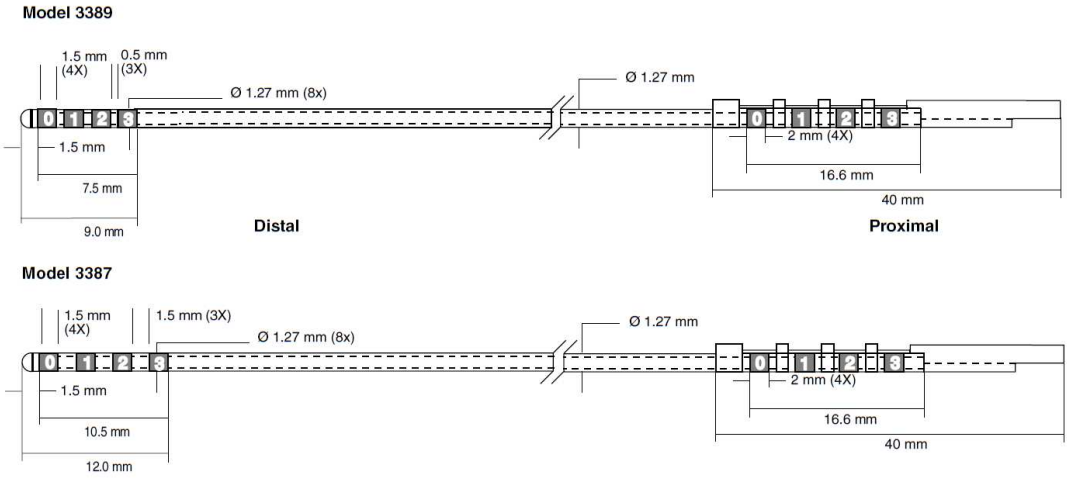


**Figure 3.3:** Electrode Lead.

The width of the electrode contacts is 1.5mm and the spacing between them depends on the electrode model. Model 3389 is characterised by 0.5 mm spacings between the contacts., whereas model 3387 contact spacing is 1.5mm. The estimation of internal resistance of the electrode lead wires can be performed by calculating the

[3]Source: www.asiinstruments.com

wire resistance as in equation 3.1. Since the resistivity of platinum/iridium alloy is found to be around $0.2\mu\Omega$m([4]), the actual wire resistance is in the order of tens of Ohms.

Additionally the capacitance between electrode contacts can be estimated in the form of a parallel plate capacitor formed by the cross-sections of the electrode contacts separated by the insulating tube according to:

$$C_{el} = \frac{A\epsilon_r\epsilon_0}{d} \tag{3.3}$$

where $\epsilon_r$ is the dielectric constant of urethane and $d$ is the spacing between electrode contacts. According to this analysis the contact capacitance is 19pF for model 3387 and 56pF for model 3389.

### 3.1.3 Electrode-Brain Interface (EBI)

The neurostimulation system is also characterised by a number of physiological processes occurring at the interface between the electrode contacts and the brain tissue (Electrode-brain interface, EBI). When a metal electrode is placed in contact with brain tissue, an interface is formed. The process occurring at the interface is a transduction of charge carriers from electrons in the metal electrodes to ions in the tissue. Charge is transferred between the two phases through two different processes: A non-faradaic and a faradaic process [38].

A non-faradaic process consists of a redistribution of charge and does not involve any transfer of electrons from the electrode to the tissue. This process represents electrode polarisation. Faradaic processes, conversely, consist of a transfer of electrons between the electrode and the tissue, resulting in a reduction reaction, if the electrons transfer from the tissue to the electrode, and oxidation reaction, if the electrons transfer from the electrode to the tissue. Reduction, which requires the

[4]Source: www.ndt.net

addition of electrons, occurs when the electrode potential is driven negative, whereas oxidation, requiring the removal of an electron, occurs when the same potential is driven positive. The non-faradaic process at EBI behaves as a capacitor, formed by a plane of charge at the surface of the metal electrode and a plane of opposite charge in the electrolyte. This process is predominant at the interface if the charge delivered to the interface is sufficiently small to generate only charge redistribution. An EBI can be modelled as the parallel combination of a double-layer capacitance, $C_{DL}$, representing the non-faradaic process and a charge transfer resistance, $R_{CT}$, representing a leakage at the interface, in series with the access resistance, $R_a$ representing the resistance of the electrolytic. For a metal in aqueous solution $C_{DL}$ is in the order of 10-20$\mu$F/cm$^2$ [38]. For a DBS electrode of surface area in the order of 0.06 cm$^2$, the actual electrode capacitance ranges between 600nF and 1.2$\mu$F.

#### 3.1.3.1 Constant phase element

According to experimental results obtained by Cole and colleagues [26], the EBI does not behave as a pure capacitor but instead reveals a frequency-dependent behaviour and it is best described by a constant phase angle (CPA) complex impedance, $Z_{CPA}$ [64, 65, 66, 67, 68] :

$$Z_{CPA}(\omega) = Z_0(j\omega)^{-\alpha} \tag{3.4}$$

where $Z_0$ is a measure of the magnitude of $Z_{CPA}$, $\omega$ is the angular frequency and $\alpha$ is a measure of the deviation from pure capacitive behaviour and describes the electrode surface roughness and absorption effects [69]. This behaviour was thoroughly studied by Onaral and Schwan [70], who found an empirical relation between the voltage transient response $V(t)$ of an electrode-electrolyte interface, the applied current step $I_{DC}$ and time, $t$. Their results showed that $V(t)$ was proportional to $t^\beta$, where $\beta$ is the exponent of the interface impedance at high frequencies. Additionally they described a relation between the current amplitude and a change of the voltage response from

a linear value, and the named this current the limit of current linearity. The aim of their study was to define a new electrode-electrolyte impedance relation that took into account applications where electrodes are operated at current densities at which the electrode impedance is no longer linear.

#### 3.1.3.2 Charge transfer resistance

The electrical excitation of the interface, by the application of electrical current, results in a potential difference that represents electrode polarisation. The difference between the polarisation potential and the equilibrium potential, $\eta$, is known as the overpotential and it is related to the current density at the interface as described by the Butler-Volmer equation [71]:

$$J = J_0\Big\{exp\Big[\frac{(1-\beta)F\eta}{RT}\Big] - exp\Big(-\frac{\beta F\eta}{RT}\Big)\Big\} \tag{3.5}$$

where $J_0$ is the current density at which the rate of oxidation and reduction reactions are equal at equilibrium, $\beta$ is a symmetry factor known as cathodic coefficient, $\eta$ is the applied overpotential, $F$ is the Faraday's constant, $R$ is the universal gas constant and $T$ is the temperature. A faradaic process is characterised by a direct transfer of charge and the formation of unrecoverable products in the solution, in conditions when the charge density exceeds safe limits [38]. The ability of the interface to pass direct current is modelled as a resistance, referred to as charge transfer resistance, $R_{ct}$, or Faradaic resistance. $R_{ct}$ represents the degree of change of the overpotential for a change in the current density at the interface. Such resistance is highly dependent of both the current density and the applied overpotential and it is therefore a source of major non-linearities [72]. A mathematical expression of the Faradaic resistance is given by [52]:

$$R_{ct} = \frac{1}{J_0\frac{F}{RT}exp[\frac{(1-\beta)F\eta}{RT}] - exp(-\frac{\beta F\eta}{RT})}. \tag{3.6}$$

For small values of overpotential $\eta$, $R_{ct}$ can be approximated as a function of the sole current density:

$$R_{ct_0} = \frac{RT}{FJ_0}. \tag{3.7}$$

Figure 3.4(A) shows the characteristic behaviour of the faradaic resistance in response to values of the current density ranging from 1n to 10nA/cm$^2$, for $\beta = 0.5$, $\alpha = 0.82$ and $Z_0$=184k$\Omega$, representing typical parameters for platinum electrodes of surface area of 10mm$^2$ [52]. $R_{ct}$ drops exponentially with the current density applied to the electrode. This relation can give indications on the selection of the metal and the electrode sizes that will provide the best isolation between the electrode and the electrolyte.

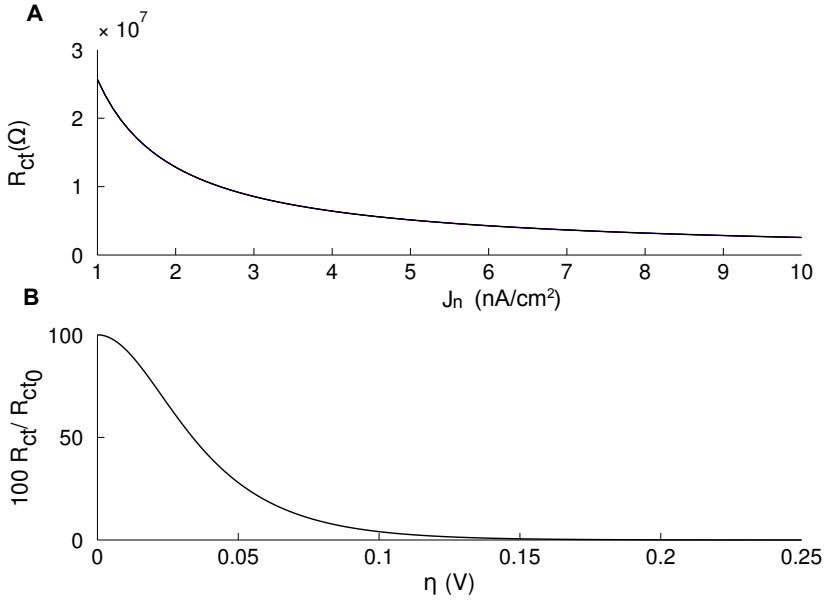


**Figure 3.4:** (A) Charge transfer resistance, $R_{ct}$ vs. current density $J_n$. (B) Normalised $R_{ct}$ versus overpotential. In both cases overpotential $\beta$ was set to 0.5.

Figure 3.4(B) represents the deviation of the $R_{ct}$ from its small-signal linear value $R_{ct_0}$. The increase in applied overpotential causes a rapid (exponential) deviation of the $R_{ct}$ from linearity. This relation can be adopted to estimate the voltage values and frequencies that will result in the onset of nonlinearity in the behaviour of the

charge transfer resistance at the interface.

#### 3.1.3.3 Electrode Impedance

Using the mathematical expressions reported in Eq 3.4, we can calculate the impedance of the EBI as a function of frequency, for values of $R_{ct}$=2MΩ, $R_a$=1kΩ, $\eta$=0 and $Z_0$=184kΩ [52]. Figure 3.5 shows the (A) magnitude and (B) phase of the EBI as we vary the parameter $\alpha$ between 0.5 and 1, where $\alpha = 1$ is used to represent the CPA as a pure capacitor. At very low frequencies, near DC, the impedance is completely dominated by $R_{ct}$, and the electrode capacitance is negligible. As the frequency is increased, the capacitance begins to influence the impedance behaviour where and the cutoff frequency depends on the value of the parameter $\alpha$.

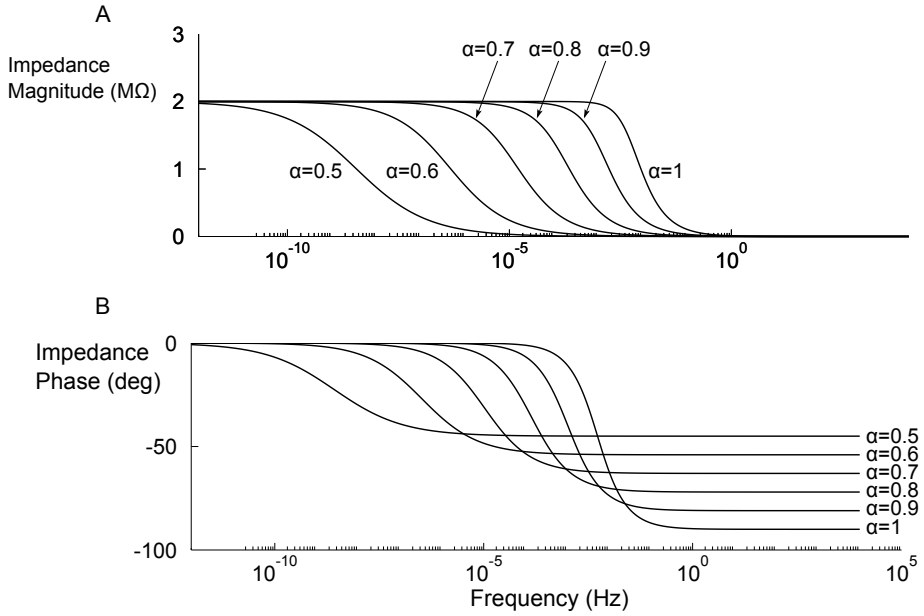


**Figure 3.5:** (A) Magnitude and (B) Phase of the CPA calculated for different values of the non-linearity parameter $\alpha$.

Figure 3.6 shows the (A) magnitude and (B) phase of the EBI impedance in a frequency range between 10 Hz and 1 kHz. The more the CPA deviates from a pure capacitor, the more the overall impedance decreases in magnitude and its phase deviates from $-90°$, which characterises the phase shift of a capacitor.

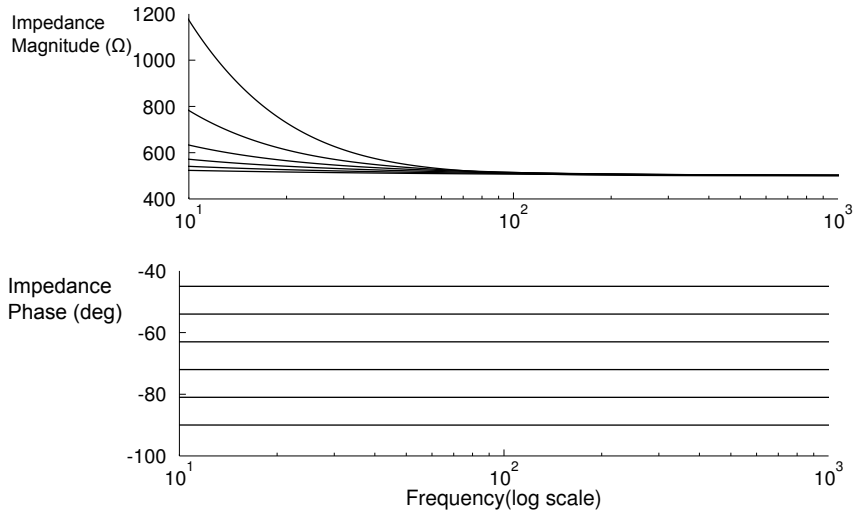


**Figure 3.6:** (A) Magnitude and (B) Phase of the CPA calculated for frequencies between 10 Hz and 1 kHz.

### 3.1.4 Bulk Resistance

An additional property of a neurostimulation system is represented by the bulk resistance. The bulk resistance represents the resistance of the medium surrounding the electrode. It is a function of the electrode size and shape, and it is modelled mathematically according to [73, 74]:

$$R_b = \frac{1}{2\pi\sigma a p} \tag{3.8}$$

where $\sigma$ is the conductivity of the electrolyte solution, $a$ denotes the radius of the hemisphere ad $p$ represents a shape factor (p=1 defines a sphere). It is useful to represent the relation between the electrode surface area A and the bulk resistance $R_b$ using the shape factor equation [73]:

$$\left(\frac{R_b}{R_b^{'}}\right)^2 = \left(\frac{A^{'}}{A}\right) \tag{3.9}$$

where $R_b^{'}$ and $A^{'}$ are the electrode surface area and the bulk resistance after the change of electrode size. Assuming tissue conductivities between 0.1 S/m and 0.3

S/m [15] and electrode radius of 1.27mm, the bulk resistance will range between 884Ω and 2652Ω.

### 3.1.5 Simulated Behaviour of a DBS system

The model in Figure 3.1 was simulated using the monophasic and biphasic square pulses in Figure 3.13 as input stimuli. Monophasic pulse are characterised by a single negative (cathodic) constant pulse lasting tens to hundreds of microseconds. Biphasic pulses consist of cathodic pulse immediately followed by anodic pulses, which aim at reversing any charge transfer processes that may have occurred during the cathodic stimulation [38]. A modification of a biphasic pulse consists of the introduction of a short delay between the cathodic and the anodic pulses. The pulses are characterised by a pulse width ($W$), a period ($T$) and in the case of biphasic pulses, by an interpulse delay (ID). The average rise/fall time of each pulse was set to 10 ns.

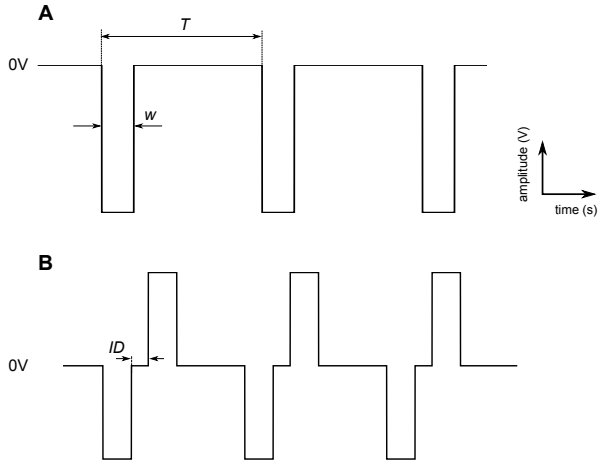


**Figure 3.7:** Model input stimuli. (A) Monophasic and (B) biphasic pulses characterised by a width, $W$, a period, $T$, and a interpulse delay, $ID$.

### 3.1.6 Loading Effects of the Electrode/Tissue Interface

The electric model in Figure 3.1 was adopted to study the effects of the ETI impedance on the pulse shape, by varying its parameters, including $C_{DL}$, $R_{ct}$ and

$R_a$ within a specific range. The input voltage $V_{in}$ was set to 4 V with a pulse width of 100 $\mu$s and a frequency of 130 Hz, representing clinical DBS settings. The series resistance $R_{in}$ was set to 200 Ω. Firstly the effects $R_{ct}$ were explored by varying its value between 500 Ω and 2M Ω. For the specified pulse settings no substantial impact on the pulse shape and amplitude was observed. The pulse shape, in fact, is expected to be highly dependent on the impedance of the high-pass filter formed by $C_{DL}$ and $R_a$. Figure 3.8 shows the effects of setting the dual layer capacitance to 100 nF and 600 nF, when $R_{ct}$ is set to 1M Ω and $R_a$=1kΩ. A value of $C_{DL}$ of 100nF is used to clearly illustrate the effects of electrode polarisation.

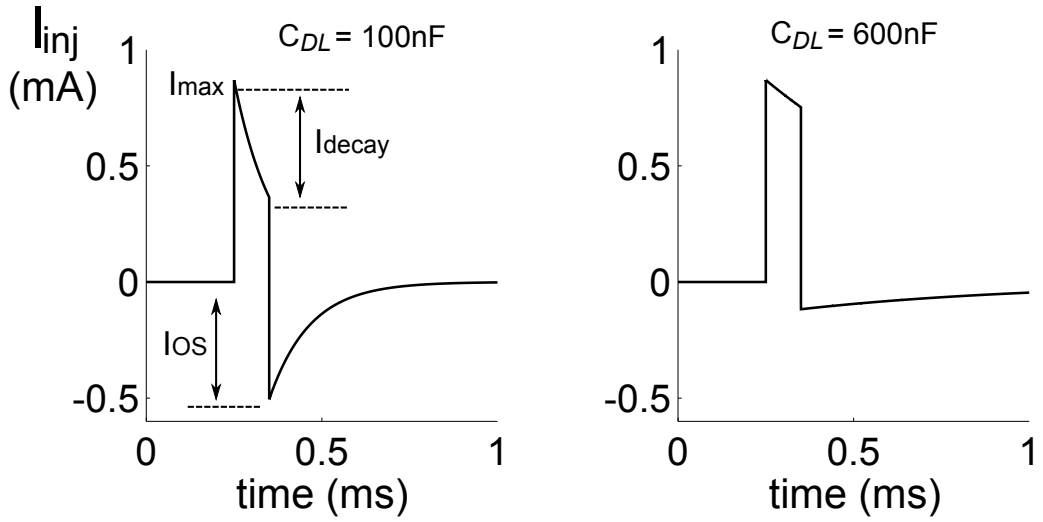


**Figure 3.8:** Simulated effects of electrode capacitance on the stimulus waveform.

Postprocessing analysis of the results included the estimation of peak amplitude, overshoot and decay rate for different values of $C_{DL}$. When the input pulse is on, the current injected through the EBI, $I_{inj}$, will be at its maximum, $I_{max}$. During the pulse plateau, the current will decay by an amount $I_{decay}$ until the input pulse is turned off. At this point in time the current will quickly reverse its polarity, causing an overshoot, $I_{OS}$. Estimates of these parameters, associated to the plots in Figure 3.8, are reported in Table 3.1.

The smaller the value of $C_{DL}$, the fastest in the decay of the current, which results in a larger overshoot current. The charge injected by the overshoot current was

**Table 3.1:** Pulse Characteristics Estimated for Different Values of the Dual Layer Capacitance, $C_{DL}$

| $C_{DL}$ **(nF)** | $I_{max}$ **(mA)** | $I_{decay}$ **m(A)** | $I_{OS}$ **(mA)** |
|---|---|---|---|
| 100 | 0.87 | 0.52 | 0.5 |
| 600 | 0.87 | 0.12 | 0.12 |

estimated to reach up to half the current injected by the applied pulse for $C_{DL}$=100 nF. The other parameter affecting the time constant of the injected current is the access resistance, $R_a$, the effects of which were studied by changing its magnitude between 100 Ω and 1k Ω in steps of 180 Ω, while $C_{DL}$ was set to 600 nF. The resulting simulated current pulse shapes are reported in Figure 3.9.

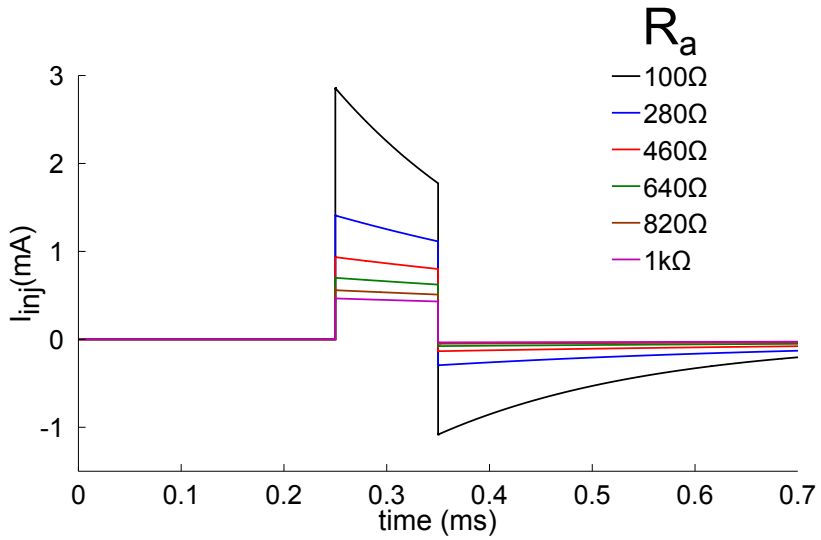


**Figure 3.9:** Simulated effects of tissue resistance, $R_a$, on the stimulus waveform.

The main impact of varying the amplitude of the access resistance is on the amplitude of the injected current and the time constant. Table 3.2 lists the values of the pulse characteristics, including peak amplitude, decay rate and overshoot current, in response to changes of $R_a$.

For small values of $R_a$, the injected current will reach large amplitude and large overshoot currents, due to the fast decay. As the value of the resistance increases, the injected current amplitude will decrease and so will the overshoot current. The decay of the overshoot however will be much longer for large values of $R_a$, resulting

**Table 3.2:** Pulse characteristics estimated for different values of the access resistance, $R_a$

| $R_a$ ($\Omega$) | $I_{max}$ (mA) | $I_{decay}$ (mA) | $I_{OS}$ (A) |
|---|---|---|---|
| 100 | 2.9 | 1.14 | 1.1m |
| 280 | 1.4 | 0.28 | 0.3m |
| 460 | 0.9 | 0.1 | 0.13m |
| 640 | 0.7 | 0.08 | $77\mu$ |
| 820 | 0.6 | 0.07 | $50\mu$ |
| 1k | 0.5 | 0.06 | $35\mu$ |

in longer time needed for the capacitor to fully discharge. We will look at the implications of this issue in the next sections.

### 3.1.7 Modeling the Effects of Pulse Width and Interpulse Delay

We have considered the effects of the electrode impedance to square pulses lasting for 100$\mu$s. If we fix the values of the $C_{DL}$ and $R_a$ (in this example to 300nF and 460$\Omega$, respectively), we can observe the effects of changing the pulse width, $W$, on the characteristics of the resulting current pulse. The injected current resulting from changing the pulse width between 60$\mu$s and 300$\mu$s is represented in Figure 3.10.

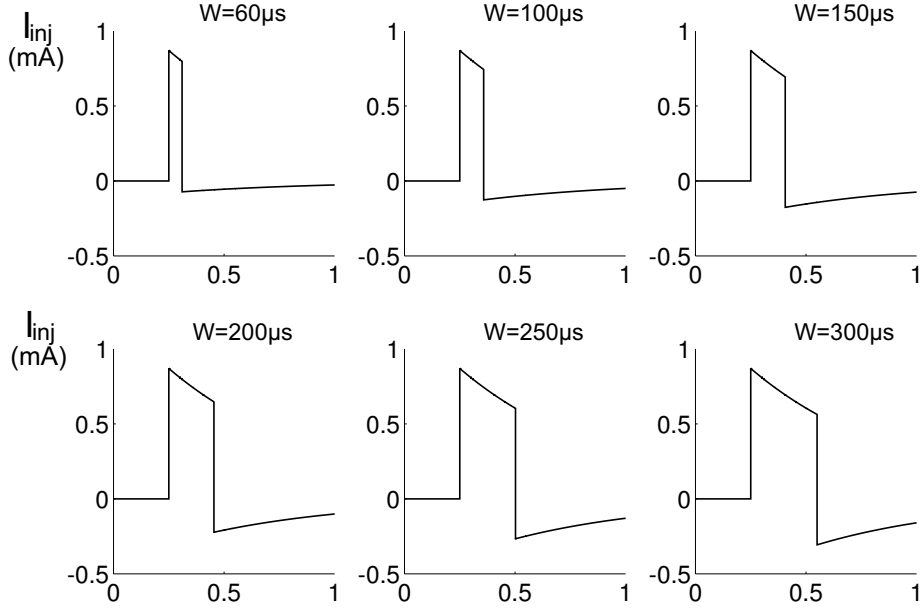


**Figure 3.10:** Simulated injected current with changes in stimulus pulse width.

The main effects of increasing the pulse width is to increase the duration of the decay, which in turn, increases the amplitude of the overshoot current. The estimated pulse characteristics are reported in Table 3.3.

**Table 3.3:** Pulse Characteristics Measured for Different Values of the Pulse Width

| **W($\mu$s)** | $I_{max}$**(mA)** | $I_{decay}$ **(A)** | $I_{OS}$ **(A)** |
|---|---|---|---|
| 60 | 0.87 | 70$\mu$ | 72$\mu$ |
| 100 | 0.87 | 0.13m | 126$\mu$ |
| 150 | 0.87 | 0.18m | 176$\mu$ |
| 200 | 0.87 | 0.2m | 0.2m |
| 250 | 0.87 | 0.28m | 0.27m |
| 300 | 0.87 | 0.3m | 0.3m |

So far we have considered the effects of the electrode impedance on monophasic (positive) pulse. Simulation results have shown how the electrode capacitance and the tissue resistance affect the shape of the injected current pulse. The current amplitude decays with a time constant approximately equal to $C_{DL} \cdot R_a$. At the end of the pulse the current overshoots to a negative value before returning to 0A following the same time course. An interpulse delay, $ID$, has to be added between the cathodic and the anodic phase of the stimulation pulse. The duration of this pulse has to be large enough for the anodic current not to overlap with the overshoot current from the previous phase, but is also limited by the stimulation frequency. Figure 3.11 shows the effects of varying the interpulse delay on the shape and characteristic of the injected current pulse, when $C_{DL}$ is set to 300nF and $R_a$ to 460$\Omega$.

When ID is set to 30 $\mu$s, the capacitor does not have time to completely discharge before the anodic pulse is applied, resulting in a larger charge injected during the anodic phase than during the cathodic phase. In this case for a 0.95 mA cathodic pulse, the amplitude of the anodic pulse was estimated to be 1.3 mA. By increasing the interpulse delay to 100 $\mu$s, the amplitude of the anodic current was estimated to be 1.1 mA. Equal anodic and cathodic current amplitudes were achieved when the interpulse delay was larger than 300 $\mu$s.

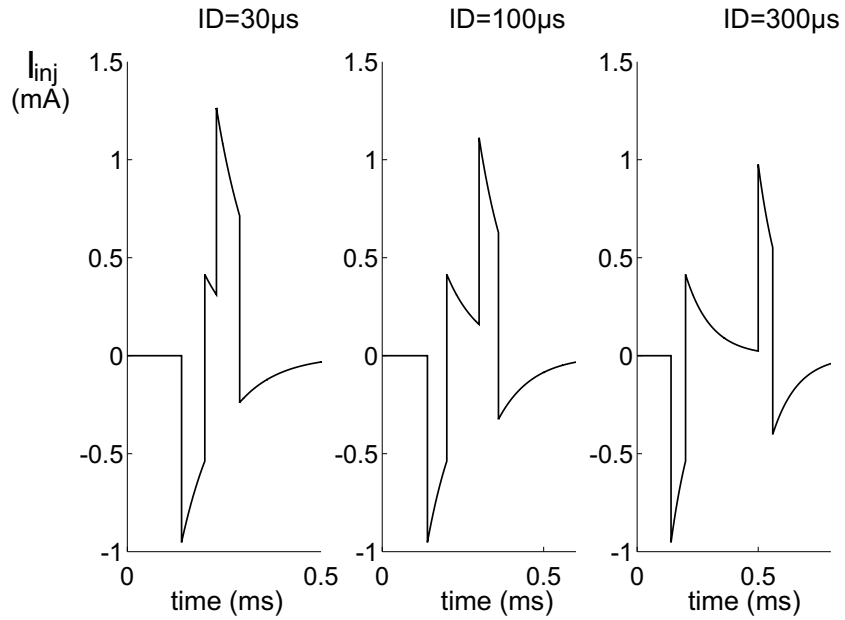


**Figure 3.11:** Simulation of the response of a DBS system to changes in interpulse delay.

The model described in this section has analysed mathematically the different electrical components of a DBS system. We have observed how the dual-layer capacitance has a major impact on the electrode polarisation, resulting in an decay of the injected current during the plateau of the applied voltage. The charge-transfer resistance has a minor impact on the electrode polarisation but represents a source of nonlinearity, when the electrode is driven a current densities higher than specific limits. When the model describes the characteristics of a standard platinum electrode (with similar properties to clinical DBS electrodes), the injected current resulting from the application of a voltage pulse, shows decays and overshooting which may influence the effects of stimulation. Due to the non-linear behaviour of the injected current profile, the charge injected to the tissue as a result of this type of configuration is difficult to control or estimate. Additionally, we have observed how the access resistance, which represents the tissue resistance in the proximity of the electrode has an influence of the injected current amplitude, suggesting that different current densities, electrode sizes and tissue properties will influence the profile of the injected current. Finally, we can highlight the importance of the interpulse

delay when voltage-controlled stimulation is applied, by observing how, for small interpulse delays, the nonlinear behaviour of the injected current may cause large overshoot which could affect or even reverse the effects of stimulation.

## 3.2 Experimental Setup and Design

Figure 3.12 shows a general block diagram of the set up used to record the behaviour of the DBS system during stimulation.

The experimental setup consists of a square pulse generator, a digital-to-analogue converter (DAC), a DBS electrode, a saline-filled water tank and a digital oscilloscope. A virtual DBS pulse generator was developed in Labview (version 8.2, National Instruments) to drive the output of a 16-bit digital-to-analog converter of a multifunction data acquisition card (NI USB-6229, National Instruments) at a sampling frequency of 250 kS/s. The pulse generator allowed to control stimulus parameters, including amplitude, pulse width, frequency and interpulse delay.

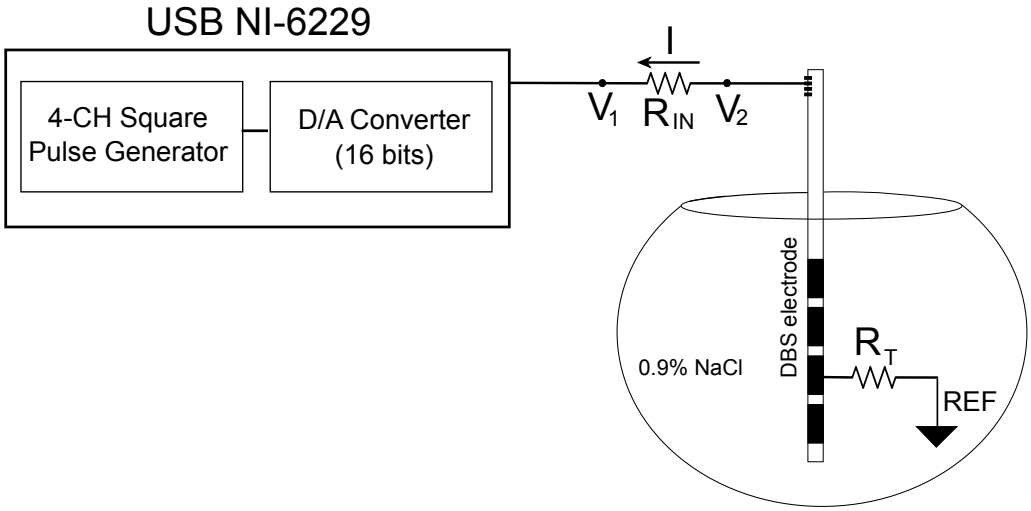


**Figure 3.12:** Set up for measuring the loading effects of a DBS electrode in a saline solution. The Labview program was used to generate monophasic and biphasic pulses and to control parameters such as pulse width, frequency and amplitude. A data acquisition card provided a 16-bit digital to analog converter and one analog output used to drive the stimulus signals. The signal was then applied to the electrode contact through a connector. The injected current was measured as the difference between $V_2$ and $V_1$ measured across a 1k$\Omega$ resistor.

A 4-contact DBS electrode (model 3387, Medtronic, USA) was placed in a 25-cm-diameter tank, filled with saline solution (0.9%NaCl) of conductivity, $\sigma$, 0.2 S/m. One electrode contact was driven by the monophasic and biphasic set of pulses, representing typical DBS stimuli, depicted in Figure 3.13. The loading effects of a DBS system were analysed by measuring the injected current, $I$, as the ratio between the potential drop, $V_2 - V_1$ and a 1k $\Omega$ resistor. The effects of changing the pulse width and the interpulse delay were recorded during monophasic and biphasic stimulation. Additionally the impedance of the system was measured with an impedance analyser (Wayne Kerr 6500B, Precision Impedance Analyzer).

## 3.3 Experimental Measurements

Pulse width, amplitude, frequency and interpulse delay are the only controllable parameters in a DBS system. In this part of the study, the focused in on the profiles of the injected current in a realistic (in vitro) environment. The amplitude and frequency of the stimuli do not represent a major factor influencing the current profile, therefore they are neglected in this study. The analysis is based on the use of ranges of clinical DBS settings, using monophasic and biphasic pulses.

### 3.3.1 Loading Effects of a DBS electrode

The experimental setup was used to measure the characteristics of the current injected in the saline solution when monophasic and biphasic voltage pulse was applied at the input. For reference we report in Figure 3.13 the monophasic and biphasic stimuli adopted in this study.

Figure 3.14A shows the current profile in response to a monophasic voltage pulse with amplitude of 2V, width of 60$\mu$s and rise time of 4$\mu$s (limited by the DAC sampling rate).

At stimulus onset the current is at its maximum, measured to be -0.61 mA. During

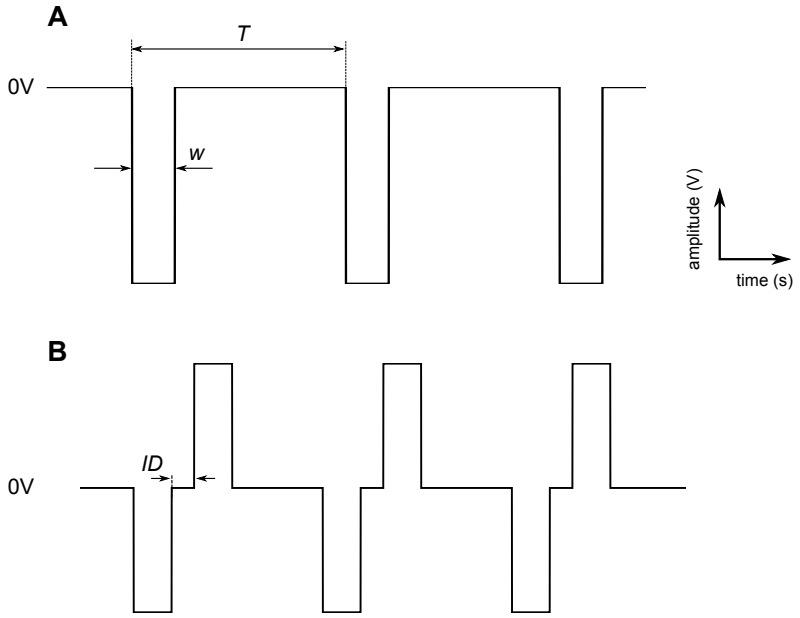


**Figure 3.13:** Model input stimuli. (A) Monophasic and (B) biphasic pulses characterised by a width, $W$, a period, $T$, and a interpulse delay, $ID$.

the pulse plateau the current decays by 0.21 mA and when the stimulus is turned off, the current overshoots to 0.24 mA, after which the current returns to 0A with a time course of approximately 150 $\mu$s. Figure 3.14B shows the profile of the injected current in response to a biphasic voltage pulse of amplitude of 4 V peak-to-peak, width of 60 $\mu$s and interpulse delay of 100 $\mu$s.

### 3.3.2 Effects of Pulse Width and Interpulse Interval

Effects of changing pulse widths were measured in response to a monophasic voltage pulse of amplitude of 2V. Figure 3.15 shows the profiles of the injected current when the pulse width was set to 60 $\mu$s, 90 $\mu$s, 120 $\mu$s and 300 $\mu$s.

In agreement with the simulated results reported in the previous section, an increase in the pulse width results in a larger decay and, consequently, in a larger overshoot. Quantitatively the characteristics of the current pulse are reported in Table 3.4.

For pulse widths greater than 120 $\mu$s, the pulse amplitude decays more than 50% its peak value, resulting in overshooting greater than half the pulse amplitude.

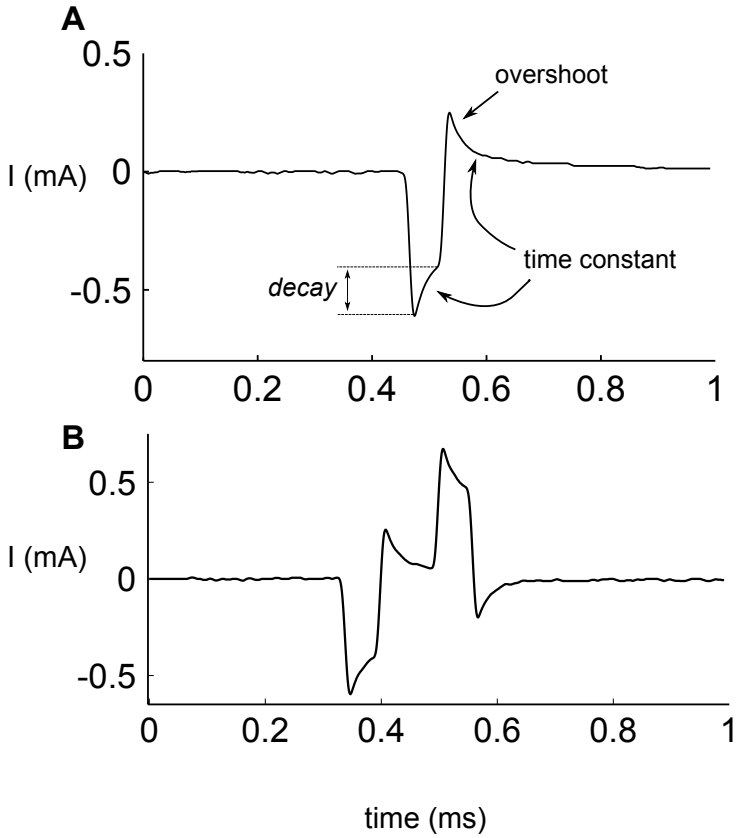


**Figure 3.14:** Loading effect of a DBS electrode. Mesured injected current in response to (A) monophasic and (B) biphasic square voltage pulses of amplitude of 2V and width of 60$\mu$s. The interpulse delay of biphasic pulses was 100$\mu$s.

**Table 3.4:** Measure pulse characteristics for different pulse widths

| **Pulse Width ($\mu$s)** | $I_{max}$ **(A)** | $I_{decay}$ **(A)** | $I_{os}$ **(A)** |
|---|---|---|---|
| 60 | -0.61m | 0.21m | 0.24m |
| 90 | -0.61m | 0.24m | 0.28m |
| 120 | -0.61m | 0.3m | 0.31m |
| 300 | -0.61m | 0.378m | 0.39m |

The effects of interpulse delay (ID) were recorded by applying biphasic pulses with IDs equal to 30 $\mu$s, 100 $\mu$s and 300 $\mu$s and are shown in Figure 3.16. For small interpulse delays, the overshooting current following a cathodic pulse overlaps with the anodic current, resulting in larger charge injected during the anodic phase, with respect to the cathodic phase (assuming the duration of the two phases is equal). For an 30 $\mu$s ID, the current during the anodic phase reaches a maximum of 0.7 mA, as compared to 0.61 mA during the cathodic phase. By increasing the ID to 100

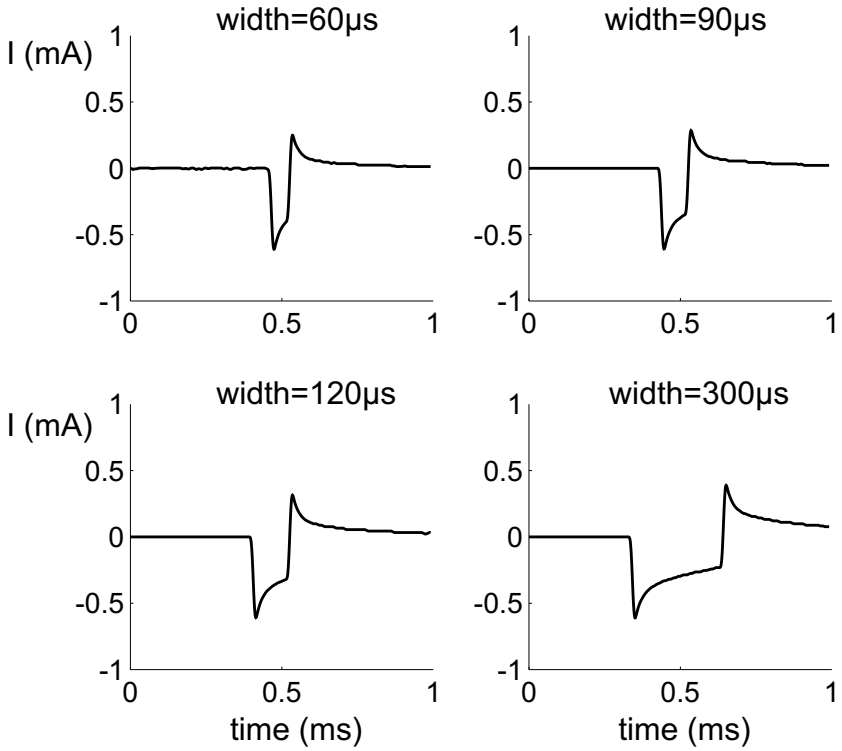


**Figure 3.15:** Effects of varying the pulse width on stimulus

$\mu$s, the peak of the anodic current was found to be 0.65 mA. The peak value of the anodic and cathodic currents were found to be equal when the ID was larger than 300 $\mu$s, which is in agreement with the simulated results reported in Figure 3.11.

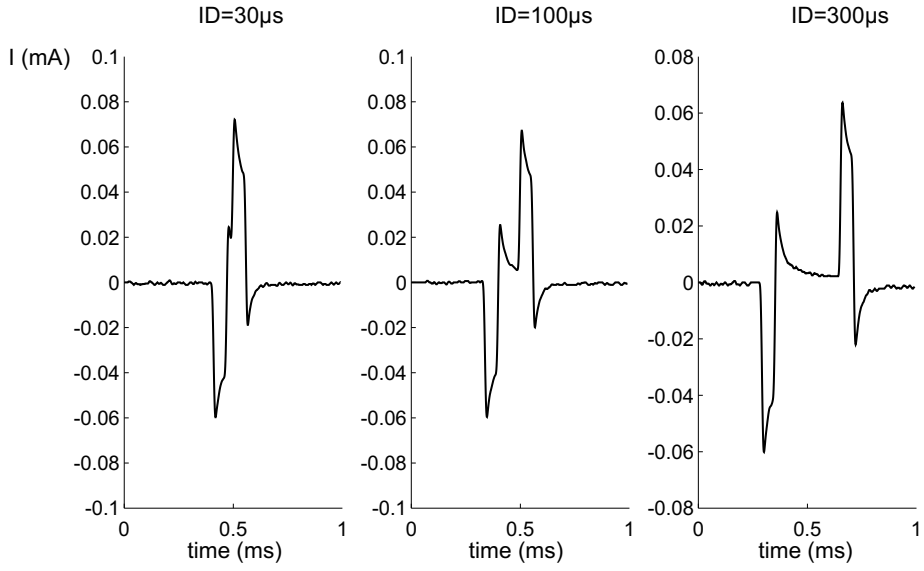


**Figure 3.16:** Measured effects of varying the Interpulse Delay (ID).

### 3.3.3 Load Impedance Measurement

The impedance of the system was measured by applying a 1V-sinusoidal voltage between two electrode contacts. The impedance was measured for 100 frequency points ranging between 20Hz[5] and 1MHz. The magnitude and phase plots are reported in Figure 3.17A and 3.17B, respectively.

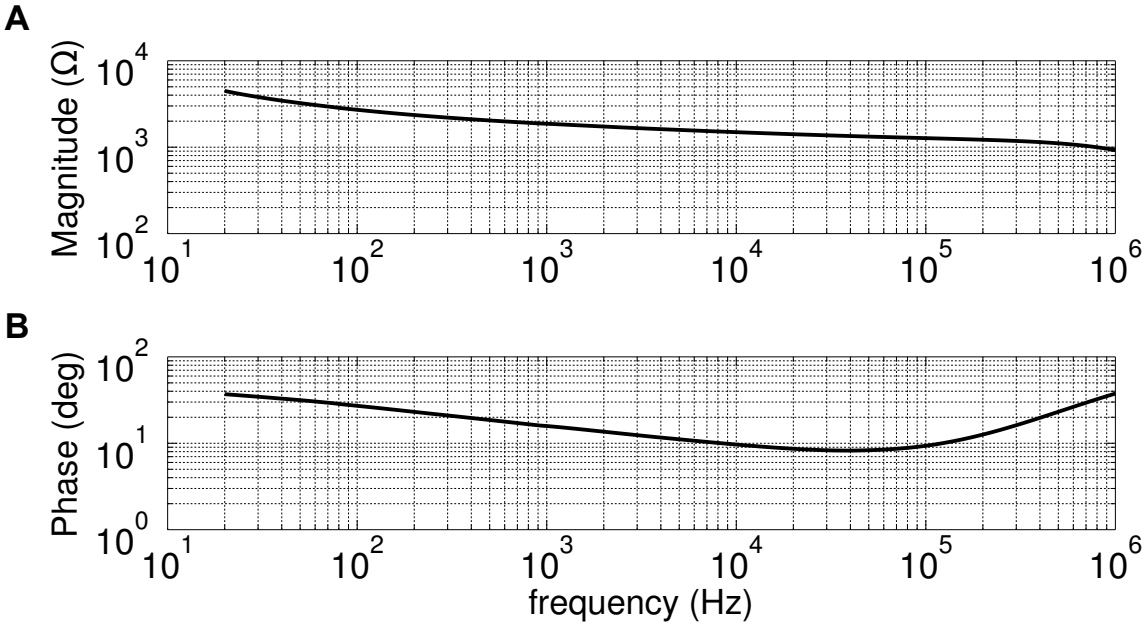


**Figure 3.17:** Measured impedance of a DBS electrode. (A) Magnitude (B) Phase measure at 100 frequency points between 20Hz and 1MHz

Indicative values of the impedance were extracted at different frequency points and are summarised in Table 3.5.

**Table 3.5:** DBS electrode impedance magnitude and phase at different frequency points

| **Frequency** (Hz) | **Magnitude** (Ω) | **Phase (deg)** |
|---|---|---|
| 20 | 4.5k | 37 |
| 100 | 2.7k | 26 |
| 200 | 2.36k | 23 |
| 1k | 1.8k | 15 |
| 2k | 1.7k | 13 |

[5]20Hz is the minimum frequency allowed by the instrumentation

## 3.4 Analysis and Discussion

A circuit model of a typical DBS system was developed to study the loading effects of a DBS system on the characteristics of DBS stimuli. These, in fact, travel along a complex circuit which drastically affects their shape, resulting in major differences between the stimuli programmed at one end of the DBS system and the stimuli delivered to the target tissue area [48].

The model explored the electrical properties of each component forming the electrical path of a DBS system. The parasitics associated to the extension and electrode lead are represented mainly by the resistance of the cables (estimated to be 67 Ω) which could sum up to few hundred ohms for long cables, affecting the overall amplitude of the stimulus. The capacitance of the cables, however, was calculated to be in the range between 127 pF and 398 pF and therefore considered negligible compared to the electrode impedance, which, for platinum electrodes of areas of few square millimetres, is usually estimated in the order of few hundred nanofarads [38].

The ETI is the major source of non-linearity in a DBS system. The mathematical model of the ETI included the charge transfer resistance and a constant angle (CPA) element, which represents the deviation of the electrode behaviour from a pure capacitor. The CPA, however, was not included in the circuit equivalent model of the ETI, due to its complex nature, and the electrode was modelled as a parallel combination of a capacitor and a resistor.

The injected current pulse is greatly influenced by the electrode capacitance and the filtering behaviour associated with the electrode capacitance and tissue impedance. The charge-transfer resistance was not found to have a major overall impact on the injected current pulse. The current pulse followed a standard pattern representing the electrode polarisation [38]. The current amplitude is at its maximum at the start of the stimulus and accommodates to a new values at the end of the stimulus. The discharging of the electrode capacitance at the end of the pulse causes the current to

overshoot. In reality the overshoot potential may reverse some of the physiological effects caused during the active stimulation phase [75]. Increasing the value of the capacitance reduces the polarisation effects.

The model validation was performed by carrying out a set of wet experiments to measure the loading effects on the applied stimulus, of a DBS electrode placed into a saline-filled tank. Measurements showed agreement with the predictions of the model, in terms of behaviour of the injected current, for electrode capacitance in the order of few hundred nanofarads. The polarisation of the electrode is very pronounced suggesting interpulse delays larger than $300\mu$A to avoid overlapping between the overshoot current and the current injected during the anodic phase.

## 3.5 Conclusion

This study presented a mathematical and circuit model of a complete DBS system, including lead parasitics and electrode-tissue interface properties. Experiments validated the behaviour of the model in terms of electrode polarisation, current decays and overshooting and minimum interpulse delays necessary to avoid large overshooting currents during the anodic (charge balancing) phase of stimulation. In addition, they provided a qualitative analysis of the loading effects of a DBS system during voltage-controlled stimulation. Some conclusions may be drawn from this analysis.

(a) The behaviour of a DBS system is determined primarily by the electrode capacitance.

(b) Voltage-controlled stimulation causes the injection of current that changes over time and it highly dependent on the load impedance, which does not allow an accurate estimation of the charge injected into the tissue during stimulation.

(c) A simple electrical model can qualitatively describe the behaviour of a DBS system, and in particular of the EEI, although more advanced model and larger

experimental datasets are needed to describe a DBS system quantitatively.

(d) The circuit model presented in this study can be used to accurately represent the load when designing DBS stimulators.

# 4

# Multipolar DBS

## 4.1 Selectivity in DBS

Conventional DBS stimulation techniques are based on the use of monopolar and bipolar electrode configurations, consisting of one or two active contacts on the electrode. In response to monopolar stimulation, the resulting potential distributes symmetrically around the electrode contact, and the area of stimulation is affected solely by the stimulus configuration [17]. Bipolar stimulation gives one more degree of flexibility, represented by the polarity of the two electrode contacts used for stimulation. To achieve additional flexibility, therefore, we need to increase the number of active contacts during stimulation. The concept of flexibility is here represented

by the idea of *electric field shaping*. The principle of electric field shaping, based on the use multipolar current-steering and current-focusing electrode configuration, in comparison with standard stimulation methods, has become of great interest in the past decades in the field of cochlear implants [76, 77, 78, 79, 80, 81], DBS [82] and functional electrical stimulation (FES) [83]. The overall goal of field shaping is to control precisely the region of tissue that will be activated by stimulation. By adopting multipolar electrode configurations, the potential distribution results from the sum of the contributions of each source (See Section 2.3.2.1 in Chapter 1). By controlling the magnitude, polarity and number of active contacts we introduce additional control capability over the shape of the potential distribution (field shaping). The principle of using multipolar configurations is strictly related to stimulation selectivity according to an experimental law, defined by Pfluger, by which a stimulus generated under the cathode cannot pass through an anodically polarised region of a fibre [84]. This principle is conventionally used in FES to block the propagation of action potentials along a fibre, thus increasing the selectivity of the location of action potential generation and propagation, and avoid unwanted stimulation [85]. In cochlear implants, different electrode arrangements have been adopted in order to shape the cathodic spread of the stimulation field, aiming at increase pitch perception by using the principle of lateral inhibition currents [76, 77]. The use of multipolar electrode configurations is a necessary, although not sufficient condition to increase stimulation focus. In fact, neural activation has been proven to occur also in the proximity of anodes, due a phenomenon known as *anodal break excitation*. This occurs at the end (break) of an anodic pulse, when the membrane potential, returning to its resting potential, exceeds the excitation threshold which has been substantially decreased during hyperpolarisation [86]. Burke and Ginsborg [87] developed a technique based on the use of exponential pulses, with time constants in the order of 30ms, that resulted in the avoidance of break excitation. Accornero and colleagues [84] succeeded in avoiding break excitation with expo-

nential pulses with decays of about 4ms. Following their successful results, several topologies of pulses, such as triangular, quasi trapezoidal and depolarising prepulses have been identified as optimal pulses to provide complete or partial anodal blocking [88, 85, 89, 90, 91, 92].

This chapter investigates the application of multipolar electrode configurations to DBS, aimed at achieving dynamic control of the focus of stimulation and the area activated during stimulation. The aim of the work presented in this chapter is to define the spatial resolution of multipolar stimulation modes, achieved by using different configurations on clinical DBS electrodes. We will limit the analysis to three different electrode configurations: A tripolar configuration, characterised by a central cathode and two lateral anodes; A quadripolar configuration, based on the use of two central cathodes and two lateral anodes, and a pentapolar configuration, where the three central contacts are used as cathodes and the two lateral ones as anodes. We will present models of the behaviour of the fields generated using these configuration and methods to dynamically control the stimulation field. Finally we will show how the concept of field shaping by multipolar electrode approaches is validated by models of neural activation in response to multipolar stimulation.

## 4.2 Multipolar Electrode Configuration

This section describes three different configurations of electrodes adopted in order to model field shaping in DBS. The tripolar electrode configuration in Figure 4.1(a) consists of an apical anode, $E_2$, sourcing current $I\alpha$, a basal anode, $E_4$, sourcing current $I(1-\alpha)$ and a central cathode, $E_3$, sinking current $I$, where $\alpha$ is a weight parameter, controlling the ratio between the anodic currents, and allowing to steer the current towards the basal or the apical anode [78].

The same concept can be extended to electrode configurations including more than three active contacts. A quadripolar current-steering configuration (Figure 4.1(b))

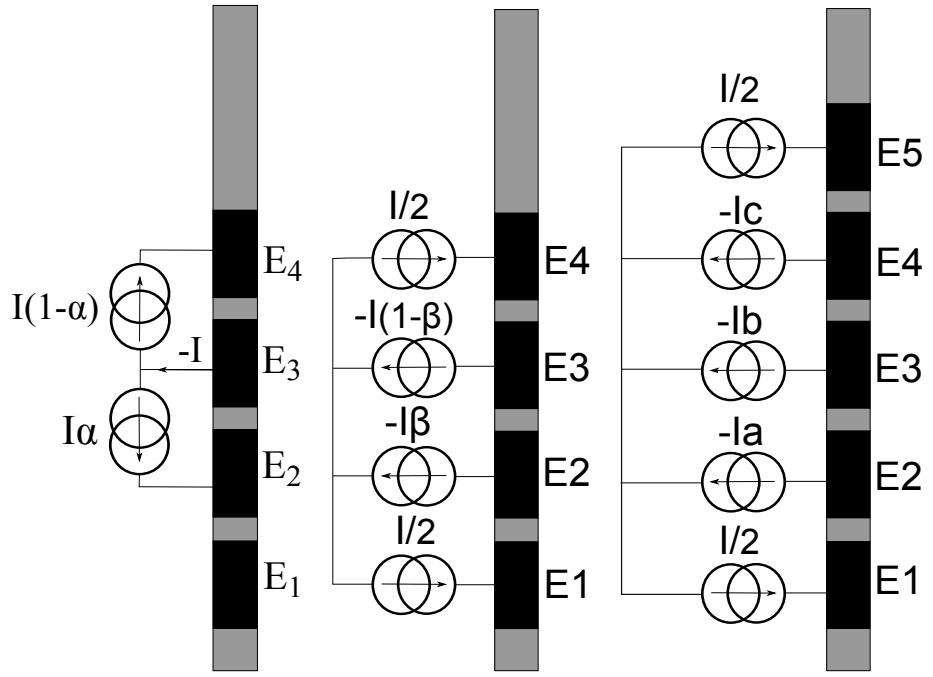


(a) Tripolar electrode configuration. (b) Quadripolar electrode configuration. (c) Pentapolar electrode configuration.

**Figure 4.1:** Multipolar Electrode Configuration

can be formed by an apical and a basal anode, each sourcing half the stimulation current, and a combination of two cathodes sinking currents $I\beta$ and $I(1-\beta)$, respectively, where $\beta$ is a weight parameter that allows to control the ratio of currents flowing between the cathodes. By keeping the same configuration, the number of cathodes can be increased to three, as depicted in Figure 4.1(c), representing a pentapolar configuration. In this case the total current, $-I$, is shared among the three central cathodes by three weight parameters, $a$, $b$ and $c$, such that $I = Ia + Ib + Ic$ and $a + b + c = 1$.

## 4.3 FEM model description

An axi-symmetric model of a DBS electrode implanted in brain tissue was constructed using the finite element method (FEM) and consisted in the circular mesh

of 13232 elements[1] (average mesh unit size: 0.5mm, range: 23$\mu$m-1mm) in Figure 4.2, characterised by homogeneous isotropic properties, with conductivity $\sigma$= 0.11 S/m [15] and permittivity $\epsilon_r = 3.9 \cdot 10^6$, representing the brain tissue properties at frequencies ranging from DC to 1 kHz [26].

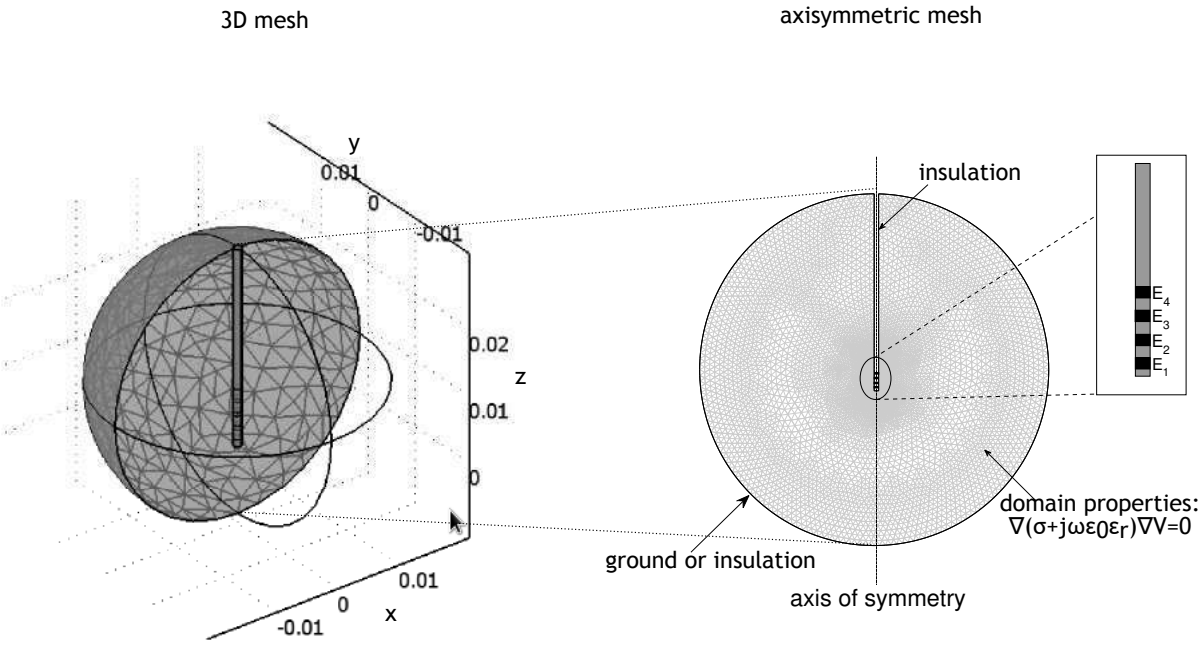


**Figure 4.2:** 2D mesh of DBS electrode in brain tissue.

The volume conductor measured 50mm in radius, which was large enough to enclose the target region. The geometry of the electrode represented the structure of a clinical DBS electrode (Model 3387, Medtronic, USA), characterised by 1.5 mm wide contacts and 1.5 mm spacing between contacts, used for stimulation of the STN. The shaft of the electrode ran up to the boundary of the volume conductor. Insulation conditions were imposed on the electrode shaft. The electrode contacts were treated as ideal current sources, although this approach may result in overestimation of the predicted volume of tissue activated [48]. The validity of the quasi-static approximation for calculating electric potentials [93] allows us to calculate the electric potentials, $V$, by solving the Laplace equation:

[1]To provide an acceptable level of accuracy this value results in a mesh unit size smaller than the internodal separation of 0.5 mm of the axon models used to predict neural activation and discussed in 4.9.1.

$$\nabla\sigma\nabla V = 0 \tag{4.1}$$

The current sources were represented as current densities, $J_n$, imposed on the boundaries of the conducting electrode $n$, as $J_n = I_n/A$, where $I_n$ is the current through the electrode $n$ and $A$ is the area of the electrode. The solution of the Laplace equation represents the voltage distribution around the electrode. The width of the mainlobe of the field distribution can be then taken as a measure of current spread [76, 94].

## 4.4 Tripolar model - Simulated potential distribution

The model in Figure 4.1(a) in Section 4.2 was used to simulate the behaviour of the potential distribution generated using a tripolar electrode configuration. The total current injected through the cathode was set to 1 mA, while $\alpha$ was varied between 0 and 1, in steps of 0.1.

Figure 4.3(a) shows the FEM surface plots of the potential distribution generated by the tripolar source for values of $\alpha$ equal to 0, 0.5 and 1 respectively. When $\alpha =$ 0 electrode $E_2$ is not conducting and the current flows between $E_3$ and $E_4$, creating two regions of opposite polarity, a cathodic area spreading around contact $E_3$ and an anodic area spreading around $E_4$. When the currents on the two anodic branches are balanced (i.e. $\alpha$=0.5), anodic spread occurs on both sides of the tripole, and the cathodic spread is bound between these two regions and focused around the centre of the tripole. By increasing $\alpha$ towards 1, the current through $E_4$ is reduced to zero, thus creating a cathodic and an anodic region centred around $E_3$ and $E_2$, respectively. The cross-section plots in 4.3(b) represent the normalised profiles of the potential distributions measured at a distance of 2mm from the electrode. The

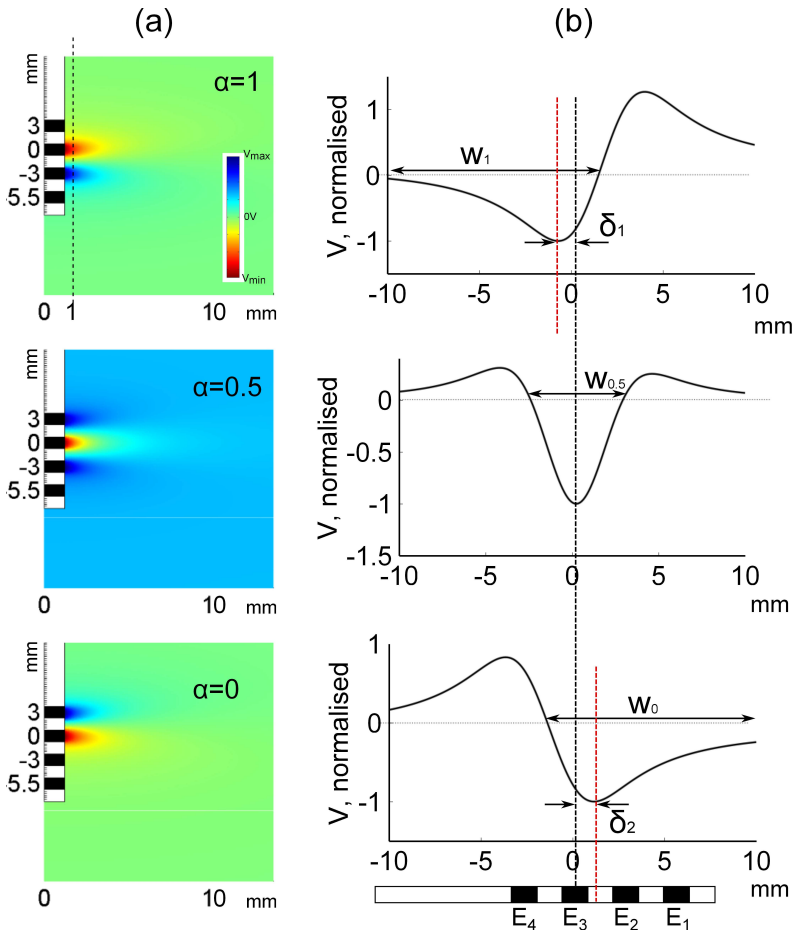


**Figure 4.3:** Tripolar potential fields. (a) FEM surface plots potential distributions generated by a current-steering tripolar source when $\alpha$ is set to 0, 0.5 and 1. Colorscale: Red represents the most negative potential, $V_{min}$, blue represents the most positive potential, $V_{max}$. (b) Normalised cross-section profiles of the potential distribution. The cathode, $E_3$, is centred at 0 mm and the two anodes, $E_2$ and $E_4$ at 3 mm and -3 mm, respectively.

smallest cathodic spread is achieved when the anodic currents are balanced. The width of the cathodic spread was estimated to be $W_{0.5}$=5.5 mm for $\alpha = 0.5$, $W_1$=10.6 mm for $\alpha = 1$ and $W_0$ greater than 15 mm for $\alpha = 0$. As we vary $\alpha$ from 0.5, the tripole becomes unbalanced and the area of cathodic spread increases, since the anodic potential is higher on one side of the cathode than on the other. When $\alpha = 0.5$, the negative peak of the potential is located at 0.01 m, which corresponds to the midpoint of the tripole. The maximum deviation of the negative peak from this point was calculated as $\delta_0$=0.7 mm, for $\alpha = 0$ and $\delta_1$=1.1 mm, for $\alpha = 1$. When $\alpha$ is set to the latter values, the peak amplitude decreased by approximately 5%

with respect to the peak value calculated for $\alpha = 0.5$.

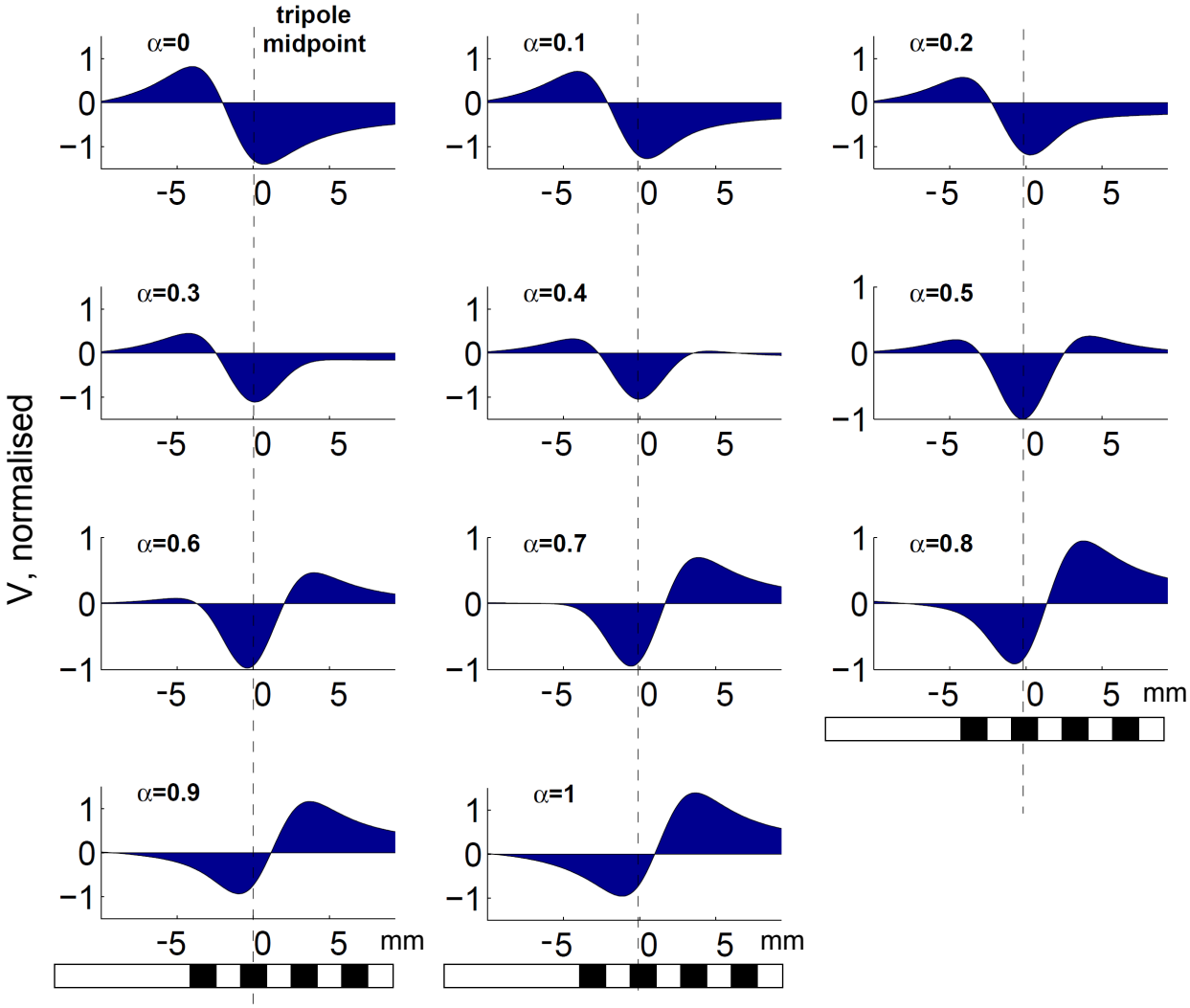


**Figure 4.4:** Field shaping achieved using a tripolar electrode configuration, by varying the weight parameter, $\alpha$, between 0 and 1.

Figure 4.4 illustrates cross-section plots of the potential distribution generated by varying $\alpha$ between 0 and 1, in steps of 0.1. The amplitude was normalised to the peak amplitude for $\alpha = 0.5$. The dashed lines represent the location of the centre of the tripole.

## 4.5 Quadripolar model - Simulated potential distribution

The quadripolar configuration in Figure 4.1(b) in Section 4.2 was modelled in FEM. The quadripole is centered at 9 mm along the axial distance. The amplitude of the total injected current was set to 1 mA and the cathodic current weight parameter $\beta$ was varied between 0 and 1, while the apical and basal anodes carried a constant current equal to half the total stimulation current, $I$.

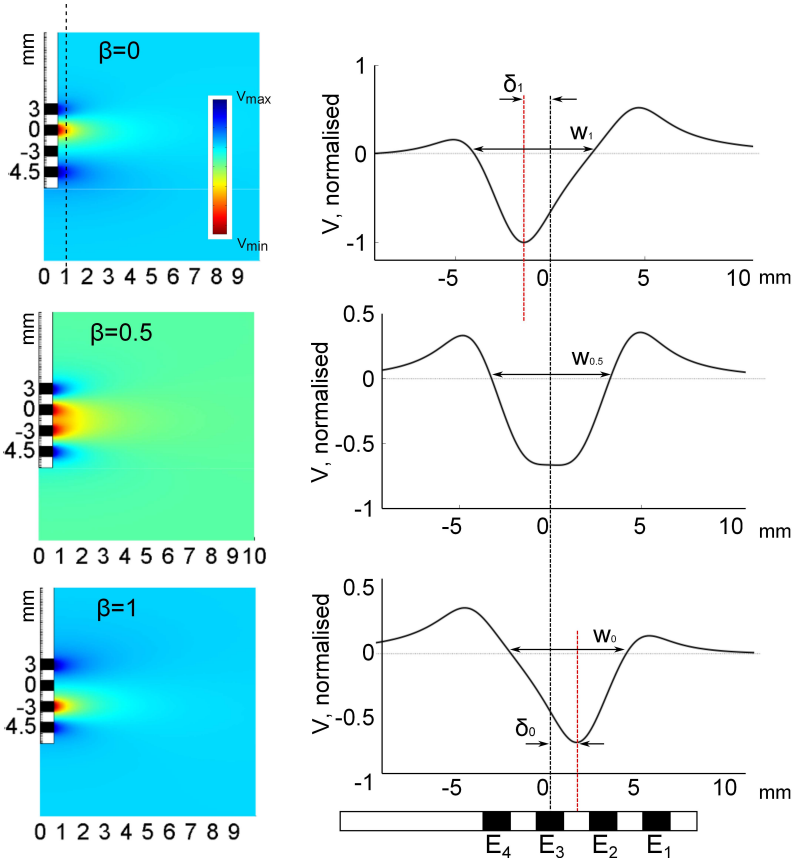


**Figure 4.5:** Quadripolar potential fields. (a) Simulated surface plots of the potential distribution and (b) simulated cross-section profiles generated by a quadrupolar electrode configuration at a distance of 2 mm from the electrode, for values of $\beta$ of 0, 0.5 and 1.

Figure 4.5(b) shows the surface profiles of the electric potential distribution obtained by setting $\beta$ to 0, 0.5 and 1. When the current through the cathodes is balanced ($\beta = 0.5$), the negative peak shows a plateau, centred at 9 mm and extending for

approximately 1 mm. As we set $\beta = 0$, the negative peak shifts by 1.8 mm ($\delta_0$) and when $\beta$ is set to 1, the peak shifts by about 1 mm ($\delta_1$) along the opposite direction. The width of the cathodic spread was largest for $\beta = 0.5$ and was estimated to be approximately 6.4 mm. For both values of $\beta$ of 0 and 1, the width was estimated to be 6 mm. When $\beta$ equals 0.5, the potential distribution shows also the smallest amplitude, calculated to be 66% of that resulting for $\beta$ equal to 0 or 1.

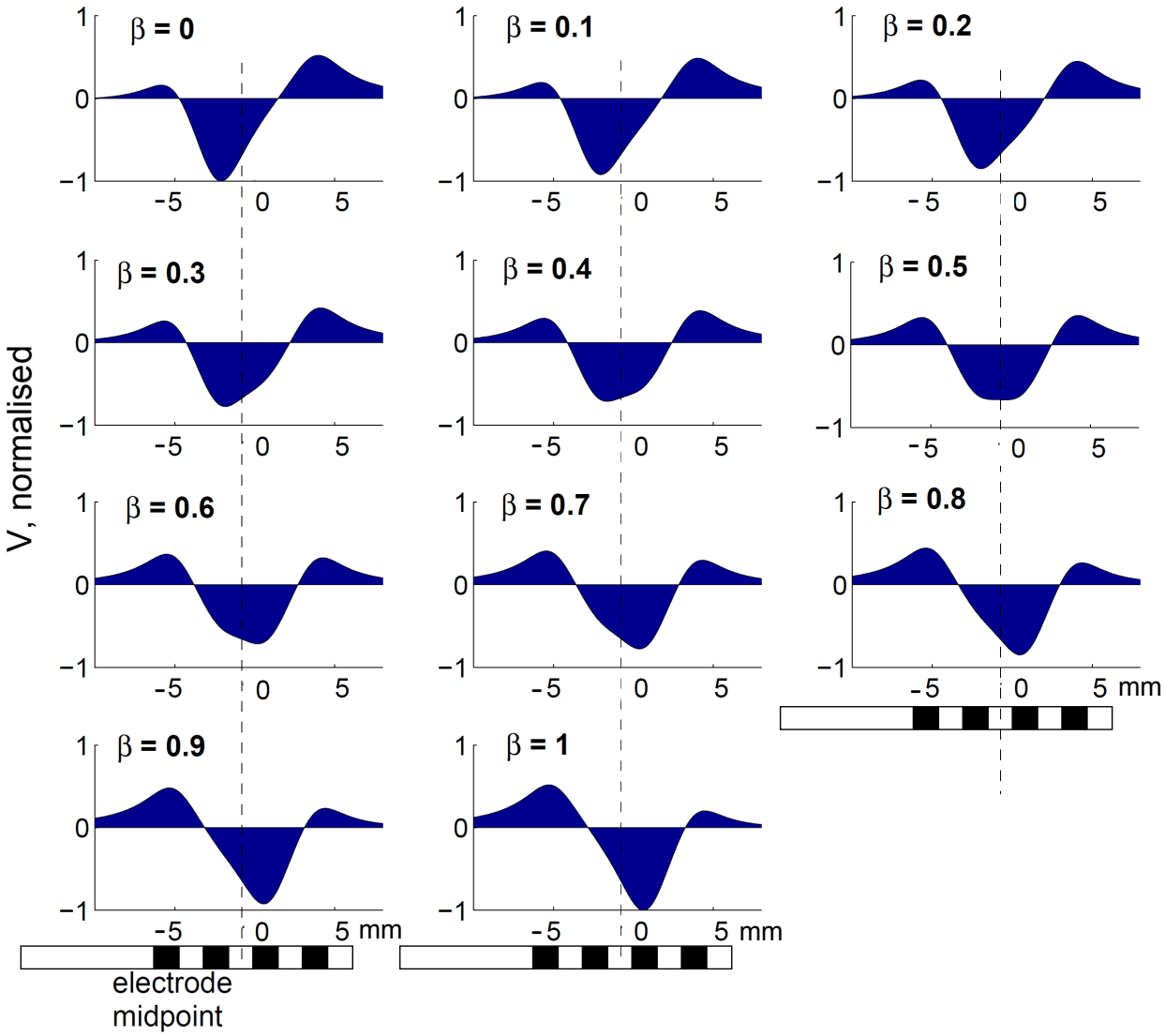


**Figure 4.6:** Field shaping performed by a quadripolar electrode configuration by varying the current-steering parameter, $\beta$, between 0 and 1.

By varying the value of $\beta$ between 0 and 1, in steps of 0.1, we can observe the field shaping illustrated by the cross-section plots in Figure 4.6.

## 4.6 Pentapolar model - Simulated potential distribution

This section reports the results of simulations of the FEM model using pentapolar configuration in Figure 4.1(c) in Section 4.2. The total injected current was set to 1 mA. The current flowing through each cathode was set by three weight parameters, $a$, $b$ and $c$, while the current flowing through each anode was set to half the total current, $I$. The FEM surface plots in Figure 4.7(a) represent the potential distribution resulting from the use of a pentapolar electrode configuration, when only one of the three cathodes is active. The profiles of the electric potential distribution generated by a pentapolar electrode configuration are illustrated in Figure 4.7(b). When b=1, all the cathodic current flows through electrode $E_3$. The voltage has a minimum centred at 21.7 mm along the axial distance of the electrode. When all the cathodic current is applied to one of the lateral cathodes ($E_2$ or $E_4$), the electric potential minimum is moved away from the centre point. When a=1, $E_2$ is carrying all the current and the minimum is shifted to 24.4 mm, resulting in a shift, $\delta_a$, of 2.7 mm towards the apical anode. When c=1, $E_4$ is carrying all the cathodic current and the minimum is shifted to 19.2 mm, resulting in a shift, $\delta_c$, of 2.5 mm towards the basal anode.

The highest peak of the electric potential occurs when b=1. The value of the peak remains nearly constant, decreasing to about 95% of the maximum value, when the current is steered towards one of the lateral cathodes. The widths of the cathodic spread, $W_a$, $W_b$ and $W_c$ are equal for the three cases, and estimated from the simulated results to be approximately 7.7 mm. The use of three cathodes allows for several combination of active contacts and current ratios, resulting in additional control over the shape of the potential distribution. Figure 4.8 shows the effect of different combinations of active cathodes on the width and peak amplitude of the cathodic spread: b=1, shown in solid line, results in a width of 7.7 mm; when the

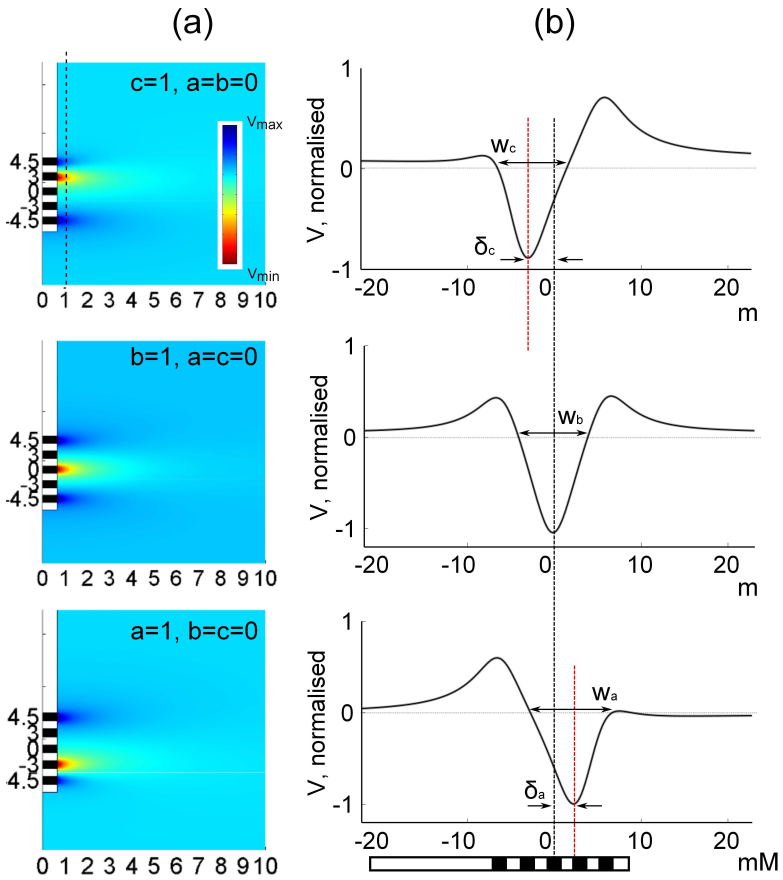


**Figure 4.7:** Pentapolar electric potential distribution. (a) FEM axisymmetric surface plots (b) Profiles of electric potential distribution at a distance of 2mm from the electrode shaft.

current is split among all three cathodic contacts as 30% of it flowing through the lateral contact and 40% of it through the central contact, the shape of the electric potential profile is that illustrated in the dotted line, which results in a width of the cathodic spread of 8.4 mm; by splitting the cathodic current between the two lateral cathodes, while the central cathode carries no current (a=0.5, b=0 and c=0.5) we obtain the plot in dashed line, which results in a width of the cathodic spread of 8.8 mm.

By applying the total cathodic current to $E_2$ (a=1), the profile of the electric potential distribution is described by the plot in the dashed line in Figure 4.9(a) and the peak of the electric potential is located at 19.2 mm, representing a shift of 2.5 mm from the electrode midpoint. When the cathodic current is split between $E_2$ and $E_3$ (c=0, a=b=0.5), the profile is represented by the plot in the dotted line in Figure

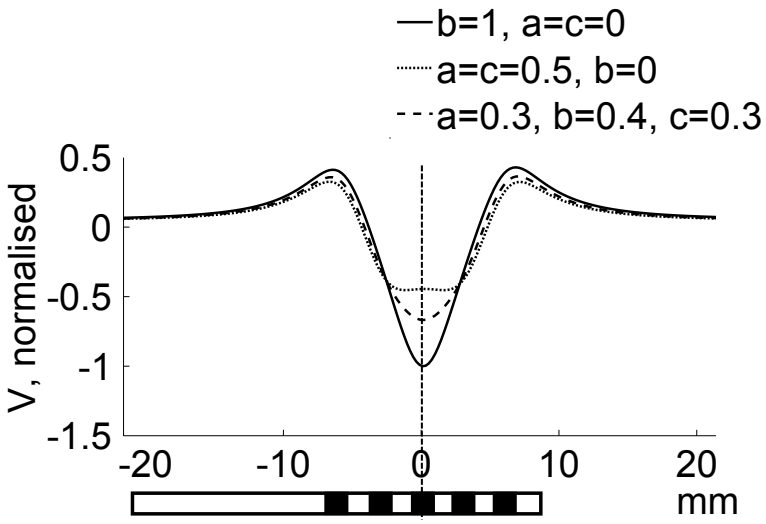


**Figure 4.8:** Effects of varying the number of active cathodes during pentapolar stimulation.

4.9(a) and the peak is then located at 20.8 mm, which represents a shift of 0.9 mm from the electrode midpoint. When the cathodic current is split such that 70% of it flows through $E_2$, 20% through $E_3$ and 10% through $E_4$, we obtain the plot in solid line in Figure 4.9(a), characterised by a peak located at 19.9 mm along the axial distance of the electrode, which results in a shift of 1.8 mm from the electrode midpoint. It is worth to notice how the area of cathodic spread for the three cases reported remains approximately constant.

When the overall cathodic current is flowing through only $E_4$ (c=1), the resulting distribution, represented by the plot in dashed line in Figure 4.9(b), has its peak located at 24.4 mm, resulting in a shift of 2.7 mm from the electrode midpoint. When the cathodic current is split between $E_3$ and $E_4$ (c=b=0.5, a=0), the profile is represented by the plot in the dotted line in Figure 4.9(b) and the peak is then located at 22.8 mm, representing a shift of 1.1 mm towards the apical anode. When the cathodic current is split such that 70% of it flows through $E_4$, 20% through $E_3$ and 10% through $E_2$, we obtain the plot in solid line in Figure 4.9(b) characterised by a peak located at 23.9 mm, representing a shift of 2.2 mm from the electrode midpoint.

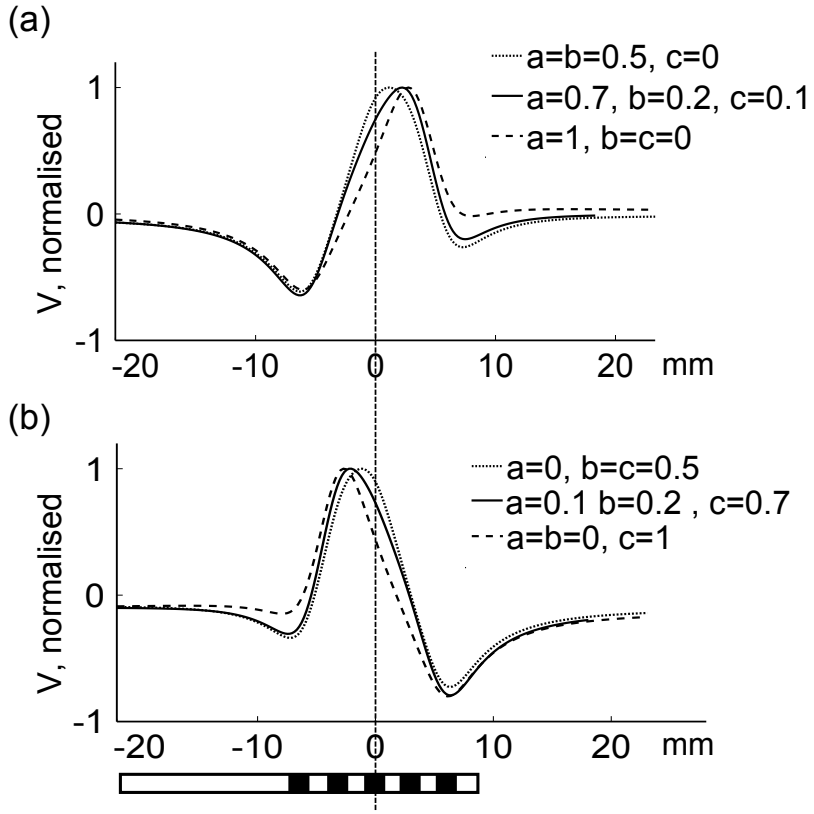


**Figure 4.9:** Field shaping achieved with a pentapolar electrode configuration. The parameters a, b and c represent the ratio of cathodic current flowing through contacts $E_2$, $E_3$ and $E_4$ respectively.

## 4.7 Effects of electrode geometry on electric field profiles

In this section we analyse the effects of varying the electrode geometry on the shape and width of the electric potential distribution. In particular, we will consider two different geometries representing the Medtronic electrode models 3387 and 3389. The former is characterised by 1.5 mm wide contacts, separated by 1.5 mm spacings. The latter has 1.5 mm wide contacts separated by 0.5 mm spacings. For the tripolar electrode configuration, the profiles of the electric potential were derived for $\alpha = 0.5$. The profiles of the potential distribution simulated using the two types of electrodes are shown in Figure 4.10. The solid line represents the profile associated with the 3387 model, while the dotted line represents the profile associated with the 3389 model. The pitch of the 3389 tripole model, measured between the edge of the basal

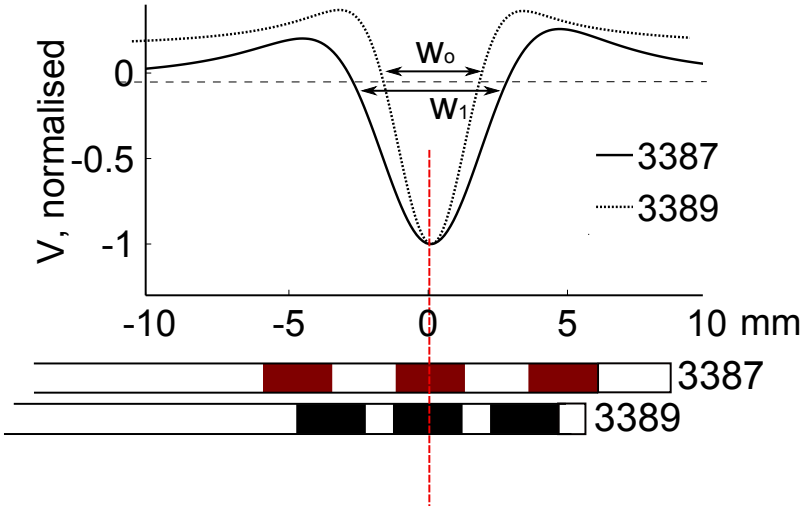


**Figure 4.10:** Effects of varying the distance between the contacts on the shape and width of the electric potential profile.

node to the edge of the apical node is 5.5 mm, while the pitch of the 3387 tripole model is 7.5 mm. The width of the cathodic spread, $W_0$, was estimated to be 3.5 mm, while $W_1$ was estimated to be 5.5 mm. The difference between the widths of the profiles is consistent with the difference between the size of the tripoles.

## 4.8 Area of tissue activated during multipolar stimulation

So far we have reported the effects of varying the electrode configuration on the electric potential profiles and the spread of the extracellular potential distribution. The potential distribution alone, however, does not provide information about the response of the neural clusters exposed to the stimulating field. In order to predict the area of tissue that will be activated by the imposed field an approach was selected, which involves the use of the activation function concept [33], according to which the second spatial derivative of the extracellular potential along the axon length, $\delta^2 V_e/\delta x^2$, is responsible for the activation within the axon (see Section 2.3.2.2 in Chapter 2). The activation function can be used as a means to estimate the spatial

extent of tissue that will be depolarised or hyperpolarised by an applied field, without any knowledge about the behaviour of the ion channels of the neuron membrane. By applying the activation function concept to the electric potential distribution derived in the previous section, we can estimate the area of tissue activated using the three electrode configurations described in this chapter.

### 4.8.1 Tripolar Stimulation

The second spatial derivative was computed for the electric potential reported in Figure 4.3. Figure 4.11(a) shows the contours[2] of the activation function generated by a tripolar electrode configurations for values of the current parameter $\alpha$ of 0, 0.5 and 1. Figure 4.11(b) shows a the normalised second spatial derivative of the electric potential calculated along the electrode axial length at a distance of 2mm from the electrode shaft.

The spread of the depolarised region for values of $\alpha$ of 0, 0.5 and 1 was estimated to be $W_0 = 7.3$mm, $W_{0.5} = 5$ mm and $W_1 = 7.1$ mm, respectively. The deviation of the peak of the function from the location of the centre of the electrode was estimated to be $\delta_0 = 0.9$ mm and $\delta_1 = 1$ mm for $\alpha = 0$ and $\alpha = 1$, respectively.

### 4.8.2 Quadrupolar Stimulation

The activation function was computed for the quadripolar potential distribution reported in Figure 4.5. The resulting activation function plots are depicted in Figure 4.12(a), representing the normalised second spatial derivative of the electric potential. The cross-section plots of the activation function, in Figure 4.12(b) were estimated at a distance of 1mm from the electrode shaft.

For $\beta = 0$ and $\beta = 1$, the spreads of the depolarised area, $W_0$ and $W_1$ were estimated to be 5 mm, whereas for $\beta = 0.5$, $W_{0.5}$ was estimated to be 6 mm. The shift of the

[2]Countours were calculated as isopotential lines.

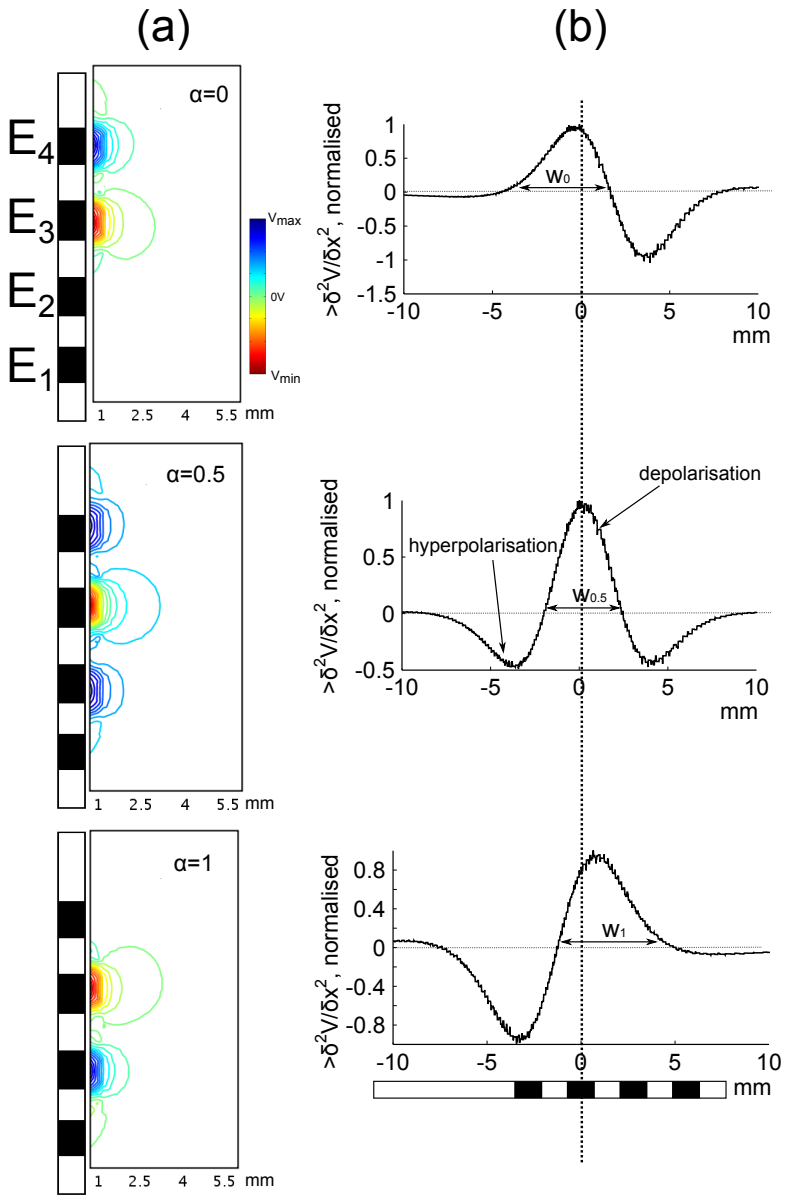


**Figure 4.11:** (a) Contour plots of activation function calculated from the potential distribution during tripolar stimulation for current-steering parameter $\alpha$ equal to 0, 0.5 and 1. (b) Profile of the second spatial derivative of the extracellular voltage calculated at a distance of 1mm from the electrode during tripolar stimulation for values of $\alpha$ equal to 0, 0.5 and 1.

peak of stimulation was estimated to be 2 mm towards the basal node, for $\beta = 0$ and 2 mm towards the apical node for $\beta = 1$.

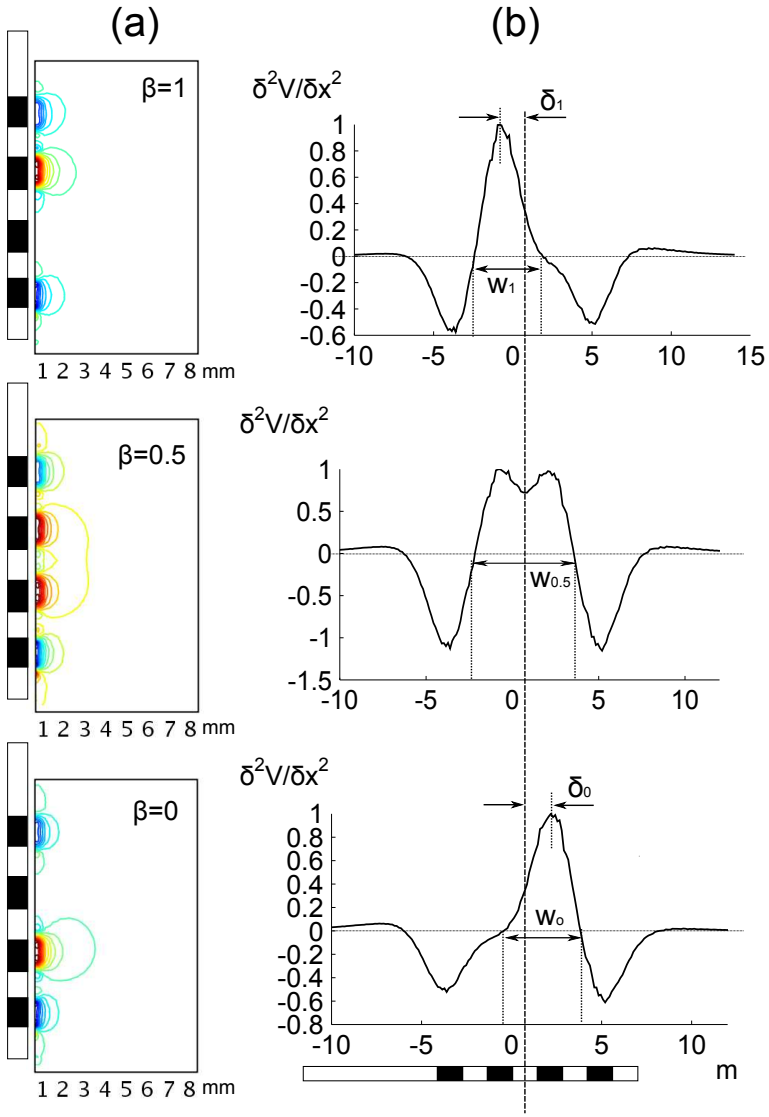


**Figure 4.12:** (a) Contour plots of the second spatial derivative of the extracellular voltage during quadripolar stimulation for values of the current-steering parameter $\beta$ equal to 0, 0.5 and 1. (b) Profile of the second spatial derivative of the extracellular voltage calculated at a distance of 1 mm from the electrode during quadripolar stimulation for values of $\beta$ equal to 0, 0.5 and 1.

### 4.8.3 Pentapolar Stimulation

In pentapolar stimulation mode, we can obtain several combinations of the shape and location of the stimulation area, by varying the current weight parameters a, b and c. The activation function was computed for different combinations of active contacts and current ratios and is represented by the contour plots in Figure 4.13. Cross-section profiles of the activation function were extracted from the activation function contours at a distance of 1 mm from the electrode and are reported in

Figure 4.14.

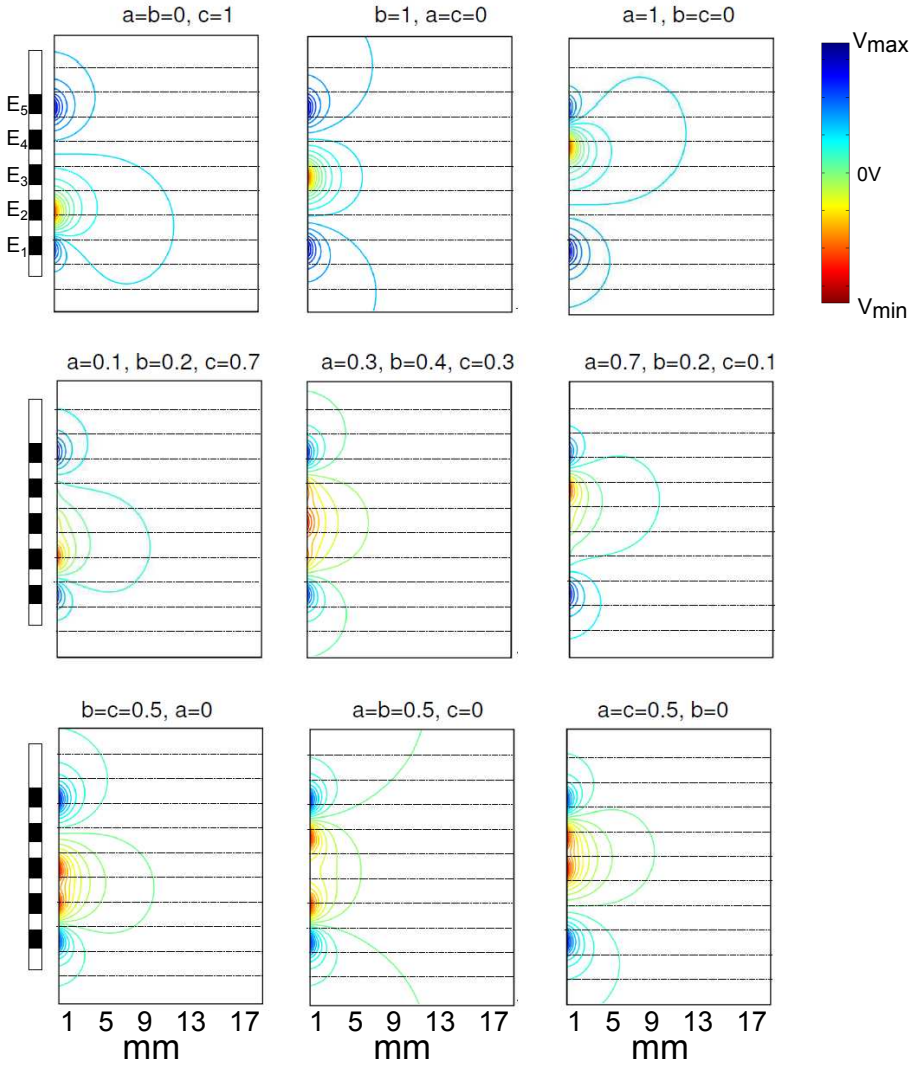


**Figure 4.13:** Contorus of the second spatial derivative of the extracellular voltage during pentapolar stimulation calculated for a range of combination of active contacts and current ratios.

In Figure 4.14(a) only one of the three cathodes is active and the pentapolar configuration turns into a tripolar configuration. The width of the depolarised area, $W$, remains constant to approximately 2.5 mm in all three cases. The peak of the stimulation is shifted by 2.5 mm ($\delta_{100}$) towards the basal node, for a=1, that is when the cathodic current in flowing only through $E_4$, and by 2.5 mm ($\delta_{001}$) towards the apical node when c=1, that is when the cathodic current is applied to $E_2$ only.

The plots in Figure 4.14 (b) represent the depolarised and hyperpolarised areas when

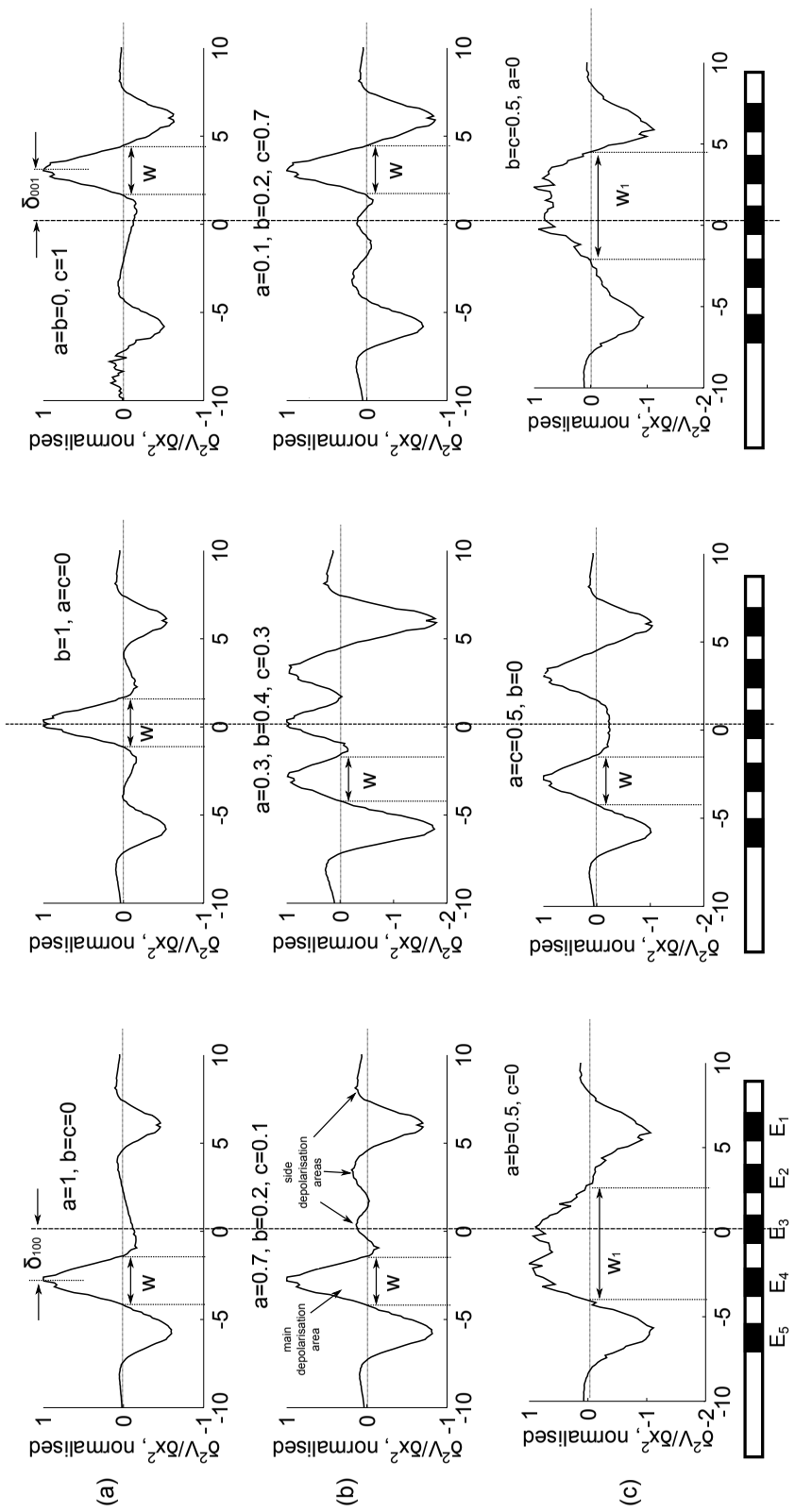


**Figure 4.14:** Profile of the second spatial derivative of the extracellular voltage calculated at a distance of 1 mm from the electrode during pentapolar stimulation for a range of combination of active contacts and current ratios.

the overall cathodic current is split among the three central cathodic contacts. No significant change in the width of the area of depolarisation and in the location of the peak of stimulation was observed as compared to case (a). One main difference consisted in the presence of more pronounced side depolarisation areas, however due to their low amplitude they may not have a significant impact on the tissue excitation. Another major observation was the occurrence of three distinguishable depolarisation areas when a=c=0.3 and b=0.4, characterised by an equal width, $W$, of 2.5 mm. Case (c) in Figure 4.14 represents the activation function plots derived when only two of the three cathodic contacts are carrying current. If the current is split between two adjacent contacts (a=b=0.5 or b=c=0.5) the depolarisation area increases to a width, $W_1$, of approximately 6.5 mm. When the current is split between the two lateral cathodes (a=c=0.5) the depolarisation area is characterised by two equal regions, of width $W$, each centred at one of the active cathode.

## 4.9 Prediction of neural activation during tripolar stimulation

The FEM model profiles of the potential distribution generated by a tripolar current source were coupled to axon models in order to predict the activation patterns resulting from tripolar stimulation. FEM-axon models were based on the application of the FEM simulations as an extracellular stimulus to a cluster of compartmental myelinated unconnected axons [58], consisting of a 40 axons, with 0.5 mm separation, oriented perpendicular to the electrode shaft, with 0.1mm inter-nodal spacing and consisting of 221 compartments, as depicted in Figure 4.15a.

Each axon will experience the voltage profiles depicted in the inset plots in Figure 4.15 along its length (b) and at its nodes (c). Simulation of the neural activation generated by tripolar fields was performed in NEURON v.6.2, by adopting the neuron model developed by McIntyre et.al [58]. Double-cable models represent both

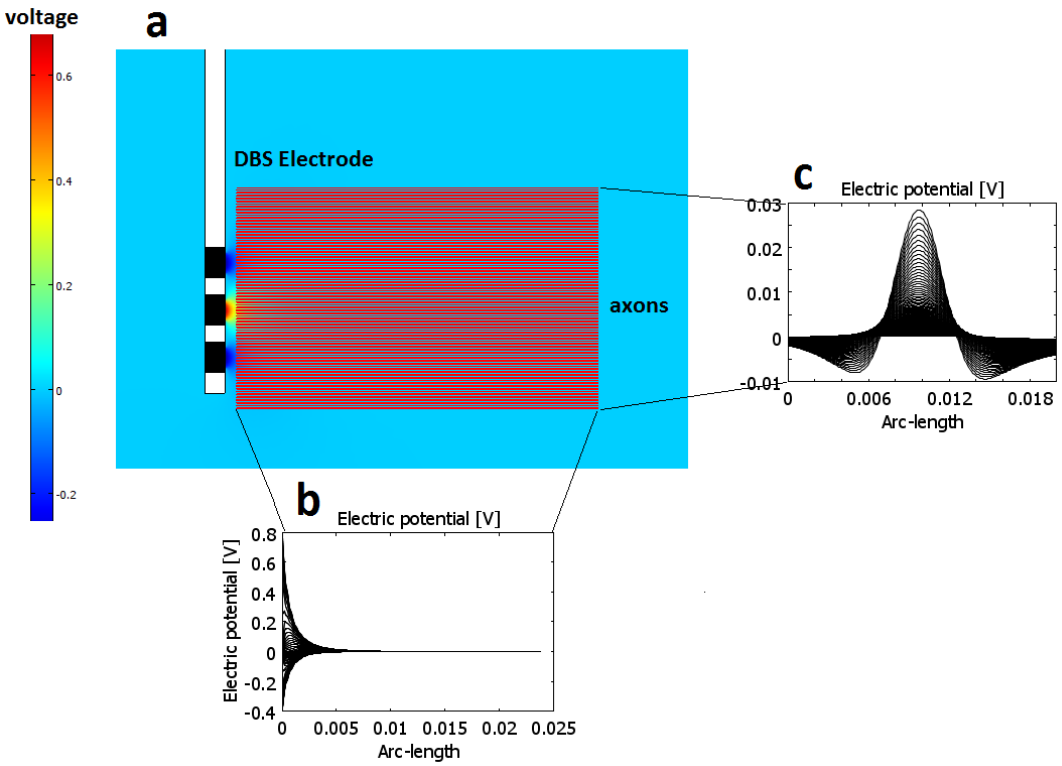


**Figure 4.15:** FEM-axon model setup. (a) Coupling between extracellular fields generated by the current-steering tripolar electrode and axon models, located parallel to one another and perpendicular to the electrode shaft. The colorbar represents the voltage values for the electric potential solution as estimated by the FEM model. Inset plots show the distribution of the potential fields generated by a fully tripolar source, along (b) the length of the 40 neurons and (c) across the axon nodes.

the myelin sheath and the axolemma, with explicit representation of the nodes of Ranvier, paranodal and internodal segments. The axons were 5.7$\mu$m in diameter and contained a fast sodium conductance, a persistent sodium conductance, and a slow potassium conductance at the nodes. The extracellular potentials derived from the FEM solution were converted into a time-dependent potential to calculate the resulting time-dependent transmembrane potentials. This conversion was implemented by combining the field potential with exponential pulses characterised by a fast rise and a variable exponential decay and containing equal charge to the one injected by square pulses. Exponential pulses were selected to implement the principle of anodal blocking, thus overcoming the limitations of using square pulses with tripolar electrode configurations, related to the unwanted break excitation occurring at the anodes at the fall of the pulse [84]. Successful activation was defined as a

one-to-one ratio between the stimulus frequency and the number of action potentials generated.

### 4.9.1 Activation patterns generated by tripolar stimulation

This section examines simulated neural activation patterns resulting from the use of a current-steering tripolar electrode configuration. The aim was to estimate the effects of shifting the electric field along the electrode axis on the area and location of neural activation.

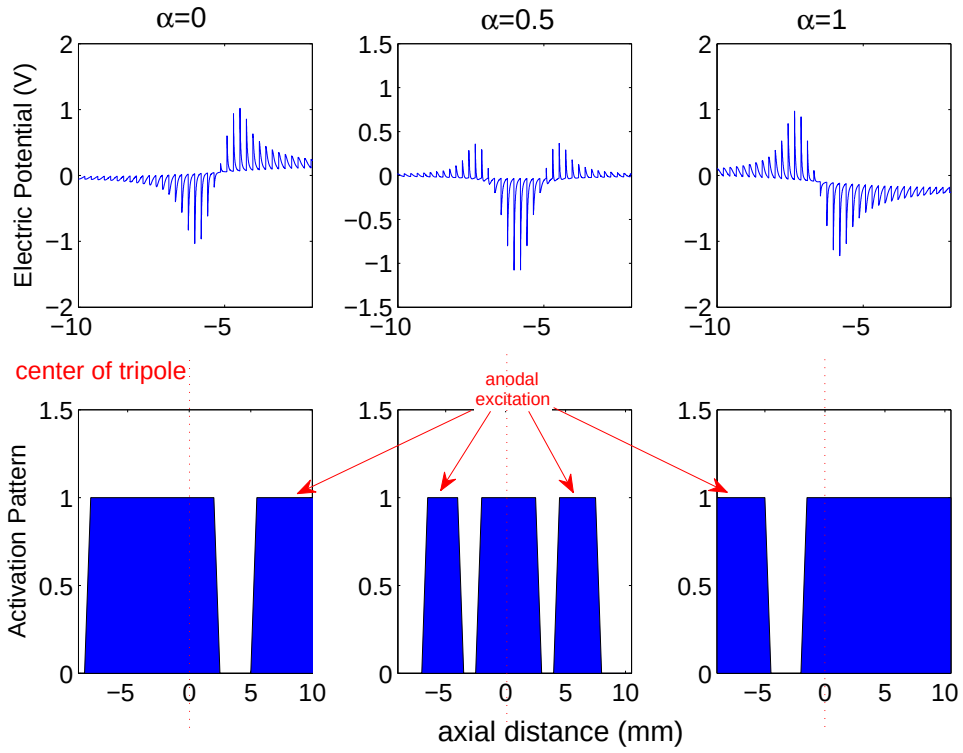


**Figure 4.16:** Activation patterns resulting from electric fields generated by square pulse stimulation

Firstly a comparison was carried out between the activation patterns generated by the adoption of square pulses and those generated by exponential pulses, characterised by a fast rise and a slow exponential decay. The top plots of Figure 4.16 illustrate the profiles of the extracellular fields generated by setting the dynamic value, $\alpha$, to 0, 0.5 and 1. The bottom plots represent the activation patterns re-

sulting from the use of square current pulses of amplitude of 1 mA and duration of 100 $\mu$s, giving a total charge of 100 nC. When $\alpha$ is set to 0 or 1, the tripolar configuration converts into a bipolar configuration. For these two cases the area of activation generated by the cathodic portion of the field is located to the left or the right with respect to the centre of the tripole (located at $x_0$=5 mm). When $\alpha$=0.5, the configuration is purely tripolar and the area of cathodic activation spreads evenly around the centre of the tripole. In the purely tripolar case ($\alpha$=0.5) the spread of activation is estimated to be approximately 4 mm, which is about one third the spread estimated during bipolar stimulation ($\alpha$=0 and 1). Additionally, the activation patterns are greatly affected by anodal excitation occurring during the fall of the pulse, resulting in a anodic spreads of nearly half the width of the cathodic spreads.

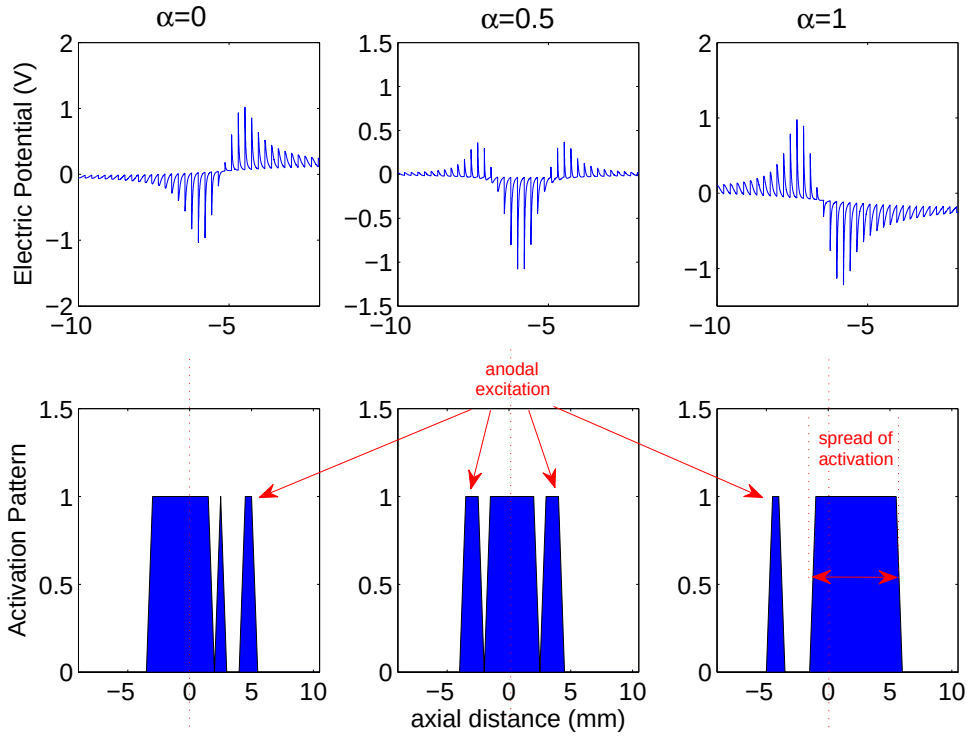


**Figure 4.17:** Activation patterns resulting from the application of electric fields generated by exponential pulse stimulation. Exponential pulses were characterised by a fast rise time and a slow decay of 4ms.

In order to reduce anodal stimulation, while maintaining the shifting properties of

the activation patterns, exponential pulses were adopted, with decay time constants up to 4 ms and delivering a total charge of 100 nC, consistent with the charge of the square pulses. Figure 4.17 shows the activation spreads resulting from exponential pulse stimulation with decay time constants of 4 ms. For $\alpha$=0.5, the spread of activation is centred at the cathode of the tripole. As $\alpha$ is varied, the cathodic activation is shifted left or right with respect to the centre of the tripole. The maximum shift is estimated to be 2 mm to the left for $\alpha$=0 and 3 mm to the right for $\alpha$=1. The total spread of cathodic activation remained approximately constant for all values of $\alpha$, ranging between 4 mm and 6 mm. Activation due to the anodic portion of the electric field was highly reduced as compared to that occurring during square pulse stimulation. Activation caused by anodic fields can be further reduced by reducing the charge contained in the exponential pulse, as shown in Figure 4.18.

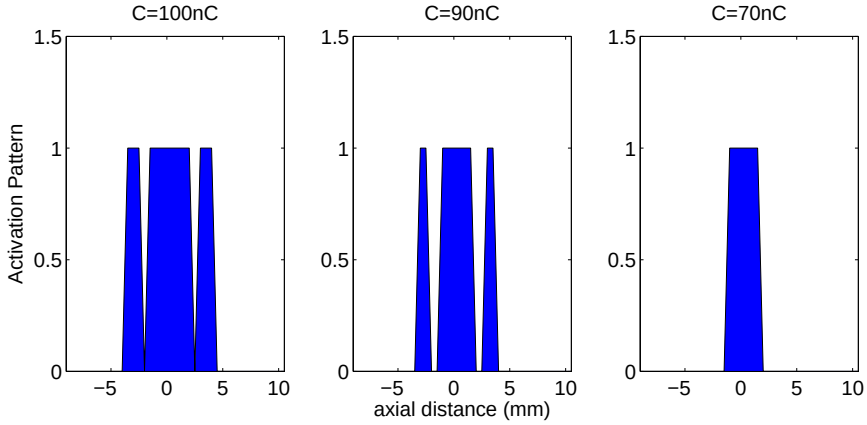


**Figure 4.18:** Effects of varying the charge of the pulse on the activation patterns.

A reduction in the injected charge can eliminate the unwanted anodic activation, only partially reducing the spread of the cathodic stimulation. It was estimated that reducing the injected charge by 30 nC resulted in elimination of anodic activation and a reduction of the cathodic activation area from approximately 4 mm to 2.5 mm. The effects of anodal stimulation can also be reduced by increasing the pulse decay time course as shown in Figure 4.19, where the pulse time constant is varied from 100$\mu$s to 4 ms. The spread of cathodic activation is kept constant to approximately

4 mm. However the spread of anodic activation is decreased by approximately one third.

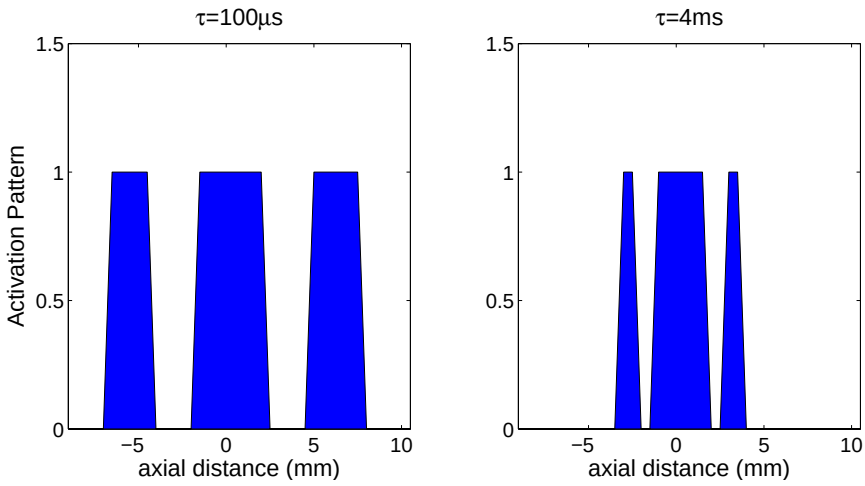


**Figure 4.19:** Effects of varying the decay time constant of the exponential pulse on the activation patterns.

## 4.10 Discussion

The benefit of field shaping in DBS is related to the better achievable stimulation focus and the active control over the location of the stimulation site. These two factors play a major role in the development of safer and more efficient DBS systems, where both patient's side effects and variability of DBS efficacy are minimised. An approach was presented in this chapter, based on the adoption of current-steering multipolar electrode configurations, where two electrode contacts are driven as anodes and one or more electrode contacts as cathode. In this chapter, we have considered three different configurations: tripolar, quadrupolar and pentapolar. A FEM model was developed to simulate the behaviour of the potential distribution resulting from the adoption of these three configurations. The model of the tripolar and quadripolar electrodes represented the geometry of a standard clinical DBS electrode, characterised by four contacts. The pentapolar electrode geometry was based on the same geometry, with the addition of an additional contact. Each contact

was driven by an ideal current source, where losses associated to the lead parasitics and electrode impedance were neglected. The targeted brain tissue was modelled as a homogeneous, isotropic medium, governed by the Laplace equation, which was solved to obtain the value of the potential within the medium, resulting from the application of a constant current. The solution of the model showed that the use of multipolar electrode configurations can influence the behaviour of the potential distribution around the electrode. However, the sole electric potential distribution provides no information on the spatial extent of activation during stimulation. The approach used to investigate the influence of an applied electric field to a cluster of target neurons was based on the computation of the activation function, which for homogeneous fibres, becomes proportional to the second spatial derivative of the extracellular potential along the axon [31]. The result of the computation of the activation function for different electrode configurations was normalised, and therefore did not take into account the resistivity, conductivity an diameter of the axon membrane. The activation function provided information about depolarised regions of tissue, where its value was greater than zero and hyperpolarised regions, where its value fell below zero. The activation function gives a first impression of the excitation process, without the knowledge of the behaviour of the ion channels in the axon membrane. The activation function was computed for the three electrode configurations presented in this chapter. In the tripolar case, a parameter $\alpha$ was used to set the ratio of the current flowing through the anodes. As $\alpha$ was equal to 0.5, the anodes carried equal current and the electrode configuration was represented by a true tripole. This configuration resulted in the smallest spread of depolarised area, due to the fact that the strong neighbouring hyperpolarised regions around the anodes, impeded further propagation of the cathodic potential distribution. As $\alpha$ was varied towards 0 or 1, the tripole became unbalanced and the area of depolarisation increased by a total of 2 mm. In the quadripolar electrode case, a parameter $\beta$ was used to determine the ratio of current flowing between the central cathodes,

whereas the lateral anodes were carrying a constant equal current. The quadripolar electrode configuration provided better stimulation focus, by reducing the average depolarised area with respect to the tripolar case, and allowing for a larger shift of the stimulation peak. The area of depolarisation, however, did not remain constant as we varied the parameter $\beta$, but increased by approximately 1 mm, when the cathodes carried equal current. The pentapolar electrode case, where three central contacts were used as cathodes sharing the total cathodic current, proved to be the best approach to provide dynamic field shaping. The use of three cathodes allows for several combinations of stimulation patterns. The pentapolar electrode can be driven as a true tripole by activating only one of the three cathodes. Depending on which cathode is selected, the area of depolarisation is shifted along the electrode axial distance, without affecting the stimulation focus, ie. the width of the area of depolarisation. By splitting the cathodic current between two or among the three cathodic contact, the width of the area remains constant but we can generate multiple areas of depolarisation, the physiological implications of which, however, should be further investigated.

This study also investigated the effects of a current-steering tripolar configuration on the activation of the neural clusters surrounding the electrode. The spread of activation was estimated by simulating the response of 40 myelinated axons, placed perpendicular to the electrode shaft with a spacing of 0.5 mm. Simulation results showed that a current-steering tripolar electrode configuration can be adopted to shift the activation area along the axial distance. The stimulation pulses however need to be characterised by a slow exponential decay, in order to reduce the effects on the activation of the anodal break excitation occurring at the end of a square pulse [84]. A longer decay constant resulted in further decrease of the impact of anodal stimulation on the activation. However for DBS applications the time constant should be kept lower than half the pulse period (approximately 8 ms) to allow for the charge recovery cycle of stimulation. The total shift of the activation spread

was estimated to be approximately 5 mm along the electrode axial distance. The maximum achievable shift is linearly related to the size of the electrode contacts and the distance between them. Further work should look into the impact of different electrode geometries on the spread of activation. The neural model adopted for this study was limited to a 2-dimensional representation of 100 parallel axons. This configuration was used to keep the computational demand low and to obtain a preliminary description of the behaviour of neural clusters during tripolar stimulation. A more accurate approach would adopt three dimensional structures of the DBS electrode and the surrounding area with fibres oriented transversally with respect to the electrode array [58]. Further accuracy would be achieved by accounting for different fibre geometries and orientation and the different conductivities of the anatomical regions surrounding the target area [15].

Although multipolar electrode approaches based on tripolar and quadripolar configurations can be readily implemented on standard DBS systems, where electrodes are characterised by four metal contacts, pentapolar configurations would require the manufacturing of custom electrodes. From the analysis reported in this chapter, it is evident how the geometry of the electrodes plays a major role in the shaping of the stimulation area. Electrode optimisation based on the size and location of the brain target areas, which was beyond the scope of this work, should be the next step towards the development of multipolar DBS.

## 4.11 Conclusion

This chapter presented a novel approach to DBS, based on the use of multipolar electrode configurations, to increase stimulation focus and provide dynamic control of the location of the peak of stimulation. The study was carried out using basic models of electrodes in homogeneous medium, ideal current sources and quasi-static approximation. This allowed us to obtain a first impression of the influence of

a multipolar electrode configuration approach on stimulation and to draw some conclusions about the application of such approach to DBS.

(a) Multipolar electrode configurations can provide better focus than conventional monopolar configurations, by decreasing the size of the stimulation area around the electrode.

(b) The inclusion of a current-steering capability allows us to shift the stimulation peak to different target sites. This was observed for all three cases of electrode configurations, where an increase of the number of active contacts, increased the value of achievable shift.

(c) The size of the stimulation area is strictly dependent on the electrode geometry, specifically contact width and spacing. This could be observed in Figure 4.10, where two DBS electrodes with different geometries were modelled.

(d) The use of a tripolar configuration allows to shift the area of tissue activated along the electrode axis, as depicted in Figures 4.16 and 4.17.

(e) Exponential pulses are needed to reduce or eliminate the occurrence of neural excitation near the anodes.

# 5

# Current-Steering Integrated CMOS Stimulator Output Stage

Over the past decades, extensive research has been dedicated to the analysis of data from DBS clinical trials, aimed at understanding the underlying mechanisms of DBS. Moreover, significant effort has been dedicated to the development of computational models for characterising the behaviour of DBS and identifying strategies to optimise the stimulus settings. Very little effort has been focused on the circuit design of stimulators for DBS. Research has lately started to address this issue in terms of device miniaturisation, by proposing new integrated circuit design solutions for DBS stimulators [60, 59], including sensing capability for closed-loop therapy [61, 62]. In-

tegration allows to include several novel functionalities to achieve better stimulation efficacy, while keeping the chip area consumption small. Future DBS systems could be designed for cranial mounting or even for active electrode implementation (where the electrode drivers are mounted directly on the electrode) thus minimising problems arising from breakage or migration of the long extension lead that characterise clinical DBS systems.

In Chapter 4 we have explored a stimulation approach involving the use of multipolar electrode configurations to achieve field shaping in DBS. The study was based on the use of FEM models to simulate the behaviour of electric potential distribution generated by an electrode driven by a set of current sources with different polarities and amplitudes. In this chapter we look at a practical implementation in CMOS technology of a current-steering tripolar programmable stimulator output stage. First we will cover the basic theory involved in the design of CMOS analogue circuits. Then we will look at existing approaches in the design of current-mode stimulator output stages and we will then move on to a detailed description of the proposed stimulator, by presenting the design and implementation of individual functional blocks forming the stimulation circuit. The layout of the chip will be then presented. The last sections of this chapter will include results of the measured performance of the stimulation chip and wet experiments, involving the use of a saline-filled tank for electric potential mapping during multipolar stimulation. The material in this chapter is limited to the design of a stimulator output stage suitable for current-steering tripolar stimulation. As we shall see, however, some of the design aspects reported here can be adopted for the design of quadrupolar or pentapolar stimulators.

## 5.1 Overview Existing CMOS Stimulation Circuits

CMOS technology is an extremely popular choice in the field of implantable stimulators, including retinal prostheses [95, 96, 97, 98], auditory systems [99], vestibular

prostheses [100] and neuroprostheses [101, 102]. Current stimulator circuits are based on monopolar or bipolar stimulation. In the former case, one electrode is driven by a high output impedance current source and the current flows from the stimulation electrode to a large counter electrode (CE) located far from the stimulation electrode and kept at a voltage $V_{CE}$. For monopolar stimulation the current source is arranged as in Figure 5.1.

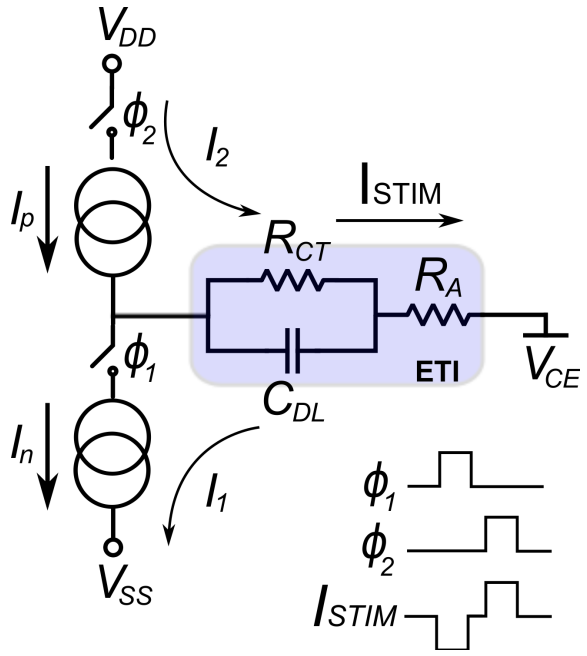


**Figure 5.1:** Illustration of stimulation current source arranged in monopolar mode

As discussed in Chapter 3, the electrode-tissue interface (ETI) is represented by the electrode dual-layer capacitance, $C_{DL}$, the charge-transfer resistance, $R_{CT}$, and the access resistance, $R_A$. During phase $\varphi_1$, the current, $I_1$, flows through the ETI to the negative supply, generating a cathodic current that provides stimulation. During phase $\varphi_2$, the current, $I_2$, drawn from the positive supply by current source $I_p$, flows back to the tissue, in order to balance the negative charge applied to the tissue during the previous cycle. Bipolar stimulation is based on the use of two electrodes, placed close to each other, where one electrode is used to source the stimulation current (anode) and the other to sink it (cathode). An illustration of the arrangement of a current source for bipolar stimulation is given in Figure 5.2.

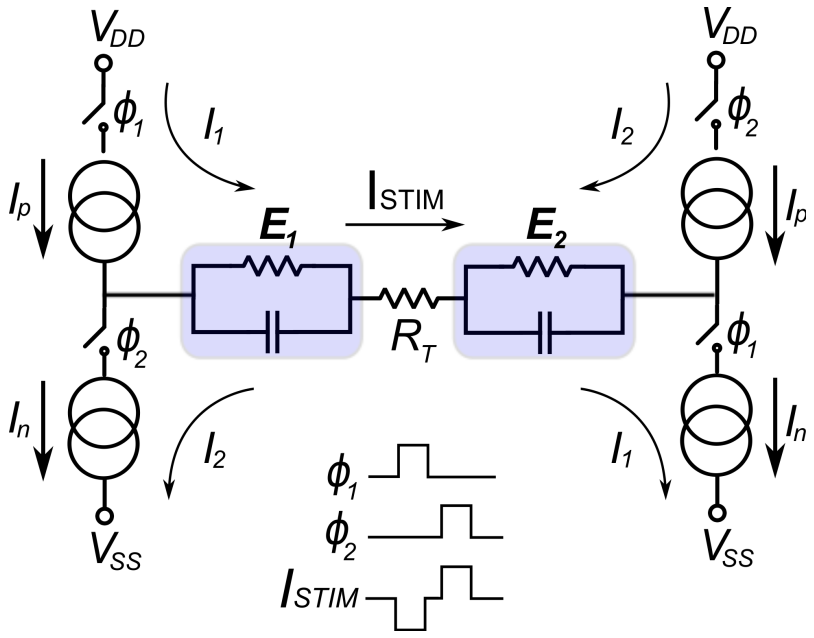


**Figure 5.2:** Illustration of stimulation current source arranged in bipolar mode

During phase $\varphi_1$, the total current $I_1$ flows from electrode $E_1$, which acts as an anode, to electrode $E_2$, which acts as the cathode. In the second phase $\varphi_2$, the charge is balanced by reversing the flow of the current from electrode $E_2$ to electrode $E_1$.

Several architectures have been adopted to implement the current sources forming the output stage of a stimulator. A popular structure consists of a digital-to-analog converter (DAC) and a current mirror [96, 97, 103] as depicted in Figure 5.3. The function of the DAC is to generate a programmable reference current that can be mirrored to the output by the current mirror $M_1$-$M_2$ and delivered to the tissue load, $R_T$, through the electrode contacts $E_1$ and $E_2$.

The main parameters involved in the design of a stimulator output stage are output impedance, voltage compliance, area and power consumption. The circuit in Figure 5.3 will work as long as $M_2$ is kept in the saturation region, that is as long as its drain-source voltage, $V_{DS_2}$, is:

$$V_{DS,sat} = \sqrt{\frac{2I_{OUT}L}{KW}} \tag{5.1}$$

where $W$ and $L$ are the width and length of the transistor and $K$ is the gain fac-

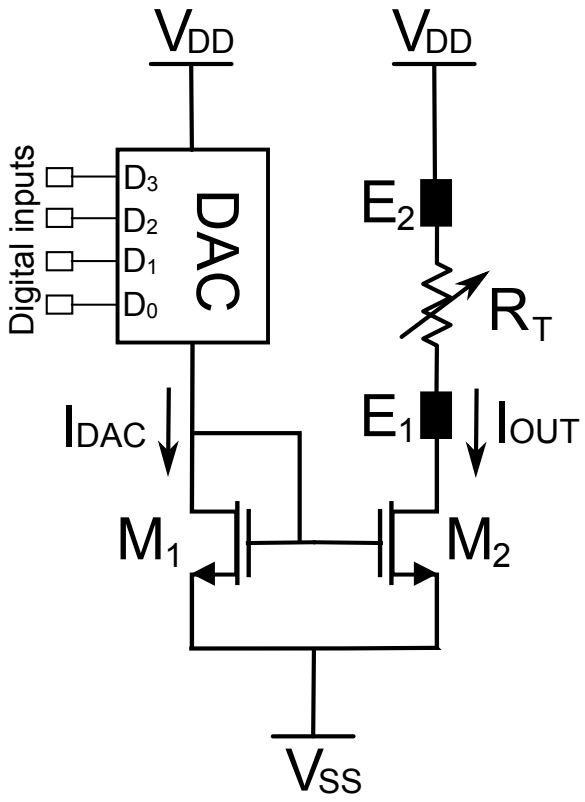


**Figure 5.3:** Basic structure of a stimulator output stage. A reference current is generated by a DAC and mirrored to the output by the current mirror $M_1$-$M_2$.

tor ($=\mu_0 C_{ox}$). This results in a maximum voltage compliance across the load, $R_T$, of $V_{DD} - V_{DS,sat}$. The output impedance of the circuit is equivalent to the output impedance of the simple current mirror, $r_{o,2} = 1/\lambda I_{OUT}$, where $r_{o,2}$ is the output resistance of $M_2$. Several techniques can be used to increase both the voltage compliance and the output impedance of the output current mirror.

A cascode structure like the one in Figure 5.4(a) can be adopted to increase the output impedance of the current source from $r_o$ of the simple current mirror to $g_m r_o^2$, where $g_m = \sqrt{2 I_{OUT} KW/L}$, is the transconductance of the stacked transistor $M_3$. This, however, comes at the expense of reduced voltage compliance to $V_{DD} - 2V_{DS,sat} - V_T$. By using the high-swing cascode structure in Figure 5.4(b), the voltage compliance can be increased to $V_{DD} - 2V_{DS,sat}$ by keeping the same output impedance. Increasing the number of cascode stages of the high-swing configuration to k, voltage compliance increases by a term $(k-1)V_T$ and the output impedance to

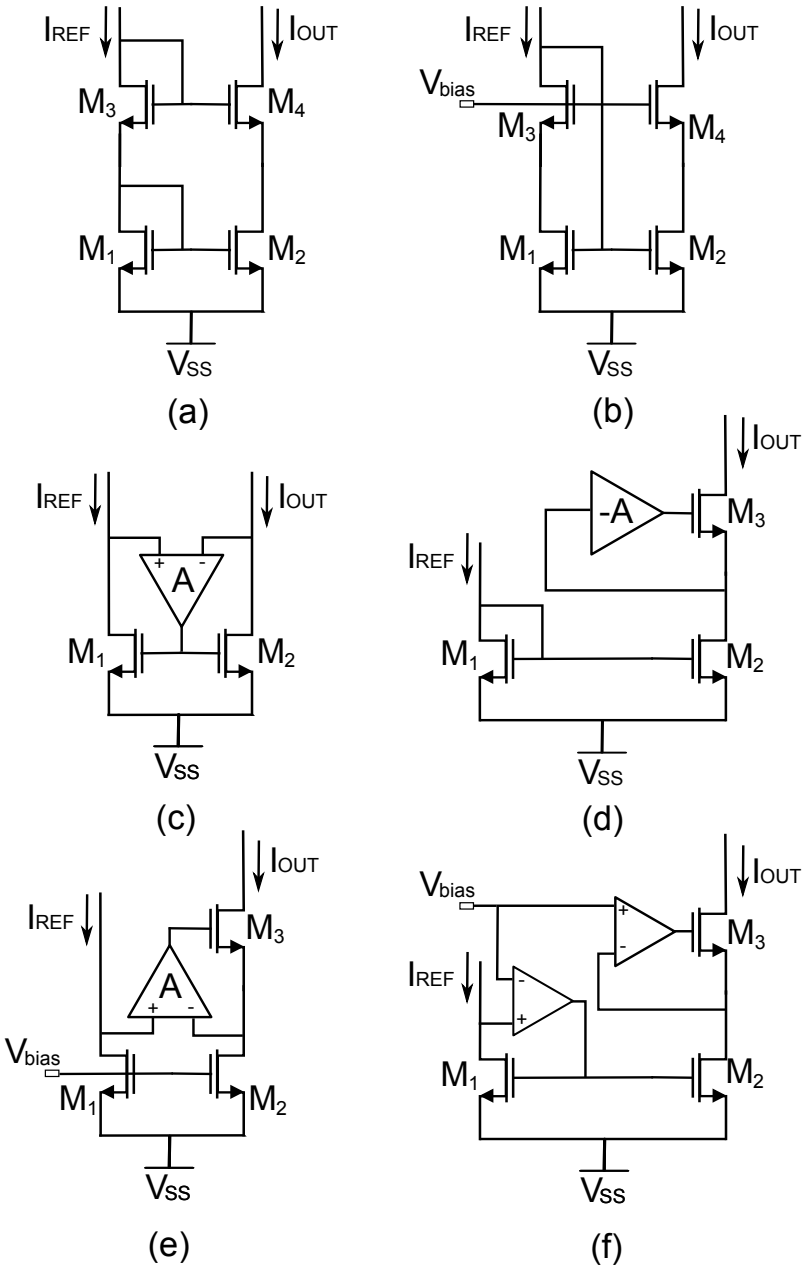


**Figure 5.4:** Current mirror topologies. (a) Simple cascode, (b) high-swing cascode, (c) active [104], (d) regulated cascode [105], (e) linear active [106] and (f) active-input regulated cascode [107].

$g_m^{k-1} r_o^k$ [108], although at the cost of increased area and bias levels needed. Schemes to improve the output impedance as well as the voltage compliance of a current source are usually based on the use of negative-feedback amplifiers [104, 105, 106, 107]. The amplifier in Figure 5.4(c) forces the drain-source voltage $M_1$ and $M_2$ to be equal thus improving the tracking between $I_{OUT}$ and $I_{REF}$. This configuration allows

to achieve an output impedance of $r_o^2 g_m$ and a voltage compliance of $V_{DD} - V_{DS,sat}$ [104]. The regulated cascode in Figure 5.4(d) makes use of the amplifier gain to boost the output resistance to $Ar_{o2}r_{o4}g_{m4}$, although at the cost of a reduced output swing to $V_{DD}-2V_{DS,sat}-V_T$ [105]. A similar principle applies to the configuration in Figure 5.4(e) [106], although transistors $M_1$ and $M_2$ are now biased in the triode region, with the result of increasing the voltage compliance to approximately $V_{DD}-V_{DS,sat3}$, if $V_{DS_2} << V_{DS,sat3}$ and the output resistance to $Ar_{o3}g_{m3}R_{M2}$, where $R_{M2}$ is the on resistance of $M_2$ is the triode region. The configuration in Figure 5.4(f) [107] uses two amplifiers to force equal drain-source voltages across $M_1$ and $M_2$ as well as boosting the output impedance to $Ar_{o2}r_{o3}g_{m3}$. By controlling the input of the amplifiers, the bias of the $M_1$-$M_2$ pair can be controlled, allowing operation in the linear region, resulting in an available output voltage swing of $V_{DD} - V_{DS,sat3} - V_{bias}$.

## 5.2 Proposed Stimulation Circuit - System Architecture

In this section we propose an architecture to implement a current-steering tripolar current source. The operation of the current source can be described with the aid of Figure 5.5. During the stimulation cycle, $\varphi_1$, current sources 3 and 4 deliver currents $I\alpha$ and $I(1-\alpha)$ to the anodes $E_1$ and $E_3$, respectively. The sum of these two currents is collected by the cathode $E_2$ and sank via current sources 1 and 2. During phase $\varphi_2$, the direction of the current is reversed to balance the charge on each electrode contact. The parameter $\alpha$ represents a current weight parameter which defines the ratio between the currents flowing through each anode. The use of push-pull current sources aims to ensure independent regulation of the current flowing through each anode. To simplify the engineering effort two identical current sources were used to source/sink current from the cathode and to minimise mismatches between the current total current flowing through the cathode and the current flowing through

the anodes.

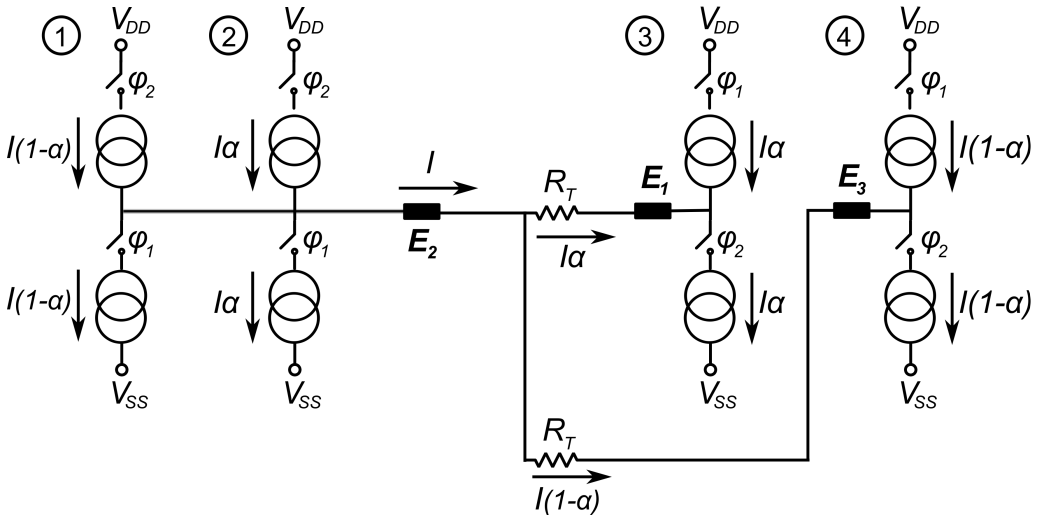


**Figure 5.5:** Illustration of stimulation current source arranged in tripolar mode.

The architecture of the stimulator ASIC is shown in Figure 5.6. It consists of four voltage-to-current converters (VICs), each controlled by a 4-bit current digital-to-analog converter (DAC). A 4-bit multibias DAC is used to control the ratio of the current flowing through the anodic branches. An RC circuit ($\tau$) is used to generate exponential decays at the end of each pulse for anodal blocking [84]. A control signal, $P$, is used to switch the VIC inputs from the 4-bit DAC to the RC circuit. An output switching network controlled by timing signals $S$ and $S1$ is used to regulate the anodic and cathodic portion of each stimulation cycle, by changing the direction of the currents through the electrodes $E_{an1}$ ($E_4$), $E_{an2}$ ($E_2$) and $E_{cat}$ ($E_3$). The digital inputs to the DACs, $B_{0:3}$ and $D_{0:3}$, and to the RC network, $S_{ota}$, and the timing signals, $P$, $S$ and $S1$ are generated off-chip.

Each push-pull current source is implemented in the architecture shown in Figure 5.7.

The basic structure of the current source is a voltage-to-current converter (VIC) [109], implemented by $A_1$, $M_1$ and $M_2$. The purpose of the opamp, $A_1$, is to boost the output impedance of the VIC to $R_{out}$=$A_1 g_{m2} r_{o2} r_{o1}$ where $g_{m2} r_{o2} r_{o1}$ is the output impedance of the simple cascode element $M_1$-$M_2$ and $A_1$ is the gain of the opamp.

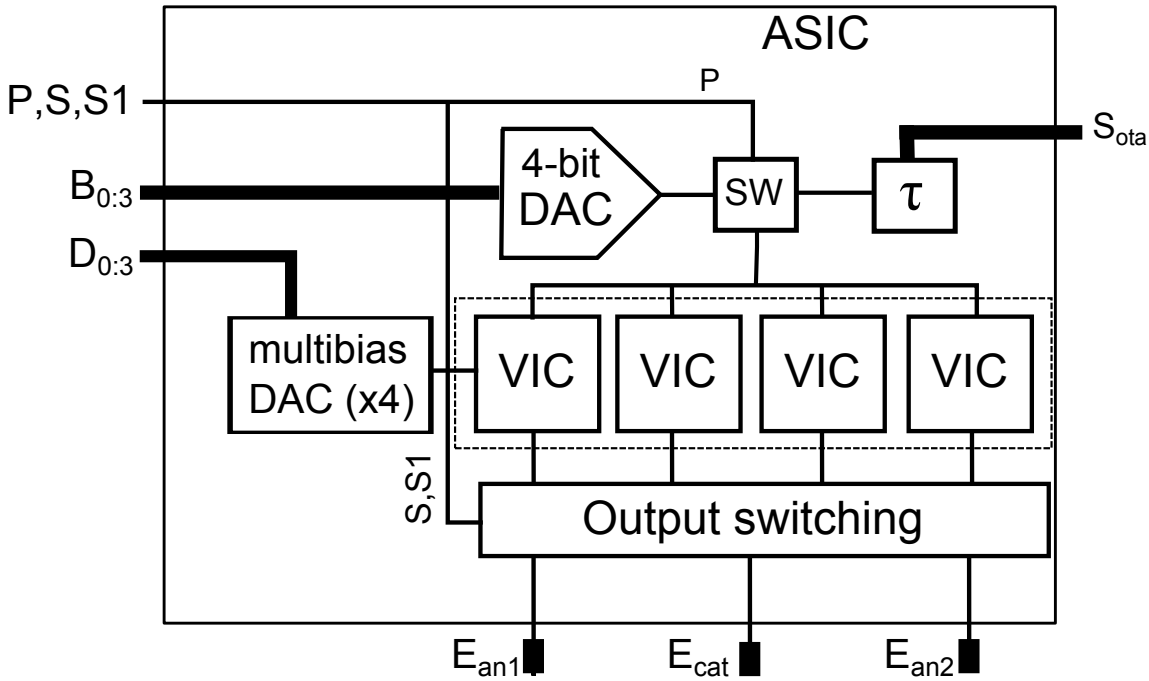


**Figure 5.6:** Architecture of the tripolar stimulator ASIC.

Thanks to the feedback path, the voltage across $M_1$ is regulated by the opamp and thus is less affected by the output voltage. By biasing $M_1$ in the triode region, which then acts as a resistor, the current flowing through $M_1$, $I_{base}$, can then be determined by the ratio between the input voltage, $V_{in}$, and the output resistance of $M_1$, $R_{M1}$, as:

$$I_{base} = \frac{V_{in}}{R_{M1}} = \mu C_{ox} \frac{W}{L} \left[ (V_{bias4} - V_{T1}) V_{in} - \frac{1}{2} V_{in}^2 \right] \tag{5.2}$$

where $V_{bias4}$ is the gate-source voltage applied to $M_1$ and $V_{in}$ is the input voltage of the opamp. For $V_{in} < 2(V_{bias4} - V_T)$ the $2^{nd}$ order term, $\frac{1}{2}V_{in}^2$, can be neglected and the output current becomes a linear function of $V_{in}$. By driving $M_1$ in deep triode region, $V_{in}$ can be very small and the VIC can achieve a large voltage compliance, useful to accommodate large variations of the load impedance. A $W/L$ ratio of $60\mu$m/$4\mu$m and a bias voltage $V_{bias4}$ of 3.45V allows to keep $M_1$ in deep triode region and vary its drain current, $I_{base}$, between 0A and $480\mu$A, with steps of $32\mu$A, by varying $V_{in}$ between 0V and 150mV. The $W/L$ ratio of $M_2$ was kept very large

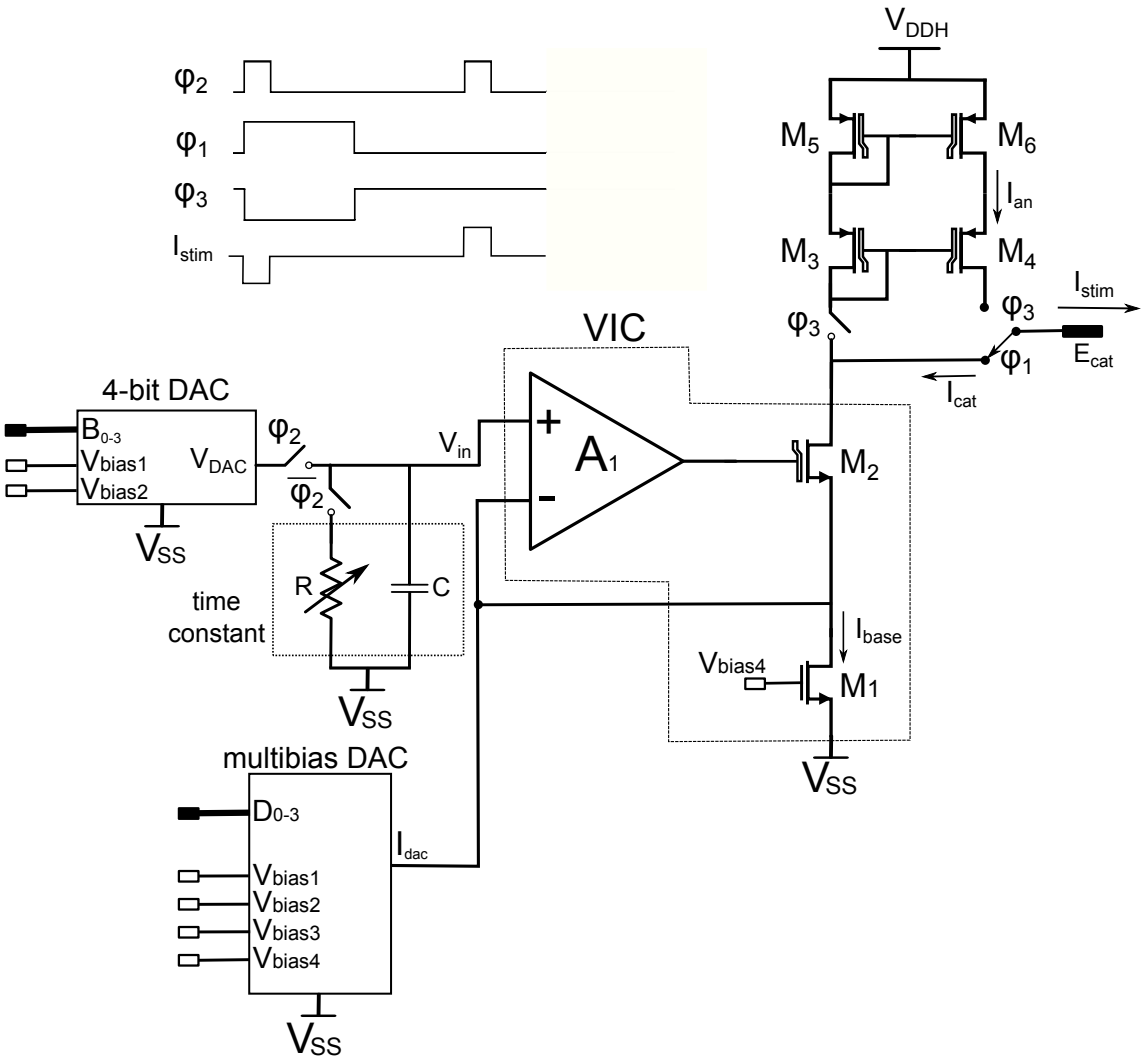


**Figure 5.7:** Architecture of a high output impedance voltage-to-current converter (VIC) used to implement each current source forming the tripolar current source. Digital control signals $P$, $S$ and $S1$ control switch phases $\phi_1$, $\phi_2$ and $\phi_3$, respectively.

($100\mu$m/$2\mu$m), in order to minimise its drain-source voltage drop, thus improving the current source output compliance. The value of the input voltage, $V_{in}$, is controlled by a standard 4-bit current-steering DAC. Transistors $M_3$-$M_6$ form an output current mirror used to source anodic current. The cascode configuration has been chosen to minimise the supply-dependence of the VIC. This however would drastically reduce the voltage headroom using a 5V supply. The supply voltage of this section of the circuit, $V_{DDH}$, has been increased to 12V and the transistors $M_2$-$M_6$ are all high-voltage (20V) MOSFETS. In order to allow for the current-steering feature, we need to provide a method to vary the current through each anode, while keeping a

constant cathodic current, ie. to generate complementary anodic currents $I\alpha$ and $I(1-\alpha)$, where $\alpha$ ranges between 0 and 1. This will be discussed in section 5.2.3. $I_{base}$ represents a minimum current always flowing in both anodes, to avoid to convert the tripolar current source into a bipolar configuration. The RC circuit at the input of the amplifier consists of a integrated switched tunable resistor, $R$, and a capacitor, $C$, to provide an exponential pulse decay, needed for anodal blocking operation[1]. During $\varphi_1$ the PMOS current mirror is off and the VIC is sinking current, $I_{cat}$, with $\varphi_2$ providing a stable $V_{in}$, which sets the output current and charges the capacitor, $C$. In $\varphi_3$ the DAC is disconnected from the VIC and $C$ discharges through $R$ with time constant $\tau = RC$. In $\varphi_3$ the current mirror is switched on and the VIC sources current, $I_{an}$, which balances the cathodic current and provides electrode discharge. We can now consider each block in detail.

### 5.2.1 Gain-Boosting Amplifier

The purpose of the amplifier, $A_1$, is to boost the gain of the output impedance of the current source. To achieve a high gain in a single stage we used the folded-cascode amplifier topology in Figure 5.8. In addition to high gain, the folded-cascode configuration was selected to obtain fast settling, large output voltage swing and allow for inputs close to the supply voltages.

Transistors $MP_0$ and $MP_1$ form a differential input pair biased by the tail current source $MP_2$, which provides a current $I_{OTA}$. PMOS transistors were used to accommodate input common-mode levels as low as zero. The two pairs $MP_0$-$M2$ and $MP_1$-$M3$ form two folded cascode elements and $M0$ and $M1$ are two current sources, used to set the current flowing through the output branches. Transistors $MP_3$-$MP_6$ form the amplifier load, arranged in cascode mode in order to achieve high output resistance.

The characteristics used for the design of the folded-cascode OTA include the volt-

[1]Refer to section 4.1 in Chapter 4

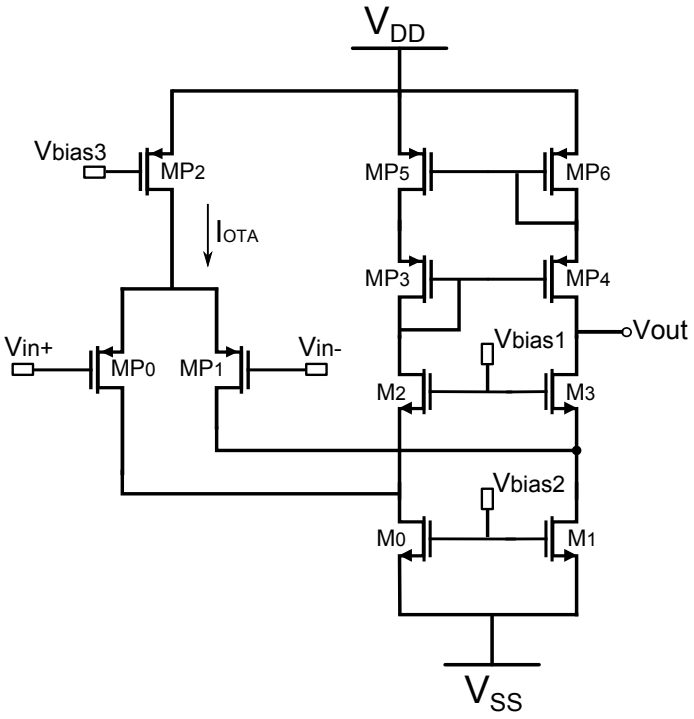


**Figure 5.8:** Architecture of a high gain folded cascode amplifier.

age gain, $A_v$, the gain-bandwidth product, $f_T$, the output node capacitance, $C_L$, the minimum input common mode level, $V_{CMmin}(V)$, and the power supply voltages, $V_{DD}$ and $V_{SS}$. The voltage gain of the amplifier is given by [110]:

$$A_V = G_m R_o \tag{5.3}$$

$$G_m = g_{mP1} = g_{mP2} \tag{5.4}$$

$$R_o = [g_{m3} r_{o3} (r_{oP1} || r_{o1})] || (g_{mP4} r_{oP4} g_{mP6}) \tag{5.5}$$

where $G_m$ is the transconductance of the OTA, equal to the transconductance of each of the input pair transistors, $g_{mP1,2}$ and $R_o$ is the output resistance of the OTA. The minimum input common mode level is derived from [111]:

$$V_{CMmin} = -V_{SS} - V_{OV0} - |V_{TP0}|. \tag{5.6}$$

The slew rate (SR) can be calculated as the ratio between the OTA current, $I_{OTA}$

**Table 5.1:** Design parameters of the folded-cascode OTA (Length of all MOSFETS set to 1$\mu$m)

| Parameter | Value |
|---|---|
| $A_v$ (dB) | >50 |
| $f_T$ (MHz) | >1 |
| $V_{CMmin}$(V) | 0 |
| $C_L$(pF) | 1 |
| $V_{DD}$(V) | 5 |
| $V_{SS}$(V) | 0 |
| $I_{OTA}$ ($\mu$A) | 30 |
| $V_{bias1}$(V) | 2.5 |
| $V_{bias2}$(V) | 1.245 |
| $V_{bias3}$(V) | 3.48 |
| $W_{P0,P1}(\mu m)$ | 24 |
| $W_{P2}(\mu m)$ | 12 |
| $W_{0,1}(\mu m)$ | 4 |
| $W_{2,3}(\mu m)$ | 2 |
| $W_{P3-P6}(\mu m)$ | 6 |

and the load capacitance, $C_L$. The gain bandwidth product of the OTA is given by:

$$f_T = \frac{G_m}{2\pi C_L} \tag{5.7}$$

The target specifications for the design of the amplifier and the simulated results are summarised in Table 5.1. Using equations B.7 and B.12, $R_o$ was calculated to be approximately 50 M$\Omega$ and $A_V$ approximately 6600 V/V (or 76 dB). The SR was estimated to be 3 V/$\mu$s, the $f_T$ to be 2MHz and the $V_{CMmin}$ to be approximately -0.4 V.

#### 5.2.1.1 Simulated performance of opamp

The performance of the opamp was assessed by simulating its DC and frequency response. To compute the frequency response the the input voltage was set to a 1V ac signal with 0 DC level, and the frequency was swept between 1Hz and 1MHz, in 8 steps for every decade. Figure 5.9 shows the resulting gain magnitude and phase of the amplifier.

The simulated performance of the opamp is summarised in Table 5.2 in terms of key

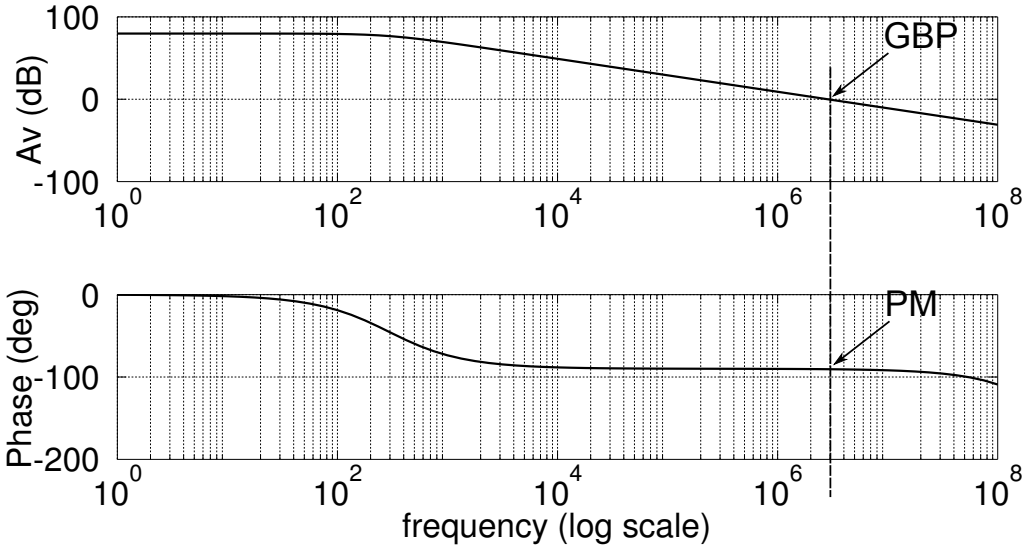


**Figure 5.9:** Frequency response of opamp. Gain and phase versus frequency.

parameters, including the operating current, $I_{OTA}$, the voltage gain, $A_V$, the gain bandwidth product, $f_T$, the phase margin, $PM$, the DC voltage, $V_{OUT}^{(DC)}$, the output voltage swing, $V_{OUT}^{(S)}$ and the static power, $PW$.

**Table 5.2:** Simulated Performance of the Folded Cascode Amplifier

| Parameter | Value |
|---|---|
| $I_{OTA}$ ($\mu$A) | 33 |
| $A_V$ (dB) | 77 |
| $f_T$(Hz) | 2M |
| $PM$ (deg) | 89 |
| $V_{OUT}^{DC}$ (V) | 2.1 |
| $V_{OUT}^{(S)}$ (V) | 4.3 |
| $PW$ (W) | 300$\mu$ |

### 5.2.2 4-bit Digital to Analogue Converter (DAC)

A 4-bit current-steering digital-to-analogue converter (DAC) was used to generate the input voltage, $V_{DAC}$ to the VIC (see Figure 5.7). In order to keep $M_1$ and the multibias DAC in the triode region, $V_{DAC}$ was selected to range between $0V$ and 150mV in 15 steps of 10mV each.

The DAC was implemented by a set of binary-weighted current sink pairs ($M_1 - M_{11}$,

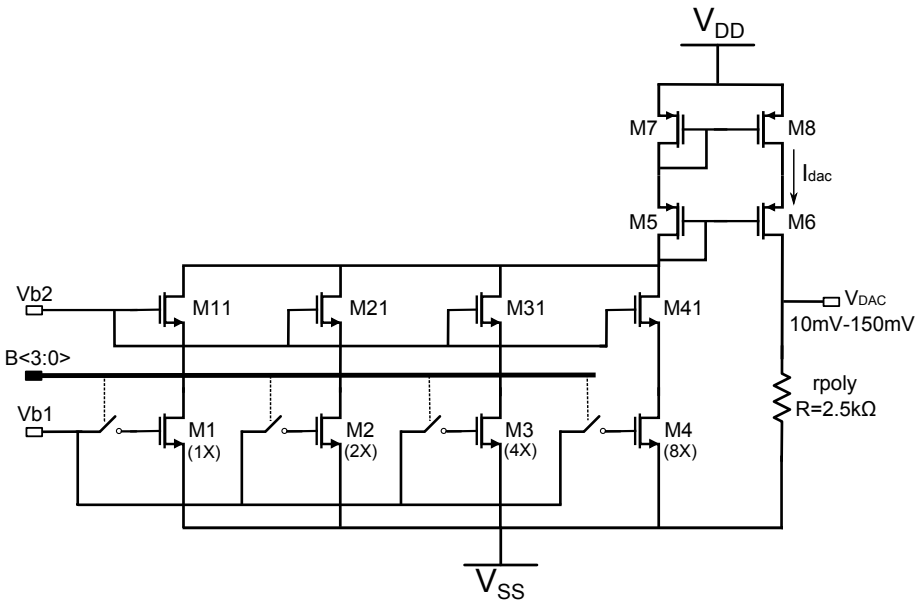


**Figure 5.10:** Architecture of a 4-bit current-steering digital to analog converter.

$M_2 - M_{21}$, etc). The currents are weighted by the $W/L$ values of the MOSFETs. The current sinks were implemented as $2^N$ matched transistors, with $N = 4$ with all the gates connected to the same bias voltages, $V_{b1}$ and $V_{b2}$. The DAC current was mirrored to the output through the current mirror $M_5 - M_8$ and sank to the negative supply (0 V) through a resistor, $R$, so that:

$$V_{DAC} = R(B_0 \cdot I + B_1 \cdot 2I + B_2 \cdot 4I + B_3 \cdot 8I) \tag{5.8}$$

where $B_{0-3}$ are the control logic signals switching the current sinks on and off. A $W/L$ ratio of 5.4$\mu$m/4$\mu$m and bias voltages $V_{b1} = 1.07$V and $V_{b2} = 1.245$V were selected so that the least-significant-bit current, $I_{LSB}$, was equal to 4$\mu$A. This value was chosen to ensure operation of the DAC is strong inversion[2]. The resistor, $R$, is integrated on chip as polysilicon film, characterised by a 10% absolute variation[3]. Figure 5.11A shows the simulated performance of the DAC (dots) compared to the ideal 4-bit DAC transfer characteristic (reference line).

Table 5.3 reports the simulated data, at typical corners from AMS 0.35$\mu$ design

[2]See Appendix B for different regions of operation of MOSFETs.
[3]Source: AMS HV 0.35$\mu$m process design kit.

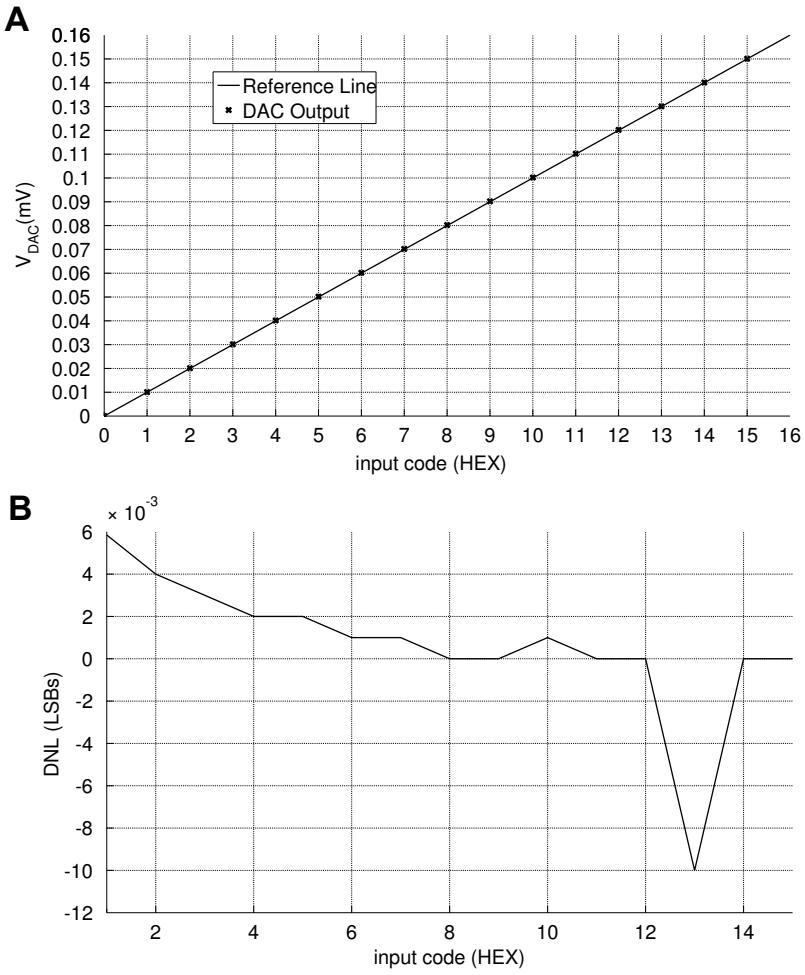


**Figure 5.11:** Output performance of the 4-bit current-steering DAC.

library, associated with the plot in Figure 5.11. The accuracy of the DAC was measured in terms of integral nonlinearity (INL) and differential nonlinearity (DNL). The INL represents the deviation of the values of the actual transfer characteristic of the DAC from a straight line. The DNL represents the difference between the actual step height of the DAC and the ideal value of 1 least significant bit (LSB), or, in other words, how much the analog output of the DAC changes in response to a change in the digital input code as compared to the ideal change. The INL was estimated to be constant to 0.015LSBs for all values of the input code. The DNL is shown in Figure 5.11B. The maximum DNL was estimated to be 0.01LSBs occurring when the input code is set to 13 (or logic '1101'). When the input logic is set to '1111', the DAC draws a full scale current of 60$\mu$A, leading to a maximum static

power of $P_{DAC} = 60\mu A \times 2 \times 5V = 600\mu W$.

**Table 5.3:** Simulated Output Voltage of the 4-bit current-steering DAC

| **Input code** | $V_{DAC}$ **(V)** | $V_{DAC}$ **(ideal) (V)** |
|---|---|---|
| 0000 | 1.5$\mu$ | 0 |
| 0001 | 10.06m | 10m |
| 0010 | 20.1m | 20m |
| 0011 | 30.13m | 30m |
| 0100 | 40.15m | 40m |
| 0101 | 50.17m | 50m |
| 0110 | 60.18m | 60m |
| 0111 | 70.19m | 70m |
| 1000 | 80.19m | 80m |
| 1001 | 90.19m | 90m |
| 1010 | 100.2m | 100m |
| 1011 | 110.2m | 110m |
| 1100 | 120.2m | 120m |
| 1101 | 130.2m | 130m |
| 1110 | 140.1m | 140m |
| 1111 | 150.1m | 150m |

### 5.2.3 Multibias DAC

To provide the stimulator with current steering capability, ie. the ability to direct a largest portion of current towards one anode and a smaller portion towards the other anode, thus dynamically controlling the ratio between the anodic currents, we need to independently vary the current flowing through each anode, while keeping the cathodic current constant. One method to achieve this is to vary the bias voltage, $V_{bias4}$ (in Figure 5.7), within a fixed range, in order to obtain small changes of $R_{M1}$ [112]. This method however requires extra transistors to linearised the transfer characteristic of $M_1$. Another method is based on the use of a current-steering DAC to directly select the value of output current [102], although at the cost of increased area. An alternative design involves the use of a multibias DAC, where each transistor forming the DAC is biased in the saturation region to a specific quiescent point on the characteristic curve [95]. For our application we designed a multibias DAC operating in the triode region, in order to keep a high output

voltage compliance, reduce the effects of bias voltage changes on the drain current of each transistor of the DAC and, additionally, reduce the number of transistors from $2^N - 1$ to $N$. Each current source is equipped with one multibias DAC, which adds an arbitrary current, $I_{dac}$, to $I_{base}$.

The architecture of the multibias DAC is shown in Figure 5.12(a). For a specific ratio $W/L$, we can define four bias voltages, $V_{bias1-bias4}$ such that $I_1$=$2I_0$, $I_2$=$4I_0$ and $I_3$=$8I_0$ (Figure 5.12(b). The drain currents for the $N$-bit DAC, operated in the linear region, becomes:

$$I_n = K\frac{W}{L}(V_{biasn} - V_{THn})V_{ref} \tag{5.9}$$

where $V_{ref}$ is the drain-source voltage across the transistors, set by the 4-bit DAC discussed in the previous section. As we vary $V_{ref}$ between 0V and 150$m$V we can linearly increase the drain current of each transistor and, thus, the overall current of the DAC, $I_{dac}$, as shown in Figure 5.12(c). The $W/L$ ratios of all transistors were set to 60$\mu$m/4$\mu$m and the bias voltages $V_{bias1-bias4}$ to 1.07V, 1.245V, 1.7V and 3.45V, respectively, giving a least-significant-bit current, $I_{LSB}$, of 4$\mu$A. An example of the behaviour of the drain current of the LSB transistor is shown in the inset of 5.12(c). The desired DC operation of the multibias DAC is reported in Table 5.4. The transistors forming the multibias DAC were placed in parallel with $M_1$ in Figure 5.7 so that $I_{dac}$ will add to $I_{base}$, which ranges between 0 and 480$\mu$A, resulting in the total output current $I_{an}$.

#### 5.2.3.1 Simulated performance of the multibias DAC

Figure 5.13(a) shows the output characteristic represented by a family of $I_{dac}$-$V_{ref}$ curves as we vary the multibias DAC digital input code from 0000 to 1111. Figure 5.13(b) represents the output current of the multibias DAC for $V_{ref}$ = 10, 100 and 150mV in response to four step changes in the DAC input code occurring every 600$\mu$s.

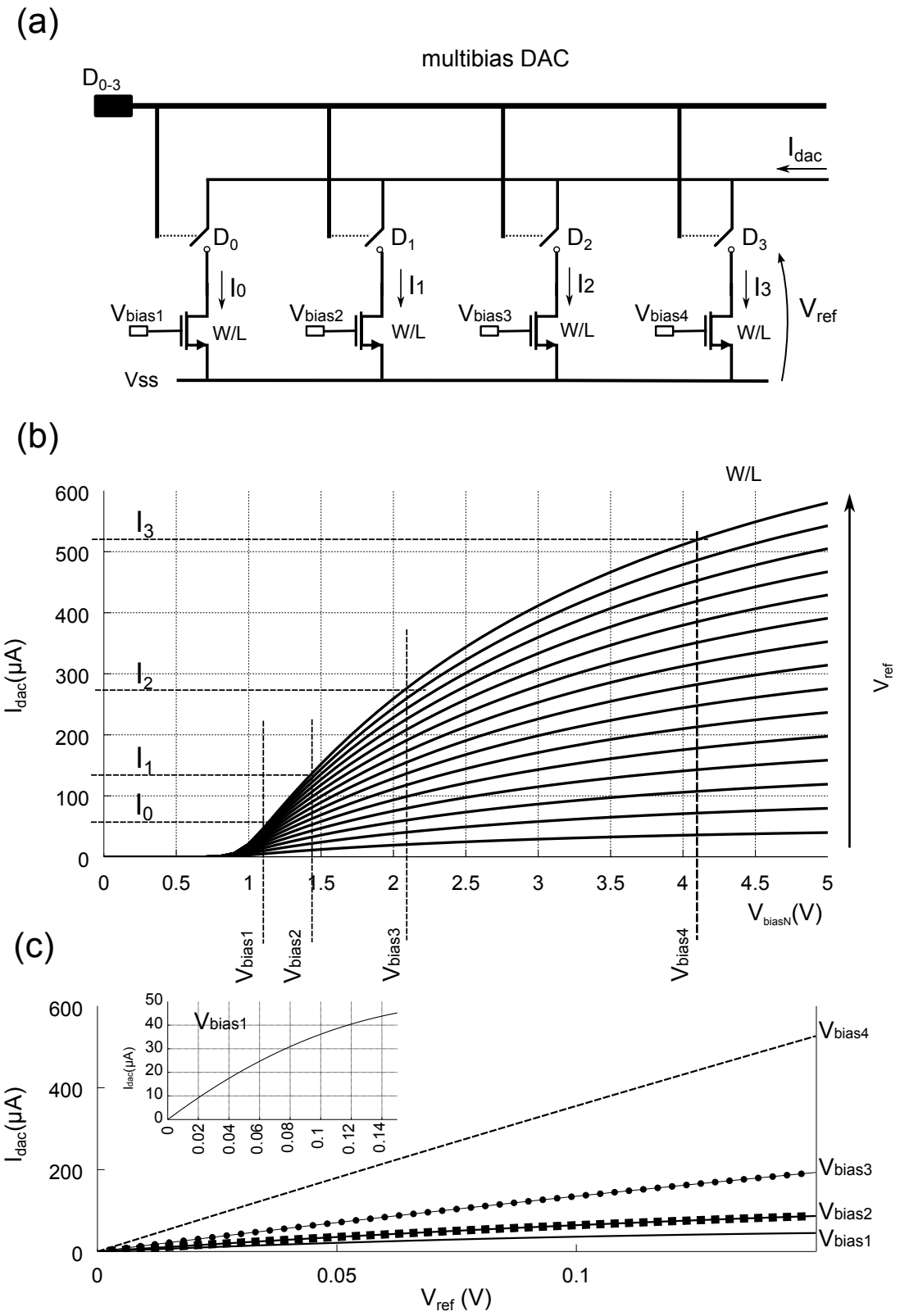


**Figure 5.12:** Design principle of a multibias DAC with transistors operating in the triode region. (a) Architecture of a 4-bit multibias DAC. (b) Transfer characteristic of a transistor biased in the triode region for different source-drain voltages, $V_{ref}$. (c) Output characteristic of a transistor biased in the triode region for different values of the gate-source voltages $V_{bias1-bias4}$.

**Table 5.4:** Design DC current values for all combination of the logic inputs B<3:0> and D<3:0>.

| $I_{dac}$ ($\mu$A) | D<3:0> 0000 | 0001 | 0010 | 0011 | 0100 | 0101 | 0110 | 0111 | 1000 | 1001 | 1010 | 1011 | 1100 | 1101 | 1110 | 1111 |
|---|---|---|---|---|---|---|---|---|---|---|---|---|---|---|---|---|
| B<3:0> 0000 | 0 | 0 | 0 | 0 | 0 | 0 | 0 | 0 | 0 | 0 | 0 | 0 | 0 | 0 | 0 | 0 |
| 0001 | 0 | 4 | 8 | 12 | 16 | 20 | 24 | 28 | 32 | 36 | 40 | 44 | 48 | 52 | 56 | 60 |
| 0010 | 0 | 8 | 16 | 24 | 32 | 40 | 48 | 56 | 64 | 72 | 80 | 88 | 96 | 104 | 112 | 120 |
| 0011 | 0 | 12 | 24 | 36 | 48 | 60 | 72 | 84 | 96 | 108 | 120 | 132 | 144 | 156 | 168 | 180 |
| 0100 | 0 | 16 | 32 | 48 | 64 | 80 | 96 | 112 | 128 | 144 | 160 | 176 | 192 | 208 | 224 | 240 |
| 0101 | 0 | 20 | 40 | 60 | 80 | 100 | 120 | 140 | 160 | 180 | 200 | 220 | 240 | 260 | 280 | 300 |
| 0110 | 0 | 24 | 48 | 72 | 96 | 120 | 144 | 168 | 192 | 216 | 240 | 264 | 288 | 312 | 336 | 360 |
| 0111 | 0 | 28 | 56 | 84 | 112 | 140 | 168 | 196 | 224 | 252 | 280 | 308 | 336 | 364 | 392 | 420 |
| 1000 | 0 | 32 | 64 | 96 | 128 | 160 | 192 | 224 | 256 | 288 | 320 | 352 | 384 | 416 | 448 | 480 |
| 1001 | 0 | 36 | 72 | 108 | 144 | 180 | 216 | 252 | 288 | 324 | 360 | 396 | 432 | 468 | 504 | 540 |
| 1010 | 0 | 40 | 80 | 120 | 160 | 200 | 240 | 280 | 320 | 360 | 400 | 440 | 480 | 520 | 560 | 600 |
| 1011 | 0 | 44 | 88 | 132 | 176 | 220 | 264 | 308 | 352 | 396 | 440 | 484 | 528 | 572 | 616 | 660 |
| 1100 | 0 | 48 | 96 | 144 | 192 | 240 | 288 | 336 | 384 | 432 | 480 | 528 | 576 | 624 | 672 | 720 |
| 1101 | 0 | 52 | 104 | 156 | 208 | 260 | 312 | 364 | 416 | 468 | 520 | 572 | 624 | 676 | 728 | 780 |
| 1110 | 0 | 56 | 112 | 168 | 224 | 280 | 336 | 392 | 448 | 504 | 560 | 616 | 672 | 728 | 784 | 840 |
| 1111 | 0 | 60 | 120 | 180 | 240 | 300 | 360 | 420 | 480 | 540 | 600 | 660 | 720 | 780 | 840 | 900 |

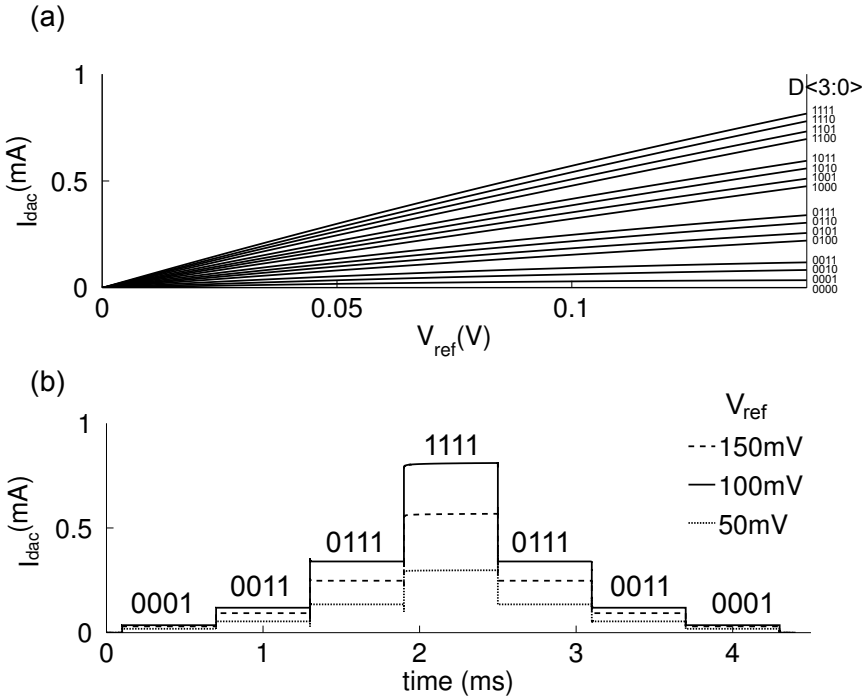


**Figure 5.13:** Output characteristic of the multibias DAC. (a) Simulated $I_{dac}$-$V_{ref}$ curves generated by varying the DAC input code. (b) Step response of the DAC for $V_{ref} = 10, 100$ and 150mV, measured by switching the 4 bits in the shown sequence every 600$\mu$s.

Representation of the nonlinearity for values of $V_{in}$ of 10, 50, 100 and 150mV across the DAC is shown by the plots in Figure 5.14(a). The measured INL and DNL for each case is shown by the plots in Figure 5.14(b) . The maximum INL and DNL were measured in LSBs and are reported in Table 5.5.

**Table 5.5:** Simulated maximum INL and DNL of the multibias DAC

| $V_{ref}$ **(mV)** | $INL_{max}$ **(LSBs)** | $DNL_{max}$ **(LSBs)** |
|---|---|---|
| 10 | 0.19 | 0.32 |
| 50 | 0.32 | 0.49 |
| 100 | 0.59 | 0.71 |
| 150 | 0.91 | 1.11 |

The simulated output current ranges of the DAC are listed in Table 5.6 for different values of $V_{ref}$. These ranges are taken between the least-significant-bit (minimum current) flowing through the DAC, $I_{LSB}$, and the full-scale (maximum) current, $I_{FS}$, flowing through the DAC when all the switches are on.

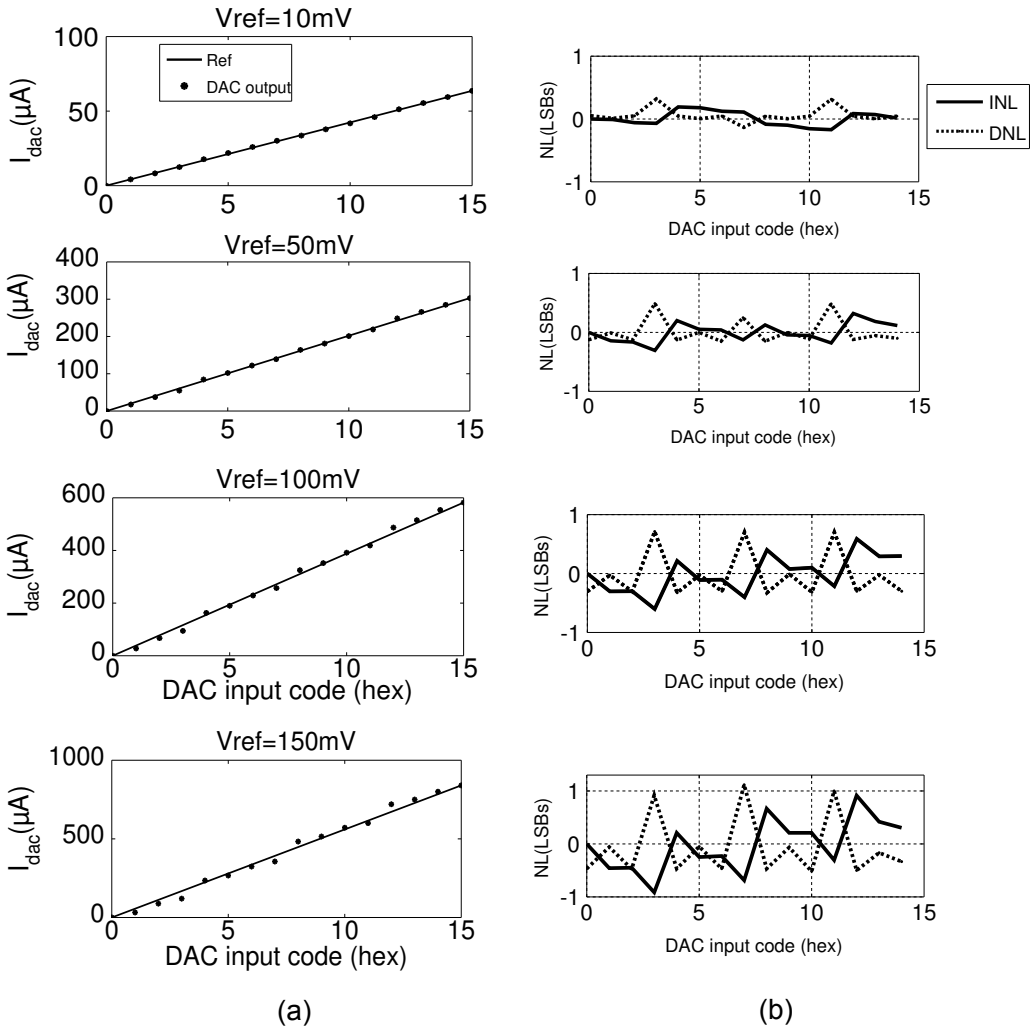


**Figure 5.14:** Linearity of the multibias DAC.

**Table 5.6:** DAC output current ranges obtained at different values of $V_{ref}$

| $V_{ref}$ **(mV)** | $I_{LSB}$-$I_{FS}$($\mu$**A**) | $I_{ideal}$ ($\mu$**A**) |
|---|---|---|
| 10 | 4.21-63.62 | 4-60 |
| 50 | 17.5-303 | 20-300 |
| 100 | 27.8-582 | 40-600 |
| 150 | 32-840 | 60-900 |

### 5.2.4 Integrated Time Constant

In order to generate quasi-trapezoidal or triangular pulses with variable time decay constant, which are necessary to achieve anodal blocking during stimulation, the design of the current source included a switched RC network as illustrated in Figure 5.15.

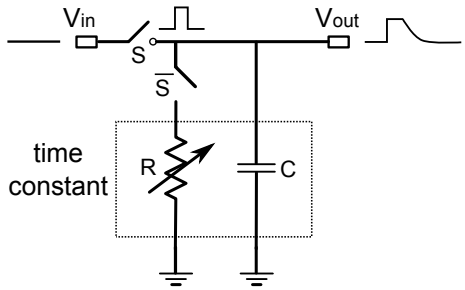


**Figure 5.15:** Schematic of a switched RC network used to generate exponential pulse decays.

As long as the switch $S$ is on, $V_{out}$ will be equal to $V_{in}$ and the voltage across the capacitor, $C$, will be kept at $V_{out}$. As $S$ is turned off, the capacitor is discharged through the resistor $R$, resulting in an exponential decay, $\tau$=$RC$. One approach to achieve a tunable $\tau$ is to fix the value of the capacitor and vary the value of the resistor. The use of integrated passive resistors is excluded a priori from the design, due to the very large area required to realise large resistances. A common technique used for the implementation of tunable resistors on-chip, is based on the use of a current-biased OTA [113, 114]. The block diagram of the circuit used to realised a tunable resistor is shown in Figure 5.16.

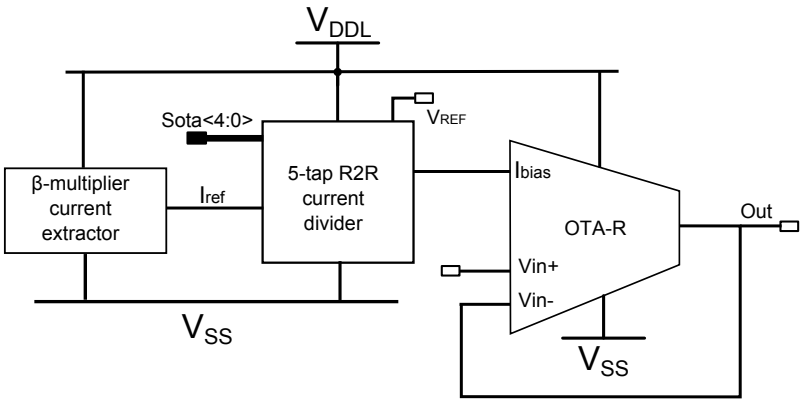


**Figure 5.16:** Block diagram of the circuit used to realise a large resistor in CMOS. It comprises a current extractor to generate a constant current, a current divider to generate ratios of the reference current, used to bias the OTA-R.

Implementation of the tunable resistor in CMOS was achieved by designing the circuit in Figure 5.16 to operate in weak inversion, in order to take advantage of the linear relationship between the transconductance and the drain current of a transistor biased in weak inversion, and, additionally, to achieve very small currents, which

would result in very small transconductance and therefore very large resistance[4]. The specifications included the design of 5 time constants between 1$\mu$s and 10ms. Using an on-chip 10pF capacitor, this results in on-chip resistances between 100k$\Omega$ and 1G$\Omega$. As we will discuss in section 5.2.4.3, in order to achieve these resistances, the bias current to the OTA-R, $I_{bias}$, was set to a range between 100pA and 1$\mu$A.

#### 5.2.4.1 Current Extractor

A $\beta$-multiplier reference current generator [115] was used to generate a constant current of 1$\mu$A. The circuit architecture is shown in Figure 5.17.

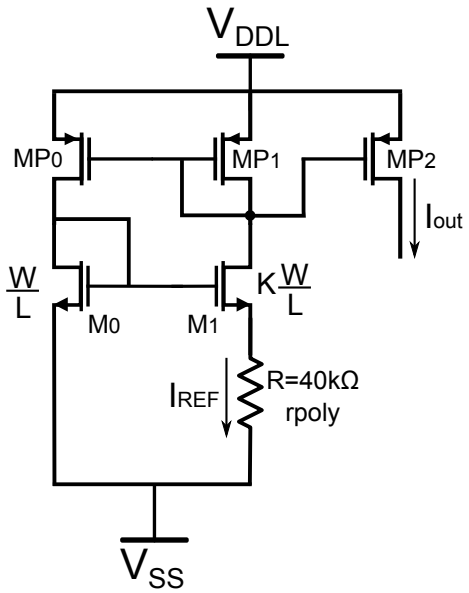


**Figure 5.17:** Architecture a $\beta$-multiplier reference current generator.

The drain current of a transistor biased in weak inversion region is given by Eq. B.13. The gate-source voltage of $M_0$ is given by:

$$V_{GS0} = nU_T ln\left[\frac{IL}{I_{D0}W}\right] + V_{Tn} \tag{5.10}$$

and the gate-source voltage of $M_1$ is given by:

[4] *Design issue*: The use of exponential pulses to achieve anodal blocking has not been yet investigated in DBS. The selection the time constants was based on research in FES, where exponential pulses of few millisecond ensured anodal blocking (see section 4.1 in Chapter 4)

$$V_{GS1} = nU_T ln\left[\frac{IL}{I_{D0}KW}\right] + V_{Tn}. \tag{5.11}$$

Since $V_{GS0} = V_{GS1} + I_{REF}R$, then, by combining Eqs. 5.10 and 5.11, we can derive an expression for $I_{REF}$ as:

$$I_{REF} = \frac{nU_T}{R} lnK. \tag{5.12}$$

$I_{REF}$ is then mirrored to the output through the current mirror formed by $MP_1$ and $MP_2$. The minimum value of the $W/L$ ratios for each transistor were calculated from the following relation [116]:

$$I_D \leq \left(\frac{n-1}{e^2}\right)\frac{W}{L}\mu C_{OX}U_T^2. \tag{5.13}$$

This lead to the design parameters listed in Table 5.7.

**Table 5.7:** Design parameters of a $\beta$-multiplier current extractor

| **Parameter** | **Value** |
|---|---|
| $I_{REF}$ ($\mu A$) | 1 |
| R ($\Omega$) | 40k |
| $V_{DD}$ (V) | 1.5 |
| $V_{SS}$ (V) | 0 |
| $(W/L)_{P0}$ | $160\mu/5\mu$ |
| $(W/L)_{P1}$ | $160\mu/5\mu$ |
| $(W/L)_{P2}$ | $160\mu/5\mu$ |
| $(W/L)_0$ | $75\mu/5\mu$ |
| $(W/L)_1$ | $300\mu/5\mu$ |
| K | 4 |

The performance of the current extractor was assessed by running DC and parametric analyses. The DC analysis looked at the DC currents and static power generated from a 1.5V supply. The results are summarised in Table 5.8.

Parametric analysis looked at the supply-dependence of the current extractor and the effects of process variations on the output current, represented by the plots in Figure 5.18.

**Table 5.8:** Simulated DC parameter of the current extractor

| Parameter | Value |
|---|---|
| $I_{REF}$ ($\mu A$) | 1.093 |
| $I_{out}$ ($\mu A$) | 1.1 |
| PW (W) | $4.92\mu$ |

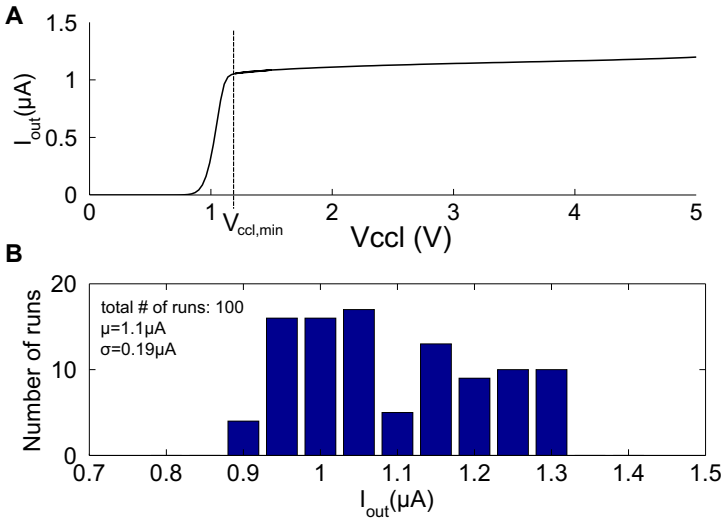


**Figure 5.18:** Dependence of the current extractor on the supply voltage. **A** Output current versus supply voltage. **B** Mean output current, $\mu$ and standard deviation, $\sigma$, for 100 runs of montecarlo analysis.

Figure 5.18A shows the output current, $I_{out}$ as a function of the supply voltage, swept between 0 and 5V. The minimum supply voltage to ensure correct operation of the current extractor, ie. for all the transistors to be saturated, was found to be approximately 1.1V. Between this value and 5V, the output current is approximately independent of the power supply, ranging between $0.96\mu$A and $1.12\mu$A. Monte Carlo analysis was performed for 100 runs for mismatch variations. The result is represented by the histogram in Figure 5.18B. Mean output current, $\mu$ and standard deviation, $\sigma$, are reported in the figure.

#### 5.2.4.2 Current Divider

A current divider was used to divide the output current of the current extractor in 5 steps. The topology of the current divider is shown in Figure 5.19 [117].

This circuit is based on a current division principle using only MOS transistors

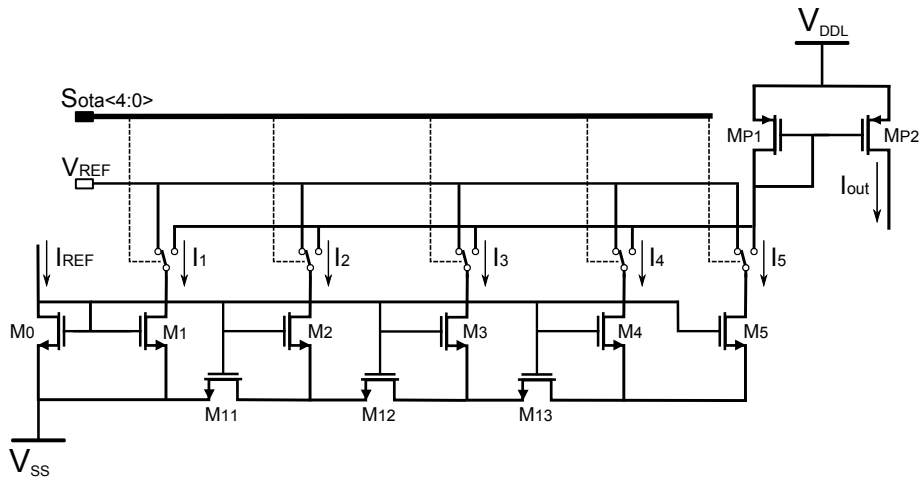


**Figure 5.19:** Architecture of a 4-bit current-steering digital to analog converter.

[118], according to which for a circuit formed by two transistors having the same gate voltage, a current flowing in or out of this circuit will be linearly divided into two parts. By accurate selection of the ratio between the sizes of the two transistors, we can define the fraction of current flowing through each transistor. By setting the transistor ratios as summarised in Table 5.9, we can achieve a $N$-fold division at each stage (tap).

**Table 5.9:** Ratios of transistors for a divide-by-$N$ operation

| **Parameter** | **Value** |
|---|---|
| $(W/L)_{0-4}$ | $N-1$ |
| $(W/L)_{11-13}$ | $N/(N-1)$ |
| $(W/L)_5$ | 1 |

A value of $N$ equal to 10 was selected for this design in order to divide the current from 1$\mu$A to 100pA. The minimum length of each transistor was set to 5$\mu$m, in order to minimise short-channel effects in weak inversion. A 5-bit digital input, $S_{ota}$, was used to selects which branch of the current divider to connect to the output. For example, when $S_{ota}$='10000', the output is connected to the $I_1$ branch while the other branches are connected to $V_{REF}$ to provide a current path for all the transistors. When $S_{ota}$=00001, the output is connected to the $I_5$ branch. The design specifications are listed in Table 5.10.

$V_{REF}$ was set to 0.8V in order to keep all the transistors in saturation. The transistors

**Table 5.10:** Design specifications of a 5-stage divide-by-10 current divider

| Parameter | Value |
|---|---|
| $(W/L)_{0-4}$ | $45\mu$m/$5\mu$m |
| $(W/L)_{11-13}$ | $4.5\mu$m/$5\mu$m |
| $(W/L)_5$ | $4\mu$m/$5\mu$m |
| $V_{DDL}$ (V) | 1.5 |
| $V_{SS}$ (V) | 0 |
| $V_{REF}$ (V) | 0.8 |

were scaled differently than specified in Table 5.9, to take into account the practical implementation of these ratios in the chip layout.

DC and Monte Carlo analyses were performed in order to estimate the output current of each stage, measure the voltage compliance and the yield of the current divider. Figure 5.20A shows the output characteristic of each stage of the current divider and Figure 5.20B plots the histogram resulting from performing 100 runs of Monte Carlo analysis of mismatch errors. The simulated performance of the current divider is summarised in Table 5.11, in terms of DC mean output current, $\mu$ and standard deviation, $\sigma$ , derived at $V_{DD}$=1.5V, and voltage compliance.

**Table 5.11:** Simulated performance of the current divider at a supply voltage $V_{DD}$=1.5V.

| $S_{ota}$ | $I_{out}$ (A) | Compliance (V) | $\mu$ ($\pm$ $\sigma$) (A) |
|---|---|---|---|
| 10000 | $1.01\mu$ | 1.39 | $0.99\mu$ ($\pm$29n) |
| 01000 | 97n | 1.38 | 96n ($\pm$6.3n) |
| 00100 | 9.7n | 1.38 | 11n ($\pm$1.9n) |
| 00010 | 0.98n | 1.29 | 1n ($\pm$0.19n) |
| 00001 | 109p | 1.28 | 100p ($\pm$19p) |

#### 5.2.4.3 OTA Resistor (OTA-R)

An operational transconductance amplifier (OTA) was chosen to implement a tunable resistor on chip. Figure 5.21 shows the architecture of a balanced single-ended OTA, consisting of a voltage-to-current converting stage, formed by transistors pairs $M_{0-1}$, $MP_{0-1}$ and $MP_{4-5}$, biased by $I_{bias}$, and unity-gain output current mirrors.

As described earlier in section B.1.3, the transconductance of a transistor in weak inversion is given by $g_m = I_D/(nU_T)$, where $n$ is the weak inversion slope factor and

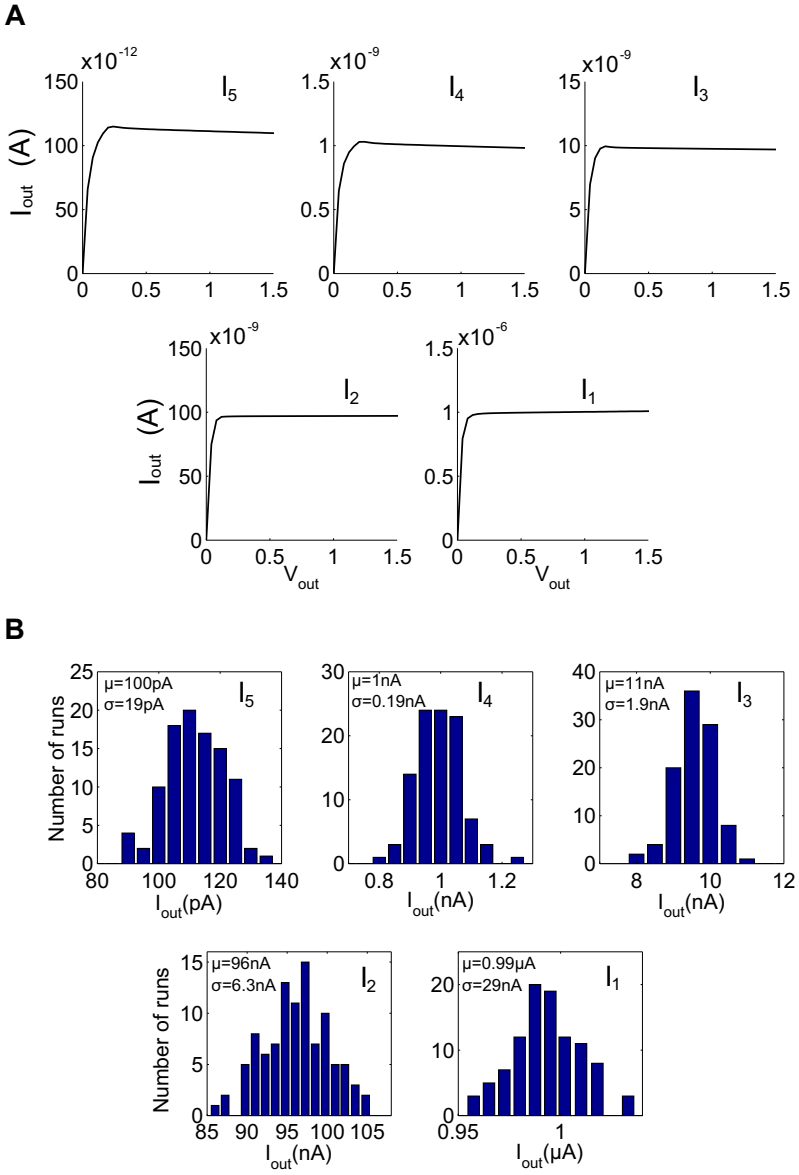


**Figure 5.20:** (A) Output characteristic of each stage of the current divider. (B) Montecarlo analysis of the variation of the output current due to mismatch errors ($\mu$, mean output current, $\sigma$, standard deviation)

$U_T$ is the thermal voltage. By providing a feedback path between the output and negative input of the OTA (see Figure 5.16), the resistance between the input and output of the OTA is simply the inverse of the transconductance of the input pair transistor, $M_1$, $g_{m1}$. The closed-loop performance of the OTA, configured as a unity feedback amplifier, was assessed in terms of simulated DC transfer characteristic and gain. Figure 5.22(a) shows the DC characteristic of the OTA when the input voltage $V_{IN}$ is varied between 0 and 2V. Input DC levels smaller than 1.05V ensure

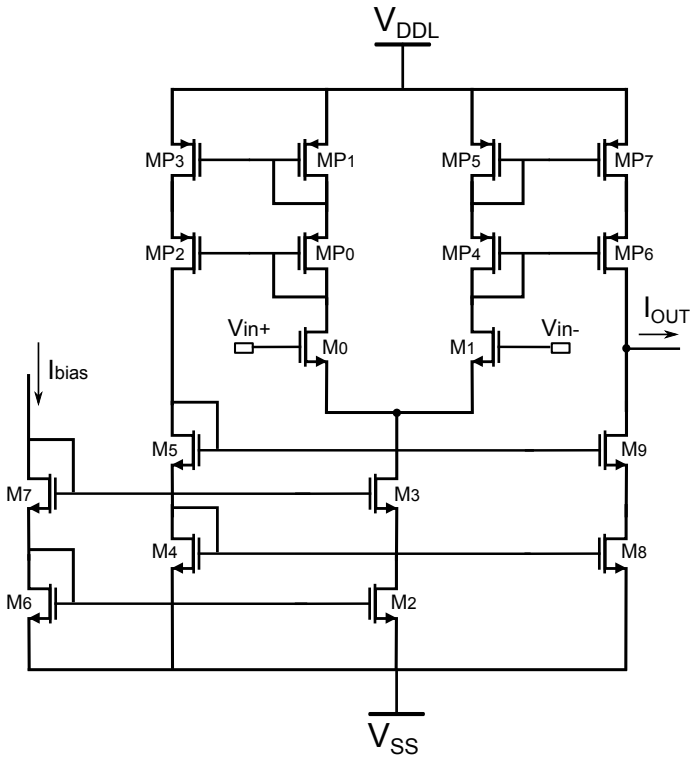


**Figure 5.21:** Architecture of a balanced single-ended OTA.

linear operation, whereas larger DC amplitudes cause the amplifier to saturate. The closed-loop gain is shown in Figure 5.22(b) and has a value of 1 (0dB) and a cut-off frequency of 80Hz.

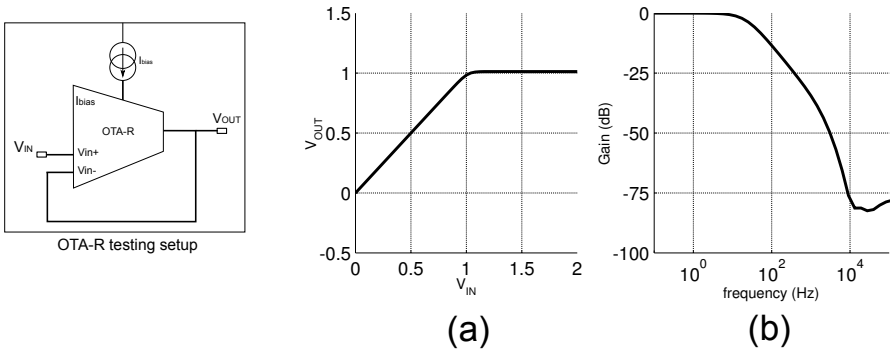


**Figure 5.22:** (a) DC transfer characteristic of the OTA-R for input voltage range between 0 and 2V. (b) Closed-loop gain of the OTA-R when driven as a unity-gain amplifier.

The value of the resistance of the OTA, $R_{OTA}$, was calculated as the reciprocal of $g_{m1}$. Figure 5.23 shows the variation of the resistance of the OTA as $I_{bias}$ is swept between 100pA and 1$\mu$A. By using the logarithmic scale for both axes, we can observe how $R_{OTA}$ maintains linearity as the bias current is varied over five orders of magnitude.

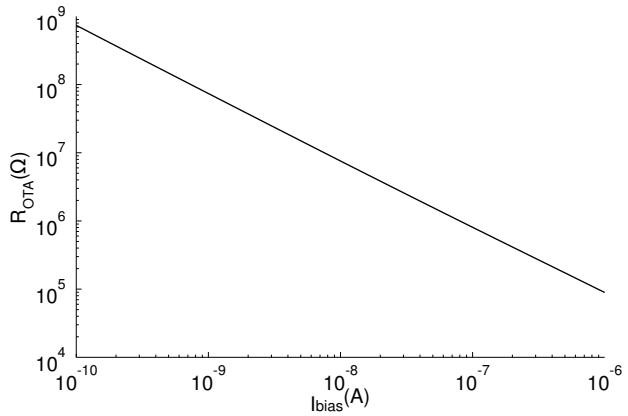


**Figure 5.23:** Variation of resistance of OTA with applied constant bias current, $I_{bias}$, between 100pA and 1$\mu$A. Logarithmic scale was used for both axes.

Table 5.12 summarised the results of the DC analysis in terms of resistance value, $R_{OTA}$, time constant, $\tau$, calculated assuming a 10pF capacitor, and power consumption, estimated as the product between the supply voltage and the different values of the input bias current.

**Table 5.12:** Simulated DC performance of the OTA

| $I_{bias}$ (A) | $R_{OTA}$ ($\Omega$) | $\tau$ (s) | Static power (W) |
|---|---|---|---|
| 100p | 739.6M | 7.39m | 1n |
| 1n | 73.9M | 739$\mu$ | 9n |
| 10n | 7.57M | 75.7$\mu$ | 90n |
| 100n | 806.9k | 8$\mu$ | 0.9$\mu$ |
| 1$\mu$ | 89k | 0.89$\mu$ | 9$\mu$ |

Figure 5.24 shows the transient response of the OTA in parallel with a 10pF capacitor. The input was a square pulse of amplitude of 100mV and width of 100$\mu$s. The bias current was varied by one order of magnitude, between 100pA and 1$\mu$A.

### 5.2.5 Voltage Reference Generator

A self-biased thermal voltage-referenced circuit [115] was adopted to generate the voltages needed to bias all the blocks of the circuit and it is shown in Figure 5.25. The circuit consists of a cascode self-biased current source formed by transistors $M_0 - M_3$ and $MP_0 - MP_3$, adopted to ensure that $V_X$ and $V_Y$ are equal, so that the

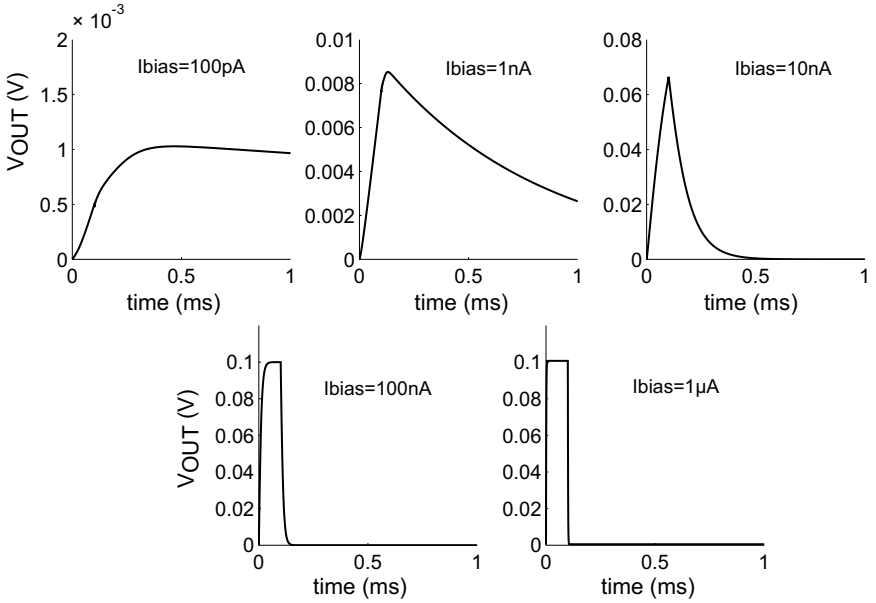


**Figure 5.24:** Simulated transient response of the OTA to a 100m-V square pulse with pulse width of 100$\mu$s and different values of $I_{bias}$.

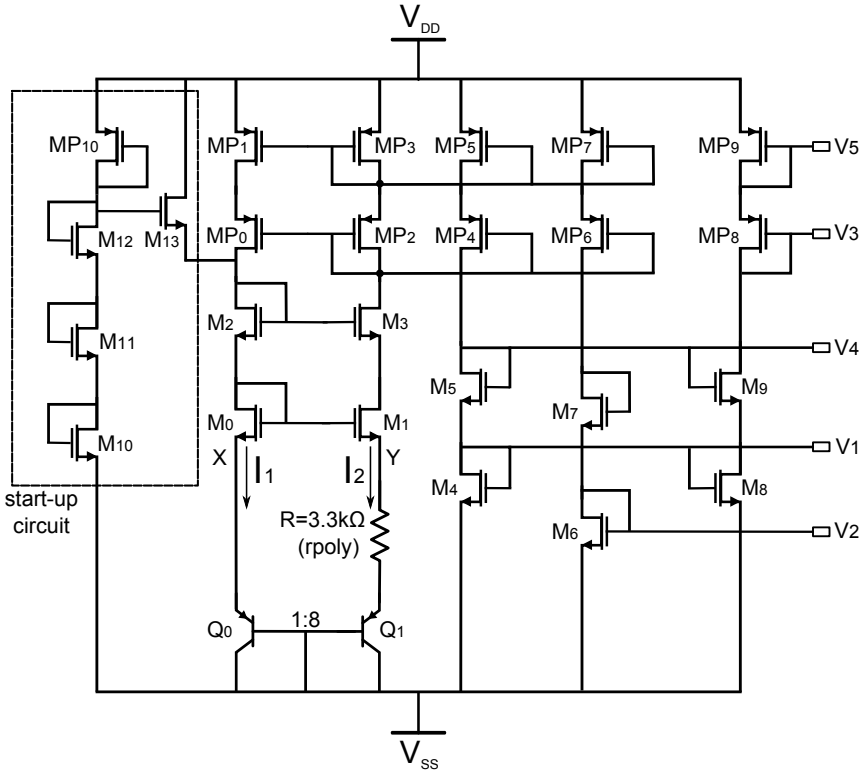


**Figure 5.25:** Reference voltage generator with start-up circuit.

voltage across $Q_0$, $V_{BE0} = I_2R + V_{BE1}$ and $RI = V_{BE0} - V_{BE1} = V_T \ln q$, where $q$ is the ratio between the emitter areas of the bipolar transistors, $Q_0$ and $Q_1$. The start-

up circuit aims at preventing the circuit to reach a stable state where no current is flowing in the circuit. The reference current $I_2$ is then mirrored to the output branch to generate different currents, used to bias diode-connected transistors. By appropriately setting the bias current and the ratios of the diode-connected loads, we can define different output voltages, $V_1 - V_5$. The design parameters and theirs values are listed in Table 5.14.

**Table 5.13:** Design parameters of a $V_T$ reference circuit

| **Parameter** | **Value** |
|---|---|
| $M_{0-3}$ | 16/1 |
| $MP_{0-5}$ | 32/4 |
| $MP_{6-7}$ | 64/4 |
| $M_{4-5}$ | 18/4 |
| $M_{6-7}$ | 15/4 |
| $M_{8-9}$ | 36/4 |
| $MP_{8-9}$ | 32/4 |
| $M_{10-13}$ | 3.2/1 |
| $MP_{10}$ | 3.2/44.8 |
| R ($\Omega$) | 3.3k |
| n | 8 |

DC analysis was performed at $V_{DD}$=5V and an annotation of the operating points is given in Table 5.14. The target reference voltages were set to $V_1$=1.07V, $V_2$=1.245V, $V_3$=1.7V, $V_4$=2.5V and $V_5$=3.6V.

**Table 5.14:** DC performance of the $V_T$ reference generator

| **Parameter** | **Value** |
|---|---|
| $I_1$ (A) | 16.76$\mu$ |
| $I_2$ (A) | 16.81$\mu$ |
| $V_1$ (V) | 1.069 |
| $V_2$ (V) | 1.251 |
| $V_3$ (V) | 1.612 |
| $V_4$ (V) | 2.48 |
| $V_5$ (V) | 3.48 |
| Static PW (W) | 580$\mu$ |

Parametric analysis was performed to assess the dependence of the voltage levels on the supply voltage. The supply voltage was swept between 4 and 6 V. The resulting traces of the 5 reference voltages are reported in Figure 5.26A.

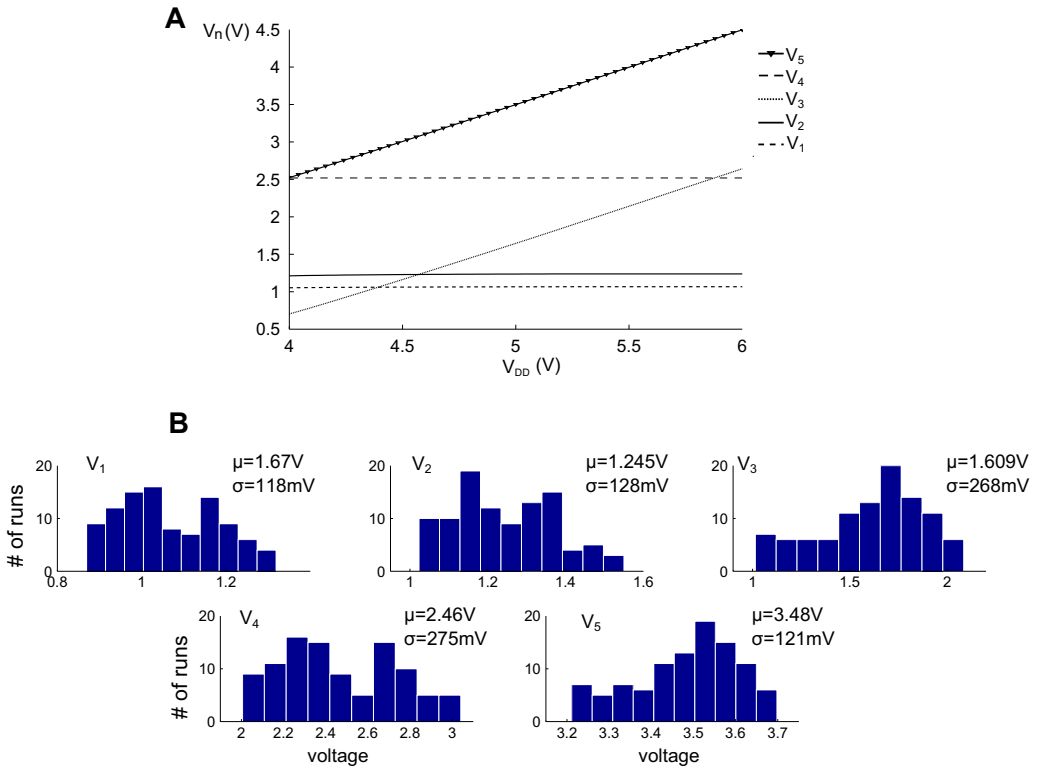


**Figure 5.26:** Dependence of reference voltages on supply voltage. The supply voltage was swept between 4 and 6V. The operating voltage of the reference circuit is 5V.

The voltages $V_1$, $V_2$ and $V_4$ are substantially independent of the supply voltage. When the supply voltage is varied between 4 and 6 V, $V_1$ varies between 1.05V and 1.067V, $V_2$ between 1.212V and 1.238V and $V_4$ between 2.5V and 2.53V. The supply voltage, however, has a major impact on $V_3$ and $V_5$, which are taken from the drain of diode-connected PMOS transistors. $V_3$ was found to vary between 0.7V and 2.64V, whereas $V_5$ between 2.53V and 4.5V. Monte Carlo analysis was performed to assess the impact of device mismatch and process variations on the output voltages. Figure 5.26B shows the histograms of all 5 output voltages resulting from 100 runs of Monte Carlo simulation, with mean output voltage, $\mu$, and standard deviation, $\sigma$, reported in the figure. We can observe a high deviation due to process mismatches, in particular in $V_3$ and $V_4$. This may be due to variations in threshold voltages and in the resistance, $R$, which affects the value of the current $I_2$.

### 5.2.6 Simulated Performance of the Tripolar Current Source

Table 5.15 lists the design bias and supply voltages used to operate the tripolar current source.

**Table 5.15:** Bias and supply voltages used to operate the tripolar current source

| Parameter | Value (V) |
|---|---|
| $V_{DDH}$ | 12 |
| $V_{DD}$ | 5 |
| $V_{DDL}$ | 1.5 |
| $V_{SS}$ | 0 |
| $V_{b1}$ | 1.07 |
| $V_{b2}$ | 1.245 |
| $V1$ | 1.07 |
| $V2$ | 1.245 |
| $V3$ | 1.7 |
| $V4$ | 2.5 |
| $V5$ | 3.6 |
| $V_{REF}$ | 0.8 |

The overall stimulation current amplitude is controlled by the 4-bit DAC which sets $V_{DAC}$, common input to all current sources. The ratio between the anodic currents is set by logic input D1<3:0> and D2<3:0>, which control the multibias DAC of each current source. The exponential decay of the current pulse is set by logic input $S_{OTA}$. The timing of the current pulse is set by input switch control, $P$ and output switch control, $S$ (and $S_1$=$\overline{S}$), which are shown in Figure 5.27. The supply voltages ($V_{DD}$, $V_{DDL}$, $V_{DDH}$ and $V_{SS}$), the control signals ($P$, $S$ and $S_1$) and the digital inputs ($D$, $B$ and $S_{OTA}$) were supplied externally.

Input logic P controls the input switches ($\phi_2$ and $\phi_3$ in Figure 5.7) and selects between $V_{DAC}$ and $R_{OTA}$. When P is set to logic '1' (5V), the input of the VIC is connected to $V_{DAC}$ (the output of the 4-bit DAC). As P is set to '0', the input of the VIC is connected to the output of the time constant circuit and the input capacitor is discharged through the resistance of the OTA. Input logic $S$ and $S_1$ control the output switches of the current source ($\phi_1$ and $\phi_4$ in Figure 5.7) and select between anodic and cathodic phase (for charge balance). When $S$ is set to logic '1' (12V),

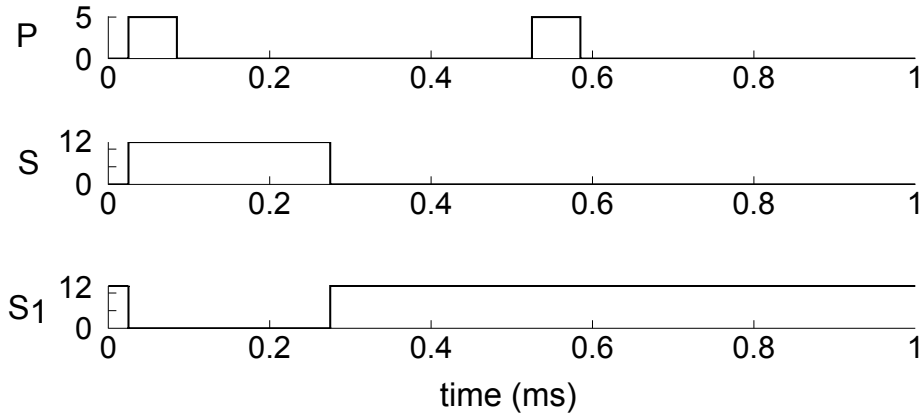


**Figure 5.27:** Timing control for tripolar stimulation. Input logic C controls the input switches of the current source and is set to 0 and 5V for logic '0' and '1', respectively. Input logic S control the output switches of the current source and is set to 0 and 12V for logic '0' and '1', respectively

the VIC is sourcing current to the electrode, whereas when S is at '0' the VIC is sinking current from the electrode.

The transient behaviour of the current source is shown in Figure 5.28, where $P$ has a width of 60$\mu$s([5]) and a period of 0.5ms and S has a width of 250$\mu$s and a period of 1ms. The values of the logic inputs used to obtain these traces are summarised in Table 5.16.

**Table 5.16:** Input logic control of the tripolar current source

| Parameter | Logic value |
|---|---|
| D1<3:0> | 0111 |
| D2<3:0> | 1000 |
| $S_{OTA}$ | 00100 |

The traces show the capability of the current source to generate biphasic quasi-trapezoidal pulses at both anodic channels. The glitches occurring at the transition between the two phases may be due to asymmetries in the rise/fall times between the switching of the two output switches that regulate the direction of the current flow. The linearity of the current source was assessed by simulating the DC transfer characteristic of one output channel, $I_{OUT}$ vs. $V_{DAC}$, at different values of D (the digital input of the multibias DAC). Figure 5.29A shows the transfer characteristic

[5]Clinical DBS pulse widths are usually in a range between 60$\mu$s and 120$\mu$s. See section 2.4 in Chapter 2.

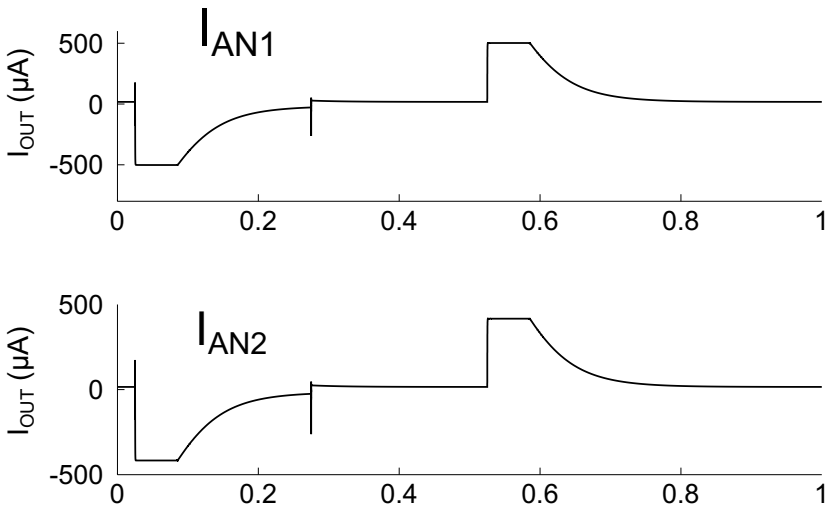


**Figure 5.28:** Transient output behaviour of the tripolar current source.

for D equal to '0000', '0111' and 1111. Table 5.17 compares the ideal and simulated ranges of output current derived at different values of D.

**Table 5.17:** Ideal and simulated $I_{OUT}$ ranges obtained at different values of the multibias DAC code, $D < 3:0 >$

| **D<3:0>** | $I_{OUT}$**(ideal)**$(\mu\mathbf{A})$ | $I_{OUT}$ $(\mu\mathbf{A})$ |
|---|---|---|
| 0000 | 0-480 | 1.2-394 |
| 0111 | 0-720 | 1.7-710 |
| 1111 | 0-1380 | 2.2-1280 |

The output compliance of the current source was simulated at full scale (D<3:0>='1111') for values of $V_{DAC}$ between 10 and 150mV, by sweeping the output voltage between 0 and 12V. The resulting traces are shown in Figure 5.29B.

For a 12-V supply the output compliance varies between 11.15V (at $V_{DAC}$=10mV) and 6.1V (at $V_{DAC}$=150mV). The anodic and cathodic current linearity (for D='0000') was simulated and is shown in Figure 5.29C. $I_{AN}$ and $I_{CAT}$ represent the output currents of the same current source during the two phases of stimulation (ie. the sinking current during the cathodic phase and the sourcing current during the anodic phase). Figure 5.29D shows the tracking error between $I_{AN}$ and $I_{CAT}$, for all values of $V_{DAC}$. The maximum error was found for $V_{DAC}$ = 150mV and ranged between 0.07% when

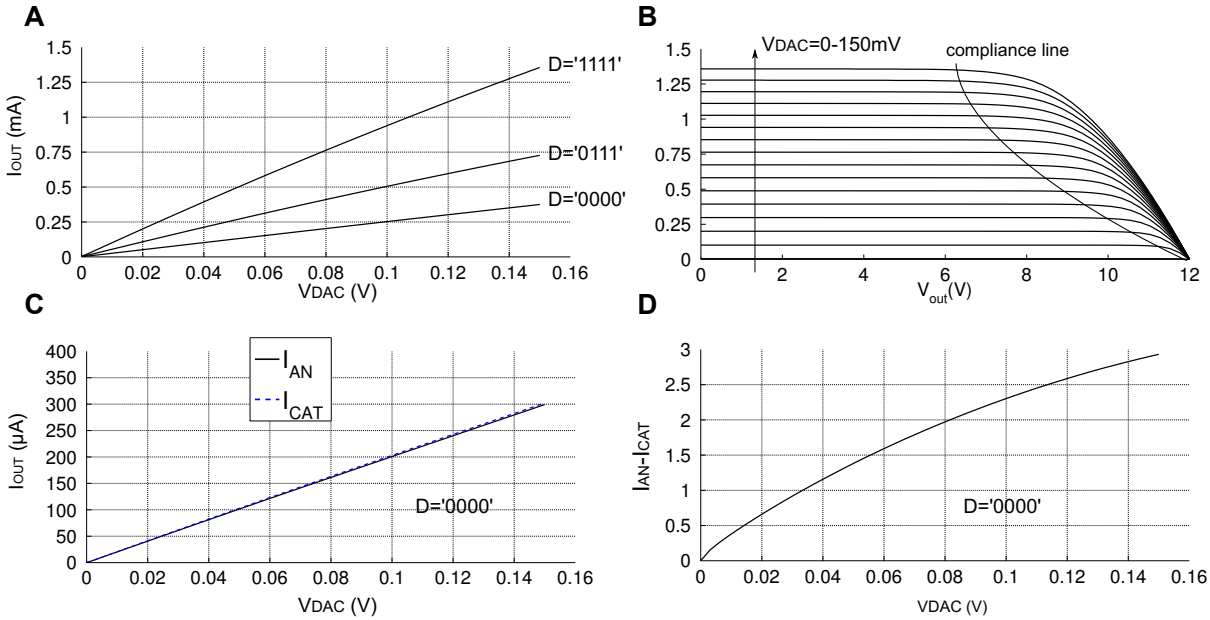


**Figure 5.29:** DC analysis. (A) DC transfer characteristic $I_{OUT}$ vs. $V_{DAC}$ for different values of D. (B) Output characteristic, $I_{OUT}$ vs. $V_{OUT}$, at full scale (D='1111') for all values of $V_{DAC}$. (C) Simulated transfer characteristic of the anodic and cathodic currents. (D) Tracking error between the anodic and the cathodic currents.

D='0000' and 1% when D='1111', with an average error of 0.43%.

The generation of a time constant was tested by performing a transient analysis of the output current in response to a 150m-V pulse of duration of 60$\mu$s for different values $S_{ota}$. The resulting traces are shown in Figure 5.30.

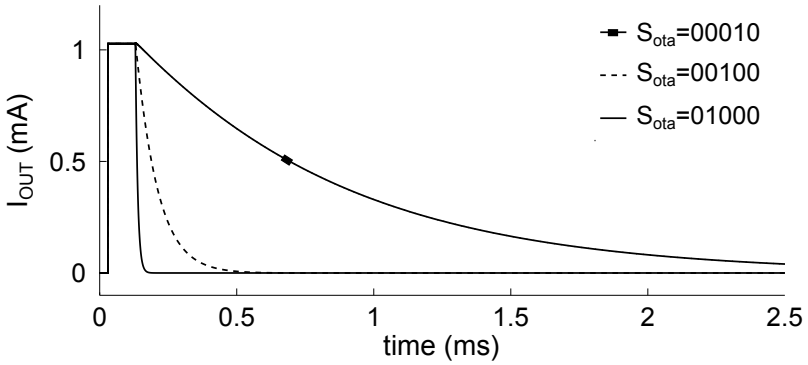


**Figure 5.30:** Different exponential decay simulated by changing the input logic to the time constant circuit, $S_{ota}$, to '01000', '00100' and '00010'.

## 5.3 Chip Layout

The layout of the chip was performed using standard analog layout techniques and following the manufacturer's design rules. Layout techniques are based on the use of multifinger transistors, where a transistor is folded into several fingers, each representing a portion of the gate of the transistor, in order to reduce the gate resistance. This process is also known as interdigitisation. An additional technique implemented in this design was the use of symmetry in the layout, in order to minimise mismatch and signal offsets. This was implemented by using common-centroid configurations, where feasible, or distribution of the layout on one axis, with the addition of dummy components, to provide an identical environment around the circuit being drawn.

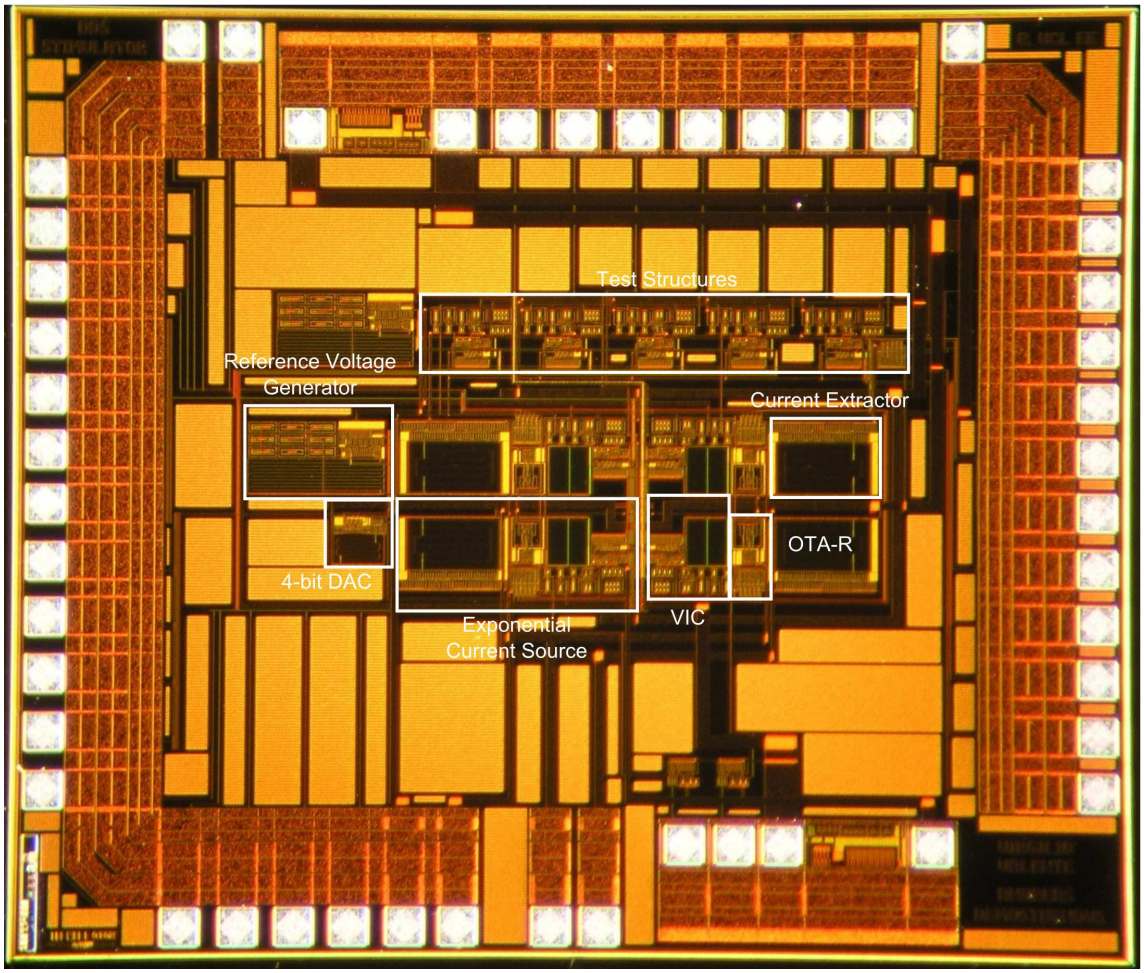


**Figure 5.31:** Die microphotograph of the fabricated stimulator chip.

Figure 5.31 shows a photo of the fabricated stimulator chip, with labels of the main

building blocks. The overall die area (including pads) is 2.3 mm x 2.7 mm, whereas the core area is 0.77 mm x 1.6 mm. Table 5.18 summarises the power consumption of individual sub-blocks of the stimulator.

**Table 5.18:** Area consumption of chip sub-blocks

| Block | Size |
|---|---|
| Reference Voltage generator | 344$\mu$m x 187$\mu$m |
| 4-bit DAC | 130$\mu$m x 120$\mu$m |
| Time-constant Circuit | 370$\mu$m x 190$\mu$m |
| VIC | 94$\mu$m x 30$\mu$m |
| Multibias DAC | 94$\mu$m x 40$\mu$m |
| Output Current Mirror | 206$\mu$m x 60$\mu$m |

## 5.4 Chip Testing and Verification

The equipment adopted for testing the operation of the chips included a waveform generator (TTi TGA1241), used to generate the clock signals $C$, $S$ and $S1$, a multimeter (HP 34401), used to measure the DC voltage and current levels during operation and a digital oscilloscope (Agilent, Infiniium), to display the output current traces. A total number of 10 chips were tested.

### 5.4.1 Chip Performance

#### 5.4.1.1 Functional testing - Generation of biphasic exponential pulses

The first stage of the testing assessed the correct operation of the chip by looking at its capability to generate biphasic square and exponential pulses. The measurements reported in this session are associated to one of the tested chips. Functional testing of the other 9 chips resulted in similar performance to the one reported here. Figure 5.32 shows the measured output current, when the input of the 4-bit DAC, $B$, was set to '1111' (equivalent to a $V_{DAC}$ of 150mV) and the input of the multibias DAC, $D$, was set to '1000' with the $S_{ota}$ set to 10000.

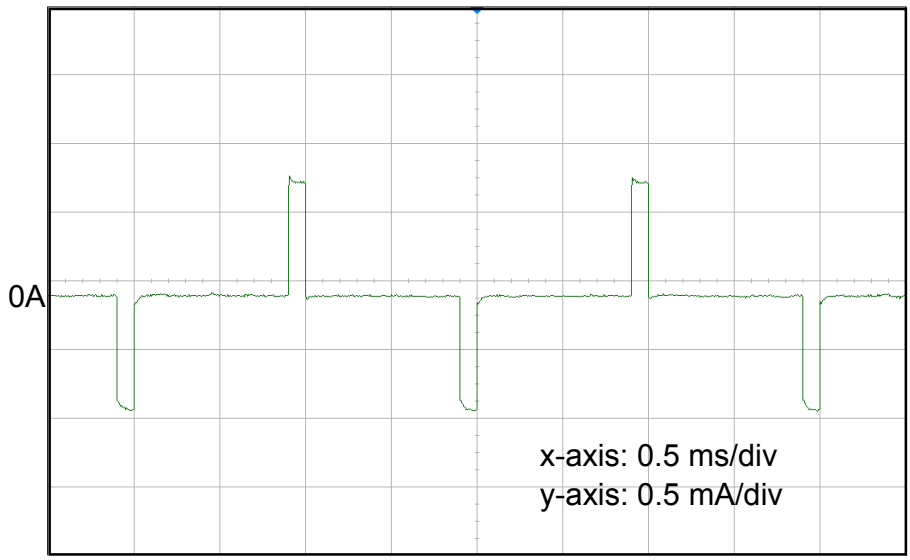


**Figure 5.32:** Functional operation of the chip. Oscilloscope snapshot of biphasic square current pulses.

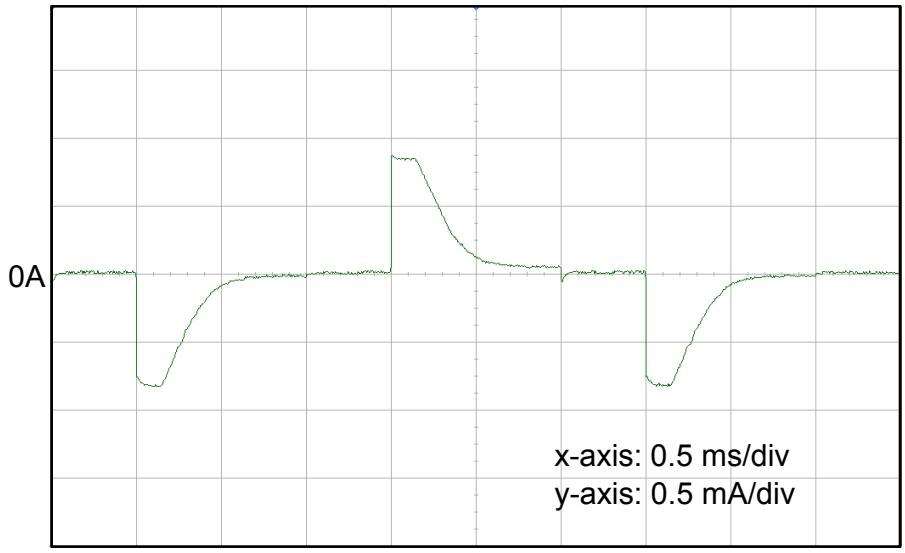


**Figure 5.33:** Functional operation of the chip. Oscilloscope snapshot of biphasic exponential current pulses.

Figure 5.33 shows the measured output current when $S_{ota}$ was set to '00100'. The generation of different exponential decays was assessed by measuring the output current as $S_{OTA}$ was switched to different states and is shown in Figure 5.34. In order to obtain the plots in the figure the pulse width, $W$, and period, $T$, of the control signal, $P$, was varied to accommodate longer pulse decays. The values are

**Table 5.19:** Comparison between measured, simulated and target exponential decays

| $\tau$ (ideal) (s) | Simulated $\tau$ (s) | Measured $\tau$ (s) |
|---|---|---|
| $1\mu$ | $0.89\mu$ | $1\mu$ |
| $10\mu$ | $8\mu$ | $15\mu$ |
| $100\mu$ | $75.7\mu$ | $160\mu$ |
| 1m | $739\mu$ | 1.8m |
| 10m | 7.39m | 28m |

reported in the figure.

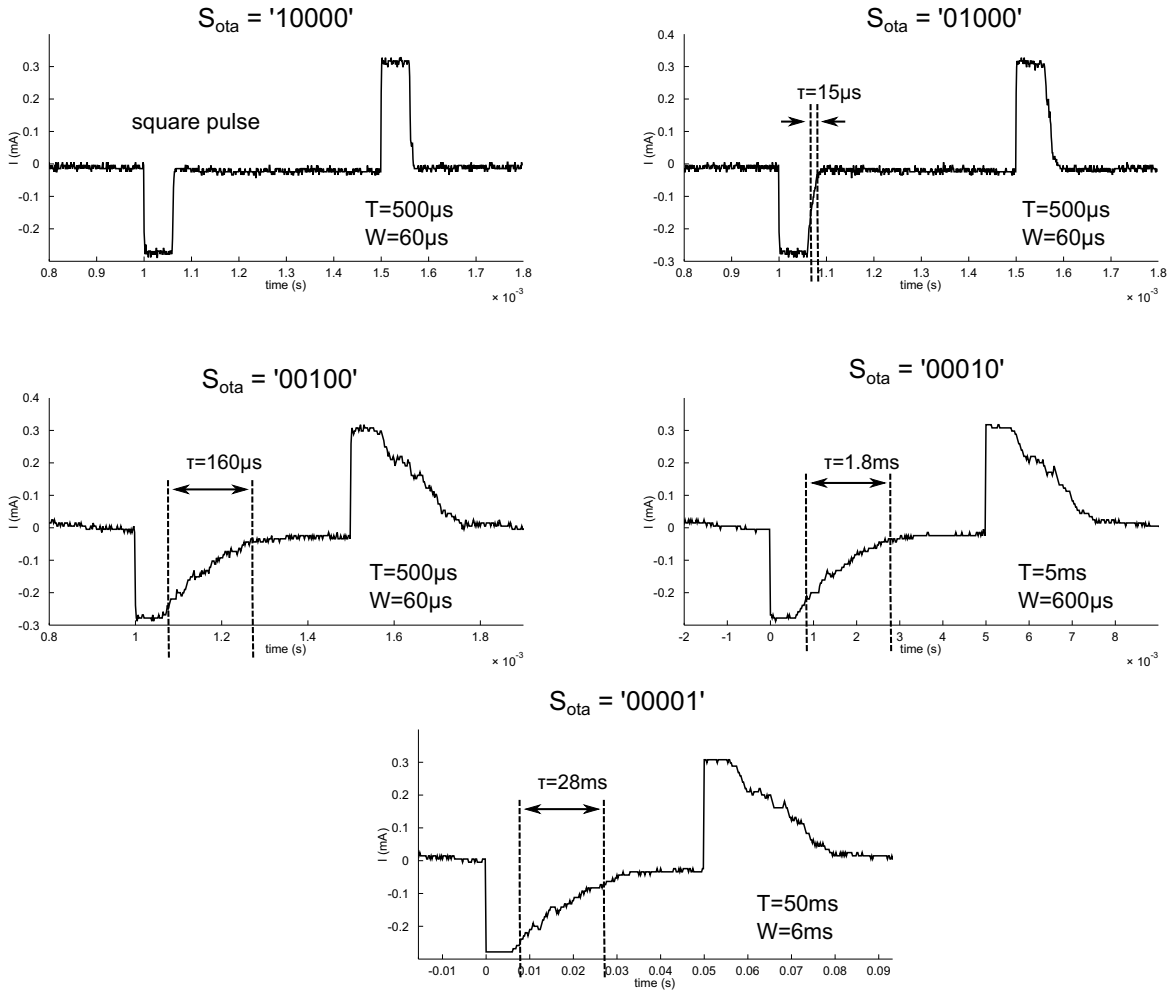


**Figure 5.34:** Measured output current with different exponential decays

The exponential decays values were estimated using the measurement feature of the oscilloscope and are reported and are reported in Figure 5.34. Comparison between the target, simulated and measured values of exponential decays is summarised in Table 5.19.

#### 5.4.1.2 DC Analysis

The DC performance of the chip was assessed in terms of output current linearity and mismatch between anodic and cathodic current and DC offset. The linearity of the output current was firstly measured by fixing the multibias input code, $D$, to different values and varying the 4-bit DAC code, $B$, between logic '0000' and '1111'. Subsequently the 4-bit DAC was fixed to different values and the output current was measured at different levels of the multibias DAC code, $D$.

**A. Linearity of the 4-bit input DAC**

The linearity of the current source was measured by changing the input DAC code, $B$ (which sets the input voltage to the VIC) for different values of the multibias DAC code, $D$, (which determines the current ratio parameter $\alpha$). Figure 5.35(a) shows the ideal and measured output current amplitudes when D is set to logic '0000'. D='0000' sets the multibias DAC off ($\alpha$=0) and the output current is defined solely by the current, $I_{base}$, flowing through the output transistor, $M_1$, of the VIC (see Figure 5.7). The non-linearity of the output current was measured as the deviation of the amplitude of measured output current step from the ideal current step of 32$\mu$A, associated to a 1-bit change of the DAC code[6]. The non-linearity when D is set to '0000' trace is shown in Figure 5.35(b).

D='1111' sets the multibias DAC fully on (ie. the current ratio parameter $\alpha$=1), and the output current is the sum of the output current of the multibias DAC, $I\alpha$, and the output current of the VIC, $I_{base}$ (see Figure 5.7). The ideal output current step associated to a 1-bit change is 92$\mu$A. Figure 5.35(c) shows the ideal and measured output current amplitudes. The non-linearity when D is set to '1111' trace is shown in Figure 5.35(d). Table 5.20 and 5.21 list the measured output versus ideal current range and the maximum DNL and INL, when the multibias DAC is off (D='0000')

[6]Recall that $I_{base}$ varies between 0 and 480$\mu$A in steps of 32$\mu$A as the voltage across $M_1$ varies between 0 and 150mV in steps of 10mV

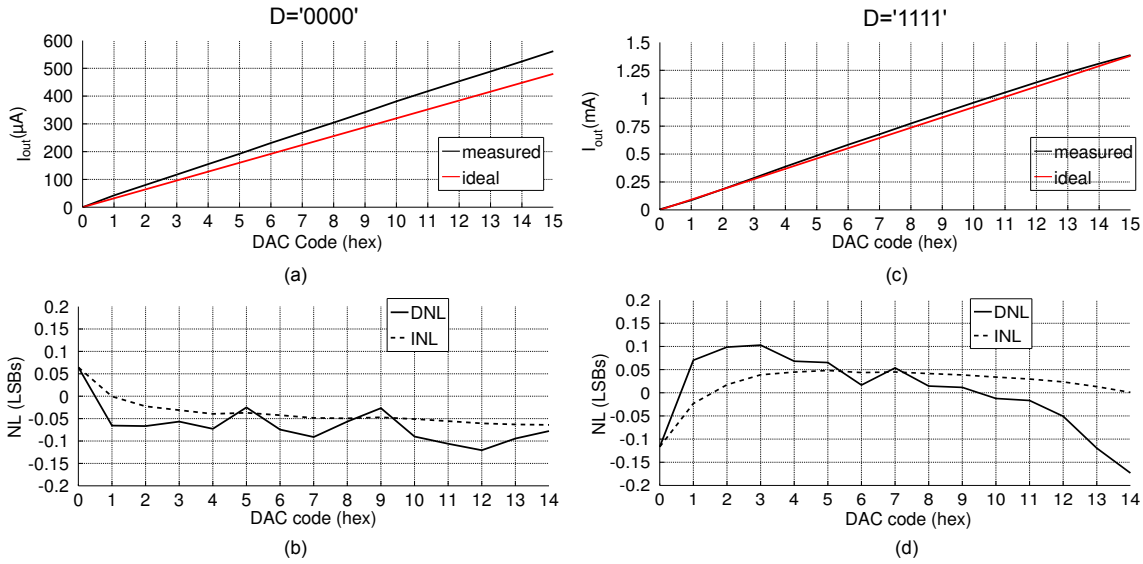


**Figure 5.35:** Measured DC current amplitudes and non-linearity versus the 4-bit DAC code ($B$) for different settings of the multibias DAC code, $D$.

**Table 5.20:** Measured and ideal output current ranges for different settings of the multibias DAC code, $D$

| D | Measured $I_{OUT}$ (A) | Ideal $I_{OUT}$ (A) |
|---|---|---|
| 0000 | 42$\mu$-561$\mu$ | 32$\mu$-480$\mu$ |
| 1111 | 81$\mu$-1.38m | 92$\mu$-1.38m |

or on (D='1111').

### B. Linearity of multibias DAC

The impact of the multibias DAC on the linearity of the output current was measured at different levels of $B$. Figure 5.36 shows the amplitude of the output current versus $D$ when the 4-bit DAC code, $B$ is set to '0001', '1000' and '1111'.

The measured and ideal output current ranges are summarised in Table 5.22.

### C. Anodic and cathodic current mismatch

The mismatch of the output currents during the cathodic phase, $\phi_1$, and anodic phase, $\phi_2$, was measured from the cathode of one chip, when the multibias DAC was off (D='0000') and fully on (D='1111'). The results are shown in Figure 5.37. To measure the DC output current during the cathodic phase, the input clocks $C$, $S$,

**Table 5.21:** Measured maximum INL and DNL for different settings of the multibias DAC code, $D$

| D | Measured $DNL_{max}$ (LSBs) | Measured $INL_{max}$ (LSBs) |
|---|---|---|
| 0000 | 0.0644 | 0.0644 |
| 1111 | 0.103 | 0.0481 |

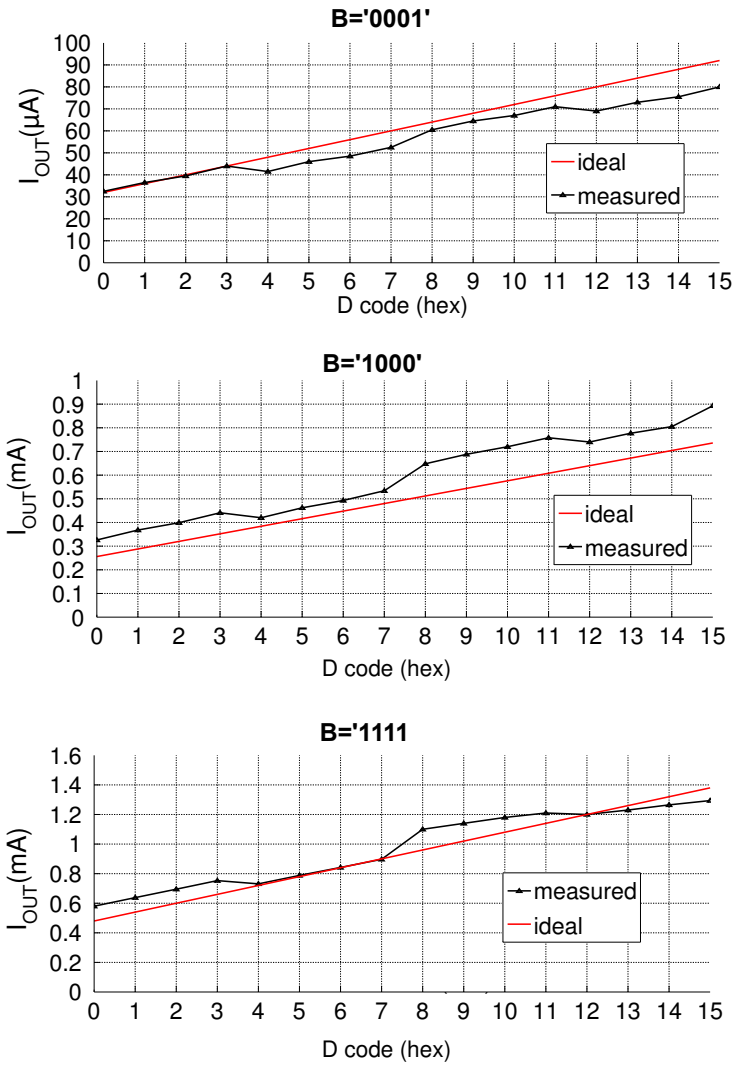


**Figure 5.36:** Measured output current amplitudes versus $D$ for different settings of the 4-bit DAC code, $B$

and $S1$ were set to DC values of 5 V, 12 V and 0 V, respectively. To measure the output current during the anodic phase $S$ and $S1$ were inverted.

The output current sank during the cathodic phase is consistently larger than the output current sourced during the anodic phase. When the multibias is off, the average mismatch was measured to be approximately 4$\mu$A, whereas when the multibias

**Table 5.22:** Measured and ideal output current ranges for different settings of the 4-bit DAC code, $B$

| B | Measured $I_{OUT}$ (A) | Ideal $I_{OUT}$ (A) |
|---|---|---|
| 0001 | 32.5$\mu$-80$\mu$ | 36$\mu$-92$\mu$ |
| 1000 | 326$\mu$-893$\mu$ | 288$\mu$-736$\mu$ |
| 1111 | 580$\mu$-1.29$m$ | 480$\mu$-1.38$m$ |

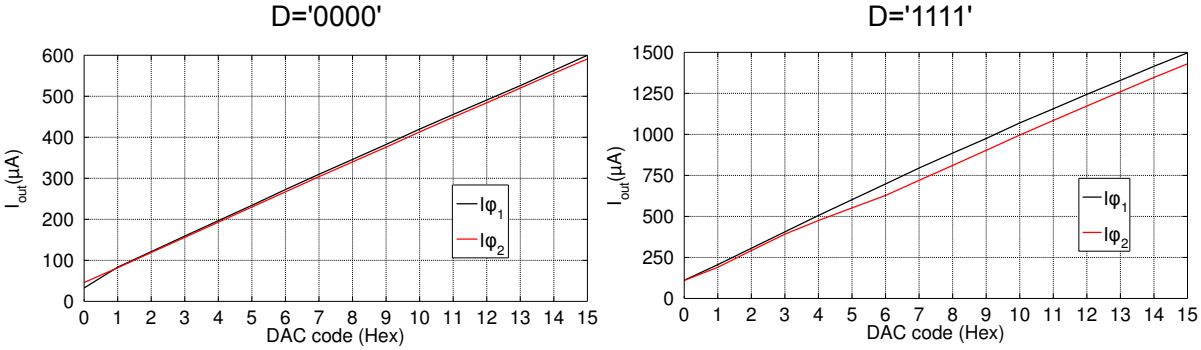


**Figure 5.37:** Measured mismatch between output currents during cathodic, $I_{CAT}$ and anodic $I_{AN}$ phases of the biphasic pulse.

DAC was fully on, the average mismatch was approximately 52$\mu$A. A summary of the chip performance is given in Table 5.23.

**Table 5.23:** Summary of Chip Performance

| | |
|---|---|
| Fabrication Technology | AMS 0.35$\mu$m CMOS (4M, 2P) |
| Number of Channels | 3 |
| Available full-scale current at cathode | 1.851mA |
| Available full-scale current at anode ($\alpha$=0) | 561$\mu$A |
| Available full-scale current at anode ($\alpha$=1) | 1.29mA |
| Anodic/Cathodic Matching (at 1.86 mA) | 2.7% |
| Range of integrated resistance | 89k$\Omega$ - 739.6M$\Omega$ |
| Supply Voltages | 12V, 5V, $\pm$1.5V |
| Chip area (including pads) | 6.21mm$^2$ |
| Static current consumption (at 1.86 mA) | 3.76mA |

## 5.4.2 System Verification - Tank Experiments

Additional set of experiments looked into mapping the electric potential distribution around the electrode, by injecting imbalanced tripolar currents. As schematic representation of the experimental setup is illustrated in Figure 5.38(a).

The chip was mounted on a printed circuit board (PCB), which was equipped with

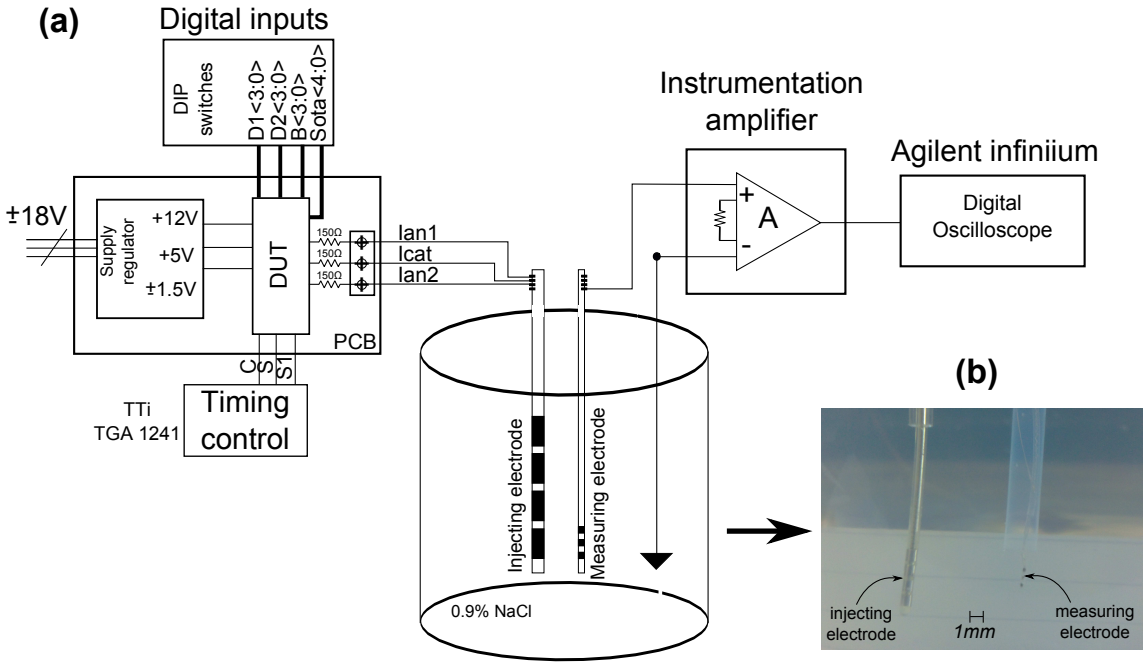


**Figure 5.38:** Experimental setup for wet experiments.

voltage regulator, for all the chip supplies, and a set of DIP switches to generate the digital controls. A 5-cm-radius plastic container was filled with a saline solution (0.9%NaCl), representing the conductivity of brain tissue (0.2S/m). Three contacts on a DBS electrode were driven by the tripolar current source. A 3-contact microelectrode was used to measure the potential at different locations around the electrode. A detailed picture of the injecting and measuring electrode is shown in Figure 5.38(b). The recording electrode was connected to a set of instrumentation amplifiers (INA121, TI, USA) followed by operational amplifiers providing a gain of 10.

A picture of the laboratory setup used for the experiments is reported in Figure 5.39. In order to map the electric potential generated by tripolar current sources, the measuring electrode was placed in parallel to the injecting electrode and shifted along the axial distance of the electrode. A 1mA current square pulse was injected in the saline and the peak-to-peak voltages of the resulting voltage pulses, were measured at a total of 9 discrete locations[7] for values of the current ratio parameter

[7]The measurements were taken along a line parallel to the injecting electrode at a distance of approximately 5mm and at axial distances of -6mm, -4.5mm, -3mm, -1.5mm, 0, 1.5mm, 3mm,

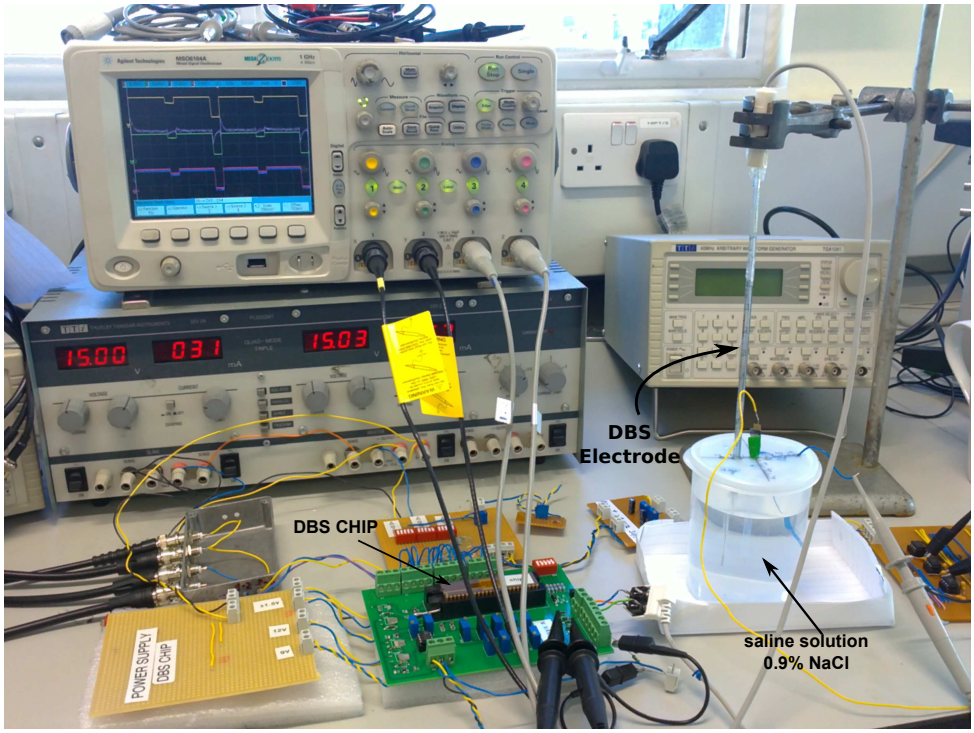


**Figure 5.39:** Picture of laboratory experimental setup for wet experiments.

$\alpha$ between 0 and 1, with steps of 0.1. This resulted in 99 measurements reported in Table 5.24.

**Table 5.24:** Measured peak-to-peak voltages in saline tank for different values of input current ratio $\alpha$

| $\alpha$ | $V_1$ (mV) | $V_2$ (mV) | $V_3$ (mV) | $V_4$ (mV) | $V_5$ (mV) | $V_6$ (mV) | $V_7$ (mV) | $V_8$ (mV) | $V_9$ (mV) |
|---|---|---|---|---|---|---|---|---|---|
| 0 | 72 | 90 | 121 | 190 | 270 | -300 | -150 | -115 | -88 |
| 0.1 | 69 | 78 | 104 | 164 | 268 | -252 | -137 | -105 | -81 |
| 0.2 | 69 | 73 | 83 | 132 | 264 | -205 | -119 | -92 | -69 |
| 0.3 | 60 | 65 | 71 | 92 | 256 | -158 | -90 | -71 | -57 |
| 0.4 | 58 | 61 | 67 | 60 | 255 | -110 | -69 | -60 | -49 |
| 0.5 | -60 | -63 | -71 | -66 | 244 | -78 | -51 | -47 | -40 |
| 0.6 | -63 | -72 | -86 | -105 | 246 | 70 | 40 | 37 | 34 |
| 0.7 | -67 | -79 | -98 | -146 | 249 | 113 | 52 | 47 | 43 |
| 0.8 | -80 | -99 | -125 | -194 | 250 | 160 | 76 | 65 | 54 |
| 0.9 | -92 | -112 | -150 | -235 | 260 | 209 | 99 | 81 | 68 |
| 1 | -106 | -130 | -171 | -286 | 270 | 267 | 122 | 103 | 82 |

These values were interpolated in order to obtain the voltage profiles in Figure 5.40. As the current ratio parameter $\alpha$ is varied between 0 and 1, the profiles of the

4.5mm and 6mm with respect to the midpoint of the injecting electrode.

voltage change and the field spread shifts along the axial distance of the electrode. The smallest field spread was measure to be approximately 3mm when $\alpha$=0.5. When $\alpha$=0 and 1 the peak of the electric potential shifts of approximately 1mm towards the apical or the basal anode and the field spread is larger than 5mm.

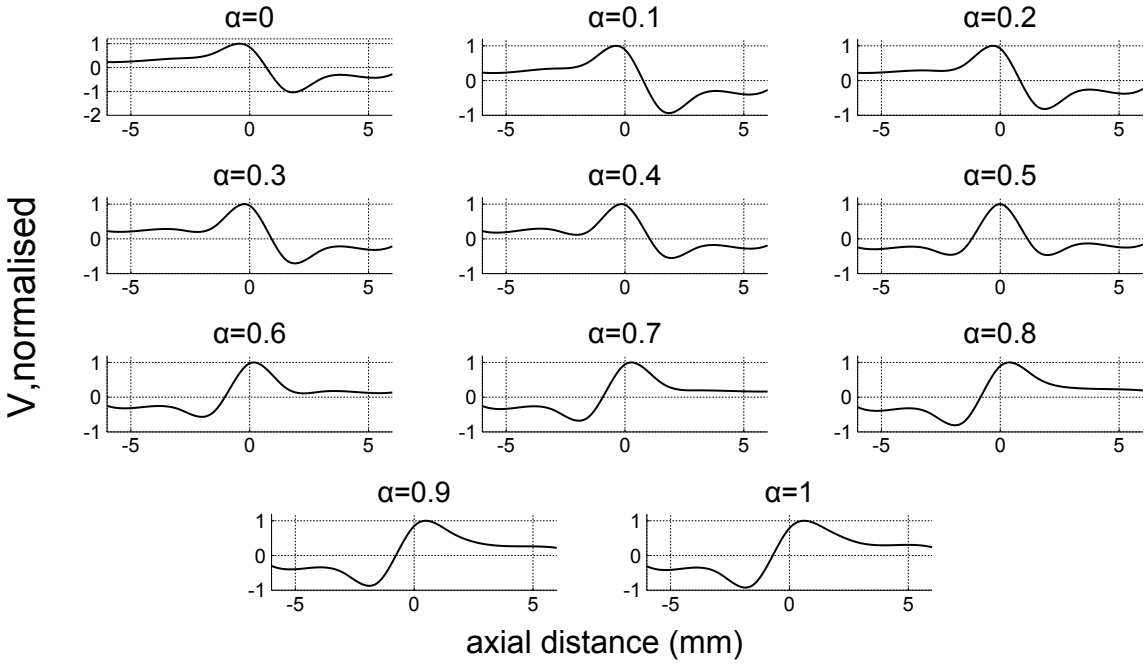


**Figure 5.40:** Profiles of measured voltage distribution is saline as $\alpha$ is varied between 0 and 1.

From the data reported in Table 5.24 we can also extract the excursions of the maxima of the potential distribution at each measurement point ($V_1$-$V_9$) as $\alpha$ is varied between 0 and 1. These are shown in Figure 5.41

We can observe that at a measurement location corresponding to the midpoint of the injecting electrode (measurement $V_5$), the peak of the electric potential varies of approximately 6mV as $\alpha$ varies between 0 and 1. For measurements adjacent to the electrode midpoint (eg. $V_4$ and $V_6$), as $\alpha$ approaches 0 or 1, the peak of the potential changes its polarity with excursions larger than 400mV.

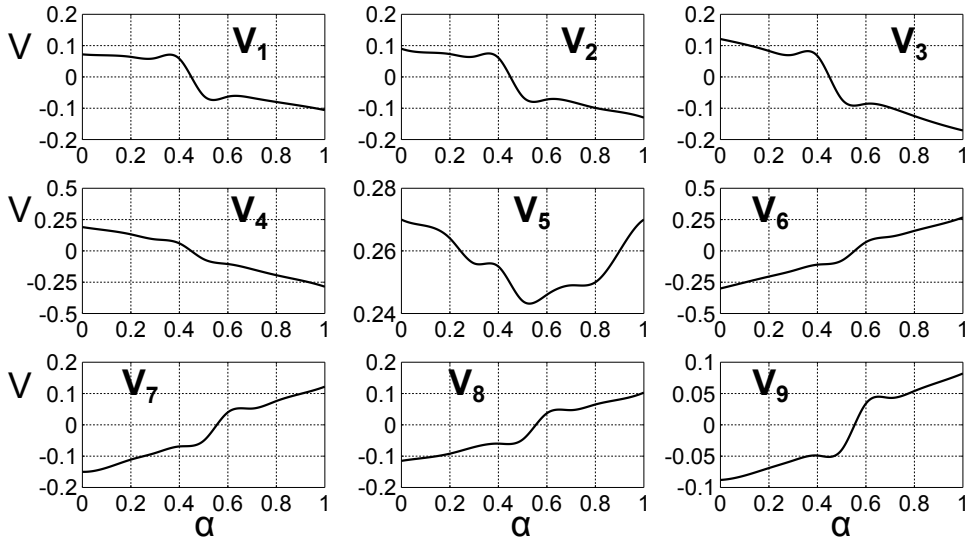


**Figure 5.41:** Voltage excursions with $\alpha$ at the 9 measurement locations.

## 5.5 Discussion

This chapter has reported the implementation in AMS 0.35$\mu$m CMOS technology of a novel architecture of the output stage circuit of a tripolar stimulator. The circuit consisted of four equal high output impedance current sources capable to generate exponential current pulses with variable time constants and control the ratio between the currents flowing through the anodes, while keeping a constant cathodic current.

The basic structure of the current source comprised of a voltage-to-current converter (VIC) [109], to achieve high output impedance and allow for larger voltage compliance than using a cascode current mirror. This topology was chosen since it provided a fairly simple implementation of an active current mirror. The input voltage of the VIC was determined by a standard 4-bit current-steering DAC [112] and its simulated behaviour showed excellent linearity for voltage level up to 150mV (See Figure 5.11).

The ratio of the anodic currents, $\alpha$, was determined by a 4-bit multibias DAC [95] that only used four transistors, instead of 15 used by a standard 4-bit DAC, for each current source. In their proposed circuit, DeMarco and colleagues [95], biased the

transistors in the saturation region, where the $I_D$-$V_{GS}$ curve has an exponential behaviour. In the circuit proposed in this thesis, the transistors of the multibias DAC were biased in the triode region, where the $I_D$-$V_{GS}$ curve is logarithmic and therefore a small variation of $V_{GS}$ has a much smaller impact on the value of the output current than in saturation region. In addition, maintaining all the transistors in the triode region, allows to keep the output voltage compliance very large. Two issues arose from the design and the simulation of the multibias DAC. Firstly, the selection of the voltage levels to obtain the desired current, depends on the behaviour of the $I_D$-$V_{GS}$ curves for different values of $V_{DS}$ (see Figure 5.12). Given the logarithmic nature of these curves, selection of bias voltages too close to the threshold voltage, will decrease the output linearity of the $I_D$-$V_{DS}$ curve. However, selection of bias voltages much larger than the threshold voltage won't allow to accommodate all four bias voltages on the same curves for one W/L ratio, but it may be necessary to scale up some of the transistors to achieve the correct current ratios ($I$, $2I$, $4I$ and $8I$), which in turn will increase the number of transistors. The linearity of the multibias DAC tends to deteriorate for larger values of $V_{ref}$ (the drain-source voltage across the transistors in Figure 5.12 ), since large $V_{ref}$ will push the transistors away from the deep triode region (where the MOS works as a small-signal resistor) into the linear region where the $I_D$-$V_{DS}$ curve is no longer a straight line. These two sources of non-linearity affected the behaviour of the multibias DAC as reported in Figure 5.13. Some linearisation techniques may be implemented in the design, such as the one reported in [119] involving the use of additional transistors to generate current patterns that would sum to the output current and adjust for its nonlinear behaviour.

The design involved the generation of time constants to provide exponential decays. Exponential pulses are essential to suppress the stimulation of neural elements in the vicinity of the anodes [84]. The use of exponential pulses in the field of DBS, however, has not been investigated. For this reason, the selection of the values of the

time constant was based on time constants used in FES applications [89, 120], and the circuit, therefore, included a range of time constants of five orders of magnitude up to 10ms. The use of a current divider [117] to bias a balanced OTA was a successful strategy to obtain a linear range of resistances by changing only the settings of a 5-bit switch. The operation in the subthreshold region allowed the derivation of very large resistances (approximately 800MΩ) with fairly low power consumption.
The use of an output current mirror to switch between anodic and cathodic current was selected as a simple implementation to generate biphasic pulses. However, the matching between the anodic and cathodic currents is highly dependent on the current mirror matching. In order to implement biphasic pulses in a tripolar current source configuration, other techniques can be explored, including the adoption of a complementary structure of the VIC [96]. The addition of a passive-discharge phase can ensure complete removal of the net charge after each stimulation cycle [102].
Measured results showed the capability of the chip to generate exponential biphasic current pulses. The overall performance of the chip showed fairly good linearity and small deviation of the output current ranges from the ideal ones. However, more accurate layout techniques can further improve the performance in terms of accuracy and linearity, offset reduction and minimisation of current mismatches.
The chip was tested in a realistic environment, involving the use of a saline-filled tank, representing the fluid surrounding the target region of DBS. Square current pulses were injected in the saline through a 4-contact DBS electrode and voltage waveforms were measured at different locations in the tank. The peak amplitudes of the voltage were measured in order to map the potential distribution within the tank as we varied the current ratio parameter $\alpha$, to steer the injected current towards the apical or the basal anode. Results have shown how current-steering produces a shifting of the potential distribution along the axial distance of the electrode as presented by the model results in Chapter 4. The measurement involved only 9 recordings at 9 locations for each value of $\alpha$. A more accurate method would require a larger

number of measuring sites to better represent the profile of the voltage distribution.

## 5.6 Conclusion

This chapter has presented the full implementation of a current-steering tripolar stimulator output stage. From the analysis of the results of the performance of each block and the overall system we can conclude that:

(a) A current-steering tripolar stimulator output stage can be implemented by four equivalent current sources, two of which sourcing/sinking a current $I\alpha$ and the other two sourcing/sinking a current $I(1-\alpha)$. The design of one current source can therefore be replicated to implement the other current sources.

(b) The design presented in this chapter can provide a benchmark for the design of multipolar current-steering stimulator output stages, involving the use of two or more cathodes and two lateral anodes, based on the configurations presented in Chapter 4.

(c) Subthreshold design techniques can be exploited to generate large time constants on chip, and vary the value of the time constant over several decades while maintaining linearity.

(d) The use of a current-steering stimulator can effectively shape the electric potential distribution around the electrode, therefore providing a degree of control over the stimulating field.

# 6

# Application of Phased Array for Field Steering in DBS

So far this thesis has explored a technique aimed at improving stimulation selectivity in DBS by increasing the number of electrode contacts active during stimulation. The fields generated by excitation of the contacts interact with other and shape the distribution of the field around the electrode. By dynamically varying the current intensity driving each contact, the field can also be shifted along the electrode axis. This approach was investigated at DBS frequencies, where the fields are governed by a quasi-static approximation. In terms of field steering, a significant improvement could be introduced by the use of high frequency (electromagnetic, EM) fields.

Phased arrays (PAs) are one example of antenna elements that allow to form an energy beam and steer it to a desired direction by varying the phase between the excitations of each element. Over the past decades PAs have been extensively applied to the field of hyperthermia as an effective treatment of cancer [20, 21, 22]. Antenna arrays are used to provide selective heating at the location of the tumor by controlling the phase and amplitude of the antenna excitation. This is typically based on narrowband sinusoidal pulses [22] or ultrawide pulses [21]. Due to the frequency-dependent behaviour of the tissue properties, the focal point and the depth of penetration of the electromagnetic (EM) field varies according to the excitation frequency and the targeted tissue [121].

Phased arrays have found applications also in the field of medical imaging [19, 122, 123].

To date the adoption of phased array systems for focused and steerable stimulation has not been investigated. Literature is scarce in defining the interactions between radiation and tissue. Evidence has been collected supporting the use of infrared energy, which represents a form of electromagnetic radiation, to provide stimulation in a similar fashion as with electrical energy [124]. This technique has also been recently applied to DBS [125, 126]. The mechanisms of stimulation provided by infrared radiation are not yet fully understood, although experimental studies so far describe the interaction between light and neural activation as due to a thermal effect, where heat activates heat-sensitive channels in the membrane [127].

This chapter will provide a theoretical study on the application of PA to DBS. This study is based on basic models that look into the frequency-dependent properties of brain and the behaviour of electromagnetic waves in brain tissue. We will look at the generation and steering of propagating wavefronts by using a 4-contact EM source. Although the design of the antenna elements is a crucial factor for the development of phase array systems, the analysis reported in this chapter is limited to the evaluation of the behaviour of an array with geometry equal to that of a

clinical DBS electrode.

## 6.1 Time Harmonic Fields and Wave Equation

In Chapter 4 we have considered static or quasi static conditions where the electric and magnetic fields and their sources, the charge density and the current density, were not a function of time. In the time-varying case, these quantities are a function of the spatial coordinates $(x, y, z)$ and time. Time-varying fields are usually represented as sinusoidal functions with an angular frequency, $\omega$. In such case they can be represented as a phasor[1], only dependent on $(x, y, z)$, as:

$$\mathbf{E}(x, y, z, t) = \Re\left[\tilde{\mathbf{E}}(x, y, z)e^{j\omega t}\right] \tag{6.1}$$

For a linear isotropic and homogeneous medium characterised by a permittivity, $\varepsilon$, conductivity, $\sigma$, charge density, $\rho_v$, and permeability, $\mu$, Maxwell's equations in the phasor domain are given by:

$$\nabla \cdot \tilde{\mathbf{E}} = \tilde{\rho_v}/\varepsilon \tag{6.2}$$

$$\nabla \times \tilde{\mathbf{E}} = -j\omega\mu\tilde{\mathbf{H}} \tag{6.3}$$

$$\nabla \cdot \tilde{\mathbf{H}} = 0 \tag{6.4}$$

$$\nabla \times \tilde{\mathbf{H}} = \tilde{\mathbf{J}} + j\omega\varepsilon\tilde{\mathbf{E}} \tag{6.5}$$

In the medium the current density $\mathbf{J}$ is related to the electric field $\mathbf{E}$, by $\mathbf{J} = \sigma\mathbf{E}$ and:

[1] A phasor is a time-invariant representation of a complex number $a+jb$ as a complex exponential $|z|e^{j\phi}$, where $|z|$ is the modulus and $\phi$ is the phase of the complex number.

$$\nabla \times \tilde{\mathbf{H}} = \tilde{\mathbf{J}} + j\omega\varepsilon\tilde{\mathbf{E}} \tag{6.6}$$

$$= (\sigma + j\omega\varepsilon)\tilde{\mathbf{E}} \tag{6.7}$$

where $(\sigma + j\omega\varepsilon)$ represents the complex permittivity, $\varepsilon_c(\omega)$. From the expression relating the electric and magnetic fields, the propagation of the electric field in a charge free medium can be derived and it is expressed as [128]:

$$\nabla^2\tilde{\mathbf{E}} + k^2\tilde{\mathbf{E}} = 0 \tag{6.8}$$

where $k$ represents the propagation wavenumber and it is a function of the properties of the medium: $k = \omega\sqrt{\mu\varepsilon}$.

## 6.2 Electromagnetic Fields in Brain Tissue

In Section 2.3 of Chapter 2, we have discussed the electric properties of brain tissue and the behaviour of electric fields in excitable tissue. In this section we will analyse the behaviour of electromagnetic fields in brain tissue.

### 6.2.1 Time-harmonic Fields in Brain Tissue

Brain behaves as a lossy dielectric (or poor conductor), therefore acting on the EM waves by imposing attenuation during their propagation. If we assume brain tissue to behave as an isotropic, homogeneous medium, then the propagation of time-harmonic waves is governed by the Helmholtz equation [129]:

$$\nabla^2\tilde{\mathbf{E}}_s - \gamma^2\tilde{\mathbf{E}}_s = 0 \tag{6.9}$$

where $\tilde{\mathbf{E}}_s$ represents the time-harmonic wave in phasor form, or $\tilde{\mathbf{E}}_s = \Re[e^{j\omega t}]$, and $\gamma$

is a complex quantity representing the propagation constant of the medium, given by:

$$\gamma^2 = j\omega\mu(\sigma + j\omega\varepsilon) \tag{6.10}$$

If we define $\gamma = \alpha + j\beta$, then we can obtain:

$$\alpha = \omega\sqrt{\frac{\mu\varepsilon}{2}\left[\sqrt{1+\left[\frac{\sigma}{\omega\varepsilon}\right]^2}-1\right]} \tag{6.11}$$

$$\beta = \omega\sqrt{\frac{\mu\varepsilon}{2}\left[\sqrt{1+\left[\frac{\sigma}{\omega\varepsilon}\right]^2}+1\right]} \tag{6.12}$$

where $\alpha$ represents the attenuation and $\beta$ is the phase constant of the medium. From Eq. 2.3 in Section 2.3 of Chapter 2 and using the measured parameter values of dielectrics of Grey matter, reported in [27], we can extract several frequency-dependent parameters, including $\sigma$, $\epsilon$ and $\mu$ that allow us to calculate the attenuation, $\alpha$, the skin depth as $d = 1/\alpha$, representing the distance to which electromagnetic waves penetrate, the propagation velocity, as $v_p = 1/\sqrt{\mu\epsilon}$, and the wavelength, as $\lambda = v_p/f$, where $f$ is the frequency. The velocity of propagation of a wave in tissue is smaller than that is air, since the permittivity of the tissue a larger than that of free space. This results in wavelengths being shorter in tissue than in air, approaching the wavelength in free space as the frequency increases.

Figure 6.1 shows a plot of the attenuation and skin depth for a frequency range between 100 Hz and $10^{14}$ Hz. Figure 6.2 shows a plot of the wavelength, $\lambda$ and propagation velocity $v_p$, for a frequency range between 100 Hz and $10^{14}$ Hz. Table 6.1 reports values for Grey matter dielectric properties at different frequencies.

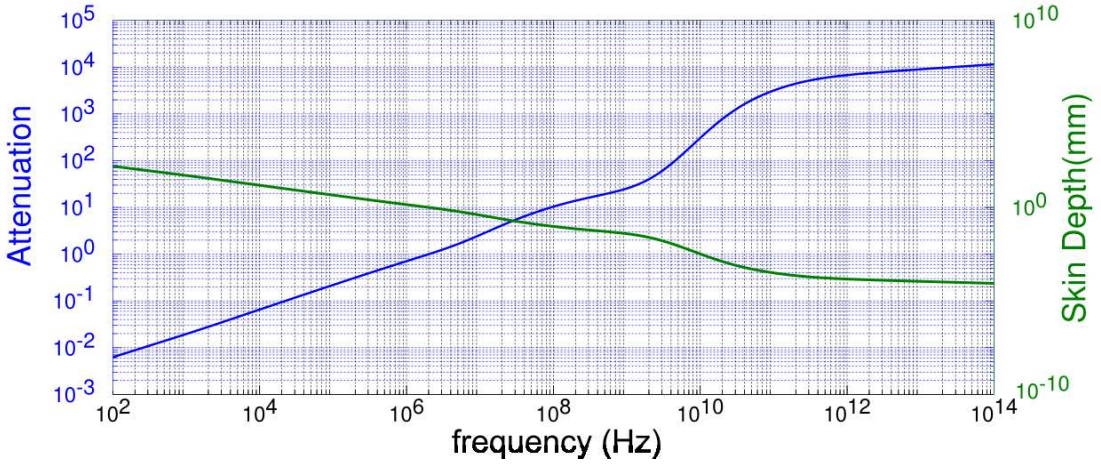


**Figure 6.1:** Attenuation and skin depth versus frequency in grey matter.

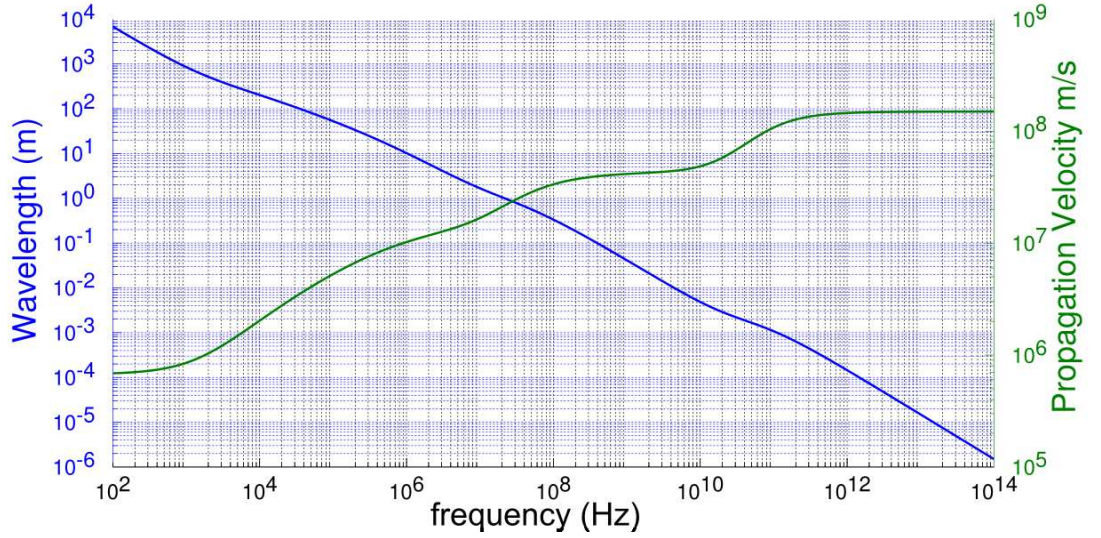


**Figure 6.2:** Wavelength and velocity of propagation of electromagnetic waves in grey matter.

### 6.2.2 FEM Model

FEM models were adopted to model an ideal 4-channel EM source, resembling the geometry 3389 Medtronic DBS electrode, characterised by four contacts, 1.27 mm in diameter, 1.5-mm long and separated by 0.5mm-wide insulating material. The source was placed at the centre of a homogeneous isotropic medium, represented as a circular mesh of radius equal to 50mm (Figure 6.3).

The array was fed with a set of phase-shifted sinusoidal voltage stimuli represented in phasor form as:

**Table 6.1:** Dielectric properties of Grey matter at different frequencies

| f (GHz) | $\sigma$ (S/m) | $\varepsilon_r$ | $\lambda$ (mm) | d (mm) |
|---|---|---|---|---|
| 1 | 0.98 | 52.28 | 40 | 40 |
| 10 | 10.31 | 38.1 | 4 | 3.3 |
| 100 | 53.2 | 7.75 | 0.9 | 0.3 |

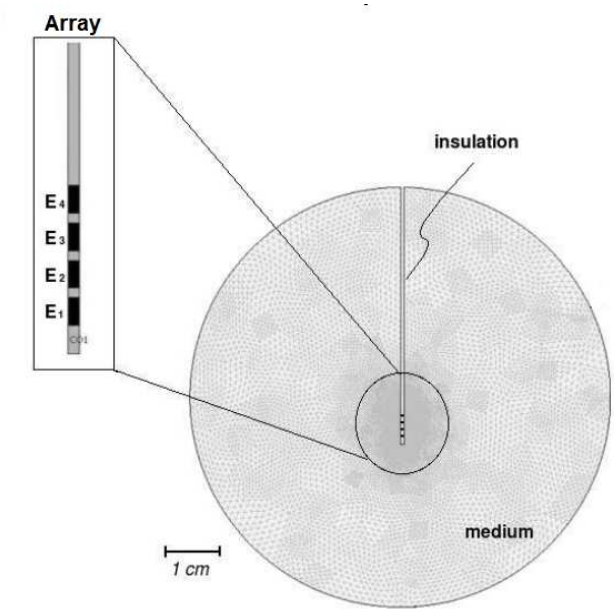


**Figure 6.3:** DBS EM source FEM model. The circular mesh represents the anatomical area surrounding the implant. For ease of computation the electrode contacts were treated as point sources.

$$E_{s,1} = A_0 \tag{6.13}$$

$$E_{s,2} = A_0 e^{\phi} \tag{6.14}$$

$$E_{s,3} = A_0 e^{2\phi} \tag{6.15}$$

$$E_{s,4} = A_0 e^{3\phi} \tag{6.16}$$

where $A_0$ is the wave amplitude and $\phi$ is the incremental phase shift between the stimuli.

## 6.3 Phased Array Fields

The fundamental goal of this study was to investigate the applicability of phased array systems to control and steer the field during DBS.

### 6.3.1 Wavefront Steering

The minimum frequency of operation was set to 1GHz, which corresponded to wavelengths of approximately 40 mm in tissue (see Figure 6.2), therefore lying within the FEM model area. The wave equation was solved for values of phase shifts between $-\pi/2$ and $\pi/2$, at input frequencies between 1 GHz and 10 GHz. Figure 6.4 shows the behaviour of the wavefronts at 5GHz for values of applied phase shifts of 0°, 55° and −55°. The plots in Figure 6.4(a) represent the location and angles of propagation of the wavefronts with respect to the array axis. The plots in Figure 6.4(b) are a detailed view of the distribution of the field around the array. The plots in Figure 6.4(c) illustrate the profiles of the field distribution measured along the array axis. As the phase shift is varied, the location of the stimulating field (shaded area) is steered to a positive or negative angle with respect to the centre of the array.

### 6.3.2 Wave Attenuation

The depth of penetration of the propagating wave is inversely proportional to the frequency of operation, as shown in Figure 6.5 for frequencies of 3GHz, 5GHz and 10GHz.

Depth of penetration was determined as the distance from the source where the amplitude of the wave falls to $e^{-1}$, or about 37%, its maximum value. This occurs at a distance from the array of 16mm at 3GHz, 8.8mm at 5GHz and 3.3mm at 10GHz.

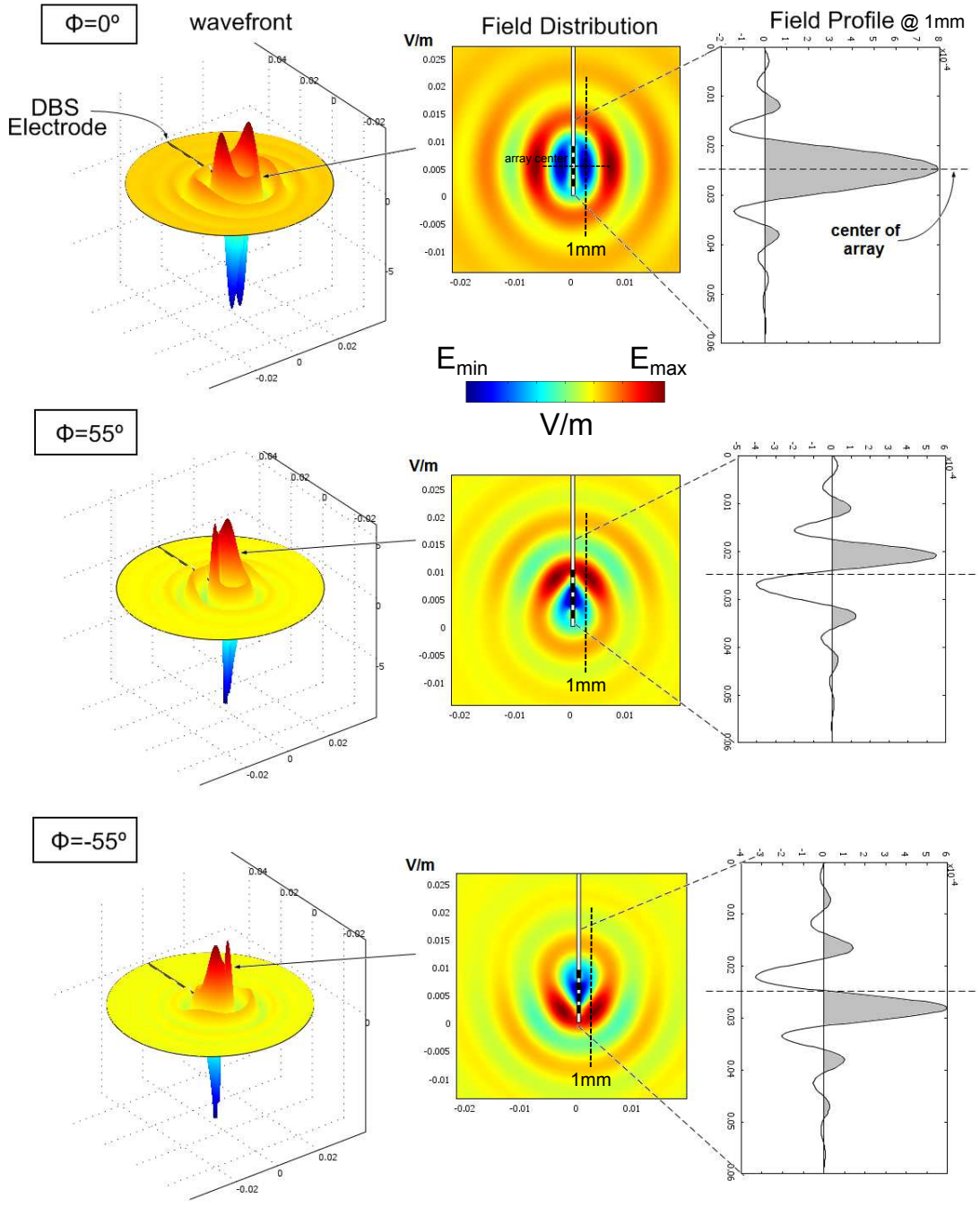


**Figure 6.4:** Wavefront Steering at f=5GHz. (a) 3D view of location of wavefront. (b) detailed view of distribution of field in proximity of the source. (c) profiles of field distributions along the array axis.

### 6.3.3 Wave Profile

The size of the travelling wavefront (ie. the area of stimulation) is also dependent on the frequency of operation. Figure 6.6 shows the profiles of the wavefronts at

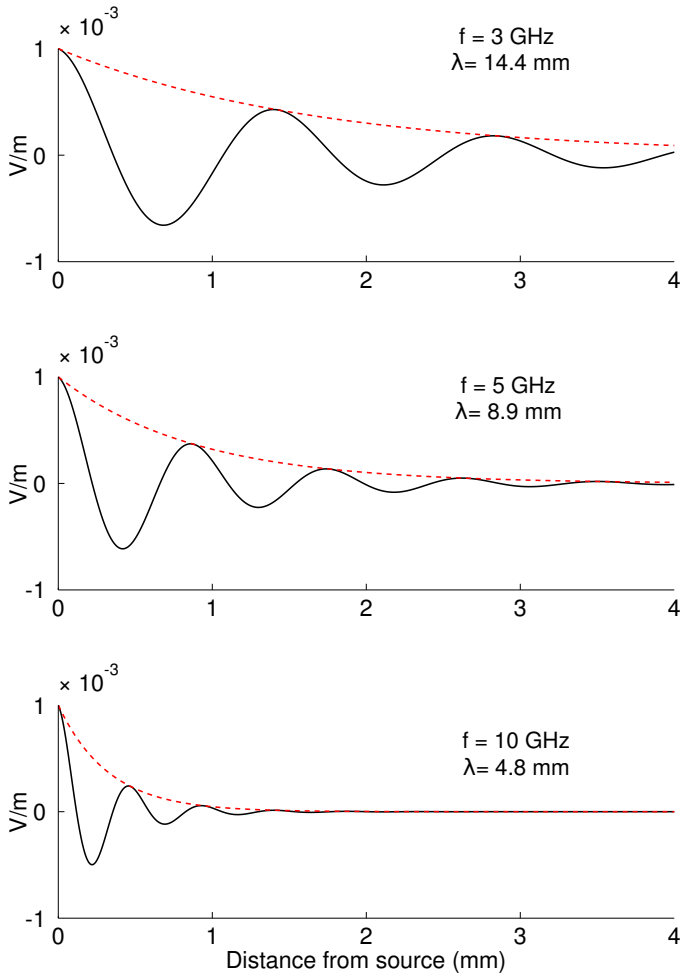


**Figure 6.5:** Attenuation of propagating waves as they travel away from the array axis. The dashed red line represents the attenuation factor described by $e^{-\alpha x}$, where x is the distance from the source. Depth of penetration, calculated as $1/\alpha$, is 16mm at 3GHz, 8.8mm at 5GHz and 3.3mm at 10GHz

3GHz, 5GHz and 10GHz with no phase shift applied.

The measured widths of the wavefront were approximately 22mm at 3GHz, 16mm at 5GHz, reducing to about 12mm at 10GHz.

## 6.4 Discussion

This study represents an analysis of the applicability of phased array systems to deep brain stimulation. The aim of this work was to evaluate the effects of tissue properties on the propagation of EM waves, and the identification of the optimal range of frequencies which would result in the ability to steer the propagating wave-

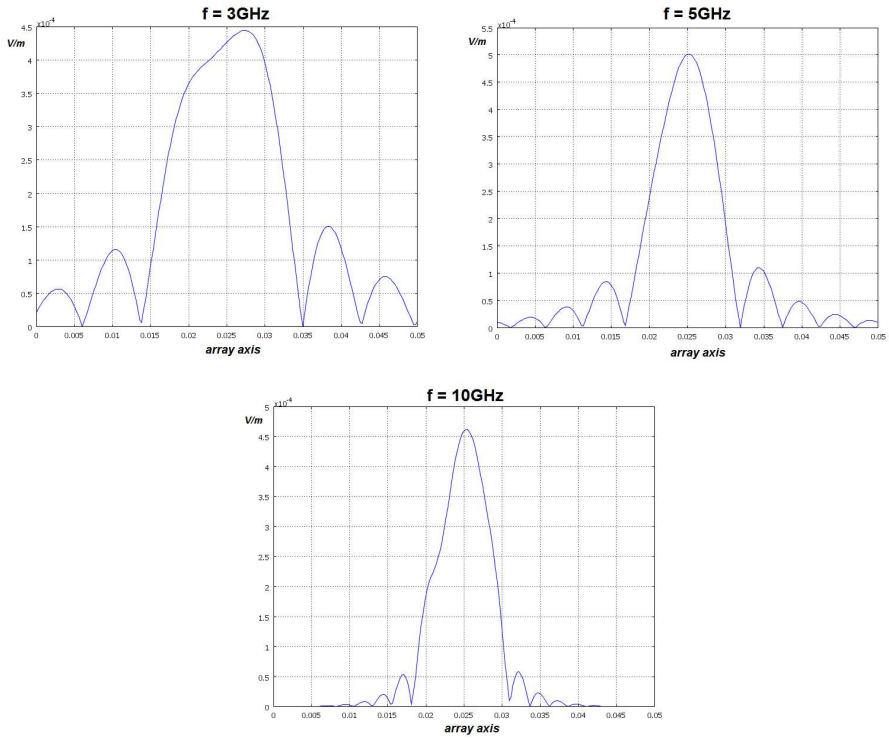


**Figure 6.6:** Profiles of wavefronts generated by the phased array source at 3GHz, 5GHz and 10GHz

front to a desired angle within the anatomical target region for DBS. By adopting standard mathematical models of the dielectric spectrum of tissue we have derived values for the dielectric parameters of Grey matter as a function of frequency. Since field steering needs to happen within millimetres from the array, the minimum frequency of operation was arbitrarily selected to correspond to wavelengths smaller than 50mm, ie. frequencies higher than 1GHz in grey matter as shown in Figure 6.2. Results have shown the ability to control the direction of the wavefront propagation by varying the incremental phase shift between the excitation of the array elements. Additionally, the frequency of operation can be used as a control parameter, to define the area (focus) and depth of penetration of the stimulating field. The ability to steer and focus the field is a major improvement on conventional DBS systems which are characterised by poor stimulation selectivity. Not only would this approach allow to reduce the side effects resulting from the stimulation of non-target areas, but also it would provide a substantial benchmark for more selective and fo-

cused stimulation of different areas of the brain, contributing to the understanding of the brain's mechanisms. This analysis has also highlighted a trade-off emerging between the selection of frequencies and the depth of penetration of the field at those frequencies. Although this work proposes optimal frequencies in the range of GHz, the analysis should be coupled to evidence of the clinical effects of the application of high-frequency fields in brain tissue. The limiting factor of this work is related to the use of the geometry of a standard DBS electrode. The design of a phase array antenna, optimised for operation at the range of frequencies selected was not part of this study, and the array was modelled as an ideal EM source. The design of the antenna needs to take into account the location of the focal point and the depth of penetration at different frequencies and for different tissue targets [121]. Additionally, the design of the antenna should account for power losses associated with the source as well as channel interaction and mutual coupling occurring in the near field region. A better characterisation of the behaviour of EM waves in brain tissue would be provided by the introduction of space-dependent conductivity and permittivity representing different anatomical regions of the brain.

This study represents a potential shift from conventional DBS methods to a technology which would allow substantial control of the stimulation field and high selectivity of stimulation of the anatomical target regions. The major implications related to the adoption of very high frequency techniques, is the use of EM fields (radiation) as opposed to electric fields to provide therapeutic stimulation. Literature is providing promising evidence of the ability of EM fields, such as infrared light, to activate neural responses similar to those generated by electrical stimulation, with the difference that heating of nerve fibres is the main cause of nerve excitation [127, 130, 131]. Recently, optical stimulation is being investigated in the field of DBS [125, 126].

## 6.5 Conclusion

This chapter has reported an alternative approach to DBS, involving the use of phased array antennas, to steer the EM wavefront to a specific location of the target region. This work constitutes preliminary work in the modelling and design of phased array systems for DBS. From this work we can draw a number of conclusions:

(a) The adoption of phased arrays allows to direct the EM field to a specific location within the target areas.

(b) Amplitude and frequency of operation can be used a parameters to vary the intensity and focus of the fields.

(c) The model presented in this chapter is not suitable for optical frequencies (>100 GHz).

(d) PA stimulation represents a substantial technology shift from conventional stimulation techniques.

# 7

# Conclusion

This thesis represents the work undertaken to investigate and propose novel methods to shape the stimulation field in DBS. Specifically, the focus of the work was set on identifying strategies that can ameliorate the stimulation approach in DBS, by allowing to vary the location and focus of stimulation around the implanted electrode. This thesis addresses a number of fundamental limitations of clinical DBS, identified in poor selectivity and limited control over the stimulus delivery. Poor selectivity leads to stimulation of untargeted areas and the rise of stimulation-related adverse events [18]. Control over the spread of current during stimulation is limited to varying the stimulus settings, including amplitude, pulse width and frequency [2]. The limited control over the current spread imposes accurate surgical lead placement for

sub-millimetre targeting [10]. The design of systems that allow to steer the electric field around the electrode after implantation are highly beneficial to maximise the therapeutic effects and minimise adverse events. These considerations drove the motivation behind the work reported in this thesis.

The first approach was based on the use of a current-steering multipolar electrode configuration, where a number of stimulating electrode contacts are dynamically employed to shape the field of stimulation around the electrode. The initial step in the development of this approach lies in the characterisation of the behaviour of multipolar electric fields in brain tissue. This involves the generation of FEM models of a multipolar electrode embedded in models of the brain tissue surrounding the electrode. The complexity of such models varies significantly whether the goal is to obtain an approximate or a more realistic behaviour of stimulation. This part of the work aimed at qualitatively validate the principle of shaping and shifting the electric field along the axial distance of the electrode, by steering the current to different electrode contacts. An approximate model was thought to be sufficient in order to study this behaviour. Therefore the model was limited to homogeneous and isotropic properties, and the electrode contacts to ideal current sources. If a quantitative analysis was required, a model should be developed, which accounted for losses associated to the long cables, the finite output resistance of the current sources and the electrode impedance, and, in addition, for anatomical structures surrounding the electrode. The multipolar electrode was modelled according to the geometry of clinical DBS electrodes. This allowed us to verify how a stimulation approach based on multipolar electrode configurations is readily applicable to existing DBS electrode designs. The results of the model simulations confirmed that the adoption of multipolar electrode configurations with the addition of a current-steering feature, allows to shape the potential distribution around the electrode. In Chapter 4, we have shown that the tripolar case allows for the least field focusing

and shifting, suggesting the electrode configurations with four or more contacts are preferred. The pentapolar case allows for a wide range of field shapes and shifting, and would provide a very flexible tool in a clinical setting, to accurately direct the stimulation current to the target area.

The work in Chapter 4 provided evidence to support the design of a current-steering stimulator output stage for tripolar electrode configurations, characterised by the generation of square and exponential current pulses. The design was limited to a tripolar configuration, although the design aspects presented in Chapter 5 can be adopted for electrode configuration involving four or more contacts. The system architecture was based on standard analogue designs specifically selected from the literature. The system, however, represented a novel design approach, since ASICs for multipolar stimulation in DBS have not yet been realised. The overall performance of the tripolar current source is found to be acceptable in terms of square and exponential current pulse generation and linearity of the transfer characteristic. Issues regarding the mismatch between the stimulation current during the anodic and the cathodic phases, due to mismatches at the output current mirror, should be further investigated by adopting advanced layout techniques that can minimise the mismatches between the two branches of the output current mirror. Among the various design blocks, the multibias DAC biased in the deep triode region represented a novelty from previous designs of multibias DACs usually based on the operation in the saturation region. The adoption of multibias DACs allowed to reduce the overall silicon area, as compared to the use of standard DACs, although the linearity of the DACs needs further improvement. Investigation of the circuit operation in the deep triode region in highly beneficial for biomedical application where low power operation is desirable. An additional novel aspect in the design is the integration of a RC network capable of providing a wide range of possible time constants. The adoption of standard analogue blocks biased in the subthreshold region allowed to

design time constants ranging 5 orders of magnitude and characterised by excellent linearity. Validation of the operation of the tripolar stimulator output stage with a phantom model (saline-filled tank) provided evidence of its capability for field shaping. The design reported in Chapter 5 can, therefore, contribute to future designs of ICs for multipolar DBS.

This thesis has proposed an alternative approach to improve the efficacy of DBS, based on the adoption of PA systems. The results of the models described in Chapter 6 support the idea that PA could be introduced in DBS as a means to steer the stimulation field to a desired location of the brain. Simulation results suggest that frequencies above GHz may be needed to allow to steer the wavefront within millimetre or sub-millimetre targets. The adoption of ideal EM sources can provide an approximate behaviour of PA fields in tissue, although several aspects related to the antenna design, including power, directivity, gain, near-field and far-field behaviour will contribute to more realistic description of PA fields. In addition, further analysis is needed, in order to assess the relation between electromagnetic field and neural clusters and investigate the mechanisms of neural activation.

We can conclude this discussion by summarising the contribution that the work reported in this thesis has brought to the field of DBS:

(a) Models of a DBS system and analysis of the loading effects of a DBS electrode on the stimulus pulse. Estimation of the current injected during DBS is essential for the design of safe DBS systems and the optimisation of DBS parameters, based on more realistic assessment of the VTA during DBS.

(b) Model-based evidence of electric field shaping by the adoption of multipolar electrode configuration with current-steering features. Multipolar electrode configurations can be used to allow dynamic control over the shape and focus of the

stimulation field. The analysis presented in this thesis can serve as a benchmark to develop realistic models of multipolar DBS.

(c) Implementation of a current-steering tripolar stimulator output stage with integrated tunable time constant, able to generate square and exponential current pulses and vary the current ratio between the anodic currents. The design aspects and steps provided in this thesis can be exploited in the development of current-steering multipolar stimulators for DBS.

(d) Introduction to the design of DBS stimulators based on phased array systems. This thesis had provided initial modelling steps and analysis towards the development of PA systems that allow for steerable and focused stimulation fields.

## 7.1 Suggestions for Future Development

In this section we discuss a number of strategies that can be adopted to further develop and improve the work presented in this thesis.

### 7.1.1 Design of Novel DBS Electrodes for Multipolar Stimulation

State-of-the-art Medtronic electrodes are clinically used in monopolar or bipolar mode (1 or 2 active contacts). In Chapter 4 we have seen that the use of multipolar electrode configuration allows to shape the spread of the potential distribution around the electrode and direct it to a specific location. The use of clinical DBS electrodes in multipolar mode, however, represents a limitation due to the large size and distance between the contacts, resulting in field spreads beyond the target area. The design of electrodes with higher contact resolution should be investigated, in order to increase the field shifting capability and stimulation selectivity [132, 133]. Martens and colleagues [133] have recently proposed the use of cylindrical DBS ar-

rays with 64 contacts, which allow a large range of combination and the possibility to adopt asymmetric configurations that allow to change the direction of the stimulating current to a desired location.

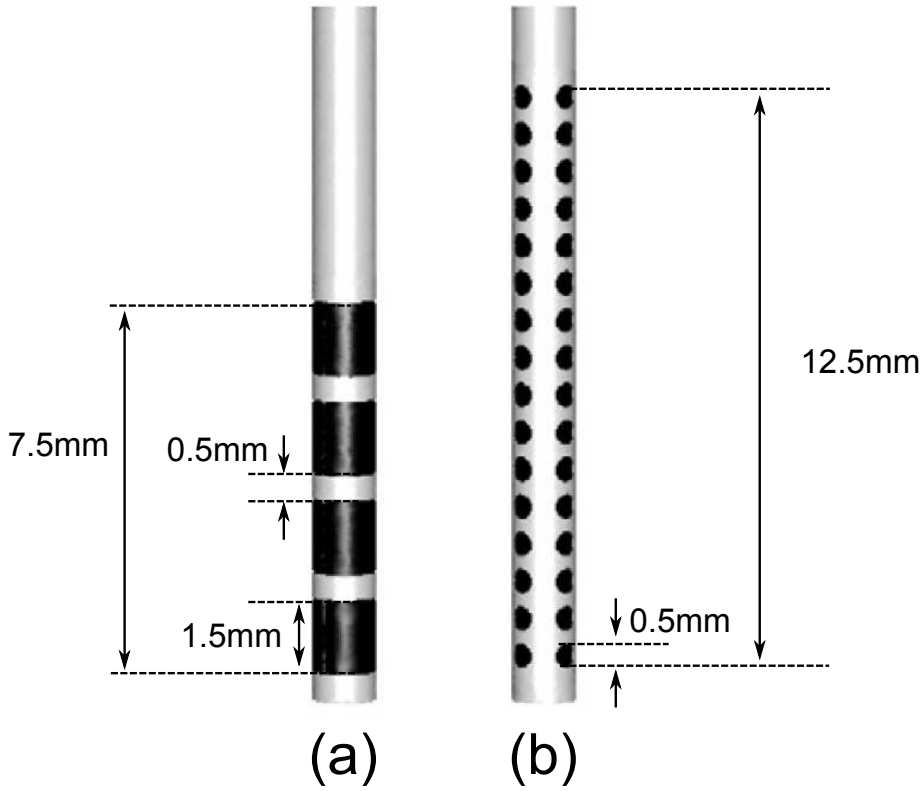


**Figure 7.1:** (a) State-of-the-art DBS electrode (Medtronic, model 3389). (b) Novel DBS electrode array design, consisting of 64 circular contacts [133].

Figure 7.1 shows an illustration of the DBS electrode array as compared to the state-of-the-art DBS electrode, currently used in clinical DBS. The array consists of a higher density of electrode contacts distributed in 16 rows of four contact per row. Simulations of the effects of using a DBS array are shown in Figure 7.2. If, during the surgical intervention, the electrode is displaced with respect to the centre of the anatomical target region, the use of higher density of electrode contact can help compensate for the displacement, by steering the current towards the target region and inhibiting the current spread to adjacent anatomical structures.

Future designs can be based on this approach, where FEM models of electrode arrays and anatomical structures of the target and adjacent regions of the brain are adopted

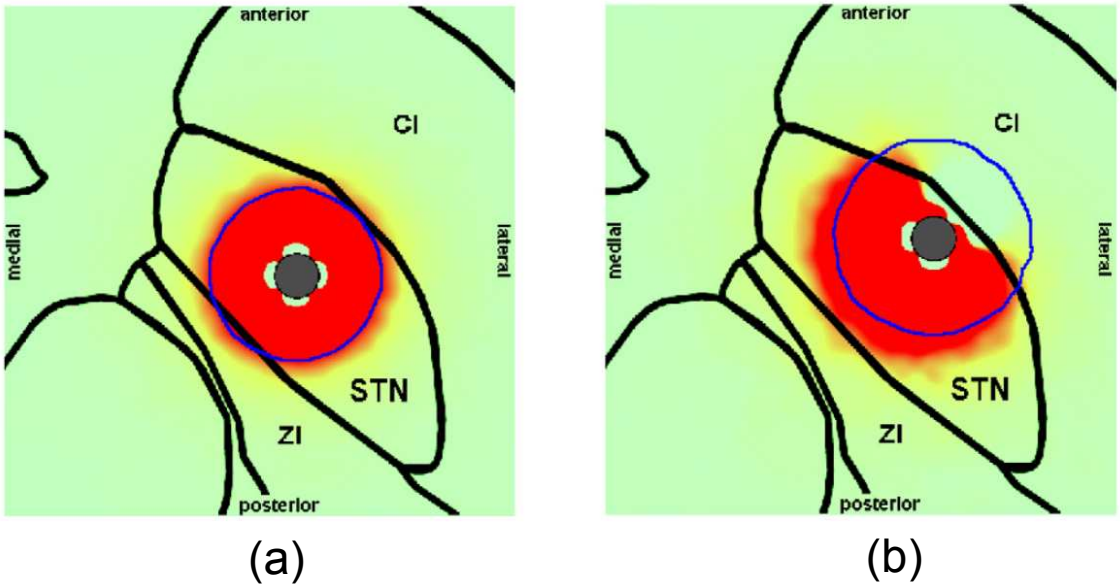


**Figure 7.2:** Field steering capability of DBS electrode array (a) The electrode array is located at the centre of the anatomical target region (b) The electrode is displaced with respect to the centre of the anatomical region. The field is then steered toward the anatomical region and spread into adjacent regions is reduced [133].

to optimise the structure and geometry of the DBS array. Figure 7.3 shows a model of a clinical DBS electrode (Medtronic 3387) located in anatomical target regions, having different conductivities and characterised by fibres with different size and orientation with respect to the implanted electrode [15].

For accurate estimation of the VTA during multipolar DBS, anisotropies and inhomogeneities should be included in the model [9]. The anisotropy of the tissue can be derived from diffusion tensor imaging (DTI), which characterises the diffusional behaviour of water in tissue, allowing to obtain the diffusion coefficient corresponding to any direction in space [10]. This process is depicted in 7.4.

### 7.1.2 Design of Output Stage for Multipolar DBS

In chapter 6 we have discussed a possible implementation of a current-steering tripolar stimulator output stage. The design concepts adopted for this specific application can be extended to output stages driving a larger number of electrode contacts. Future developments should focus on improving the proposed circuit by designing a

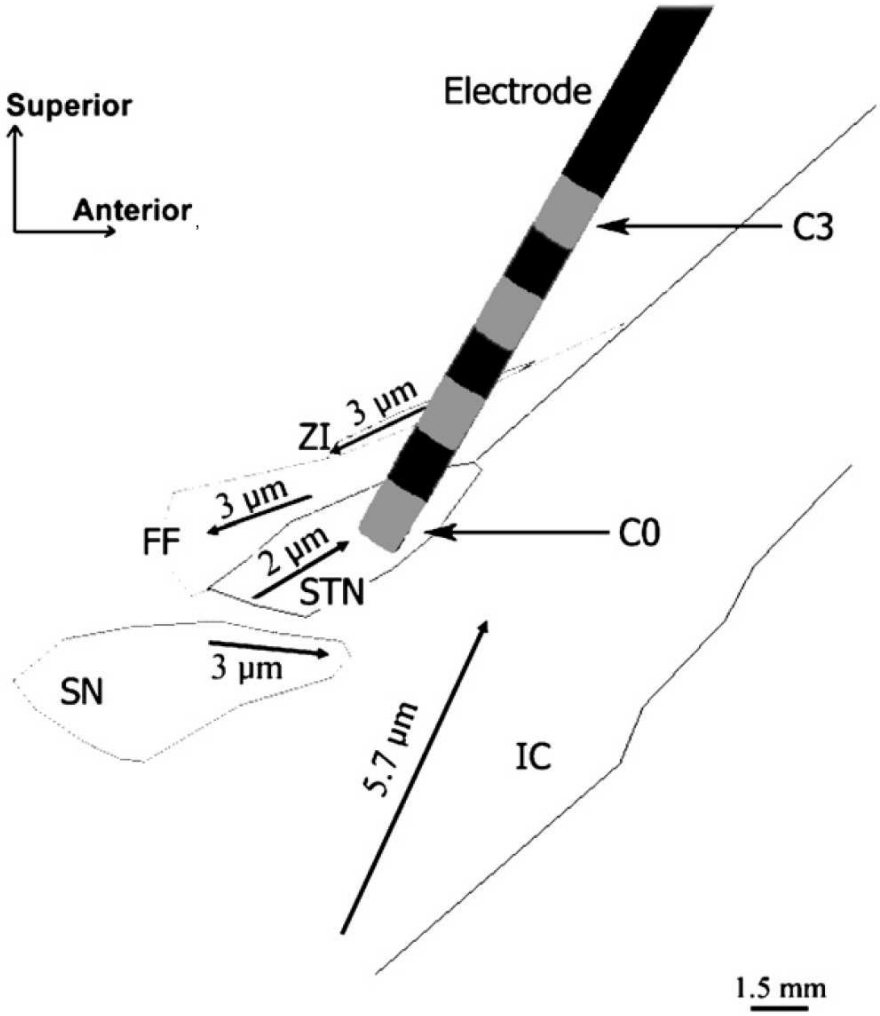


**Figure 7.3:** Sagittal slice of DBS electrode in anatomical target regions. The DBS electrode model (Medtronic 3387) has four contacts, labelled C0-C3. The labelled arrows represent the orientation and the size of the fibres within individual neural structures [15].

push-pull configuration consisting of a pair complementary active current mirrors [96], to increase the matching between the output current during the anodic and cathodic cycles. Figure 7.5 shows a possible implementation of a stimulator output stage based on a complementary version of the VIC presented in Chapter 5.

Keeping $M_1$ and $MP_1$ in the triode region allows to achieve a large output compliance of $V_{CC} - V_{SS} - V_{low} - V_{MP1} - 2V_{OV}$, where the design in the deep triode region requires the drop voltages across $M_1$ and $MP_1$ to be within 100mV and $M_2$ and $MP_2$ can be scaled to obtain a very small drain-source voltage of few hundreds of mV. Future developments should also investigate and implement techniques for

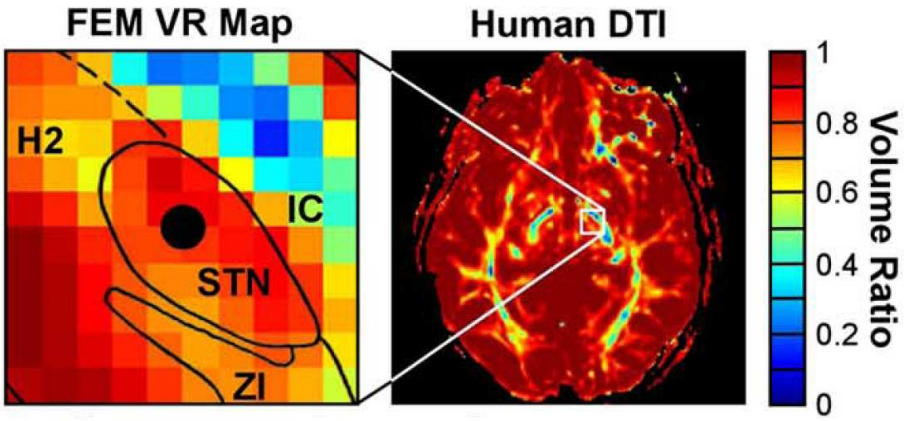


**Figure 7.4:** FEM of Volume ratio map based on DTI data [10].

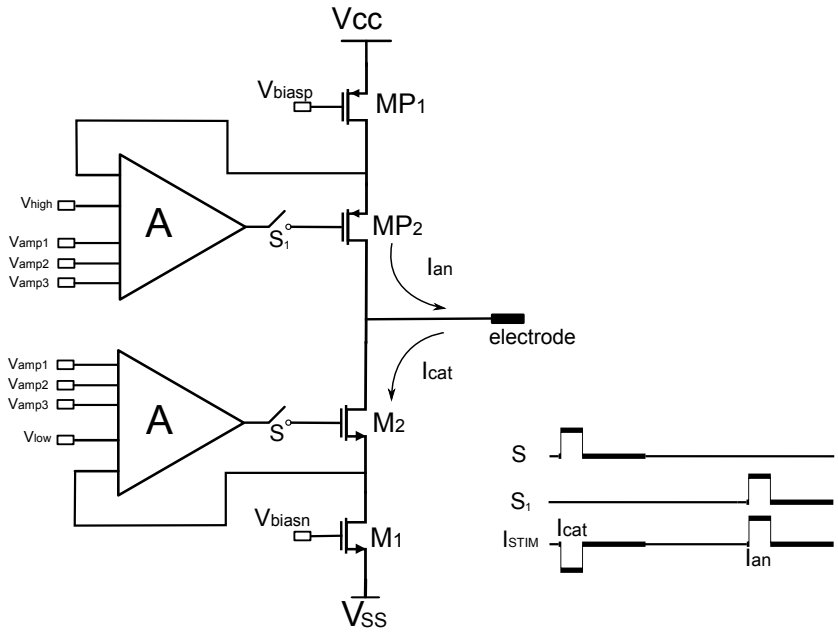


**Figure 7.5:** Complementary VIC. Adapted from [96].

output charge cancellation, to remove additional charge from the electrodes at the end of the biphasic pulse cycle. This can be accomplished by the adoption of active discharge circuitry [96, 97] or by passively discharging the electrode through a switch at the end of the stimulation cycle [102, 119]. Active discharge can be implemented as illustrated in Figure 7.6. At the end of the biphasic stimulation pulse, a comparator is adopted to compare the voltage on each working electrode to the voltage of a reference electrode. If the voltage exceeds a predefined safe window, charge balancing

current pulses are injected with the correct polarity to achieve a zero overall net charge within the stimulation window.

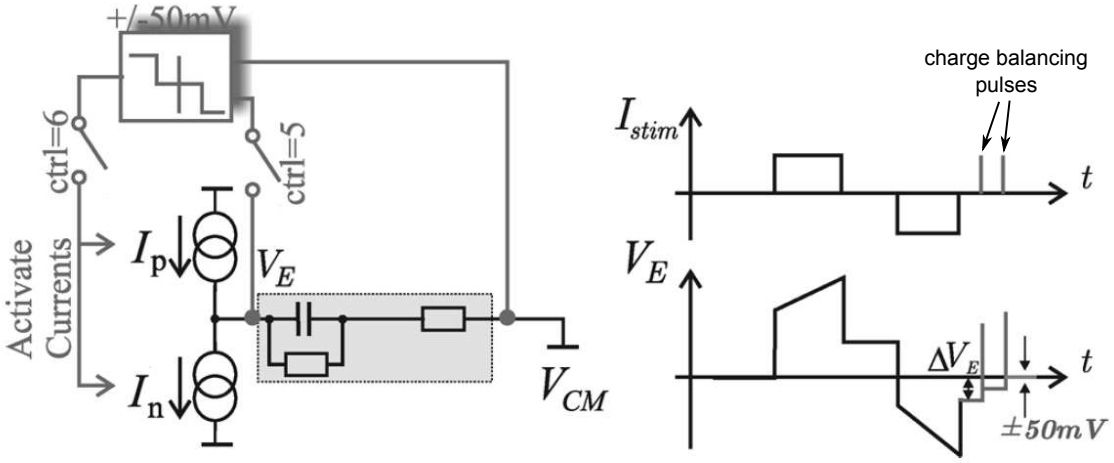


**Figure 7.6:** Active charge balancer [97].

Circuits driving electrodes with 4 or more active contacts, should also include an electrode selector stage at the output stage, in the form of a switch matrix [98], or a multiplexing unit capable of selecting any combination of three or more active contacts. Figure 7.7 shows a possible architecture of a multipolar DBS stimulator output stage. The system consists of $n$ DACs to control the amplitude of the VIC input voltage, which is then converted to an output current. A multiplexing unit allows to select the combination of active electrode needed for stimulation and the output switching network is used to control the timing and polarity of the output current pulses. A charge balancing circuit is used to ensure zero net charge at the end of the stimulation cycle.

A potential sensing unit, represented by the amplifier $A$, can be included to measure the field distribution during stimulation for a closed-loop control of the location and spread of the field.

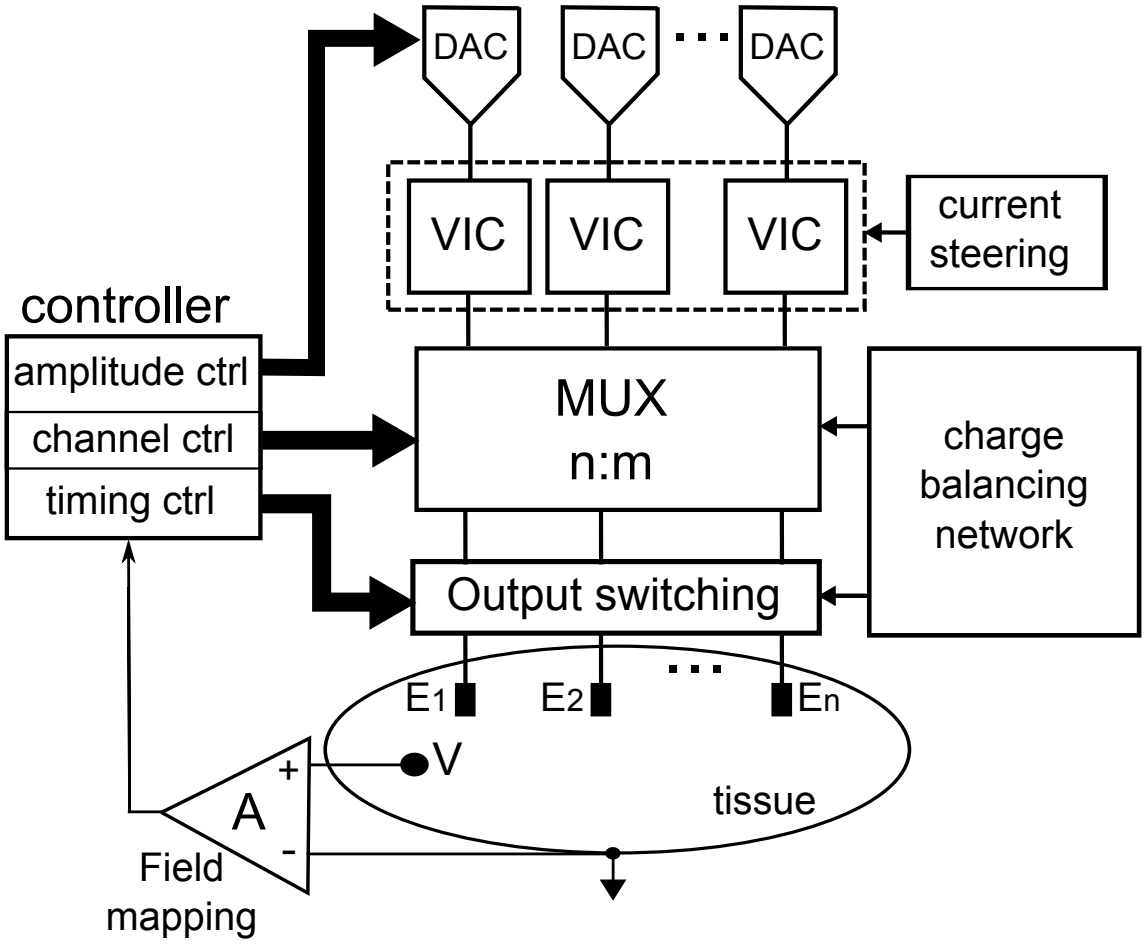


**Figure 7.7:** Architecture of a multipolar DBS system.

### 7.1.3 Design of PA DBS

Chapter 7 presented a preliminary analysis of the applicability of PA systems to DBS. The work was based exclusively on modelling the behaviour of EM waves in brain tissue at different frequencies, and showed promising results in terms of field steering in tissue for frequencies above the GHz region. Future work should include a number of developments that can further investigate PA DBS. The main important aspect consists of the selection of the stimulation frequency to adopt, which determines the design approach. At frequencies above GHz, the non-ionising EM spectrum includes microwave and infrared. Microwave stimulation of excitable tissue has not been yet demonstrated. Optical stimulation, on the other hand, is gathering substantial supporting evidence of its capability for neural stimulation

[130] with applicability to DBS [125, 126].

#### 7.1.3.1 Microwave PA DBS

The development of microwave-based PA DBS systems should include investigation on the effect of microwave on biological tissue, by looking at the heat-induced generation of action potentials [134]. The development should then focus on the design and optimisation of antenna array, based on the cylindrical structure of clinical DBS electrodes, which is optimised for the highly invasive surgical procedure required in DBS. The principal aspects of the design of a phased array antenna are the number of array elements, $N$ and the separation between them, $d$, which depend on the frequency of operation and have a direct impact on the antenna gain, the beamwidth and the sidelobes [135]. Further development should then focus on the design of the excitation network, including phase shifters or delay units, to drive the antenna at specific frequencies. CMOS implementation of phase shifters in the GHz region have already been demonstrated [136, 137, 138]. Figure 7.8 shows different architectures implementing phase shift in CMOS technology at 24GHz.

Figure 7.8(a) shows an architecture where the time delay is implemented directly in the RF signal path. A different approach consists of replacing the delay in the RF path with a delay in the IF path and a phase shift in the LO path as shown in Figure 7.8(b). The delay can also be implemented directly in the digital domain (Figure 7.8(c)).

#### 7.1.3.2 Optical PA DBS

The design of an optical PA DBS consists of two main stages. The integrated optical stimulation driver and the optical phase shifters. An integrated optical stimulation engine has been proposed in [126]. An illustration of the system architecture is given in Figure 7.9.

Light is conveyed to the tissue by means of an optical fibre from a light source (laser

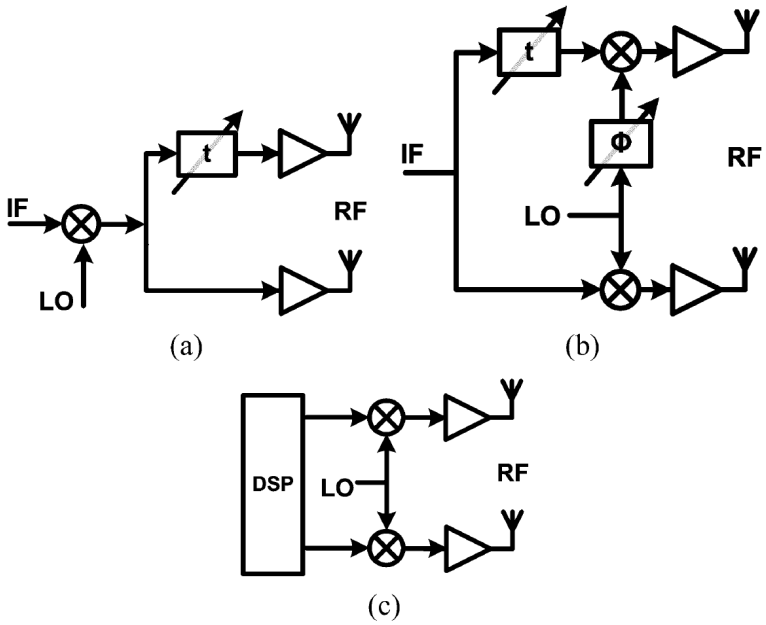


**Figure 7.8:** Different architecture of a phase shift element. (a) Delay in the RF path. (b) Delay in the IF path and LO phase shift. (c) Digital delay at baseband [137].

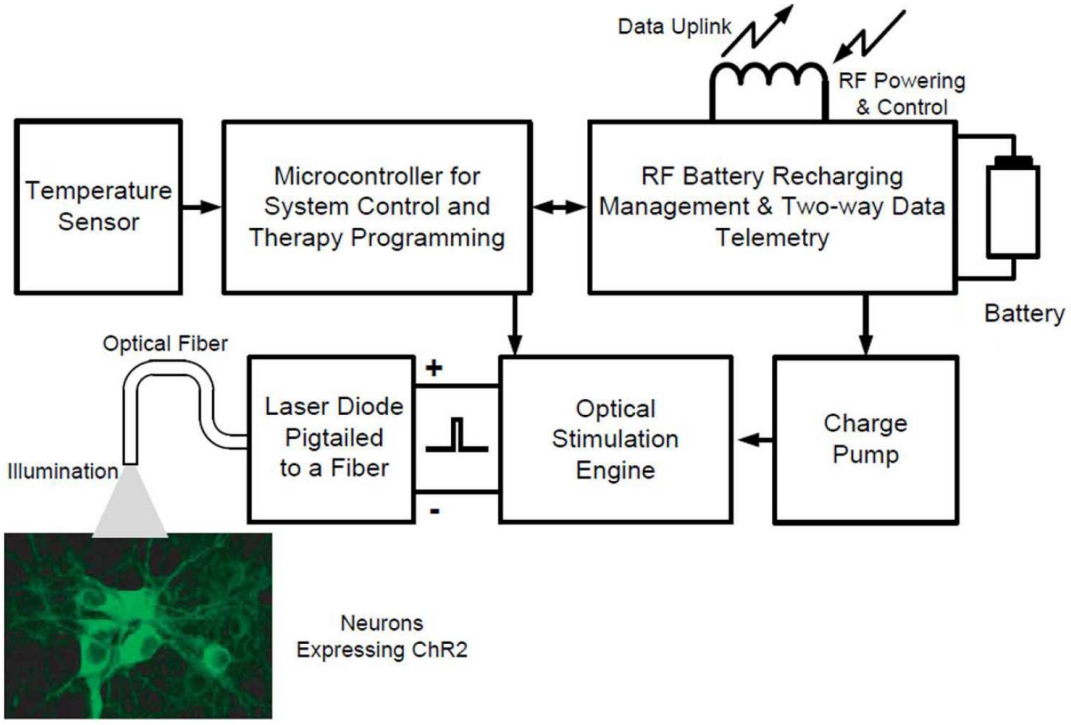


**Figure 7.9:** Optical stimulator system architecture [126].

diode) controlled by a stimulation engine, which provides the required power pulses. Power and data are managed by a telemetry unit in combination with a battery

and a charge pump. The system is equipped with a microcontroller to control the stimulation strategy to achieve the required neural modulation and a temperature sensor to monitor power dissipation in the implant. To achieve field steering such as system should be combined with the use of optical phase shifters, that can allow to steer the light beam to a desired location. Different techniques adopted to implement optical phased arrays include liquid crystal on silicon [139], microlens array [140] or silicon on insulator [141]. A comprehensive review of the main concepts in optical phased array technology is provided in [142].

# Bibliography

[1] A. Benabid, P. Pollak, D. Hoffmann, C. Gervason, M. Hommel, J. Perret, J. De Rougemont, and D. Gao, "Long-term suppression of tremor by chronic stimulation of the ventral intermediate thalamic nucleus," *The Lancet*, vol. 337, no. 8738, pp. 403–406, 1991.

[2] M. L. Kringelbach, N. Jenkinson, S. L. F. Owen, and T. Z. Aziz, "Translational principles of deep brain stimulation." *Nat Rev Neurosci*, vol. 8, no. 8, pp. 623–635, Aug. 2007.

[3] C. Halpern, H. Hurtig, J. Jaggi, M. Grossman, M. Won, and G. Baltuch, "Deep brain stimulation in neurologic disorders." *Parkinsonism & related disorders*, vol. 13, no. 1, pp. 1–16, Feb. 2007.

[4] F. L. H. Gielen, "Deep brain stimulation: current practice and challenges for the future," in *Proc. First Int Neural Engineering IEEE EMBS Conf*, 2003, pp. 489–491.

[5] A. Kuncel and W. Grill, "Selection of stimulus parameters for deep brain stimulation," *Clinical neurophysiology*, vol. 115, no. 11, pp. 2431–2441, 2004.

[6] C. McIntyre, C. Butson, C. Maks, and A. Noecker, "Optimizing deep brain stimulation parameter selection with detailed models of the electrode-tissue

interface," in *Engineering in Medicine and Biology Society, 2006. EMBS'06. 28th Annual International Conference of the IEEE*, 2006, pp. 893–895.

[7] N. Yousif and X. Liu, "Modelling the current distribution across the depth electrode-brain interface in deep brain stimulation," *Expert review of medical devices*, vol. 4, no. 5, p. 623, 2007.

[8] N. Yousif, R. Bayford, S. Wang, and X. Liu, "Quantifying the effects of the electrode-brain interface on the crossing electric currents in deep brain recording and stimulation." *Neuroscience*, vol. 152, no. 3, pp. 683–91, Mar. 2008.

[9] C. McIntyre, S. Mori, D. Sherman, N. Thakor, and J. Vitek, "Electric field and stimulating influence generated by deep brain stimulation of the subthalamic nucleus," *Clinical neurophysiology*, vol. 115, no. 3, pp. 589–595, 2004.

[10] C. C. McIntyre, M. Savasta, L. Kerkerian-Le Goff, and J. L. Vitek, "Uncovering the mechanism(s) of action of deep brain stimulation: activation, inhibition, or both." *Clinical neurophysiology : official journal of the International Federation of Clinical Neurophysiology*, vol. 115, no. 6, pp. 1239–48, June 2004.

[11] M. A. Moffitt and C. C. McIntyre, "Model-based analysis of cortical recording with silicon microelectrodes." *Clinical neurophysiology*, vol. 116, no. 9, pp. 2240–50, Sept. 2005.

[12] C. Butson, C. Maks, and C. McIntyre, "Sources and effects of electrode impedance during deep brain stimulation," *Clinical neurophysiology*, vol. 117, no. 2, pp. 447–454, 2006.

[13] X. F. Wei and W. M. Grill, "Current density distributions, field distributions and impedance analysis of segmented deep brain stimulation electrodes." *Journal of Neural Engineering*, vol. 2, no. 4, pp. 139–47, Dec. 2005.

[14] C. McIntyre and W. Grill, "Selective microstimulation of central nervous system neurons," *Annals of Biomedical Engineering*, vol. 28, no. 3, pp. 219–233, 2000.

[15] S. Sotiropoulos and P. Steinmetz, "Assessing the direct effects of deep brain stimulation using embedded axon models," *Journal of Neural Engineering*, vol. 4, pp. 107–119, 2007.

[16] N. Yousif, R. Bayford, P. G. Bain, and X. Liu, "The peri-electrode space is a significant element of the electrode-brain interface in deep brain stimulation: a computational study." *Brain research bulletin*, vol. 74, no. 5, pp. 361–8, Oct. 2007.

[17] C. Butson, S. Cooper, and J. Henderson, "Patient-specific analysis of the volume of tissue activated during deep brain stimulation," *Neuroimage*, vol. 34, pp. 661–670, 2007.

[18] J. Volkmann, "Deep brain stimulation for the treatment of Parkinson's disease." *Journal of Clinical Neurophysiology*, vol. 21, no. 1, pp. 6–17, 2004.

[19] Y. Mendelsohn and E. Wiener-Avnear, "Simulations of circular 2D phase-array ultrasonic imaging transducers." *Ultrasonics*, vol. 39, no. 9, pp. 657–66, Aug. 2002.

[20] A. Fenn and G. King, "Experimental investigation of an adaptive feedback algorithm for hot spot reduction in radio-frequency phased-array hyperthermia," *IEEE Transactions on Biomedical Engineering*, vol. 43, no. 3, pp. 273 –280, march 1996.

[21] M. Converse, E. Bond, S. Hagness, and B. Van Veen, "Ultrawide-band microwave space-time beamforming for hyperthermia treatment of breast cancer: a computational feasibility study," *IEEE Transactions on Microwave Theory and Techniques*, vol. 52, no. 8, pp. 1876 – 1889, aug. 2004.

[22] L. Wu, R. J. McGough, O. A. Arabe, and T. V. Samulski, "An rf phased array applicator designed for hyperthermia breast cancer treatments." *Phys Med Biol*, vol. 51, no. 1, pp. 1–20, Jan 2006.

[23] J. W. Mink, "The basal ganglia: focused selection and inhibition of competing motor programs." *Progress in neurobiology*, vol. 50, no. 4, pp. 381–425, Nov. 1996.

[24] L. L. Rubchinsky, N. Kopell, and K. A. Sigvardt, "Modeling facilitation and inhibition of competing motor programs in basal ganglia subthalamic nucleus-pallidal circuits." *Proc Natl Acad Sci U S A*, vol. 100, no. 24, pp. 14 427–14 432, Nov 2003.

[25] M. R. DeLong and T. Wichmann, "Circuits and circuit disorders of the basal ganglia." *Archives of Neurology*, vol. 64, no. 1, pp. 20–4, Jan. 2007.

[26] K. Cole and R. Cole, "Dispersion and absorption in dielectrics II. Direct Current Characterisic," *The Journal of Chemical Physics*, vol. 10, 1942.

[27] S. Gabriel, R. Lau, and C. Gabriel, "The dielectric properties of biological tissues: II. Measurements in the frequency range 10 Hz to 20 GHz," *Physics in Medicine and Biology*, vol. 41, p. 2251, 1996.

[28] A. Vargese, *The Biomedical Engineering Handbook - Chapter 11. Membrane Moldes.*, J. D. Bronzino, Ed. CRC Press, 2000.

[29] J. D. Bronzino, Ed., *The Biomedical Engineering Handbook*. CRC Press, 2000.

[30] A. L. Hodgkin and A. F. Huxley, "A quantitative description of membrane current and its application to conduction and excitation in nerve." *Journal of Physiology*, vol. 117, no. 4, pp. 500–544, Aug 1952.

[31] F. Rattay, "The basic mechanism for the electrical stimulation of the nervous system." *Neuroscience*, vol. 89, no. 2, pp. 335–346, Mar. 1999.

[32] D. Durand, *The Biomedical Engineering Handbook. Chapter 17. Electrical Stimulation of Excitable Tissue*, J. D. Bronzino, Ed. CRC Press, 2000.

[33] F. Rattay, "Analysis of models for external stimulation of axons." *IEEE Transactions on Biomedical Engineering*, vol. 33, no. 10, pp. 974–7, Oct. 1986.

[34] R. L. Testerman, M. T. Rise, and P. H. Stypulkowski, "Electrical stimulation as therapy for neurological disorder." *IEEE Eng Med Biol Mag*, vol. 25, no. 5, pp. 74–78, 2006.

[35] D. Boinagrov, J. Loudin, and D. Palanker, "Strength-duration relationship for extracellular neural stimulation: numerical and analytical models." *Journal of Neurophysiology*, vol. 104, no. 4, pp. 2236–2248, Oct 2010.

[36] J. B. Ranck, "Which elements are excited in electrical stimulation of mammalian central nervous system: a review," *Brain Research*, vol. 98, no. 3, pp. 417–440, 1975.

[37] J. Holsheimer, H. Demeulemeester, B. Nuttin, and P. D. Sutter, "Short communication. identification of the target neuronal elements in electrical deep brain stimulation," *Neuroscience*, vol. 12, no. January, 2000.

[38] D. Merrill, M. Bikson, and J. Jefferys, "Electrical stimulation of excitable tissue: design of efficacious and safe protocols," *Journal of Neuroscience Methods*, vol. 141, no. 2, pp. 171–198, 2005.

[39] R. V. Shannon, "A model of safe levels for electrical stimulation." *IEEE Transactions on Biomedical Engineering*, vol. 39, no. 4, pp. 424–426, Apr 1992.

[40] R. J. Coffey, "Deep brain stimulation devices: a brief technical history and review." *Artificial Organs*, vol. 33, no. 3, pp. 208–220, 2009.

[41] A. L. Benabid, P. Pollak, D. Gao, D. Hoffmann, P. Limousin, E. Gay, I. Payen, and A. Benazzouz, "Chronic electrical stimulation of the ventralis intermedius nucleus of the thalamus as a treatment of movement disorders." *Journal of neurosurgery*, vol. 84, no. 2, pp. 203–14, Feb. 1996.

[42] A. L. Benabid, A. Koudsie, A. Benazzouz, V. Fraix, A. Ashraf, J. F. L. Bas, S. Chabardes, and P. Pollak, "Subthalamic stimulation for Parkinson's disease." *Arch Med Res*, vol. 31, no. 3, pp. 282–289, 2000.

[43] J. O. Dostrovsky, R. Levy, J. P. Wu, W. D. Hutchison, R. R. Tasker, and a. M. Lozano, "Microstimulation-induced inhibition of neuronal firing in human globus pallidus." *Journal of Neurophysiology*, vol. 84, no. 1, pp. 570–4, July 2000.

[44] A. Benazzouz, S. Breit, A. Koudsie, P. Pollak, P. Krack, and A.-L. Benabid, "Intraoperative microrecordings of the subthalamic nucleus in Parkinson's disease." *Movement Disorders*, vol. 17 Suppl 3, pp. S145–S149, 2002.

[45] D. B. McCreery, W. F. Agnew, T. G. Yuen, and L. Bullara, "Charge density and charge per phase as cofactors in neural injury induced by electrical stimulation." *IEEE Transactions on Biomedical Engineering*, vol. 37, no. 10, pp. 996–1001, Oct 1990.

[46] C. C. McIntyre and W. M. Grill, "Finite element analysis of the current-density and electric field generated by metal microelectrodes." *Annals of Biomedical Engineering*, vol. 29, no. 3, pp. 227–35, Mar. 2001.

[47] D. R. Cantrell, S. Inayat, A. Taflove, R. S. Ruoff, and J. B. Troy, "Incorporation of the electrode-electrolyte interface into finite-element models of metal microelectrodes." *Journal of Neural Engineering*, vol. 5, no. 1, pp. 54–67, Mar. 2008.

[48] C. Butson and C. McIntyre, "Tissue and electrode capacitance reduce neural activation volumes during deep brain stimulation," *Clinical Neurophysiology*, vol. 116, no. 10, pp. 2490–2500, 2005.

[49] ——, "Role of electrode design on the volume of tissue activated during deep brain stimulation," *Journal of Neural Engineering*, vol. 3, no. 1, p. 1, 2006.

[50] C. McIntyre and W. Grill, "Extracellular stimulation of central neurons: influence of stimulus waveform and frequency on neuronal output," *Journal of Neurophysiology*, vol. 88, no. 4, p. 1592, 2002.

[51] G. Chunping, "Finite element modelling of the human brain and application in neurological procedures," Ph.D. dissertation, National University of Singapore, 2007.

[52] E. T. McAdams and J. Jossinet, "Physical interpretation of Schwan's limit voltage of linearity." *Medical & biological engineering & computing*, vol. 32, no. 2, pp. 126–30, Mar. 1994.

[53] P. F. Grant and M. M. Lowery, "Electric field distribution in a finite-volume head model of deep brain stimulation." *Medical engineering & physics*, vol. 31, no. 9, pp. 1095–103, Nov. 2009.

[54] C. M. Zierhofer, "Analysis of a linear model for electrical stimulation of axons–critical remarks on the "activating function concept"." *IEEE Transactions on Biomedical Engineering*, vol. 48, no. 2, pp. 173–184, Feb. 2001.

[55] D. R. McNeal, "Analysis of a model for excitation of myelinated nerve," *IEEE Transactions on Biomedical Engineering*, no. 4, pp. 329–337, 1976.

[56] A. M. Kuncel, S. E. Cooper, and W. M. Grill, "A method to estimate the spatial extent of activation in thalamic deep brain stimulation," *Clinical Neurophysiology*, vol. 119, pp. 2148–2158, 2008.

[57] N. Yousif, N. Purswani, R. Bayford, D. Nandi, P. Bain, and X. Liu, "Evaluating the impact of the deep brain stimulation induced electric field on subthalamic neurons: a computational modelling study." *Journal of Neuroscience Methods*, vol. 188, no. 1, pp. 105–12, Apr. 2010.

[58] C. C. McIntyre, A. G. Richardson, and W. M. Grill, "Modeling the excitability of mammalian nerve fibers: influence of afterpotentials on the recovery cycle." *Journal of Neurophysiology*, vol. 87, no. 2, pp. 995–1006, Feb. 2002.

[59] J. Vidal and M. Ghovanloo, "Towards a Switched-Capacitor based Stimulator for efficient deep-brain stimulation," *Conference of the IEEE Engineering in Medicine and Biology Society.*, pp. 2927–30, Jan. 2010.

[60] D.-L. Shen and Y.-J. Chu, "A linearized current stimulator for deep brain stimulation," *Conference of the IEEE Engineering in Medicine and Biology Society.*, pp. 6485–8, Jan. 2010.

[61] S. Jensen, G. Molnar, J. Giftakis, W. Santa, R. Jensen, D. Carlson, M. Lent, and T. Denison, "Information, energy, and entropy: Design principles for adaptive, therapeutic modulation of neural circuits," *ESSCIRC 2008 - 34th European Solid-State Circuits Conference*, pp. 32–39, Sept. 2008.

[62] J. Lee, D. Kipke, and M. Flynn, "A 64 Channelprogrammable closed-loop deep brain stimulator with 8 channel neural amplifier and logarithmic ADC," *2008 IEEE Symposium on VLSI Circuits*, pp. 76–77, June 2008.

[63] M. Sahin and Y. Tie, "Non-rectangular waveforms for neural stimulation with practical electrodes." *Journal of Neural Engineering*, vol. 4, no. 3, pp. 227–233, Sept. 2007.

[64] R. W. de Boer and a. van Oosterom, "Electrical properties of platinum electrodes: impedance measurements and time-domain analysis." *Medical & biological engineering & computing*, vol. 16, no. 1, pp. 1–10, Jan. 1978.

[65] H. P. Schwan and B. Onaral, "Linear and nonlinear properties of platinum electrode polarisation III: Equivalence of frequency- and time-domain behaviour." *Medical & biological engineering & computing*, vol. 23, no. 1, pp. 28–32, Jan. 1985.

[66] E. T. McAdams and J. Jossinet, "Tissue impedance: a historical overview." *Physiological Measurement*, vol. 16, no. 3 Suppl A, pp. A1–13, Aug. 1995.

[67] P. Zoltowski, "On the electrical capacitance of interfaces exhibiting constant phase element behaviour," *Journal of Electroanalytical Chemistry*, vol. 443, no. 1, pp. 149–154, 1998.

[68] W. Franks, I. Schenker, P. Schmutz, and A. Hierlemann, "Impedance characterization and modeling of electrodes for biomedical applications." *IEEE Transactions on Biomedical Engineering*, vol. 52, no. 7, pp. 1295–302, July 2005.

[69] E. T. McAdams and J. Jossinet, "The detection of the onset of electrode-electrolyte interface impedance nonlinearity: a theoretical study." *IEEE Transactions on Biomedical Engineering*, vol. 41, no. 5, pp. 498–500, May 1994.

[70] B. Onaral and H. P. Schwan, "Linear and nonlinear properties of platinum electrode polarisation. ii: Time domain analysis." *Medical & biological engineering & computing*, vol. 21, no. 2, pp. 210–216, Mar. 1983.

[71] A. Bard and L. Faulkner, *Electrochemical methods, fundamentals and applications. 2nd edition.* John Wiley, New York, 2001.

[72] S. Mayer, L. Geddes, J. Bourland, and L. Ogborn, "Faradic resistance of the electrode/electrolyte interface," *Medical & biological engineering & computing*, vol. 30, no. 5, pp. 538–542, 1992.

[73] J. Weinman and J. Mahler, "An analysis of electrical properties of metal electrodes," *Medical & biological engineering & computing*, vol. 2, no. 3, pp. 299–310, 1964.

[74] X. Wang, B. Wang, P. J. Bos, and J. E. Anderson, "Finite-difference time-domain simulation of a liquid-crystal optical phased array," *Simulation*, vol. 22, no. 2, pp. 346–354, 2005.

[75] N. Donaldson and P. Donaldson, "When are actively balanced biphasic ('Lilly') stimulating pulses necessary in a neurological prosthesis? I Historical background; Pt resting potential; Q studies," *Medical & biological engineering & computing*, vol. 24, no. 1, pp. 41–49, 1986.

[76] C. N. Jolly, F. a. Spelman, and B. M. Clopton, "Quadrupolar stimulation for Cochlear prostheses: modeling and experimental data." *IEEE Transactions on Biomedical Engineering*, vol. 43, no. 8, pp. 857–65, Aug. 1996.

[77] A. Kral, R. Hartmann, D. Mortazavi, and R. Klinke, "Spatial resolution of cochlear implants: the electrical field and excitation of auditory afferents." *Hearing research*, vol. 121, no. 1-2, pp. 11–28, July 1998.

[78] S. Miyoshi, S. Shimizu, J. Matsushima, and T. Ifukube, "Proposal of a new method for narrowing and moving the stimulated region of cochlear implants: animal experiment and numerical analysis." *IEEE Transactions on Biomedical Engineering*, vol. 46, no. 4, pp. 451–60, Apr. 1999.

[79] G. S. Donaldson, H. A. Kreft, and L. Litvak, "Place-pitch discrimination of single- versus dual-electrode stimuli by cochlear implant users (L)." *J Acoust Soc Am*, vol. 118, no. 2, pp. 623–626, Aug. 2005.

[80] J. B. Firszt, D. B. Koch, M. Downing, and L. Litvak, "Current steering creates additional pitch percepts in adult cochlear implant recipients." *Otol Neurotol*, vol. 28, no. 5, pp. 629–636, Aug. 2007.

[81] B. H. Bonham and L. M. Litvak, "Current focusing and steering: modeling, physiology, and psychophysics." *Hearing research*, vol. 242, no. 1-2, pp. 141–153, Aug. 2008.

[82] C. R. Butson and C. C. Mcintyre, "Current Steering To Control The Volume Of Tissue Activated During Deep Brain Stimulation," *Journal Of Brain Stimulation*, vol. vol, pp. 7–15, 2008.

[83] C. Veraart, W. M. Grill, and J. T. Mortimer, "Selective control of muscle activation with a multipolar nerve cuff electrode." *IEEE Transactions on Biomedical Engineering*, vol. 40, no. 7, pp. 640–53, July 1993.

[84] N. Accornero, G. Bini, G. L. Lenzi, and M. Manfredi, "Selective Activation of peripheral nerve fibre groups of different diameter by triangular shaped stimulus pulses." *The Journal of Physiology*, vol. 273, no. 3, pp. 539–60, Dec. 1977.

[85] N. J. Rijkhoff, J. Holsheimer, E. L. Koldewijn, J. J. Struijk, P. E. van Kerrebroeck, F. M. Debruyne, and H. Wijkstra, "Selective stimulation of sacral nerve roots for bladder control: a study by computer modeling." *IEEE Transactions on Biomedical Engineering*, vol. 41, no. 5, pp. 413–424, May 1994.

[86] R. Guttman and L. Hachmeister, "Anode Break Excitation in Space-Clamped Squid Axons," *Biophysical Journal*, vol. 12, no. 5, pp. 552–563, May 1972.

[87] W. Burke and B. Ginsborg, "The electrical properties of the slow muscle fibre membrane," *The Journal of Physiology*, vol. 132, no. 3, p. 586, 1956.

[88] G. S. Brindley and M. D. Craggs, "A technique for anodally blocking large nerve fibres through chronically implanted electrodes." *Journal of Neurology, Neurosurgery, and Psychiatry*, vol. 43, no. 12, pp. 1083–90, Dec. 1980.

[89] M. Bugbee, N. N. Donaldson, a. Lickel, N. J. Rijkhoff, and J. Taylor, "An implant for chronic selective stimulation of nerves." *Medical engineering & physics*, vol. 23, no. 1, pp. 29–36, Jan. 2001.

[90] N. Bhadra, V. Grünewald, and G. Creasey, "Selective suppression of sphincter activation during sacral anterior nerve root stimulation," *Neurourol Urodyn*, vol. 64, no. December 2000, pp. 55–64, 2001.

[91] A. Vucković and N. J. M. Rijkhoff, "Different pulse shapes for selective large fibre block in sacral nerve roots using a technique of anodal block: an experimental study." *Medical & biological engineering & computing*, vol. 42, no. 6, pp. 817–24, Nov. 2004.

[92] A. Vuckovic, M. Tosato, and J. J. Struijk, "A comparative study of three techniques for diameter selective fiber activation in the vagal nerve: anodal block, depolarizing prepulses and slowly rising pulses." *Journal of Neural Engineering*, vol. 5, no. 3, pp. 275–86, Sept. 2008.

[93] C. A. Bossetti, M. J. Birdno, and W. M. Grill, "Analysis of the quasi-static approximation for calculating potentials generated by neural stimulation." *Journal of Neural Engineering*, vol. 5, no. 1, pp. 44–53, Mar. 2008.

[94] B. Townshend and R. L. White, "Reduction of electrical interaction in auditory prostheses," *IEEE Transactions on Biomedical Engineering*, vol. 34, no. 11, pp. 891–897, 1987.

[95] S. DeMarco, P. Singh, G. Lazzi, M. Humayun, and J. Weiland, "An arbitrary waveform stimulus circuit for visual prostheses using a low-area multibias dac," *IEEE Journal of Solid-State Circuits*, vol. 38, no. 10, pp. 1679–1690, Oct. 2003.

[96] M. Sivaprakasam, J. Granacki, J. Lacoss, and J. Wills, "Implantable biomimetic microelectronic systems design," *IEEE Engineering in Medicine and Biology Magazine*, vol. 24, no. 5, pp. 66–74, Sept. 2005.

[97] M. Ortmanns, "Charge balancing in functional electrical stimulators: A comparative study," *Circuits and Systems, 2007. ISCAS 2007. IEEE*, pp. 573–576, 2007.

[98] J. Coulombe, M. Sawan, and J.-F. Gervais, "A Highly Flexible System for Microstimulation of the Visual Cortex: Design and Implementation," *IEEE Transactions on Biomedical Circuits and Systems*, vol. 1, no. 4, pp. 258–269, Dec. 2007.

[99] T. R. Gheewala, R. D. Melen, and R. L. White, "A cmos implantable multielectrode auditory stimulator for the deaf," *IEEE Journal of Solid-State Circuits*, vol. 10, no. 6, pp. 472–479, 1975.

[100] D. Jiang, A. Demosthenous, T. Perkins, X. Liu, and N. Donaldson, "A stimulator asic featuring versatile management for vestibular prostheses," *IEEE Transactions on Biomedical Circuits and Systems*, vol. 5, no. 2, pp. 147–159, 2011.

[101] K. Arabi and M. Sawan, "Electronic design of a multichannel programmable implant for neuromuscular electrical stimulation," *IEEE Transactions on Rehabilitation Engineering*, vol. 7, no. 2, pp. 204–214, 1999.

[102] X. Liu, A. Demosthenous, and N. Donaldson, "An Integrated Implantable Stimulator That is Fail-Safe Without Off-Chip Blocking-Capacitors," *IEEE Transactions on Biomedical Circuits and Systems*, vol. 2, no. 3, pp. 231–244, 2008.

[103] J. D. Techer, S. Bernard, Y. Bertrand, G. Cathebras, and D. Guiraud, "New implantable stimulator for the fes of paralyzed muscles," in *Proc. Proceeding of the 30th European Solid-State Circuits Conf. ESSCIRC 2004*, 2004, pp. 455–458.

[104] F. You, H. K. Embabi, J. F. Duque-Carrillo, and E. Sanchez-Sinencio, "Am improved tail current source for low voltage applications," *IEEE Journal of Solid-State Circuits*, vol. 32, no. 8, pp. 1173–1180, 1997.

[105] E. Sackinger, "A high-swing, high-impedance MOS cascode circuit," *IEEE Journal of Solid-State Circuits*, vol. 25, no. 1, pp. 289–298, 1990.

[106] D. Schmitt and T. S. Fiez, "A low voltage CMOS current source," *Proceedings of the 1997 international symposium on Low power electronics and design - ISLPED '97*, vol. 3, no. 2, pp. 110–113, 1997.

[107] T. Serrano, "The active-input regulated-cascode current mirror," *IEEE Transactions on Circuits and Systems I: Fundamental Theory and Applications*, vol. 41, no. 6, pp. 464–467, June 1994.

[108] P. J. Crawley and G. W. Roberts, "High-swing mos current mirror with arbitrarily high output resistance," *Electronics Letters*, vol. 28, no. 4, pp. 361–363, 1992.

[109] B. Fotouhi, "All-MOS Voltage-to-Current Converter," *IEEE Journal of Solid-State Circuits*, vol. 36, 2001.

[110] A. S. Sedra and K. C. Smith, *Microelectronic Circuits.*, 5th ed. Oxford University Press, 2004.

[111] B. Razavi, *Design of Analog CMOS Integrated Circuits.* McGraw-Hill, 2001.

[112] M. Ghovanloo and K. Najafi, "A Small Size Large Voltage Compliance Programmable Current Source for Biomedical Implantable Microstimulators," *Proceedings of the 25" Annual lntematianal Conference of the IEEE EMBS*, Sept. 2003.

[113] R. Rieger, A. Demosthenous, and J. Taylor, "A 230-nw 10-s time constant cmos

integrator for an adaptive nerve signal amplifier," *IEEE Journal of Solid-State Circuits*, vol. 39, no. 11, pp. 1968–1975, 2004.

[114] D. Ma, B. M. Wilamowski, and F. F. Dai, "A tunable cmos resistor with wide tuning range for low pass filter application," in *Proc. IEEE Topical Meeting Silicon Monolithic Integrated Circuits in RF Systems SiRF '09*, 2009, pp. 1–4.

[115] R. J. Baker, *CMOS: Circuit Design, Layout and Simulation.* Wiley-IEEE, 2000.

[116] E. Vittoz and J. Fellrath, "CMOS analog integrated circuits based on weak inversion operations," vol. 12, no. 3, pp. 224–231, 1977.

[117] B. Linares-Barranco and T. Serrano-Gotarredona, "On the design and characterization of femtoampere current-mode circuits," *IEEE Journal of Solid-State Circuits*, vol. 38, no. 8, pp. 1353–1363, 2003.

[118] K. Bult and G. J. G. M. Geelen, "An inherently linear and compact most-only current division technique," *IEEE Journal of Solid-State Circuits*, vol. 27, no. 12, pp. 1730–1735, 1992.

[119] M. Ghovanloo and K. Najafi, "A compact large voltage-compliance high output-impedance programmable current source for implantable microstimulators," *IEEE Transactions on Biomedical Engineering*, vol. 52, no. 1, pp. 97–105, 2005.

[120] K. Hennings, L. Arendt-Nielsen, S. S. Christensen, and O. K. Andersen, "Selective activation of small-diameter motor fibres using exponentially rising waveforms: a theoretical study." *Medical & biological engineering & computing*, vol. 43, no. 4, pp. 493–500, July 2005.

[121] R. Knoechel, "Capabilities of multiapplicator systems for focussed hyperther-

mia," *IEEE Transactions on Microwave Theory and Techniques*, vol. 31, no. 1, pp. 70–73, 1983.

[122] A. Sarti and P. Bassi, "3D modeling of phased array generated ultrasounds in lossy media," *Computerized Medical Imaging and Graphics*, vol. 17, pp. 339–343, 1993.

[123] Y. Chen, S. Zhou, C. Xie, S. Nioka, M. Delivoria-Papadopoulos, E. Anday, and B. Chance, "Preliminary evaluation of dual wavelength phased array imaging on neonatal brain function." *Journal of Biomedical Optics*, vol. 5, no. 2, pp. 194–200, Apr. 2000.

[124] J. Wells, C. Kao, E. D. Jansen, P. Konrad, and A. Mahadevan-Jansen, "Application of infrared light for in vivo neural stimulation." *Journal of Biomedical Optics*, vol. 10, no. 6, 2005.

[125] V. Gradinaru, M. Mogri, K. R. Thompson, J. M. Henderson, and K. Deisseroth, "Optical deconstruction of parkinsonian neural circuitry." *Science*, vol. 324, no. 5925, pp. 354–359, Apr. 2009.

[126] K. Paralikar, P. Cong, O. Yizhar, L. Fenno, W. Santa, C. Nielsen, D. Dinsmoor, B. Hocken, G. Munns, J. Giftakis, and Others, "An Implantable Optical Stimulation Delivery System for Actuating an Excitable Biosubstrate," *IEEE Journal of Solid-State Circuits*, vol. 46, no. 1, pp. 321–332, 2011.

[127] J. Wells, P. Konrad, C. Kao, E. Jansen, and A. Mahadevan-Jansen, "Pulsed laser versus electrical energy for peripheral nerve stimulation," *Journal of Neuroscience Methods*, vol. 163, no. 2, pp. 326–337, 2007.

[128] F. T. Ulaby, *Fundamentals of applied electromagnetics*. Pearson/ Prentice Hall, 2001.

[129] M. N. O. Sadiku, *Elements of elctromagnetics*. Oxford University Press, 2001.

[130] J. Wells and A. Mahadevan-jansen, "Application of infrared light for in vivo neural," *Journal of Biomedical Optics*, vol. 10, no. December, 2005.

[131] J. Zhang, F. Laiwalla, J. Kim, H. Urabe, R. Van Wagenen, Y. Song, B. Connors, F. Zhang, K. Deisseroth, and A. Nurmikko, "Integrated device for optical stimulation and spatiotemporal electrical recording of neural activity," *Journal of Neural Engineering*, vol. 6, p. 055007, 2009.

[132] J. Gimsa, B. Habel, U. Schreiber, and U. Rienen, "Choosing electrodes for deep brain stimulation experiments-electrochemical considerations," *Journal of Neuroscience*, vol. 142, no. 2, pp. 251–265, 2005.

[133] H. C. F. Martens, E. Toader, M. M. J. Decré, D. J. Anderson, R. Vetter, D. R. Kipke, K. B. Baker, M. D. Johnson, and J. L. Vitek, "Spatial steering of deep brain stimulation volumes using a novel lead design." *Clinical Neurophysiology*, vol. 122, no. 3, pp. 558–66, Mar. 2011.

[134] S. Schwarz, W. Greffrath, D. BÃ$\frac{1}{4}$sselberg, and R. D. Treede, "Inactivation and tachyphylaxis of heat-evoked inward currents in nociceptive primary sensory neurones of rats." *J Physiol*, vol. 528, no. Pt 3, pp. 539–549, Nov 2000.

[135] R. J. Mailloux, *Phased array antenna handbook*. Artech House, 2005.

[136] A. Hajimiri, "Fully Integrated Millimeter-Wave CMOS Phased Arrays Invited," *Evolution*, pp. 45–48, 2005.

[137] A. Natarajan, A. Komijani, and A. Hajimiri, "A fully integrated 24-ghz phased-array transmitter in cmos," *IEEE Journal of Solid-State Circuits*, vol. 40, no. 12, pp. 2502–2514, 2005.

[138] K.-J. Koh and G. Rebeiz, "0.13-um cmos phase shifters for x-, ku-, and k-band phased arrays," *IEEE Journal of Solid-State Circuits*, vol. 42, no. 11, pp. 2535 –2546, nov. 2007.

[139] S. Serati and J. Stockley, "Advanced liquid crystal on silicon optical phased arrays," in *Proc. IEEE Aerospace*, vol. 3, 2002, pp. 3–1395.

[140] E. A. Watson, W. E. Whitaker, C. D. Brewer, and S. R. Harris, "Implementing optical phased array beam steering with cascaded microlens arrays," in *Proc. IEEE Aerospace*, vol. 3, 2002, pp. 3–1429.

[141] K. Van Acoleyen, W. Bogaerts, J. Jágerská, N. Le Thomas, R. Houdré, and R. Baets, "Off-chip beam steering with a one-dimensional optical phased array on silicon-on-insulator." *Optics letters*, vol. 34, no. 9, pp. 1477–9, May 2009.

[142] P. F. McManamon, T. A. Dorschner, D. L. Corkum, L. J. Friedman, D. S. Hobbs, M. Holz, S. Liberman, H. Q. Nguyen, D. P. Resler, R. C. Sharp, and E. A. Watson, "Optical phased array technology," *Proceedings of the IEEE*, vol. 84, no. 2, pp. 268–298, 1996.

[143] S. Quek and G. Liu, *The finite element method: A practical course*. Butterworth-Heinemann, 2003.

# A

# Finite Element Method

The finite element method (FEM) represents an advanced technology for modelling and simulating engineering systems in various fields. FEM is a numerical method aiming at deriving an approximated solution for problems whose solutions are not easily found analytically. For example FEM can be adopted to reduce complex partial differential equations (PDE) that describe the problem, into a set of ordinary differential equations (ODE). The behaviour of a system depends on its geometry (domain), the properties of the material or medium, and the boundary, initial and loading conditions. Some systems may be too complex to understand analytically and they are solved with numerical methods. The procedure of the FEM consists of four main steps: Modelling the system's geometry, subdivide it into several basic

elements (meshing), specify material properties and specify boundary, initial and loading conditions. The accuracy of the representation of the model depends on the number of element used to derive the model mesh. However, a trade-off exists between the number of elements selected and the computational time and power required.

## A.1 Meshing

Meshing is performed to subdivide the geometry in small pieces called elements. Figure A.1 shows an example of a triangular mesh for (a) a sphere and (b) a model of a DBS electrode.

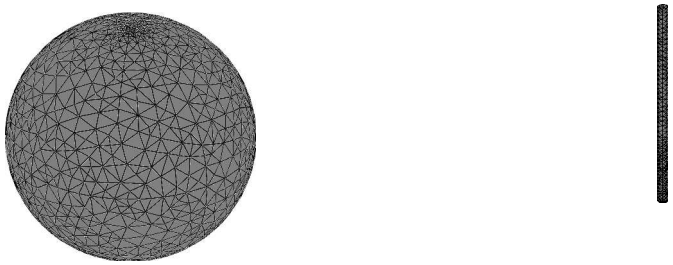

(a) Mesh of a sphere (b) Mesh of a DBS Electrode

**Figure A.1:** Meshing.

Meshing is useful in order to reduce the complexity of a system by providing elements where the solution can be approximated by simple mathematical functions such as polynomials. Triangulation is the most common way in which meshes are created. The model geometry is subdivided into triangles, which allow high flexibility to model complex geometry, although at the cost of accuracy. FEM takes into account different properties of the material or medium proper of the system under investigation. Properties can be different in different regions of the geometry.

## A.2 Axial Symmetry

A solid or structure has axial symmetry when it can be generated by rotating a planar shape about one axis, as illustrated in Figure A.2

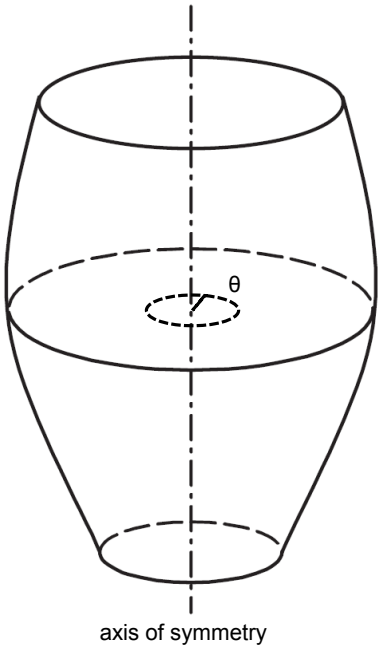


**Figure A.2:** Axial symmetry. Adapted from [143].

Such a solid can be modelled by using a 2D or 1D element, called an axisymmetric element. Hence a 3D solid can be modelled simply by using 1D or 2D elements that will substantially reduce the modelling and computational effort required.

## A.3 Model Solution

Solving a FEM problem means to solve the set of differential equation that describe the behaviour of the model. Once the model geometry has been defined and the mesh derived, we need to impose specific equations on the different domains of the model and identify boundary conditions. Boundary conditions are an essential part of the FEM to solve the model problem. The basic boundary conditions are know as *Dirichlet boundary condition* (DBC) and *Neumann boundary condition* (NBC).

For a function $y = f(x)$, DBC specifies the value of the function within an interval $[x_0,x_1]$ as:

$$y(x_0) = y_0 \tag{A.1}$$

$$y(x_1) = y_1, \tag{A.2}$$

while the NBC specifies the value that the derivative of the function has to take on the boundary:

$$\frac{dy}{dx}(x_0) = y_0 \tag{A.3}$$

$$\frac{dy}{dx}(x_1) = y_1 \tag{A.4}$$

$$\tag{A.5}$$

To solve the model a set of discrete simultaneous equations can be formulated based on the mesh generated and fed to a solver which computes a solution of the equations for the defined field variable at each node of the mesh. The solution is based on Gaussian Elimination, LU Factorisation or Iterative Method depending on the complexity of the problem. The software package used to perform the simulations reported in this thesis was COMSOL Multiphysics Modelling (www.comsol.com).

# B

# Fundamental MOSFET Design Equations

## B.1 CMOS Analogue Design

Metal-oxide-silicon field-effect transistors (MOSFETs) have a number of properties that make them extremely attractive in the field of implantable stimulator design, including their low fabrication cost, fast device scaling and the possibility to include both analog and digital circuits on the same chip. From an early stage when only n-type transistors were available, we now have access to complementary MOS (CMOS) technology, where both n-type and p-type transistors can be used in the same chip. This section provides basic information about the operation of MOSFETs and issues related to the design of CMOS circuits, which will be useful for the reader to interpret

the topologies and behaviour of the circuits presented in this chapter. We will limit the analysis of MOSFETs to their electrical properties, in terms of current/voltage characteristics in all regions of operation.

### B.1.1 MOSFETs

The conventional symbols adopted to describe an n-type MOSFET is given in Figure B.1(a). The symbol consists of four terminals, namely the gate, $G$, the source, $S$, the drain, $D$ and the bulk, $B$.

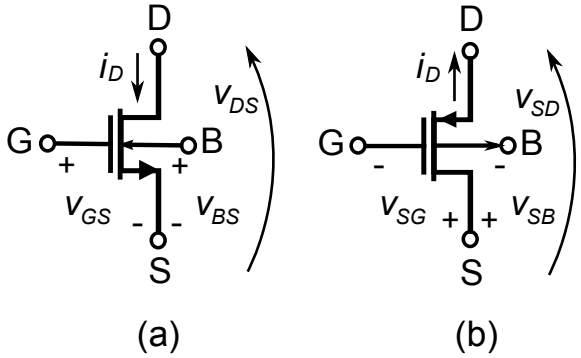


**Figure B.1:** Symbol and sign convention for (a) n-channel and (b) p-channel MOS transistor

Electrically, an MOS device works as a voltage-controlled switch that effectively conducts current[1] when the gate-source voltage, $V_{GS}$, is approximately equal to a threshold voltage, $V_T$. If the applied drain-source voltage, $V_{DS}$ is less than $V_{GS} - V_T$, then the MOS will operate in what is known as the *triode region*[2]. In this region the drain current is given by:

$$I_D = \mu_n C_{ox} \frac{W}{L} \left[ (V_{GS} - V_T) V_{DS} - \frac{1}{2} V_{DS}^2 \right], \tag{B.1}$$

where $\mu$ is the mobility of electrons, $C_{ox}$ is the gate oxide capacitance per unit area, $W$ and $L$ are the width and length of the MOS device, respectively. Eq. B.1 forms a parabola with a peak at $V_{DS} = V_{OV} = V_{GS} - V_T$, where $V_{OV}$ is known as the

[1] As we shall see later in the chapter an MOS can conduct current also under different conditions from the one described here

[2] This region is also known as the linear region.

*overdrive voltage* and plays a major role in the design of analogue CMOS circuits as we shall see later in this chapter. If $V_{DS} << 2(V_{GS} - V_T)$, then the drain current approximates to:

$$I_D \approx \mu_n C_{ox} \frac{W}{L}(V_{GS} - V_T)V_{DS} \tag{B.2}$$

and the drain current is a linear function of $V_{DS}$. This region of operation is called *deep triode region*, where the MOS can be represented by a linear resistor equal to:

$$R_{ON} = \frac{1}{\mu_n C_{ox} \frac{W}{L}(V_{GS} - V_T)}. \tag{B.3}$$

For $V_{DS} > V_{GS} - V_T$ the drain current no longer follows the parabolic behaviour described by Eq. B.1, but enters what is known as the *saturation region*, where it is modelled as:

$$I_D = \frac{1}{2}\mu_n C_{ox} \frac{W}{L}(V_{GS} - V_T)^2. \tag{B.4}$$

In this case the MOS can be operated as a current source, as the drain current is no longer dependent on the voltage drop across the MOS[3]. Operated in the saturation region, the MOS effectively converts an input voltage into an output current. A figure of merit describing such behaviour is the *transconductance*, expressed as:

$$g_m = \left[\frac{\partial I_D}{\partial V_{GS}}\right]_{V_{DS,const}} \tag{B.5}$$

$$= \mu_n C_{ox} \frac{W}{L}(V_{GS} - V_T). \tag{B.6}$$

The transconductance, $g_m$, can also be expressed as a function of $I_D$ as:

[3]In reality $I_D$ is still slightly dependent on $V_{DS}$ due to an effect known as *channel length modulation.*

$$g_m = \sqrt{2\mu_n C_{ox} \frac{W}{L} I_D}. \tag{B.7}$$

### B.1.2 Channel Length Modulation

The channel length modulation represents a second-order effect occurring due to the fact that the effective length of the channel that forms between the source and gate during conduction, depends of $V_{DS}$. In turn, the drain current still depends on $V_{DS}$ and it is expressed as:

$$I_D = \frac{1}{2}\mu_n C_{ox} \frac{W}{L}(V_{GS} - V_T)^2(1 + \lambda V_{DS}) \tag{B.8}$$

where $\lambda$ is the channel-length modulation coefficient, which represents the relative variation in length for a given increment of $V_{DS}$ and becomes smaller as $L$ increases. The expression of the transconductance $g_m$ is then modified to:

$$g_m = \mu_n C_{ox} \frac{W}{L}(V_{GS} - V_T)(1 + \lambda V_{DS}). \tag{B.9}$$

In addition, Eq. B.4 assumed an infinite output resistance. However, due to the channel length modulation, the output resistance of a MOS in saturation region is finite and given by:

$$r_o = \frac{1}{\partial I_D / \partial V_{DS}} \tag{B.10}$$

$$= \frac{1}{\frac{1}{2}\mu_n C_{ox} \frac{W}{L}(V_{GS} - V_T)^2 \cdot \lambda} \tag{B.11}$$

$$\approx \frac{1}{\lambda I_D}. \tag{B.12}$$

### B.1.3 Sub-threshold Conduction

So far we have assumed that a MOS can be operated only when $V_{GS} \geq V_T$ and the MOS is off otherwise. When the gate-source voltage is less than the threshold voltage, however, the MOS will still be conducting, while operating in the *subthreshold region*. In this region $I_D$ exhibits an exponential dependence on $V_{GS}$ and, in saturation, it is expressed as:

$$I_D = I_{spec} e^{\frac{V_{GS}}{nU_T}} \tag{B.13}$$

where $I_{spec}$ is the specific current given by $I_{spec} = 2n\beta U_T^2$, with $\beta = \mu C_{ox}$, $n$ is a slope factor (usually between 1 and 2), representing a nonideality behaviour and $U_T$ is the thermal voltage, given by $U_T = kT/q$. For a square MOS ($W = L$), $I_{spec}$ is in the range between 10n and 1$\mu$A. To operate the MOS in saturation, therefore, $I_D$ needs to be smaller than 1$\mu$A. This value can be increased by increasing the $W/L$ ratio. Additionally, to ensure operation in the saturation region, $V_{DS}$ must be 4 or 5 times $U_T$. In subthreshold region, the transistor is greatly affected by channel-length modulation. Figure B.2 compares the output characteristic of a short-channel (L=800nm) and long-channel (L=10$\mu$m) transistor operated in subthreshold region.

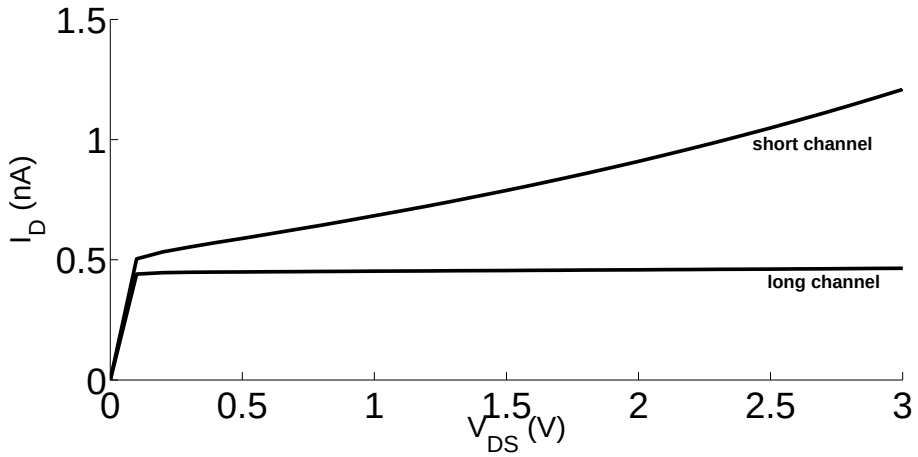


**Figure B.2:** Output characteristic of short and long channel transistor operating in subthreshold region.

## B.2 Transistor Mismatch

Mismatch can be observed between the parameters of equally designed MOS transistors. This is the result of random processes that occur during device fabrication. The matching properties of MOS transistors can be calculated in terms of the drain current as:

$$I_D = \beta \left\{ \frac{(V_{GS} - V_T - V_{DS}/2)V_{DS}}{1 + \vartheta(V_{GS} - V_T)} \right\} \tag{B.14}$$

in linear region and:

$$I_D = \frac{\beta}{2} \left\{ \frac{(V_{GS} - V_T)^2}{1 + \vartheta(V_{GS} - V_T)} \right\} \tag{B.15}$$

in saturation region, where $\beta = C_{ox}\mu W/L$ is the gain factor and the threshold voltage, $V_T$ is given by a constant $V_{T0}$ and a component dependent of the source-bulk voltage, $V_{SB}$:

$$V_T = V_{T0} + K(\sqrt{|V_{SB}| + 2\phi_F} - \sqrt{2\phi_F}) \tag{B.16}$$

The current mismatch of a MOSFET is related to the mismatch of the device parameters $V_T$, $\beta$, and $\vartheta$. A mismatch model takes into account the variances $\sigma^2(\Delta V_T)$, $\sigma^2(\Delta\beta)$ and $\sigma^2(\Delta\vartheta)$ of the threshold voltage difference, the gain factor difference and the mobility reduction difference. The total variance of the drain current is given by:

$$\sigma^2 \left( \frac{\Delta I_D}{I_D} \right) = S_{V_T}^2 \sigma^2(\Delta V_T) + S_\beta^2 \sigma^2(\Delta\beta) + S_\theta^2 \sigma^2(\Delta\theta) \tag{B.17}$$

where S is the variation of the parameter with spacing, $D$. The variance of each parameter is a function of the area proportionality constant, $A$ , $S$ and $D$ according the following relations:

$$\sigma^2(\Delta V_T) = \frac{A_{V_T}^2}{WL} S_{V_T}^2 D^2 \tag{B.18}$$

$$\sigma^2(\Delta \beta) = \frac{A_{\beta}^2}{WL} S_{\beta}^2 D^2 \tag{B.19}$$

$$\sigma^2(\Delta \vartheta) = \frac{A_{\vartheta}^2}{WL} S_{\vartheta}^2 D^2 \tag{B.20}$$

## B.3 Summary of MOS I-V Equations

### B.3.1 Cut-off region

$$V_{GS} < V_T \tag{B.21}$$

$$I_D = 0 \tag{B.22}$$

### B.3.2 Linear region

$$V_{GS} > V_T \tag{B.23}$$

$$V_{DS} < V_{GS} - V_T \tag{B.24}$$

$$I_D = \mu_n C_{ox} \frac{W}{L} \left[ (V_{GS} - V_T) V_{DS} - \frac{1}{2} V_{DS}^2 \right] \tag{B.25}$$

$$R_{ON} = \frac{1}{\mu_n C_{ox} \frac{W}{L} (V_{GS} - V_T)} \tag{B.26}$$

### B.3.3 Saturation region

$$V_{GS} > V_T \tag{B.27}$$

$$V_{DS} > V_{GS} - V_T \tag{B.28}$$

$$I_D = \frac{1}{2}\mu_n C_{ox}\frac{W}{L}(V_{GS} - V_T)^2(1 + \lambda V_{DS}) \tag{B.29}$$

$$\tag{B.30}$$

### B.3.4 Subthreshold region

$$V_{GS} < V_T \tag{B.31}$$

$$I_D = I_{spec}e^{\frac{V_{GS}}{nU_T}} \tag{B.32}$$

$$I_{spec} = 2n\beta U_T^2 \tag{B.33}$$

## B.4 MOS Parameters

$$K_n = \mu_n C_{OX} \tag{B.34}$$

$$\beta_n = K_N\frac{W}{L} \tag{B.35}$$

$$\lambda = \frac{1}{V_A} \tag{B.36}$$

$$V_T = V_{T0} + \gamma(\sqrt{2\phi_f + V_{SB}} - \sqrt{2\phi_f}) \tag{B.37}$$

## B.5 MOS Small-signal Parameters

$$g_m = \mu_n C_{ox} \frac{W}{L}(V_{GS} - V_T)(1 + \lambda V_{DS}) \tag{B.38}$$

$$g_m = \sqrt{2\mu_n C_{ox} \frac{W}{L} I_D} \tag{B.39}$$

$$r_o \approx \frac{1}{\lambda I_D} \tag{B.40}$$